

Stable, ultra-relativistic electron beams by laser-wakefield acceleration

JENS OSTERHOFF



München, den 10. Februar 2009

Stable, ultra-relativistic electron beams by laser-wakefield acceleration

DISSERTATION
AN DER FAKULTÄT FÜR PHYSIK
DER LUDWIG-MAXIMILIANS-UNIVERSITÄT IN MÜNCHEN

von

JENS OSTERHOFF
AUS DAMME (OLDB.)

München, den 10. Februar 2009

Erstgutachter: Prof. Dr. Ferenc Krausz
Zweitgutachter: Prof. Dr. Klaus Witte

Tag der mündlichen Prüfung: 28. Januar 2009

Abstract

The method of creating ultra-relativistic electron beams from wakefields of relativistically intense ultra-short laser pulses, which plow through dilute plasma environments, may announce a revolution in particle-accelerator engineering. By harnessing the extreme electric-potential gradients along the propagation direction of these wakes, this technology permits the generation of GeV-energy electrons on just a centimeter-scale. Thus, it fuels the quest for a drastic miniaturization of accelerator components compared to conventional radio-frequency cavities, and at the same time raises hopes to substantially reduce costs for future machines. Hence, if this technology could be advanced to reach technical maturity, it would benefit the spread of these particle sources for applications in hospitals and mid-scale research facilities with profound implications on the fields of medicine, biology, chemistry, physics and material sciences. State-of-the-art wakefield-driven electron sources almost match and sometimes even outperform their traditional counterparts with respect to certain beam parameters such as contained charge, transverse emittance, energy, or pulse duration, whereas they lag behind in other areas, such as repetition rate, longitudinal emittance, and most notably in shot-to-shot reproducibility. This inconstancy manifests itself in fluctuations of all crucial pulse parameters and may be attributed to a nonlinear dependence of the acceleration mechanism on small variations in laser and plasma conditions. Since this arguably comprises the major obstacle for a deployment of laser-driven electron bursts in real-world applications, the stabilization of the acceleration process marks a primary goal on many research agendas.

The work at hand addresses the reproducibility issue by utilizing a steady-state-flow gas cell to host the laser-plasma-interaction medium, hence reducing plasma fluctuations, and thus for the first time demonstrates high-quality electron pulses of unprecedented simultaneous shot-to-shot stability in key parameters such as energy, charge, divergence and beam pointing. These stable ultra-fast electron packages have proven to be of high quality by being suited for the routine synthesis of XUV-radiation from a table-top undulator structure. En route to these results, studies of laser guiding and laser-wakefield acceleration in capillary discharge waveguides allowed for the creation of high-energy electron beams with relativistic gamma-factors exceeding one thousand. These achievements not only provide the basis for an ongoing systematic investigation of laser-wakefield acceleration by means of methods relying on meaningful statistics facilitated by stable electron conditions, such as the investigation of the influence of laser intensity-front tilt on the acceleration process, but also might enable first applications in the near future.

Table of contents

Abstract	v
Table of contents	vii
Introduction	2
I Theoretical foundations	6
I.I Attributes of light	6
I.II Relativistic laser-matter-interaction	8
I.II.I Electron motion in an electro-magnetic field	8
I.II.II Atomic ionization mechanisms	11
I.III Attributes of plasma	16
I.III.I Debye length and characteristic spatial scales	16
I.III.II Plasma frequencies and characteristic time scales	17
I.III.III Definition of plasma	17
I.IV Laser propagation in underdense plasma	18
I.IV.I Excitation of large-amplitude Langmuir waves	18
I.IV.II Wave-breaking and electron injection	26
I.IV.III Self-modulation effects	30
I.IV.IV Laser guiding in preformed plasma-density structures	34
I.IV.V Laser wakefield acceleration scaling laws and limits	36
I.V Experimental consequences and conclusions	44
II The ATLAS high-field laser facility	45
II.I Bandwidth limit and pulse duration	45
II.II The concept of chirped-pulse amplification	47
II.III ATLAS layout and laser pulse properties	49
II.IV Concluding remarks	58
III Propagation of relativistic laser pulses through a discharge waveguide	59
III.I The slow capillary discharge waveguide	60
III.II Experimental setup and laser diagnostics	62
III.III Guiding of relativistic laser pulses	67

IV	Acceleration of electrons in a laser guiding plasma channel	72
IV.I	Electron diagnostics	72
IV.II	Generation of ultra-relativistic electron beams	77
IV.III	Summary and conclusion	85
V	Acceleration of stable electron beams from steady-state-flow gas cells	86
V.I	Context and motivation of the study	86
V.II	Steady-state-flow gas-cell properties and experimental setup	87
V.III	Experimental results and interpretation	89
V.IV	Summary and conclusion	95
VI	Electron-betatron-motion excitation by angularly chirped laser pulses	97
VI.I	Basics of particle-in-cell calculations	97
VI.II	Formation of electron-betatron oscillations	99
VI.III	Asymmetric wakefield excitation by angularly chirped laser pulses	100
VI.IV	The phenomenology of induced collective electron-betatron orbits	103
VI.V	Concluding remarks	107
VII	Concluding thoughts on future applications and developments	108
VII.I	Laser-driven undulator-radiation sources and table-top FELs	108
VII.II	Controlled injection for low energy spread electron-beam generation	110
VII.III	Staged accelerator concepts	111
VII.IV	Temporal electron-bunch characterization	111
A	An analytical dipole-spectrometer model	113
B	Electron-beam scattering off plasma particles and gas molecules	116
C	List of fundamental constants	119
	References	120
	Acknowledgements	142
	Curriculum vitae	144
	Scientific publications and honors	146

Introduction

Ultra-relativistic particle beams have developed into an essential tool currently penetrating many facets of the forefront of natural science. In this thriving field of activity, monoenergetic electron bursts at particle energies in excess of a GeV allow for the generation of coherent X-ray pulses, which are useful in medical applications, where they enable unprecedented high-resolution phase-contrast tomography, a sophisticated technology for human tissue diagnostics [BONSE and HART 1965; MOMOSE et al. 1996]. Such X-ray pulses can likewise be applied to facilitate the structural analysis of complex molecules and proteins of interest in biology and chemistry [SOLEM 1986; HENDERSON 1995], which with the advent of ultra-bright and ultra-fast free-electron-laser sources [KONDRATENKO and SALDIN 1979] may open up the possibility of time-resolved single-shot single-molecule imaging [NEUTZE et al. 2000; CHAPMAN et al. 2006]. In return, this technique will considerably advance pharmacology and medicine. Healthcare also benefits from the deployment of relativistic heavy-ion beams, which are starting to profoundly impact cancer therapy [EICKHOFF et al. 2003]. These particle beams therefore possess direct influence on our everyday lives through a diversity of applied medical research. However, in addition to a plethora of implications on practical scientific aspects, they also grant insight into fundamental principles of nature. With the commissioning of the large hadron collider, particles at TeV energies could trigger a revision of one of the basic building blocks of contemporary physics, namely the standard model of particle theory [WEINBERG 1967]. Thus, they might help to initiate a revolution of our view on the most elementary events that led to the creation of the universe as we experience it today [RANDALL 2002; ACHENBACH 2008]. Conventional sources providing these beams are based on resonantly excited radio-frequency cavities (see e.g. HUMPHRIES [1999]) and therefore are limited by material breakdown to accelerating electric-field strengths of no more than $\sim 100 \text{ MVm}^{-1}$. Given that the aforementioned applications rely on high energy particles in the multi-hundred MeV to TeV range, the size of and hence the necessary budget for high-end accelerators including the required infrastructure needs to become enormous¹. For these reasons, clearly, a novel approach in technology is desired, which allows for increased acceleration gradients in order to shrink the dimensions and the required investments for the next generation TeV-particle source. This at the same time would facilitate a more widespread distribution of current state-of-the-art multi-GeV machines. A promising route for the formation of ultra-strong particle-accelerating fields utilizes electric

¹The planned International Linear Collider (ILC), for example, would need to extend over tens of kilometers in order to enable the collision of two TeV electron bursts, driving its costs beyond the 10 billion € barrier.

potential gradients arising in large-amplitude plasma waves. Such waves can be excited by relativistic particle beams [CHEN et al. 1985] or intense laser pulses [TAJIMA and DAWSON 1979]. Hence, these processes are called beam-driven plasma wakefield acceleration (PWFA) and laser wakefield acceleration (LWFA), respectively. The latter scheme is of particular interest, since it permits the efficient creation of ultra-short and ultra-relativistic electron bunches from a setup fitting on a table-top, which is possible nowadays owing to the rapid evolution of laser technology in the past decades. This development was catalyzed by the invention of chirped-pulse amplification [STRICKLAND and MOUROU 1985], which fast-tracked the progress made in the race towards ever more powerful light flashes compressed to time scales as short as a few light-oscillation cycles. These ultra-intense bursts may be used to create extreme states of matter by exerting Gbar pressures, setting up environments heated to MeV temperatures and providing electric-field strengths exceeding those that bind inner-shell electrons to atomic cores. Hence, modern tera- to petawatt laser facilities represent tools which access plasma physics over a wide range of parameters and consequently over a manifold of different physical domains. This includes the fields of fast ignition in inertial confinement fusion [NUCKOLLS et al. 1972; TABAK et al. 1994] and laboratory astrophysics [KANE et al. 1997], requiring exceptional energy densities. Also, modern short-pulse laser systems drive secondary light sources emitting X-rays (see e.g. DAIDO [2002] and DROMEY et al. [2006]) or VUV-beams possibly suitable for attoscience² [NOMURA et al. 2008]. In addition, high-intensity laser-plasma interaction allows for the provision of compact particle sources releasing fusion neutrons [DITMIRE et al. 1999; TAYLOR et al. 2007], beamed ions [MAKSIMCHUK et al. 2000; SNAVELY et al. 2000], or, as mentioned before, ultra-relativistic electron bunches.

The vision of TAJIMA and DAWSON [1979] prepared the development of such laser-driven electron beams, which harness gigantic electric-field strengths that may only be realized in a plasma setting. In laser wakefield acceleration, an intense light pulse in a dilute plasma expels electrons from its axis of propagation by its ponderomotive force and thereby creates a plasma wake with one or more electron voids trailing the electro-magnetic driver. Inside such a cavity, longitudinal field-strengths of considerably more than 10 GVm^{-1} are created. If the intensity of the driving laser-pulse is high enough, then the plasma wave may break and inject electrons into the wakefield troughs, which in this case are violently accelerated capitalizing on the prevailing colossal electric fields. However, it took more than ten years before laser technology had become mature enough for a first successful demonstration of wakefield acceleration of externally injected 1.5 MeV electrons [CLAYTON et al. 1993]. This result in combination with further advances in laser engineering for the generation of shorter pulse durations ($\sim 1 \text{ ps}$) and increased powers ($> 1 \text{ TW}$) acted as the starting point of a number of ensuing experimental campaigns in the mid-1990s. These showed the feasibility of accelerating laser-self-injected electrons in the self-modulated laser wakefield acceleration (SM-LWFA) regime³ achieving energies well be-

²For details confer PAUL et al. [2001], HENTSCHEL et al. [2001], DRESCHER et al. [2001], and e.g. UIBERACKER et al. [2007] or CAVALIERI et al. [2007].

³See MODENA et al. [1995], TING et al. [1996], UMSTADTER et al. [1996b], GORDON et al. [1998] and LEEMANS et al. [2002].

yond 100 MeV over an effective acceleration distance of only a millimeter. Nevertheless, the obtained electron spectra were thermal in nature with an energy spread on the order of 100 % and therefore not comparable to the specifications reached at conventional accelerators.

At about the same time, an exponential increase in available computing power, a refinement of numerical algorithms and a reduction of the effective laser-plasma-interaction volume facilitated by the availability of laser pulses with ever shorter pulse durations enabled fully three-dimensional simulations of LWFA with the help of particle-in-cell (PIC) codes⁴. These codes illuminated wakefield physics in detail and predicted the existence of a continuously broken-wave scheme, dubbed bubble regime [PUKHOV and MEYER-TER-VEHN 1998], which would allow for the acceleration of laser-driven quasi-monoenergetic electron distributions, but required laser pulses of longitudinal extent of less than half the characteristic plasma wavelength. When powerful light bursts approaching this limit became accessible with durations of $\lesssim 50$ fs, first measurements reported on improved acceleration gradients of ~ 200 GVm⁻¹ [MALKA et al. 2002] and demonstrated electron beams with a normalized emittance of ~ 1 mm·mrad [FRITZLER et al. 2004], which is comparable to the emittances from the best photocathode sources. Just a few months later, the intended breakthrough result was prominently published by three independent groups. GEDDES et al. [2004], MANGLES et al. [2004] and FAURE et al. [2004] obtained well collimated electron beams with quasi-monoenergetic distributions of a few percent energy spread around ~ 100 MeV containing ~ 100 pC of charge. For the first time, laser accelerated electrons constituted a true beam with key attributes comparable to those of established sources, but generated on only a few millimeters of acceleration distance. Subsequently, progress came fast-paced⁵, which was associated with LWFA electron-bunch parameters rapidly approaching those generated from conventional machines. This endeavor spawned some high-light results, such as surpassing the GeV-energy frontier by channeling of wake-driving laser pulses [LEEMANS et al. 2006], or the controlled injection of electrons into the wake bucket by counterpropagating laser beams [FAURE et al. 2006]. Furthermore, the shot-to-shot beam reproducibility improved tremendously through careful control of various laser-pulse parameters [MANGLES et al. 2007; NAKAMURA et al. 2007; HAFZ et al. 2008], the implementation of new injection schemes [FAURE et al. 2006; GEDDES et al. 2008], and most notably by use of steady-state-flow gas cells [OSTERHOFF et al. 2008] as developed in this work.

Currently, these high-quality laser-driven electron bunches are on the verge of entering the realm of applications. Based upon this approach, an intriguing prospect represents the generation of undulator radiation and ultimately the construction of a free-electron laser (FEL) on a table-top scale [GRÜNER et al. 2007]. Albeit never measured, the duration of laser-accelerated electron bunches is expected to be on the order of a few femtoseconds, corresponding to currents in the several 10 kA range. Such charge flux would allow for greatly reduced undulator sizes by

⁴Information about three-dimensional PIC simulations can be found in numerous publications, e.g. in PUKHOV [1999], LEE et al. [2000], NIETER and CARY [2004] or GEISSLER et al. [2006].

⁵Only two years after the observation of first quasi-monoenergetic spectral features, researchers from more than twenty laboratories around the world had reproduced such ultra-relativistic electron beams. Among these are MIURA et al. [2005], HAFZ et al. [2006], HIDDING et al. [2006], HOSOKAI et al. [2006] and HSIEH et al. [2006].

a factor of ~ 10 and thus renders possible a miniaturization of the FEL concept. As an initial step, recent experiments have observed undulator light in the visible to near-infrared range [SCHLENVOIGT et al. 2008] and, employing the stable all-optical electron source described in this thesis, detected radiation with photon energies in excess of 100 eV [FUCHS et al. 2009].

All in all, laser wakefield acceleration remains among the hot topics in modern accelerator and laser-plasma science. Its prospects are captivating, their realization a formidable challenge. This dissertation reports on advances in this exciting field, and for doing so in a structured way, it is divided into the following parts:

- Chapter I** – Details the theory of wakefield acceleration and accompanying effects occurring in high-intensity laser-plasma interaction in order to facilitate the understanding of the results discussed in the following chapters.
- Chapter II** – Presents pulse properties and architecture of the ATLAS laser system, which was rebuilt partially in the framework of this study to provide sufficient intensities for the execution of LWFA experiments.
- Chapter III** – Reports on the mode-quality maintaining, efficient propagation of relativistically intense ATLAS beams through a capillary discharge waveguide over distances longer than eight times their Rayleigh length.
- Chapter IV** – Reviews experiments employing the aforementioned channeled light bursts to drive strong wakefields along the capillary waveguide, which then break, inject electrons and accelerate them to several hundred MeV of energy. Moreover, well collimated electron bunches with the smallest divergences published to-date have been observed. However, the attributes of all these beams are found to suffer from significant shot-to-shot instabilities.
Affiliated publication: KARSCH et al. [2007].
- Chapter V** – Introduces the stabilization of laser-driven electron bunches by reduction of plasma fluctuations through the operation of the capillary channel in a steady-state-flow gas-cell mode, resulting in unprecedented beam stability.
Affiliated publications: OSTERHOFF et al. [2008, 2009].
- Chapter VI** – Discusses the excitation of electron-betatron oscillations inside a wakefield structure by means of controlling the laser pulse angular chirp on the basis of experimental measurements and PIC calculations.
Affiliated publication: POPP et al. [2009].
- Chapter VII** – Outlines future developments in the field of laser wakefield acceleration and addresses a possible application with the consideration of LWFA-fed table-top undulator-radiation sources and free-electron lasers.
Affiliated publication: FUCHS et al. [2009].

The affiliated papers quoted above either form the backbone of this work [KARSCH et al. 2007; OSTERHOFF et al. 2008, 2009] or are a direct result of it [POPP et al. 2009; FUCHS et al. 2009]. For a better overview, a comprehensive list of the author's publications can be found on p. 146.

Chapter I

Theoretical foundations

Intense laser pulses propagating through plasma allow for the acceleration of electrons to ultra-relativistic energies. This chapter provides the theoretical foundations, explains the mechanism of laser wakefield acceleration (LWFA) and details other physical effects involved in this process, e.g. laser self-focusing. All this is accomplished on the basis of an analytic model. The limits of such an analytical approach are discussed in section I.IV.V and a more complete description by means of numerical calculations will be introduced subsequently. From these considerations the demands for wakefield acceleration towards laser- and plasma-parameter space are derived and summarized (section I.V), which therefore motivate the choice of conditions for the electron-acceleration experiments and simulations discussed in the following parts of this work.

I.1 Attributes of light

Light is an electro-magnetic wave. It is fully characterized by its electric and magnetic fields \vec{E} and \vec{B} , which vary in space \vec{x} and time t . These fields can be expressed by a vector potential \vec{A} and a scalar potential Φ (e.g. JACKSON [1975] or ZINTH and KÖRNER [1998]):

$$\begin{aligned}\vec{E} &= -\frac{\partial}{\partial t}\vec{A} - \nabla\Phi \\ \vec{B} &= \nabla \times \vec{A}\end{aligned}\tag{1.1.1}$$

These potentials must fulfill the corresponding wave equations that can be derived from the Maxwell equations using the Lorenz gauge:

$$\begin{aligned}\frac{1}{c^2}\frac{\partial^2\vec{A}}{\partial t^2} - \nabla^2\vec{A} &= \mu_0\vec{J} \\ \frac{1}{c^2}\frac{\partial^2\Phi}{\partial t^2} - \nabla^2\Phi &= \frac{\rho}{\epsilon_0}\end{aligned}\tag{1.1.2}$$

Here and in the following, c denotes the vacuum speed of light, ϵ_0 refers to the electric permittivity of free space and μ_0 is the vacuum magnetic permeability. These quantities are related to each other through $c = (\epsilon_0\mu_0)^{-1/2}$. Moreover, ρ represents a charge density and \vec{J} describes an electric current density. It is immediately clear that a solution of (1.1.2) propagates with c

in the absence of any charge distribution and flux. Such a solution can be given as:

$$\vec{A}(\vec{x}, t) = \vec{A}_0 \cos(\omega t - \vec{k}\vec{x} + \phi) \quad (1.1.3)$$

This expression describes a plane wave with its amplitude and polarization determined by \vec{A}_0 . \vec{k} is called the wave vector and defines the wave propagation direction, $\omega = 2\pi c\lambda^{-1}$ is the angular frequency of the wave and λ the wavelength. ϕ represents an absolute phase offset. With the above mentioned lack of charge and current, the vector-potential solution also fulfills the wave equation for Φ , since they are coupled by the employed gauge. Hence, it is possible to obtain simple expressions for the electric and magnetic fields by taking into account (1.1.1) and (1.1.3):

$$\begin{aligned} \vec{E}(\vec{x}, t) &= \vec{E}_0 \sin(\omega t - \vec{k}\vec{x} + \phi) \\ \vec{B}(\vec{x}, t) &= \vec{B}_0 \sin(\omega t - \vec{k}\vec{x} + \phi) \end{aligned} \quad (1.1.4)$$

The electric and magnetic field amplitudes are related to the vector potential amplitude by $|\vec{E}_0| = c|\vec{B}_0| = \omega|\vec{A}_0|$. From (1.1.1) and the Maxwell equations it further follows that $\vec{E} \parallel \vec{A}$, $\vec{E} \perp \vec{B}$ and $\vec{k} \perp \vec{B}$. $\vec{E} \perp \vec{k}$ is true here, but is not valid in the more general case of optical anisotropy. Combining (1.1.2) with (1.1.3) yields the dispersion relation for light in vacuum:

$$|\vec{k}|^2 = \frac{\omega^2}{c^2} \quad (1.1.5)$$

An important feature of electro-magnetic waves is their ability to transport energy with their energy flux density given by the Poynting vector (e.g. POYNTING [1920]):

$$\vec{S} = \epsilon_0 c^2 (\vec{E} \times \vec{B}) \quad (1.1.6)$$

An expression for the corresponding intensity I may be found by temporal averaging over one oscillation period of the fields in (1.1.6) and making use of the fact that $\vec{E} \perp \vec{B}$:

$$I = \langle |\vec{S}| \rangle = \epsilon_0 c \langle |\vec{E}|^2 \rangle \quad (1.1.7)$$

This intensity can also be expressed as $I = E_L (A_L \tau_L)^{-1}$. E_L represents the energy transported by a light wave within a time window τ_L through a cross-section A_L . Today's ultra-high intensity laser systems achieve energy flux densities at focus of $10^{18} \text{ W cm}^{-2}$ or more¹. According to (1.1.7), the electric field strength within the focal volume of such laser pulses can be estimated to surpass $2 \cdot 10^{12} \text{ V m}^{-1}$. These field strengths are significantly larger than the fields that tie an electron to the core inside a hydrogen atom ($\sim 5 \cdot 10^{11} \text{ V m}^{-1}$).

Electro-magnetic waves exchange energy and interact with their environment only in discrete quantities of measure E_{ph} [PLANCK 1901; EINSTEIN 1905b], the so called quanta or photons:

$$E_{\text{ph}} = \hbar\omega \quad (1.1.8)$$

¹Currently, the published record stands at $\sim 2 \cdot 10^{22} \text{ W cm}^{-2}$ [YANOVSKY et al. 2008].

\hbar is the reduced Planck constant. The photon energies in the visible light spectrum can be evaluated from relation (1.1.8) to range from 1.5 eV at $\lambda = 800$ nm to 3.1 eV at $\lambda = 400$ nm. Modern laser technology allows for the storage of several joules of energy within a few tens of femtoseconds and thus reaches peak powers $P = E_L \tau_L^{-1}$ well beyond 100 TW. Hence, the number of photons in such a light burst around 800 nm wavelength is on the order of 10^{19} . Moreover, each photon carries a quantized momentum \vec{p}_{ph} [EINSTEIN 1909]:

$$\vec{p}_{\text{ph}} = \hbar \vec{k} \quad (1.1.9)$$

As a consequence, photons can be assigned a relativistic mass $m_{\text{ph}} = \vec{p}_{\text{ph}} c^{-1} = E_{\text{ph}} c^{-2}$, meaning they obey gravity [EINSTEIN 1905a, 1911, 1915]. This is true, although light quanta feature no rest mass for they travel with c . Photon momentum has yet another important implication: light momentum transfer results in radiation pressure $P_L = I c^{-1}$. For high intensity laser beams with $I \geq 10^{18}$ W cm $^{-2}$, P_L is substantial and exceeds 300 Mbar.

I.II Relativistic laser-matter-interaction

Very intense light pulses exhibit extreme electric fields ($|\vec{E}_0| \geq 2 \cdot 10^{12}$ V m $^{-1}$), exert extreme pressures ($P_L \geq 300$ Mbar) and carry extreme powers ($P \geq 100$ TW) as shown in section I.I. The interaction of such kind of radiation with matter therefore proceeds under extraordinary conditions. The influence of these electro-magnetic waves on isolated electrons (section I.II.I) as well as on single atoms and ions (section I.II.II) will be investigated in the following.

I.II.I Electron motion in an electro-magnetic field

The equation of motion for a free electron of charge e and mass m_e in an oscillating light field of the form (1.1.4) albeit with temporally and spatially changing field envelopes $\vec{E}_0(\vec{x}, t)$ and $\vec{B}_0(\vec{x}, t)$ can be compiled under consideration of the Lorentz force [MAXWELL 1861]:

$$m_e \frac{d}{dt} (\gamma \vec{v}) = -e \left(\vec{E} + \vec{v} \times \vec{B} \right) \quad (1.2.1)$$

\vec{v} represents the electron velocity. The corresponding relativistic factors are $\gamma = (1 - \beta^2)^{-1/2}$ and $\beta = |\vec{v}| c^{-1}$. For sub-relativistic speeds ($\vec{v} \ll c$) the $\vec{v} \times \vec{B}$ component is negligible since $|\vec{B}| = |\vec{E}| c^{-1}$ (cf. section I.I). In this case $\gamma \approx 1$ and (1.2.1) reduces to $m_e \frac{d\vec{v}}{dt} = -e \vec{E}$ from which the electron quiver velocity can easily be found by integrating over time:

$$\vec{v}(\vec{x}, t) = -\frac{e}{m_e} \int \vec{E}_0(\vec{x}, t) \cdot \sin(\omega t - \vec{k}\vec{x} + \phi) dt + \vec{v}_0 \quad (1.2.2)$$

Here, the integration constant \vec{v}_0 describes the initial electron velocity, which will be set to zero for the sake of simplicity. The electron quiver energy is defined as $E_q = \frac{1}{2} m_e |\vec{v}|^2$. Averaging over one oscillation period of E_q yields an expression for the ponderomotive potential U_P . Generally,

this can only be done in the slowly varying envelope approximation, meaning the envelope of the electric field $\vec{E}_0(\vec{x}, t)$ must change insignificantly on the time scale of an electric field oscillation and therefore can be regarded as constant over one field cycle. That leads to:

$$U_P = \langle E_q \rangle = \frac{e^2}{4m_e\omega^2} |\vec{E}_0|^2 \approx 9.33 \cdot 10^{-6} I \lambda^2 \text{ in eV} \quad (1.2.3)$$

The ponderomotive potential U_P results in a force $\vec{F}_P = -\vec{\nabla}U_P$ directed along the intensity gradient of a laser-pulse envelope perpendicular to the laser propagation direction and hence pushes electrons towards regions of lower energy flux density, e.g. for Gaussian shaped beams out of focus. This statement and eq. (1.2.3) are valid for light pulses that are not strong enough to accelerate electrons to relativistic speeds and which do not feature substantial intensity modulations on the time scale of an electric field oscillation. A more rigorous derivation of the ponderomotive force in the case of relativistic field amplitudes has been accomplished by BAUER et al. [1995], STARTSEV and MCKINSTRIE [1997], and QUESNEL and MORA [1998]. However, the resulting expressions are complex and do not considerably further the understanding of the concept of ponderomotive pressure in this context. Hence they are not explicitly given here.

A convenient way to assess the relative strength of an electro-magnetic pulse and therefore to determine the importance of relativistic effects in the interaction of a light wave with matter is provided by the normalized vector potential (e.g. GIBBON [2005]):

$$a_0 = \frac{e|\vec{A}|}{m_e c} \approx 8.5 \cdot 10^{-6} \sqrt{I} \lambda \quad (1.2.4)$$

a_0 equals unity when the kinetic energy gain of an electron in half a light wave cycle is comparable to its rest mass energy $E_{\text{rest}} = m_e c^2$. Thus $a_0 = 1$ marks the transition from sub-relativistic kinetics ($a_0 \ll 1$) to the relativistic regime ($a_0 \gtrsim 1$). Today's ultra-intense laser systems readily cross this threshold, which is reached at:

$$I_{\text{rel}} = \frac{2\pi^2 \epsilon_0 m_e^2 c^5}{e^2 \lambda^2} \approx 1.37 \cdot 10^6 \lambda^{-2} \text{ in W cm}^{-2}$$

For such intensities the $\vec{v} \times \vec{B}$ term in (1.2.1) cannot be neglected anymore. It will result in an additional electro-magnetic-force component pointing into the direction of laser propagation \vec{k} . Unlike in the non-relativistic case this entails an electron ejection from high intensity regions under an angle Θ against \vec{k} of decisively less than 90° . This Θ may be determined by comparing the momentum components parallel p_{\parallel} and perpendicular p_{\perp} to \vec{k} of an electron initially at rest, which is done by investigating its kinetic energy boost ΔE_{kin} after being expelled from the interaction zone:

$$\Delta E_{\text{kin}} = E_{\text{tot}} - E_{\text{rest}} = (\gamma - 1) m_e c^2$$

with $E_{\text{tot}} = \gamma m_e c^2$ identifying the total relativistic electron energy. The energy gain ΔE_{kin} is extracted from the radiation field by photon momentum transfer of N light quanta (see

equation 1.1.9). It follows from conservation of parallel momentum and by application of the dispersion relation for electro-magnetic waves in vacuum (1.1.5):

$$p_{\parallel} = N\hbar|\vec{k}| = (\gamma - 1) m_e c$$

Next, a correlation between p_{\parallel} and p_{\perp} can be derived by inserting the laser-field potentials (1.1.1) into the Lorentz force equation (1.2.1). Under consideration of the Lorenz gauge an integration of the longitudinal and transverse force components yields (for additional details see e.g. BARDSLEY et al. [1989] or GIBBON [2005]):

$$p_{\parallel} = \frac{p_{\perp}^2}{2m_e c}$$

Consequently, the emission angle Θ is given by:

$$\tan \Theta = \frac{p_{\perp}}{p_{\parallel}} = \sqrt{\frac{2}{\gamma - 1}}$$

MOORE et al. [1995] and MEYERHOFER [1997] verified this result in experiments and simulations. When Θ is sufficiently small, an ultra-relativistic electron can be captured within the laser field and travel almost parallel with the accelerating pulse over long distances and by this in theory reach energies in excess of 1 GeV [WANG et al. 2001]. Numerous other laser-driven electron-acceleration schemes in vacuum have been proposed such as the beat-wave scheme [ESAREY et al. 1995], tailored laser focii [STUPAKOV and ZOLOTOREV 2001] or the deployment of additional static magnetic fields [KATSOULEAS and DAWSON 1983; CHERNIKOV et al. 1992]. Hence it can be summarized that the acceleration of electrons by light waves in vacuum is possible with a net energy gain². This does not contradict the Lawson-Woodward Theorem [WOODWARD 1947; LAWSON 1979] which states that an isolated electron cannot experience a net energy gain by interacting with an electro-magnetic field when obeying certain restrictions:

- a - The interaction region is infinite.
- b - No boundaries are present.
- c - The electron is highly relativistic along the acceleration path.

² This is principally not only true for electrons but for all charged particles including ions of mass m_i and charge $Z_i e$. As may be shown in an equivalent fashion to the derivation of equations (1.2.1) and (1.2.2) with the help of (1.2.4), accelerating an ion to sub-relativistic velocities v_i scales with:

$$\frac{v_i}{c} = \frac{1}{2} Z_i \frac{m_e}{m_i} a_0$$

Therefore, the speed of an ion and also its displacement from the stationary position is smaller by a factor of $m_e m_i^{-1} < 5.5 \cdot 10^{-4}$ compared to an electron inside the same laser field due to its higher inertia. This implies that the minimum intensity that is needed to accelerate ions to relativistic intensities scales with $m_e^2 m_i^{-2}$, which sets a lower intensity threshold of $\sim 10^{24} \text{ W cm}^{-2}$ at $\lambda = 800 \text{ nm}$ for the most mobile ions available, ionized hydrogen. Such strong laser pulses do not exist up to date. Hence all ion movement on the time scale of a laser-field oscillation can be neglected in the following parts of this work and all ions will be regarded as part of an immobile background.

- d - No static electric or magnetic fields are present.
- e - Non-linear effects can be neglected.

As a result, one or more of these requirements must be violated for net electron acceleration to occur. It is immediately clear that restriction - a - cannot be fulfilled under realistic conditions since every interaction region is limited to the laser spot size. In a plasma most constrictions above do not apply. This leads to the existence of efficient ways of electron acceleration in such a medium, e.g. wakefield acceleration (see section I.IV.I) or direct laser acceleration in analogy to an inverse free-electron laser [PUKHOV and MEYER-TER-VEHN 1998; PUKHOV et al. 1999].

I.II.II Atomic ionization mechanisms

Owing to the extreme field and energy-density properties of high intensity laser beams (confer section I.I) they constitute ideal tools for the purpose of atomic ionization and hence plasma production. In a simplified way plasma can be described as a medium of ionized matter in which one or more free electrons are present (for a thorough definition see section I.III.III). This section will investigate the different interaction regimes of intense light waves with single atoms and ions leading to ionization. Whether multi-photon mechanisms or strong-field effects dominate in such an interaction process is determined by the ratio of atomic ionization potential I_P to the ponderomotive potential of the electromagnetic field U_P and is expressed by the Keldysh parameter [KELDYSH 1965; PERELOMOV et al. 1966]:

$$\gamma_K = \sqrt{\frac{I_P}{2U_P}}$$

Here, two cases must be distinguished: when $\gamma_K > 1$, then the electric field of a light wave does not alter the inner-atomic electric fields significantly. Therefore the incident electro-magnetic wave can be considered as a small perturbation to the Coulomb potential to which the bound electrons are exposed. Hence this regime can be treated quantum mechanically by perturbation theory (see multi-photon ionization below). For $\gamma_K \ll 1$, the propagating light fields may not be regarded as small perturbations anymore. The inner-atomic fields are distorted in a way that bound electron states tunnel out of the deformed potential well (see tunnel ionization) or escape over the modified Coulomb barrier (see barrier-suppression ionization). The meaning of the Keldysh-parameter picture becomes a little vague for many-electron systems, in which the two γ_K -regimes are not separable as easily anymore [LAMBROPOULOS 1985].

Multi-photon ionization

Light with an intensity not sufficient to significantly modify the electric field of an atomic nucleus may ionize matter by multi-photon processes. During multi-photon ionization an electron in state $|i\rangle$ must absorb N photons each with an energy E_{ph} in order to overcome its ionization potential I_P and enter into an unbound state $|f\rangle$, so that $I_P \leq NE_{ph}$ holds true (confer figure

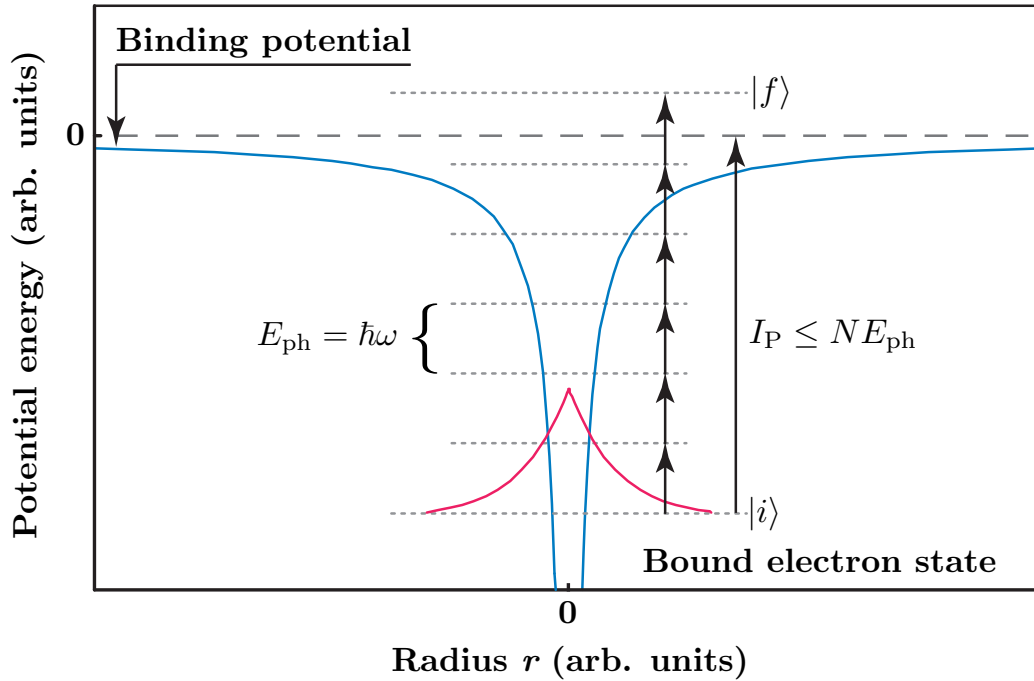


Figure 1.2.1 – Multi-photon ionization is a process in which an electron bound to an atomic core absorbs N photons of frequency ω such that it overcomes its ionization potential $I_P \leq N\hbar\omega$ and therefore shifts from state $|i\rangle$ to a free state $|f\rangle$ into the continuum.

1.2.1). The probability for this mechanism to occur depends on the photon density or intensity I to the power of N . The corresponding ionization rate $\Gamma_{i \rightarrow f}$ can be derived through perturbation theory by including N -th order photon dipole transitions [MAINFRAY and MANUS 1991] and is given by:

$$\Gamma_{i \rightarrow f} = \sigma_{i \rightarrow f}^{(N)} I^N$$

The cross-section $\sigma_{i \rightarrow f}^{(N)}$ is defined according to Fermi's golden rule [DIRAC 1927; FERMI 1950]:

$$\sigma_{i \rightarrow f}^{(N)} = 2\pi (2\pi\alpha\omega)^N g_N(\omega) \cdot \left| \sum_{|l_{N-1}\rangle} \sum_{|l_{N-2}\rangle} \cdots \sum_{|l_1\rangle} \frac{\langle f|H'|l_{N-1}\rangle \langle l_{N-1}|H'|l_{N-2}\rangle \cdots \langle l_1|H'|i\rangle}{[\omega_{i \rightarrow l_{N-1}} - \omega(N-1)][\omega_{i \rightarrow l_{N-2}} - \omega(N-2)] \cdots [\omega_{i \rightarrow l_1} - \omega]} \right|^2$$

All intermediate states $|l_j\rangle$ with $(j \in \mathbb{N}) \wedge (1 \leq j < N)$ must be included in the sum. The frequency corresponding to a certain dipole transition can be obtained as $\omega_{a \rightarrow b} = \hbar^{-1}(E_b - E_a)$ with E_a and E_b being the binding energies of state $|a\rangle$ and $|b\rangle$, respectively. α is the atomic fine structure constant, H' denotes a perturbed Hamiltonian describing the quantum mechanical system and $g_N(\omega)$ represents the frequency dependent density of states, i.e. the number of available quantum mechanical states at each energy level.

Historically, first measurements of multi-photon-ionization generated free electrons were reported by VORONOV and DELONE [1965] and AGOSTINI et al. [1968]. In the experimental part

of this work, which is discussed in chapters III, IV and V, multi-photon ionization plays just a peripheral role. Here, the Keldysh parameter decreases below 1 for laser intensities above $1.1 \cdot 10^{14} \text{ W cm}^{-2}$. Since the average energy flux density in the presented experiments is on the order of $10^{18} \text{ W cm}^{-2}$, this type of multi-photon processes can be made responsible only for ionization events in the spatial and temporal low-intensity wings of the light wave, which may nevertheless become critical in the case of an insufficient laser contrast (confer chapter II).

Tunnel ionization

When γ_K drops significantly below unity, the modification to the electric field of an atom induced by an approaching electro-magnetic wave cannot be considered a small perturbation anymore. Therefore the mathematical description discussed in the previous subsection breaks down. The incoming light wave alters the atomic potential in a way that bound electron states may tunnel through the now finite thickness Coulomb barrier (see figure 1.2.2). This interaction is still a multi-photon process, but can be treated quasi-classically with the help of the so called WKB-approximation [WENTZEL 1926; KRAMERS 1926; BRILLOUIN 1926] which simplifies the description of the tunneling event. AMMOSOV, DELONE, and KRAINOV [1986] have developed a tunnel-ionization-model (the ADK-model) introducing the cycle-averaged tunneling rate Γ_{ADK} , which is valid for complex atoms as well as multiply charged ions:

$$\Gamma_{\text{ADK}} = C_{n^*l^*}^2 f_{lm} \sqrt{2} |I_P| e^{-\Sigma} [\pi \Sigma]^{-\frac{1}{2}} [3\Sigma]^{2n^* - |m| - 1} \quad (1.2.5)$$

$$\text{with} \quad C_{n^*l^*}^2 = \frac{2^{2n^*}}{n^* \Gamma(n^* + l^* + 1) \Gamma(n^* - l^*)}$$

$$f_{lm} = \frac{(2l + 1) (l + |m|)!}{2^{|m|} |m|! (l - |m|)!}$$

$$\Sigma = \frac{2 (2|I_P|)^{\frac{3}{2}}}{3 |\vec{E}_0|}$$

The effective principal and azimuthal quantum numbers are given by $n^* = Z(2|I_P|)^{-1}$ and $l^* = n^* - 1$, respectively. l represents the default azimuthal and m the magnetic quantum number, Z denotes the charge state of the atom. Equation (1.2.5) is given in atomic units and includes the Gamma function Γ . The validity of this expression has been experimentally confirmed by AUGUSTE et al. [1992] over an intensity range spanning five orders of magnitude up to $\sim 10^{18} \text{ W cm}^{-2}$. The ADK-model will fail at even higher photon densities when approaching the relativistic threshold $a_0 \approx 1$ since it does not include magnetic-field effects, which then start to kick in. This part of parameter space has not been explored thoroughly yet and is part of ongoing experimental and theoretical [MILOSEVIC et al. 2002] research.

Barrier suppression ionization

Once the electric field strength of a light wave is strong enough to not just deform an atomic potential barrier, but to suppress it completely below a given bound electron state, the electron

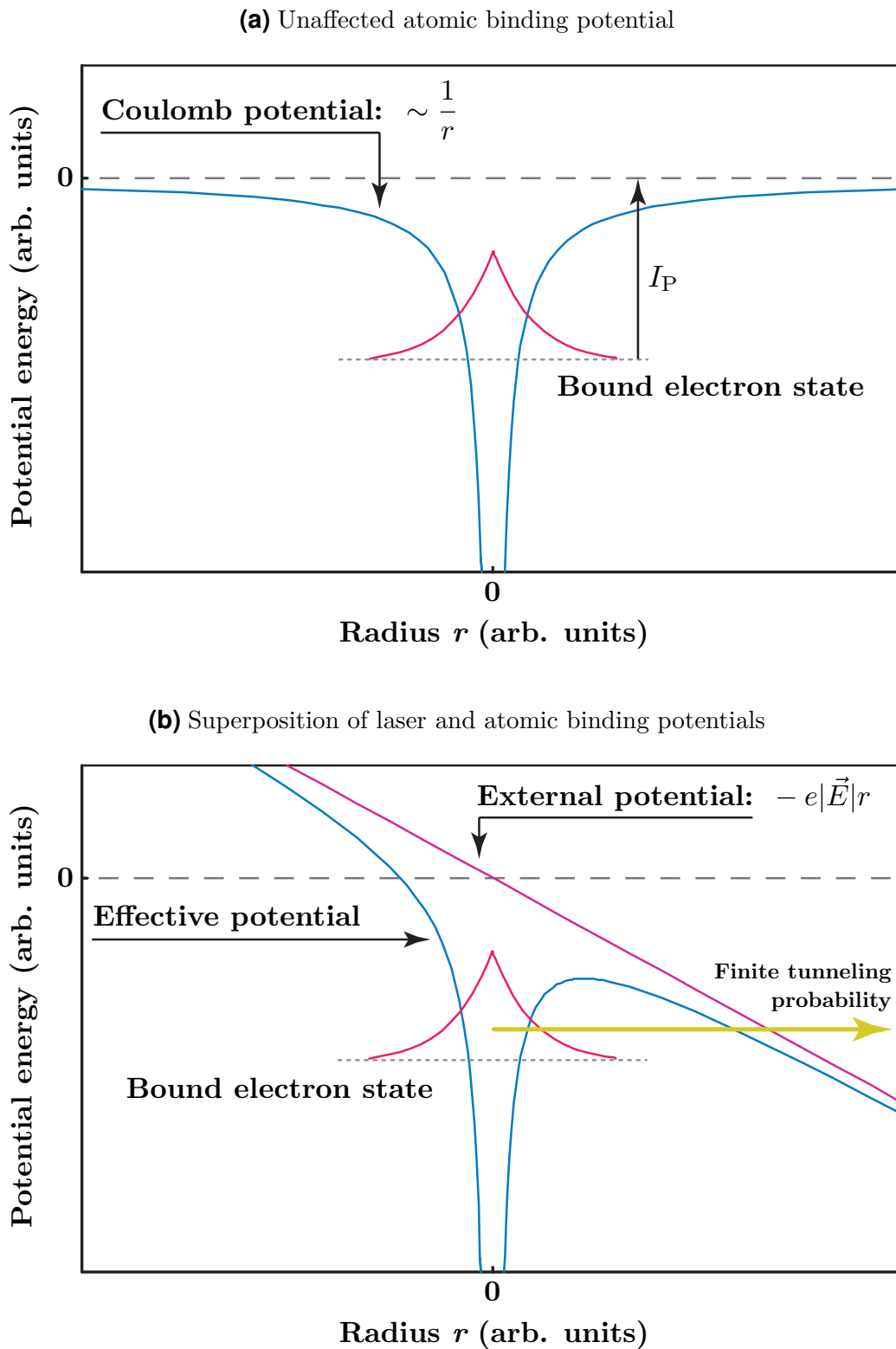


Figure 1.2.2 – Tunnel ionization describes the process during which a bound electron may tunnel through a deformed atomic potential barrier. This ionization mechanism is prohibited in an undisturbed potential well due to its infinite Coulomb wall thickness (a). However, if a strong electric field is present (e.g. a very intense laser), the atomic binding potential can be significantly altered in such a way that the tunneling probability becomes finite (b).

(a) Noble gas ions			(b) Miscellaneous ions		
Ion	I_P (eV)	I_{BSI} (W cm $^{-2}$)	Ion	I_P (eV)	I_{BSI} (W cm $^{-2}$)
He $^+$	24.59	$1.4 \cdot 10^{15}$	H $^+$	13.61	$1.4 \cdot 10^{14}$
He $^{2+}$	54.42	$8.8 \cdot 10^{15}$	C $^+$	11.2	$6.4 \cdot 10^{13}$
Ne $^+$	21.6	$8.6 \cdot 10^{14}$	C $^{4+}$	64.5	$4.3 \cdot 10^{15}$
Ne $^{2+}$	40.96	$2.8 \cdot 10^{15}$	N $^{5+}$	97.9	$1.5 \cdot 10^{16}$
Ne $^{7+}$	207.3	$1.5 \cdot 10^{17}$	O $^{6+}$	138.1	$4.0 \cdot 10^{16}$
Ar $^{8+}$	143.5	$2.6 \cdot 10^{16}$			
Xe $^+$	12.13	$8.6 \cdot 10^{13}$			
Xe $^{8+}$	105.9	$7.8 \cdot 10^{15}$			

Table 1.2.1 – Barrier suppression intensities I_{BSI} and ionization potentials I_P for noble gas ions (a) and miscellaneous other ions (b) treatable by (1.2.6).

escapes and the atom is left ionized. This mechanism is called barrier suppression ionization (BSI). Strictly speaking BSI represents nothing else than a special case of tunnel ionization with a potential barrier lowered below I_P , therefore the ADK-model (1.2.5) still applies. In addition, a simple classical estimate of the barrier-suppression threshold in intensity can be obtained by analyzing the electric potential V for an electron in the vicinity of a central charge Ze under the presence of an external electric field \vec{E} changing linearly with radius r :

$$V(r) = -\frac{Ze^2}{4\pi\epsilon_0 r} - e|\vec{E}|r$$

The temporal variation of \vec{E} must be small on the time scale of electron dynamics in the given potential well. Then an expression for the radius r_{max} where $V(r_{\text{max}})$ has a local maximum, i.e. where the barrier peak is located, can be derived by solving $dV(r)(dr)^{-1} = 0$ for $r = r_{\text{max}}$:

$$r_{\text{max}} = \sqrt{\frac{Ze}{4\pi\epsilon_0|\vec{E}|}}$$

The light intensity I_{BSI} corresponding to a minimum $|\vec{E}|$ necessary to suppress a barrier below the ionization threshold I_P is thus given by evaluating $V(r_{\text{max}}) = I_P$ and obeying (1.1.7):

$$I_{\text{BSI}} \geq \frac{I_P^4 \pi^2 c \epsilon_0^3}{2Z^2 e^6} \gtrsim 4.00 \cdot 10^9 \frac{I_P^4}{Z^2} \text{ in W cm}^{-2} \text{ with } [I_P] = \text{eV} \quad (1.2.6)$$

This estimate yields good results for a number of ions. It works particularly well for noble-gas-like shell configurations (verified by AUGST et al. [1989] and AUGUSTE et al. [1992]). An in-depth analysis of tunnel-ionization mechanisms and the interaction of laser pulses with single atoms in general can be found in DELONE and KRAINOV [1994]. Barrier suppression ionization constitutes the predominant process generating plasma from diatomic hydrogen in the experiments described in chapter V. The employed light intensities there exceed 10^{18} W cm $^{-2}$, whereas the I_{BSI} -threshold for hydrogen is four orders of magnitude less than that (cf. tab. 1.2.1).

I.III Attributes of plasma

The ionization of matter as discussed previously entails the presence of unbound electrons in a volume filled with positively charged atomic trunks. Under certain conditions, which will be defined below, this mixture of electrons and ions is called a plasma. The properties of plasma are unique and therefore plasma is sometimes referred to as one of the five states of matter (besides Bose-Einstein-condensate, solid, liquid and gas). Inside such a medium diverse collective effects between the electrically interacting species can occur, which will be investigated in the following and which ultimately allow for electron acceleration in laser-driven plasma wakefields.

I.III.I Debye length and characteristic spatial scales

Plasmas typically feature the property of quasi-neutrality³, meaning they appear electrically neutral on length scales larger than the Debye length λ_D over which contrarily charged particles of different species start to shield each other (e.g. GOLDSTON and RUTHERFORD [1998]):

$$\lambda_D = \sqrt{\frac{\epsilon_0 k_B}{e^2} \left(\frac{n_e}{T_e} + \sum_{\text{ion sorts}} \frac{Z_i n_i}{T_i} \right)^{-1}} \quad (1.3.1)$$

Here, k_B is Boltzmann's constant, n_e and T_e are the electron density and temperature, respectively. Correspondingly, n_i denotes the density of an ion species, T_i specifies its temperature and Z_i represents the charge state. This equation requires the particles in each population to reside in thermal equilibrium. However, thermal balance between particles of differing species is no precondition for the expression to be valid. Such a multi-temperature scenario may appear on short time scales in weakly-coupled systems (see below) of two or more particle sorts with different temperatures, e.g. as encountered in plasmas for wakefield acceleration, in which the electron thermal energies significantly exceed the ion thermal energies $T_e \gg T_i$.

The Debye length is directly connected to another important quantity, the plasma parameter:

$$\Lambda = \frac{4\pi}{3} n_x \lambda_D^3 \propto n_x^{-1/2}$$

which represents the number of particles of species x and of density n_x located within a sphere of radius λ_D (e.g. FITZPATRICK [2006]). In the case of $\Lambda \ll 1$, the plasma is called strongly coupled. This entails the Debye volume being sparsely populated, the kinetics of charged particles being dominated by one another's electrostatic influence and thus, individual scattering events being responsible for the particle motion. Strictly, such a system cannot be defined a plasma anymore due to its lack of collective behavior. These media are cold and dense in contrast to systems with $\Lambda \gg 1$, which are hot and dilute. Those plasmas are termed weakly coupled, since the Debye volume is densely populated and individual scattering events are rare compared to collective interactions. Owing to the fact that laser generated plasmas in LWFA environments

³An example of a non-neutral plasma is a beam of charged particles.

are usually weakly coupled, the following description focuses on the latter regime and neglects the complicated strongly coupled case without losing its validity.

I.III.II Plasma frequencies and characteristic time scales

On scale lengths smaller than λ_D there is no electric screening effect and hence, an infinitesimal displacement $\delta\vec{x}$ of a slab of plasma electrons against an ion background will result in a restoring force of the form $\vec{F}_{\text{res}} = -q_{\text{dis}}\vec{E}_{\text{res}} = m_{\text{dis}}\ddot{\delta\vec{x}}$ with the total displaced charge $q_{\text{dis}} = -en_e A_{\text{dis}}|\delta\vec{x}|$ and the total displaced mass $m_{\text{dis}} = m_e n_e A_{\text{dis}}|\delta\vec{x}|$. A_{dis} characterizes the area over which the displacement $\delta\vec{x}$ is executed. From Gauss' Law follows $|\vec{E}_{\text{res}}| = \epsilon_0^{-1}\sigma$ with $\sigma = -en_e|\delta\vec{x}|$ being the plasma slab surface charge density. This yields an equation of motion of the following form:

$$\frac{d^2}{dt^2}|\delta\vec{x}| + \frac{e^2 n_e}{m_e \epsilon_0}|\delta\vec{x}| = 0$$

As can easily be seen, this expression describes a harmonic oscillation with the frequency:

$$\omega_{p,e} = \sqrt{\frac{e^2 n_e}{m_e \epsilon_0}} \quad (1.3.2)$$

The electron plasma frequency $\omega_{p,e}$ is the basic angular oscillation frequency of so called plasma or Langmuir waves and defines a time scale τ_e on which collective electron effects in a plasma take place. Analogously, plasma frequencies for each ion population set the corresponding time scales τ_i of ion dynamics and can be defined as $\omega_{p,i} = [(Z_i e)^2 n_i (m_i \epsilon_0)^{-1}]^{1/2}$. m_i is the characteristic ion mass for a certain species. In the following chapters, the name plasma frequency ω_p will be used to exclusively address the electron frequency $\omega_p \equiv \omega_{p,e}$. This is justified since the ion motion in the experimental part of this work is negligible in amplitude (sec. I.II.I) and does not occur on time scales of the investigated processes $\tau_i \tau_e^{-1} \sim \omega_{p,e} \omega_{p,i}^{-1} > 42$ [ADAMS 1979]. Moreover, a similar reasoning allows for the Debye length (1.3.1) to be redefined and written as $\lambda_D = [\epsilon_0 k_B T_e (e^2 n_e)^{-1}]^{1/2}$ by considering the ions to form an immobile charged background.

The aforementioned plasma waves obey the dispersion relation by BOHM and GROSS [1949]:

$$\omega_L^2 = \omega_p^2 + \frac{3k_B T_e}{m_e} |\vec{k}_L|^2 \quad (1.3.3)$$

\vec{k}_L is the Langmuir wave vector. This will be important for discussing the interaction of charged particles with propagating plasma waves. Energy may be transferred from these particles to the wave and vice versa by means of Landau damping (e.g. CHEN [1984]), which can be exploited to generate relativistic electron beams in a process called wakefield acceleration (cf. sec. I.IV.V).

I.III.III Definition of plasma

In a nutshell, the following conditions must be fulfilled for ionized matter to be considered a plasma and for plasma physics to apply to the description of a given physical system:

- a - Spatial quasi-neutrality. The Debye screening length λ_D must be small compared to the physical dimensions of the plasma volume and of the studied processes.
- b - Temporal quasi-neutrality. The plasma frequency ω_p must be larger than a characteristic frequency describing the time scale of the processes under investigation, such that charges can be shielded rapidly.
- c - Ideal plasma conditions. Collective electrostatic interactions must dominate over binary particle collisions inside an ideal plasma. Thus, a plasma only rigorously obeys text-book plasma physics for $\Lambda \gg 1$.

I.IV Laser propagation in underdense plasma

Intense laser pulses traveling through underdense ($\omega_p < \omega$) plasma give rise to a number of unique phenomena such as relativistic self-focusing, temporal self-modulation effects and wakefield generation. The latter process permits the acceleration of electrons to relativistic energies with a corresponding $\gamma > 10^3$, which is a key result of this work (chap. IV). Therefore it is absolutely mandatory to understand the mechanism of LWFA in great detail. In the following sections an in-depth derivation of the fully relativistic one-dimensional plasma wakefield theory will be given and discussed. In addition, those laser propagation effects which are most important in the context of the experimental observations presented later will be examined, i.e. relativistic self-focusing (sec. I.IV.III) and laser guiding in plasma channels (sec. I.IV.IV).

I.IV.I Excitation of large-amplitude Langmuir waves

A high-intensity laser pulse can efficiently excite large-amplitude Langmuir waves by its ponderomotive force. The propagation of such plasma oscillations in a cold, collisionless environment was first described in a nonlinear theory by AKHIEZER and POLOVIN [1956], which has analytical solutions for a large set of initial and boundary conditions (cf. DECOSTER [1978] and NOBLE [1985]). However, this theory does not take into account the wave generation process itself, e.g. by an electro-magnetic burst. Indeed, the latter may easily be appended to this model in the limit of $a_0 \ll 1$ [GORBUNOV and KIRSANOV 1987; SPRANGLE et al. 1988]⁴. Nevertheless, a completely new ansatz was necessary to develop a fully nonlinear description for arbitrary

⁴ This automatically leads to an expression for the dispersion relation of non-relativistic light waves ($a_0 \ll 1$) in cold, collisionless plasma (see KRUER [2003] or GIBBON [2005]):

$$\omega^2 = \omega_p^2 + c^2 |\vec{k}|^2$$

From this equation the non-relativistic refractive index η of cold plasma can be determined as:

$$\eta = \frac{c}{v_\phi} = \sqrt{1 - \left(\frac{\omega_p}{\omega}\right)^2} \quad (1.4.1)$$

with $v_\phi = \omega |\vec{k}|^{-1}$ being the phase velocity of an electro-magnetic wave.

laser amplitudes with $a_0 \geq 1$. Several groups have been successful in this undertaking⁵, albeit at first under the constraint of a light-wave group velocity v_g fixed to c . Subsequently, this restriction could be removed⁶. The resulting generalized theory of relativistic Langmuir waves supporting an arbitrary a_0 and an arbitrary v_g will be derived and discussed below.

General conventions and basic assumptions

Henceforth, the indices x , y and z will identify the spatial components of the corresponding vector quantities. Furthermore, collisions and thermal plasma effects will be neglected. This is valid since the characteristic collision-time in a weakly-coupled environment is far longer than a typical laser-pulse duration that can be used for this type of experiment. The neglect of thermal effects is justified due to the thermal energy of the plasma electrons being considerably smaller than their average quiver energy inside the laser field. In order to further simplify the problem, the electro-magnetic wake-driver is assumed to be a linearly polarized plane wave propagating through plasma along the x -direction. Hence, the light wave comprises only the electric field E_y and the magnetic field B_z and can be written as a vector potential $\vec{A} = \hat{y}A_y(x - v_g t)$ with \hat{y} being the unit vector in y -direction.

A closed set of fundamental equations

In the following, a set of equations will be determined, which describes the physical system under investigation and combines arbitrary-amplitude electro-magnetic wave propagation with the appropriate plasma response. These relations are listed below and for the sake of simplicity will be rewritten in normalized coordinates with the normalized laser-vector potential $a_0 = eA_y(m_e c)^{-1}$, the normalized scalar-field potential $\phi_0 = e\Phi(m_e c^2)^{-1}$ and the normalized electron velocities $\beta_x = v_x c^{-1}$ and $\beta_y = v_y c^{-1}$.

Transverse momentum equation. The time-derivative of the transverse electron momentum p_y is found by making use of the total derivative operator for functions $f(x, y_1, y_2, \dots, y_j)$:

$$\frac{df}{dx} = \frac{\partial f}{\partial x} + \sum_j \left(\frac{\partial f}{\partial y_j} \frac{dy_j}{dx} \right)$$

and applying it to the Lorentz equation while considering eqs. (1.1.1):

$$\begin{aligned} \frac{dp_y}{dt} &= -e(E_y - v_x B_z) \\ &= e \left(\frac{\partial A_y}{\partial t} + v_x \frac{\partial A_y}{\partial x} \right) = e \frac{dA_y}{dt} \end{aligned} \tag{1.4.2}$$

⁵ For further details see TSYTOVICH et al. [1989], BEREZHIANI and MURUSIDZE [1990], BULANOV et al. [1990] and SPRANGLE et al. [1990].

⁶ For in depth derivations see DALLA and LONTANO [1993], ESAREY et al. [1997b], KINGHAM and BELL [1997] and MORI [1997].

In this one-dimensional description the scalar field potential Φ does not vary in transverse direction with respect to the x-axis, hence $(\partial\Phi)(\partial y)^{-1} = 0$ does not appear in the expression above. Consequently, the temporal integration of (1.4.2) gives a relation for p_y assuming a negligible initial transverse drift:

$$p_y = eA_y \quad (1.4.3)$$

In normalized measures, this corresponds to:

$$\gamma\beta_y = a_0 \quad (1.4.4)$$

Longitudinal momentum equation. The Lorentz equation for the longitudinal electron-momentum component in laser propagation direction p_x yields:

$$\frac{dp_x}{dt} = -e(E_x + v_y B_z)$$

Similar to eq. (1.4.2), the electric and magnetic fields can be expressed also in this case by scalar and vector potentials with $E_x = -(\partial\Phi)(\partial x)^{-1}$ and $B_z = (\partial A_y)(\partial x)^{-1}$, respectively. Here it is assumed that $A_x = 0$, which will be justified retroactively with the application of the Coulomb gauge later in the derivation. The longitudinal Lorentz equation can be further transformed by making use of (1.4.3) and by substituting the quantities A_y , Φ and v_x with their normalized counterparts:

$$\frac{d}{dt}(\gamma\beta_x) = c \left(\frac{\partial\phi_0}{\partial x} - \frac{1}{2\gamma} \frac{\partial a_0^2}{\partial x} \right) \quad (1.4.5)$$

Continuity equation. The total charge contained inside the fluid-like plasma medium is preserved as long as ionization and recombination do not play a role. Hence a continuity equation can be introduced:

$$\frac{\partial n_e}{\partial t} + c \frac{\partial}{\partial x}(n_e\beta_x) = 0 \quad (1.4.6)$$

Electro-magnetic wave equation. The propagating electro-magnetic modes may be formalized by expressing the electric and magnetic fields through potentials (1.1.1) as done before, which then are combined with Ampere's law under consideration of the Coulomb gauge $\nabla\vec{A} = 0$ (compare to eqs. 1.1.2):

$$\frac{1}{c^2} \frac{\partial^2 A_y}{\partial t^2} - \nabla^2 A_y = -\mu_0 e n_e v_y$$

Here, the vector identity $\nabla \times (\nabla \times \vec{A}) = \nabla(\nabla\vec{A}) - \nabla^2\vec{A}$ was used and, as noted above, A_x and $(\partial\Phi)(\partial y)^{-1}$ equal zero. This expression can be rewritten in normalized units when considering eq. (1.4.3) and the definition of the plasma frequency ω_p in the unperturbed system:

$$\frac{\partial^2 a_0}{\partial t^2} - c^2 \frac{\partial^2 a_0}{\partial y^2} = -\omega_p^2 \frac{n_0 a_0}{\gamma} \quad (1.4.7)$$

with the electron density normalized to the initial electron background density $n_0 = n_e(Zn_i)^{-1}$.

Poisson's equation. Local charge separation sets up electric potentials, which can be ob-

tained from Poisson's equation:

$$\nabla^2 \Phi = -\frac{e}{\epsilon_0} (Zn_i - n_e)$$

In normalized units this transmutes into:

$$\frac{\partial^2 \phi_0}{\partial x^2} = \frac{\omega_p^2}{c^2} (n_0 - 1) \quad (1.4.8)$$

The relativistic γ -factor. γ can be expressed more conveniently by substituting eq. (1.4.4) for the transverse velocity:

$$\gamma = \frac{1}{\sqrt{1 - \beta_x^2 - \beta_y^2}} = \frac{\sqrt{1 + a_0^2}}{\sqrt{1 - \beta_x^2}} \quad (1.4.9)$$

Then, the light amplitude a_0 constitutes the only influence on the electron velocity β_y normal to the longitudinal component β_x , which is governed by both the wake potential and the laser vector potential. Therefore, it is common to split γ into an a_0 -dependent transverse factor and a longitudinal part:

$$\gamma = \gamma_{\perp} \gamma_{\parallel} \quad \text{with} \quad \begin{cases} \gamma_{\perp} = (1 + a_0^2)^{1/2} \\ \gamma_{\parallel} = (1 - \beta_x^2)^{-1/2} \end{cases}$$

Coordinate transformation into a co-moving frame

The just presented expressions for the longitudinal momentum (1.4.5), electron density continuity (1.4.6), the electro-magnetic modes (1.4.7), the potentials originating from local charge separation (1.4.8) and the factor γ (1.4.9) constitute a closed set of equations coupling electro-magnetic and plasma waves. For further progress it is convenient to apply a coordinate transformation of the form $\tau = t$ and $\xi = x - v_g t$ to these relations, which converts them into a frame co-moving with the light wave at its group velocity v_g . Then the spatial and temporal derivatives become:

$$\frac{\partial}{\partial x} = \frac{\partial}{\partial \xi} \quad \text{and} \quad \frac{\partial}{\partial t} = \frac{\partial}{\partial \tau} - v_g \frac{\partial}{\partial \xi}$$

As may be seen, the transformation is of the Eulerian type and not Lorentz invariant. A Lorentz transformation would be applicable as well, but leads to more complicated formulas and entails a reinterpretation of the results in the laboratory frame [MCKINSTRIE and DUBOIS 1988].

Now, the identity (1.4.9) can be solved for $\partial a_0^2 (\partial \xi)^{-1}$:

$$\frac{\partial a_0^2}{\partial \xi} = 2\gamma \left(\frac{\partial \gamma}{\partial \xi} - \gamma \beta_x \frac{\partial \beta_x}{\partial \xi} - \beta_x^2 \frac{\partial \gamma}{\partial \xi} \right) \quad (1.4.10)$$

This will soon turn out to be useful for applying the transformation on the longitudinal momentum equation. In the new coordinate system eq. (1.4.5) yields:

$$\frac{d}{dt} (\gamma \beta_x) = \left(\frac{\partial}{\partial \tau} - v_g \frac{\partial}{\partial \xi} + c \beta_x \frac{\partial}{\partial \xi} \right) (\gamma \beta_x) = c \left(\frac{\partial \phi_0}{\partial \xi} - \frac{1}{2\gamma} \frac{\partial a_0^2}{\partial \xi} \right)$$

Together with expression (1.4.10) and the definition of the normalized group velocity $\beta_g = v_g c^{-1}$, it follows for the partial time derivative of the longitudinal momentum:

$$\begin{aligned} \frac{1}{c} \frac{\partial}{\partial \tau} (\gamma \beta_x) &= \frac{\partial \phi_0}{\partial \xi} - \frac{\partial \gamma}{\partial \xi} + \gamma \beta_x \frac{\partial \beta_x}{\partial \xi} + \beta_x^2 \frac{\partial \gamma}{\partial \xi} + \beta_g \frac{\partial}{\partial \xi} (\gamma \beta_x) - \beta_x \frac{\partial}{\partial \xi} (\gamma \beta_x) \\ &= \frac{\partial}{\partial \xi} [\phi_0 - \gamma (1 - \beta_g \beta_x)] \end{aligned} \quad (1.4.11)$$

In an analogous fashion the continuity equation may be shifted into the co-propagating system:

$$\frac{1}{c} \frac{\partial n_0}{\partial \tau} = \frac{\partial}{\partial \xi} [n_0 (\beta_g - \beta_x)] \quad (1.4.12)$$

The transformation of Poisson's equation is trivial and gives:

$$\frac{\partial^2 \phi_0}{\partial \xi^2} = \frac{\omega_p^2}{c^2} (n_0 - 1)$$

The now following steps do not demand to apply the coordinate conversion to the electro-magnetic-wave equation as well. Instead, an expression for the normalized local electron density n_0 must be compiled, which only depends on known initial conditions. Such a relation can be found by introducing an additional constraint and is required in order to arrive at a solution for this set of partial differential equations in a frame co-moving with the excited wakefield.

The quasi-static approximation (QSA)

A helpful simplification in general for the study of interactions between short-pulse lasers and plasma is the quasi-static approximation [ESAREY et al. 1997b]. The QSA assumes, that the laser pulse envelope does not evolve significantly on the time scale it takes the light wave to pass a plasma electron. This means $\tau_L \ll \tau_E$ with the laser pulse duration τ_L and the characteristic spatial laser evolution time τ_E , which is on the order of the diffraction time $z_R c^{-1}$ with z_R representing the Rayleigh length (see definition in section I.IV.III). Thus, the laser field can be regarded as static in the co-moving frame for plasma interactions with respect to τ . Therefore $\partial(\partial\tau)^{-1}$ vanishes in those fluid equations that determine the plasma response to the fields, which are the longitudinal momentum equation (1.4.11) and the continuity equation (1.4.12). However, inside the electro-magnetic wave equation $\partial(\partial\tau)^{-1}$ has to be retained. As a consequence, (1.4.11) and (1.4.12) may be integrated over $d\xi$:

$$\phi_0 - \gamma (1 - \beta_g \beta_x) = C' \quad (1.4.13)$$

$$n_0 (\beta_g - \beta_x) = C'' \quad (1.4.14)$$

C' and C'' are constants and are determined by the boundary conditions for $\xi \rightarrow \infty$:

$$\lim_{\xi \rightarrow \infty} n_0 = \lim_{\xi \rightarrow \infty} \gamma = 1 \quad \text{and} \quad \lim_{\xi \rightarrow \infty} \beta_x = \lim_{\xi \rightarrow \infty} \phi_0 = 0$$

From this, it follows that $C' = -1$ and $C'' = \beta_g$. Now, (1.4.13) and (1.4.14) become:

$$\phi_0 = \gamma(1 - \beta_g \beta_x) - 1 \quad (1.4.15)$$

$$n_0 = \frac{\beta_g}{\beta_g - \beta_x} \quad (1.4.16)$$

Owing to the fixed electro-magnetic fields on the fluid timescale, the wakefield quantities can be given independently of the laser evolution only depending on the normalized amplitude a_0 . The square of (1.4.15) yields after utilizing (1.4.9) and introducing $\gamma_g = (1 - \beta_g)^{-1/2}$:

$$\gamma = \gamma_g^2 (1 + \phi_0) (1 - \beta_g \psi) \quad \text{with} \quad \psi = \sqrt{1 - \frac{1 + a_0^2}{\gamma_g^2 (1 + \phi_0)^2}}$$

This explicit expression for γ allows to solve (1.4.15) for β_x :

$$\beta_x = \frac{\beta_g - \psi}{1 - \beta_g \psi} \quad (1.4.17)$$

That result may be used to eliminate β_x from (1.4.16) to obtain the sought-after expression:

$$n_0 = \gamma_g^2 \beta_g \left(\frac{1}{\psi} - \beta_g \right) \quad (1.4.18)$$

Numerical solution and discussion of the results

Finally, this leads to a set of differential equations, which details the temporal and spatial evolution of electron density and electric potentials in a laser-driven plasma wake. The total scalar potential is determined by Poisson's equation (1.4.8), which can be written as:

$$\begin{aligned} \frac{\partial^2 \phi_0}{\partial \xi^2} &= \frac{\omega_p^2}{c^2} (n_0 - 1) \\ &= \frac{\omega_p^2}{c^2} \gamma_g^2 \left[\frac{\beta_g (1 + \phi_0)^2}{\sqrt{(1 + \phi_0)^2 - \frac{1 + a_0^2}{\gamma_g^2}}} - 1 \right] \end{aligned} \quad (1.4.19)$$

This is a nonlinear ordinary differential equation and can be solved numerically. When applying the QSA for the case of $\beta_g \rightarrow 1$, (1.4.19) transforms into:

$$\frac{\partial^2 \phi_0}{\partial \xi^2} = \frac{\omega_p^2}{2c^2} \left[\frac{1 + a_0^2}{(1 + \phi_0)^2} - 1 \right] \quad (1.4.20)$$

Once ϕ_0 is determined, β_x and n_0 are easily calculated with the help of (1.4.17) and (1.4.18). An example of a relativistic laser-driven plasma wake is depicted in figure 1.4.1. There, the wakefield quantities ϕ_0 , n_0 and the normalized longitudinal electric field $e_0 = -c\omega_p^{-1} \partial \phi_0 / \partial \xi$ display typical behavior for the relativistic regime such as spiked electron-density maxima at the local minima of the electric potential and almost linear electric fields trailing those spikes.

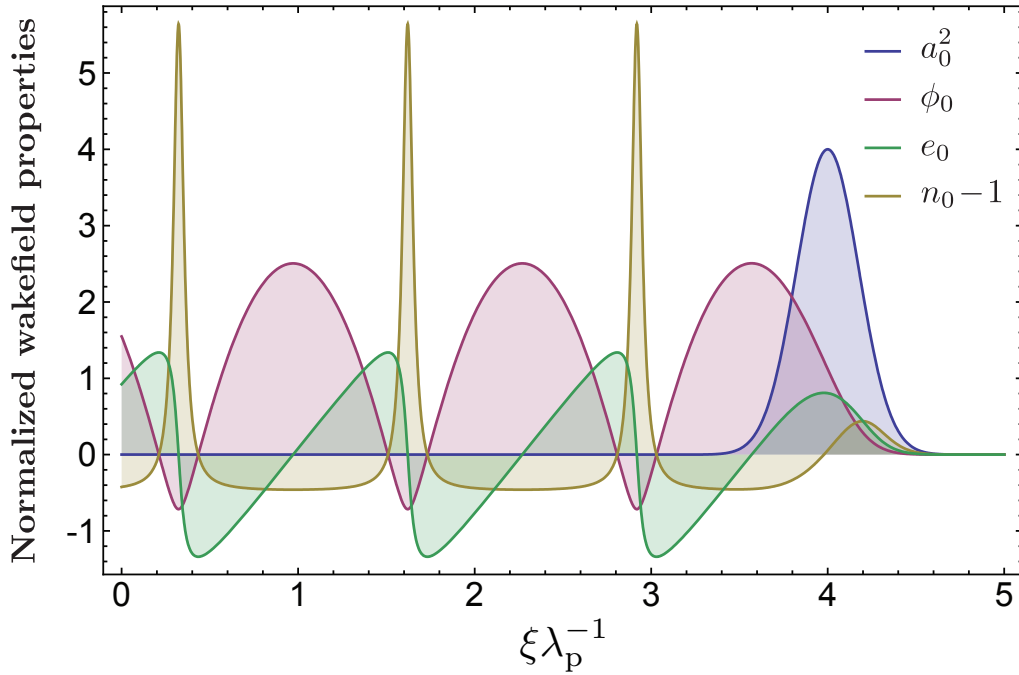


Figure 1.4.1 – The properties of a wakefield generated by a Gaussian shaped laser pulse of relativistic intensity are shown. The laser envelope has the form $a_0^2(\xi) = \tilde{a}_0^2 \exp[-(\xi - \xi_0)^2 (4 \ln 2)^{-1} L^{-2}]$ with $\tilde{a}_0 = 2$ being the peak laser amplitude, $L = c\tau_L = 0.15\lambda_p$ referring to the spatial pulse length measured full width at half maximum (FWHM) and τ_L being the FWHM pulse duration. All spatial scales are normalized to the non-relativistic plasma wavelength $\lambda_p = 2\pi c\omega_p^{-1}$. The laser pulse center was chosen to be situated at $\xi_0 = 4\lambda_p$. Since only its envelope is taken into account (by using the QSA), the effects of the individual field cycles are not reflected in the depicted properties.

Scaling laws for the maxima of ϕ_0 , e_0 and $p_0 = p_x(m_e c)^{-1}$ have been derived by BEREZHIANI and MURUSIDZE [1990] in the case of the laser group velocity approaching the speed of light:

$$\phi_{0,\max} \propto a_0^2 \quad \text{and} \quad e_{0,\max} \propto \frac{a_0^2}{\sqrt{a_0^2 + 1}} \quad \text{and} \quad p_{0,\max} \propto \frac{1 + \frac{1}{2}a_0^2}{1 + a_0^{-2}} \quad (1.4.21)$$

The efficiency of the wake-generation process itself strongly depends on the ratio of laser-pulse length L over plasma wavelength λ_p . Figure 1.4.2 shows the maximum absolute value of e_0 normalized to its corresponding scaling factor for several different laser amplitudes against L . The electric field is obtained at a distance far away from the driving light wave, where the field of the wake is not altered by the electric field of the laser, which otherwise would yield false results in the case of small amplitude oscillations. The data is produced from the numerical solution of (1.4.20) for a laser pulse of the same shape as used in the calculations to figure 1.4.1. As may be seen, for $a_0 \lesssim 1$ there exists a resonant pulse duration L_{res} at which the wakefield is driven most efficiently. L_{res} depends on the laser pulse shape, e.g. in the case of a Gaussian pulse $L_{\text{res}}\lambda_p^{-1} \approx 0.14$, for a box-shaped envelope $L_{\text{res}}\lambda_p^{-1} = 0.5$ [GIBBON 2005].

This situation changes when a_0 becomes significantly larger than 1. Then the resonance effect

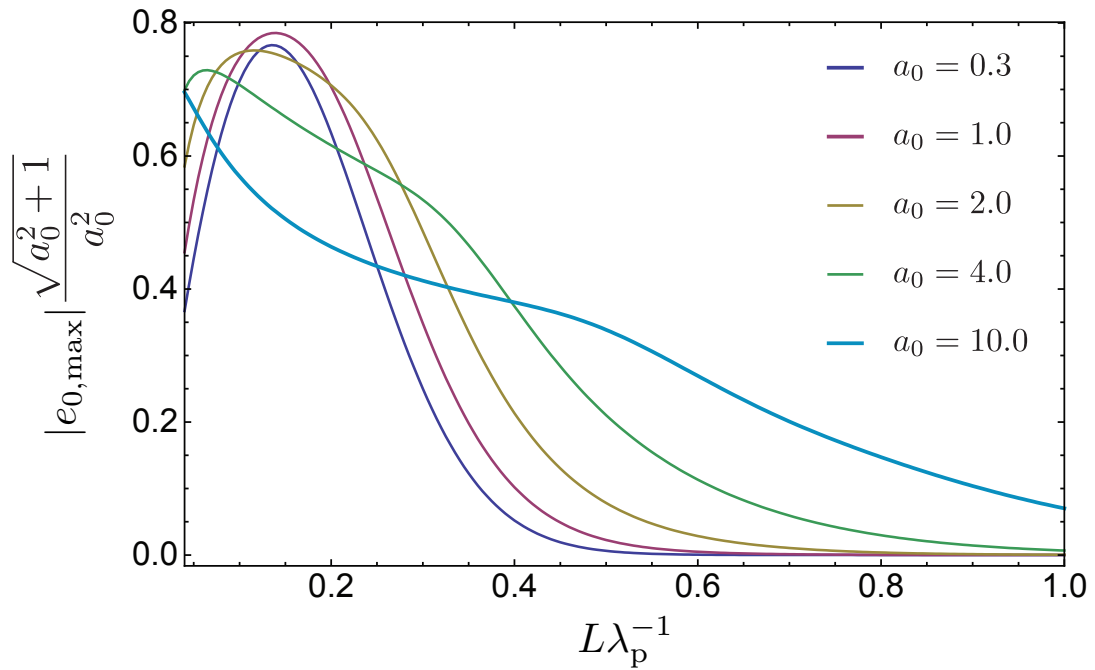


Figure 1.4.2 – Normalized peak field strength e_0 of a wake depending on the laser pulse length L and the maximum of the normalized amplitude a_0 . In this example the laser envelope is described by a Gaussian function as given in the caption to figure 1.4.1.

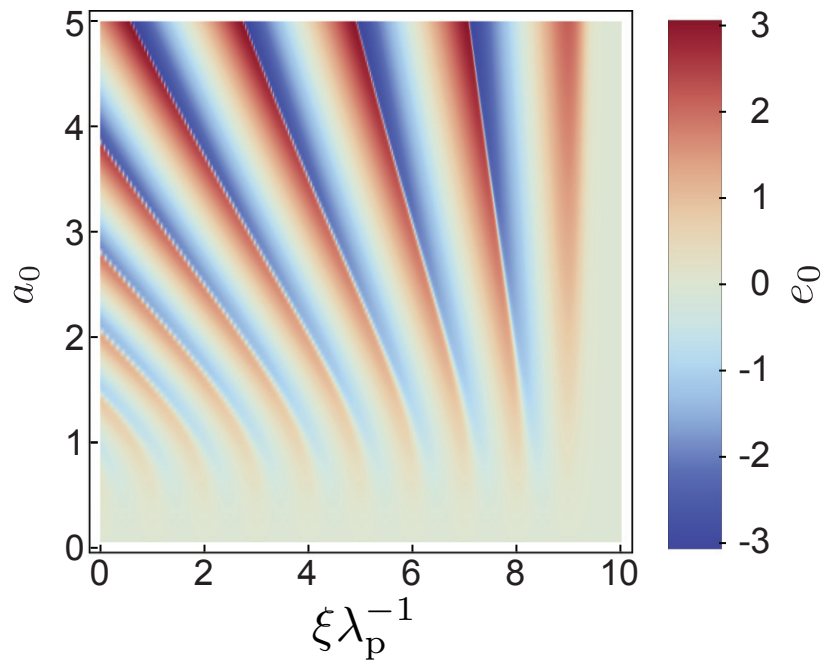


Figure 1.4.3 – The scale lengths of longitudinal plasma oscillations deviate for relativistic intensities from the non-relativistic plasma wavelength λ_p . These calculations again assume a Gaussian pulse (see figure 1.4.1).

starts to show an amplitude dependence, which results in the peak moving towards shorter pulse durations for increasing a_0 , but also benefits longer laser pulses due to the more gently decreasing slope. It needs to be mentioned here, that the employed relativistic model does not include the effect of wave-breaking, which sets an upper limit to the electric field inside a plasma wave. This will be discussed in section I.IV.II.

The increase of a_0 beyond unity has other interesting consequences. In the non-relativistic limit the plasma-wave period length equals λ_p . However, figure 1.4.3 indicates that for relativistic intensities the scale-length of the periodicity grows. This can be attributed to a change in plasma frequency ω_p due to an increase of electron inertia when accelerated to relativistic speeds. Moreover, in two- or three- dimensional geometry⁷ laser pulses do possess transverse pulse envelopes and therefore may excite plasma waves with varying frequencies across their profiles. This can lead to a reduced wave-breaking threshold on the propagation axis (for details see BULANOV et al. [1997]) and to self-focusing, which will be investigated in sec. I.IV.III.

Another important effect appearing in multi-dimensional space is a result of the radial wakefield properties, from which the direction of the total electric-field vector inside the wake structure can be determined as focusing (radially) and simultaneously accelerating (longitudinally) within $-1 < \xi\lambda_p^{-1} < -\frac{3}{4}$ of each wake period. Hence, the radial field distribution counteracts the Coulomb repulsion, allowing for the acceleration of dense electron bunches over long distances. This can be derived from the Panofsky-Wenzel theorem [PANOFSKY and WENZEL 1956]. That focusing effect is further enhanced by the laser group velocity dependence on the plasma refractive index (see equation 1.4.27 in section I.IV.III), which leads to a focusing horseshoe-like wakefield pattern (confer ESAREY et al. [1996]).

I.IV.II Wave-breaking and electron injection

A fundamental question of wakefield excitation concerns the maximum possible amplitude of longitudinal plasma oscillations. Is there an upper limit? This is crucial to the design and feasibility of laser driven particle accelerators. The maximization of the electric field in laser propagation direction $E_x = e_0 m_e c \omega_p e^{-1}$ is desirable, since it provides the accelerating force in LWFA. AKHIEZER and POLOVIN [1956] derived from the cold plasma equations:

$$e_0(\tau') = \pm \sqrt{2[\gamma_m - \gamma(\tau')]}$$

This expression is given in a retarded frame with $\tau' = t - xv_p^{-1}$ and v_p being the plasma-wave phase velocity. If a laser pulse acts as the wakefield driver, then $v_p = v_g$. γ_m refers to the relativistic factor associated with the maximum wave oscillation velocity, i.e. the maximum plasma-particle velocity corresponding to γ . This number cannot exceed $\gamma_p = (1 - \beta_p^2)^{-1/2}$ with $\beta_p = v_p c^{-1}$. If it did, then neighboring electric charge sheets could cross each other, which would result in a density singularity. This is one possible definition of wave-breaking according

⁷ The 1D nonlinear wakefield theory presented in the previous paragraphs can be generalized to three spatial dimensions [ESAREY et al. 1997b]. In 2D however, analytical solutions do not exist [ESAREY et al. 1996].

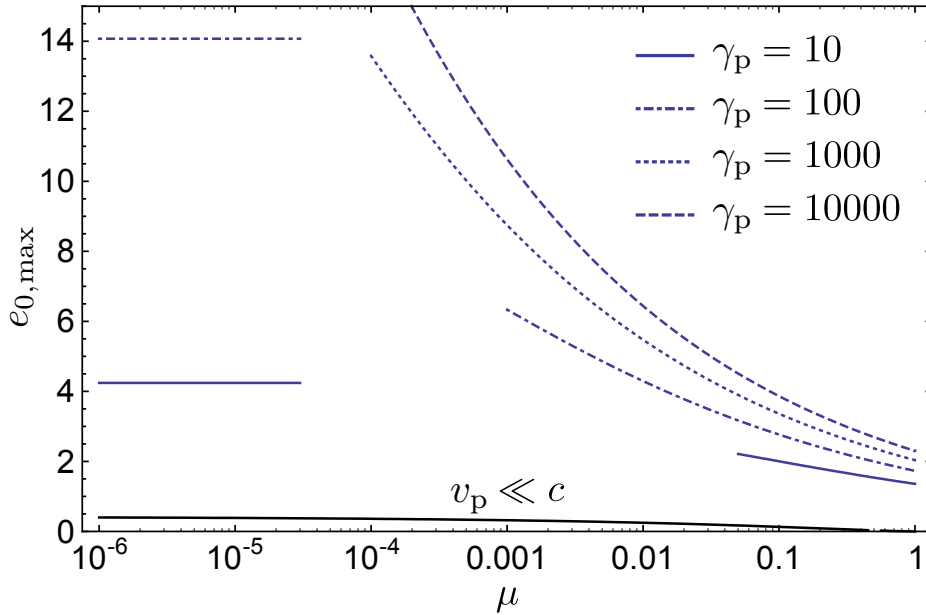


Figure 1.4.4 – Wave-breaking thresholds depending on the normalized plasma temperature μ for various relativistic factors γ_p associated with different plasma-wave phase velocities v_p . Here, each relativistic solution (blue) is exclusively plotted within its interval of validity. The black curve at the bottom displays the non-relativistic approximation.

to DAWSON and OBERMAN [1962]. Moreover, e_0 will have an extremum for the minimum $\gamma = 1$, yielding in the broken-wave limit:

$$e_{0,\max} = \sqrt{2(\gamma_p - 1)}$$

For non-relativistic phase velocities follows $\gamma_p - 1 \approx \beta_p^2/2$, giving the cold wave-breaking limit:

$$e_{0,\max} = \beta_p \quad \text{or} \quad E_{x,\max} = \frac{m_e \omega_p v_p}{e} \quad (1.4.22)$$

Thermal effects reduce this threshold inside plasma with a non-zero electron temperature (confer figure 1.4.4). This is due to two reasons. First, a non-negligible plasma pressure reduces the amplitude of localized electron density spikes, which set up the electric fields. Second, those thermal electrons, which are co-propagating with the plasma wave, may be trapped into the wave-bucket more easily at lower amplitudes in comparison to a cold plasma. According to ESAREY and PILLOFF [1995] wave-breaking can be defined as the process of background plasma electron trapping owing to a sufficiently large wave amplitude. The meaning of electron injection or trapping will be discussed below. COFFEY [1971] considered these thermal processes and used the Bohm-Gross dispersion relation (1.3.3) to introduce the so called waterbag-model of a thermal electron distribution, from which he deduced the wave-breaking limit for a non-relativistic plasma of electron temperature T_e with $\mu = 3k_B T_e (m_e v_p^2)^{-1}$:

$$e_{0,\max} = \beta_p \left(1 - \frac{\mu}{3} - \frac{8}{3} \sqrt[4]{\mu} + 2\sqrt{\mu} \right)^{\frac{1}{2}}$$

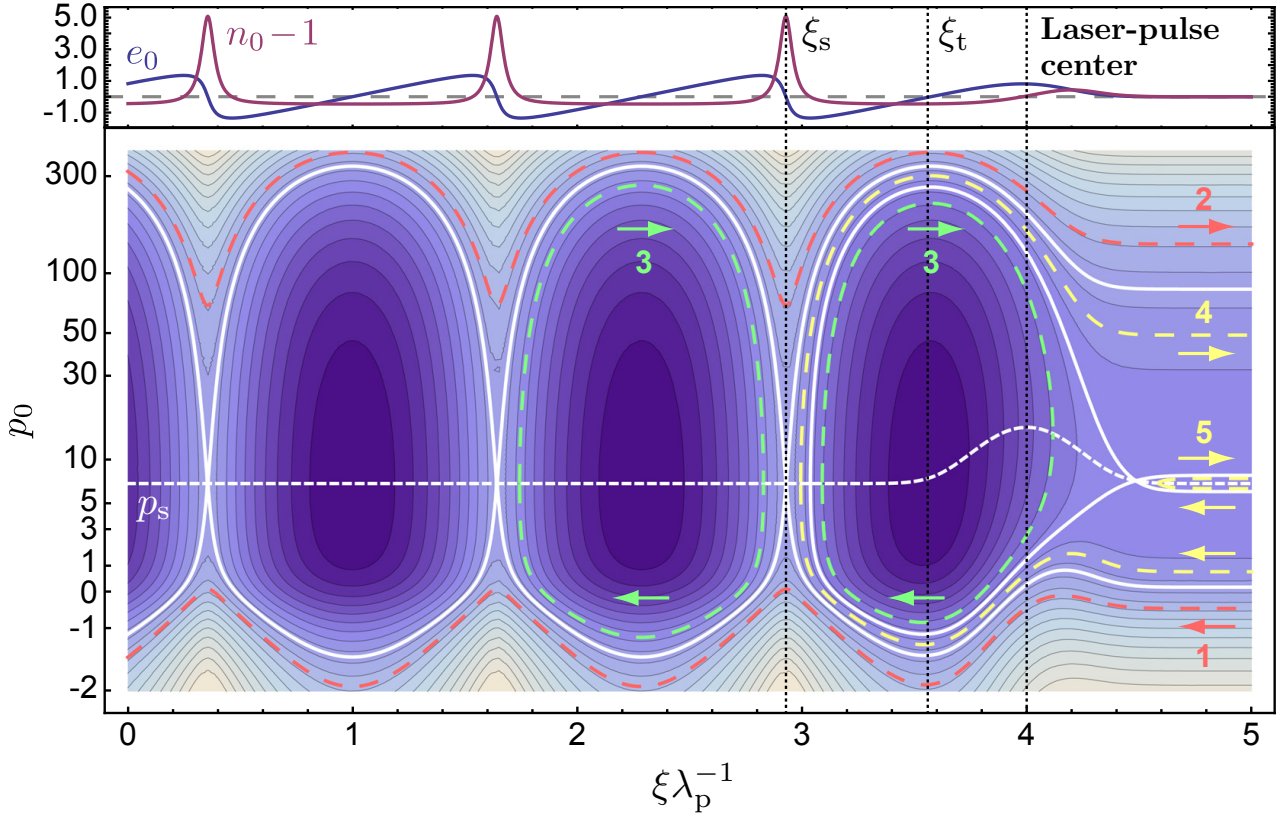


Figure 1.4.5 – The plot at the top shows the electric field e_0 and the electron density ($n_0 - 1$) in a wakefield generated by a short laser pulse in a fully ionized hydrogen plasma (same conditions as in figure 1.4.1 but with $\beta_g = 0.99$). Below, the corresponding phase space of electron momentum p_0 versus $\xi\lambda_p^{-1}$ can be seen. A selection of possible electron orbits, i.e. states of equal sums of potential and kinetic electron energies, is depicted by colored lines (cases 1 to 5). Some of these lines are closed (case 3), which indicates trajectories of electrons trapped inside the wakefield. These and the so called runaway trajectories (case 4) are the only orbits on which particles can effectively be accelerated by the longitudinal wake forces. The different phase-space areas are separated by the so-called separatrix (white solid lines).

KATSOULEAS and MORI [1988] generalized the waterbag-model to include relativistic momenta:

$$e_{0,\max} = \frac{1}{\sqrt[4]{\mu}} \left[\ln \left(2\sqrt{\gamma_p} \sqrt[4]{\mu} \right) \right]^{\frac{1}{2}} \quad \text{for} \quad \gamma_p \gg \frac{1}{2\sqrt{\mu}} \ln \left(2\sqrt{\gamma_p} \sqrt[4]{\mu} \right)$$

All these relativistic and non-relativistic wave-breaking thresholds are summarized in figure 1.4.4 showing solutions for their respective regions of validity for a selection of different γ_p spanning several orders of magnitude in normalized thermal plasma energy μ . From this, characteristic wave-breaking field strengths can be estimated to range from several hundred to several thousand GVm^{-1} for conditions found in the experimental part of this work. These fields are a minimum of three orders of magnitude larger than electric fields which are regularly employed in conventional radio-frequency particle accelerators, and thus allow for a reduction of the acceleration distance for a given particle energy by the same amount. The question,

which remains to be answered, is how particles can be injected into the wakefield structure in order to be efficiently accelerated. This can be seen from figure 1.4.5. It illustrates the electron-momentum phase space versus location inside a relativistic, laser-driven wakefield. The data for this plot is generated by defining the Hamiltonian of the system according to ESIRKEPOV et al. [2006], which yields a motion integral of the form:

$$h(\xi, p_0) = \sqrt{1 + p_0^2 + a_0^2(\xi)} - \phi_0(\xi) - \beta_p p_0 = h_0$$

h_0 is a constant, representing the sum of potential and kinetic energy for a single electron. Segments of equal h_0 are indicated by equal colors in figure 1.4.5 and constitute possible electron orbits $\{\xi(\tau), p_0(\tau)\}$. Some of these trajectories are selectively marked by colored dashed lines, which exemplarily display five different types of allowed electron paths. These cases (1 to 5) are separated from each other by so called separatrices (white solid lines). Case 1 symbolizes the orbits of low-momentum electrons forming the wake itself and the plasma background, which are too slow to be captured and sustainably accelerated. In the here shown co-moving frame of reference they travel to the left. Also electrons with very large initial momenta do not efficiently interact with the wakefield (case 2). They are too energetic to be trapped and slowly overtake the wake structure towards the right. However, if the wakefield is intended to be used as an energy booster in a staged acceleration scheme, i.e. if preaccelerated electrons from an external source should be injected, then care must be taken to use tailored wake properties matched to the respective electron phase-space distribution. The next class of orbits (case 3) identifies truly trapped and confined trajectories. Electrons populating these basins of equal energy may travel along with the wakefield and can effectively gain a maximum amount of momentum (see below). Nevertheless, these are not the only orbits that lead to substantial kinetic energy gain. Case 4 represents an ensemble of runaway paths, which forces electrons to asymptotically overtake the laser field and enables the formation of monoenergetic high-momentum distributions similar to case 3. The exclusive occurrence of this special kind of orbit in the first wake trough originates from the modified and lowered electrostatic potential barrier at the position of the light pulse (cf. fig. 1.4.1), which does not allow to decelerate this class of electrons below β_g . Hence, class 4 electrons can be considered as being reflected by the wake potentials, whereas electrons reflected by the laser ponderomotive potential are combined in class 5.

Owing to the fact that a laser pulse driving a wake as shown in the top part of figure 1.4.5 forms an electron density distribution as displayed there, electron injection by wave-breaking will occur at the positions of highest charge density right at the rear sides of each wake period. An electron, which receives an initial momentum kick bigger than $p_s(\xi) = \beta_p \gamma_p (1 + a_0^2(\xi))^{1/2}$ corresponding to $\gamma > \gamma_p$ will be trapped [ESIRKEPOV et al. 2006] and then accelerated by the electric field along its trajectory to the respective momentum predetermined by h_0 . The momentum gain is highest at position ξ_t for an electron injected at ξ_s , where also injection is most likely. This distance relates to the electron-dephasing length (cf. sec. I.IV.V). The necessary momentum kick can be transmitted by various mechanisms. Wave-breaking has been

mentioned, which may occur as a longitudinal [BULANOV et al. 1991] or in polydimensional space as a transverse effect [BULANOV et al. 1997]. Also the beat-wave pattern of two interfering laser pulses (see ESAREY et al. [1997a] and others⁸) or Raman backscattering [ESAREY et al. 1999] can be utilized. Finally, electrons could be conventionally preaccelerated, then captured into the wakefield and boosted to very high energies [JAROSZYNSKI et al. 2006].

I.IV.III Self-modulation effects

A mandatory condition for electron self-injection to occur by means of wave-breaking is a sufficiently high laser amplitude a_0 . Indeed, even today's ultra-short multi-terawatt laser systems often cannot provide the wave-breaking intensities necessary for desirable plasma-density regimes at the very instant of first laser-plasma interaction. Therefore most LWFA experiments performed to date have relied to some extent on nonlinear laser-pulse self-modulation effects to increase a_0 up to a value which allows for self-trapping. In order to understand the physical processes that lead to an increased intensity by laser-pulse evolution in plasma, it is helpful to investigate how the plasma refractive index η depends on electron density n_e and on a_0 .

This topic has been touched peripherally in section I.IV.I leading to an expression for the non-relativistic index of refraction (1.4.1). KAW and DAWSON [1970] showed that in the relativistic case the dispersion relation for light in plasma can be written as:

$$\omega^2 = \tilde{\omega}_p^2 + c^2|\vec{k}|^2 \quad \text{with} \quad \tilde{\omega}_p^2 = \frac{\omega_p^2}{\gamma} \quad (1.4.23)$$

From this expression it becomes clear, why non-relativistic light pulses cannot propagate inside a plasma with a frequency $\omega_p > \omega$, which is called an overdense plasma. In this case $|\vec{k}|$ is a complex number leading to reflection or attenuation of the electro-magnetic waves. In physical terms, the plasma electrons are able to shield fields, which are oscillating at a smaller frequency than the plasma frequency⁹. For $\omega_p < \omega$ the plasma is referred to as underdense. For a given laser wavelength the threshold frequency and density connected by (1.3.2) are called the critical plasma frequency $\omega_{p,\text{crit}}$ and the critical plasma density $n_{e,\text{crit}}$, respectively. In the case of light centered around $\lambda = 800$ nm as provided by the ATLAS laser facility (see chap. II), the critical density is reached for $n_{e,\text{crit}} \approx 1.7 \cdot 10^{21} \text{ cm}^{-3}$, which is more than two orders of magnitude above the density at which the experiments leading to this work were conducted.

Furthermore, equation (1.4.23) is useful to relate γ_p to the light field amplitude. The relativistic laser group velocity $v_g = c(1 - \tilde{\omega}_p^2\omega^{-2})^{1/2}$ equals the plasma wave phase velocity v_p and therefore:

$$\gamma_p = \frac{1}{\sqrt{1 - \frac{v_g^2}{c^2}}} = \frac{\omega}{\omega_p}$$

⁸ A variety of different laser-interference-assisted injection schemes have been proposed [UMSTADTER et al. 1996a; MOORE et al. 1999; SCHROEDER et al. 1999; FUBIANI et al. 2004].

⁹ A consequence of the γ -dependence of $\tilde{\omega}_p$ is relativistically induced transparency. This means a laser pulse may propagate through plasma with $\omega_p > \omega$ if its light amplitude is large enough to wiggle the plasma electrons violently, so that their γ becomes high enough to lead to $\tilde{\omega}_p < \omega$.

During the interaction with the laser pulse, the relativistic factor γ of a plasma electron may be expressed only by its perpendicular component $\gamma_{\perp} = (1 + a_0^2)^{1/2}$, due to the fact that $\gamma_{\parallel} \ll \gamma_{\perp}$ within an electro-magnetic field envelope with a_0 less than unity. Then a Taylor-expansion results in $\gamma \approx 1 + a_0^2/2$, leading to $\gamma_{\text{p}} \approx \omega\omega_{\text{p}}^{-1}(1 + a_0^2/2)$. From this, the cold relativistic wave-breaking limit is estimated to be reached at 1.2 TVm^{-1} under conditions found in the experiments described in chapters IV to VI with $n_e = 7 \cdot 10^{18} \text{ cm}^{-3}$, $\lambda = 800 \text{ nm}$ and $a_0 = 0.9$. This injection threshold is almost an order of magnitude above the maximum longitudinal wakefield amplitude generated with the mentioned laser parameters. Also thermal effects cannot be responsible for such a drastic reduction of the wave-breaking limited, for which plasma temperatures in excess of $\mu \approx 0.4$ or $k_{\text{B}}T_e \approx 70 \text{ keV}$ would be required. Since ultra-relativistic electrons have been observed from such laser pulses, it is a strong indication that a_0 must have been boosted prior to the injection and acceleration process and/or that a different, e.g. transverse wave-breaking mechanism occurred (see BULANOV et al. [1997]). An increase in a_0 can be attributed to laser self-modulation effects, which will be discussed now. These processes may depend on the radial beam profile. Hence, in the following a laser pulse with a cylindrically symmetric transverse Gaussian intensity distribution will be considered:

$$I(r, z) = I_0 \left(\frac{w_0}{w(z)} \right)^2 e^{-\frac{r^2}{w^2(z)}} \quad \text{with} \quad w(z) = w_0 \sqrt{1 + \left(\frac{z}{z_{\text{R}}} \right)^2} \quad (1.4.24)$$

I_0 represents the maximum intensity at the beam waist of radius w_0 , $w(z)$ denotes the beam radius along the propagation axis z , and r describes the radial coordinate. The beam radius is determined by Gaussian optics with the Rayleigh range $z_{\text{R}} = \pi w_0^2 \lambda^{-1}$ describing the propagation distance from the waist to a point, where the beam cross-section doubles and thus the intensity halves. $b = 2z_{\text{R}}$ is the confocal parameter. For such a pulse the refractive index varies along r and z [MORI 1997]:

$$\eta(r, z) = \sqrt{1 - \left(\frac{\omega_{\text{p}}}{\omega} \right)^2 \frac{n'_e(r, z)}{n_e \gamma(r, z)}}$$

The altered electron density n'_e and γ now are both functions of the spatial dimensions. Given that n_e changes only little with r and z and a_0 is small as discussed, then η may be expressed in the following way using the density perturbation $\delta n_e = n'_e - n_e$:

$$\eta(r, z) = 1 - \frac{1}{2} \left(\frac{\omega_{\text{p}}}{\omega} \right)^2 \left(1 + \frac{\delta n_e(r, z)}{n_e} - \frac{\langle a_0^2(r, z) \rangle}{2} \right) \quad (1.4.25)$$

As a result both the laser phase velocity v_{ϕ} and group velocity v_{g} will vary accordingly (see also DECKER and MORI [1994] and MORI [1997]):

$$v_{\phi}(r, z) = c \left[1 + \frac{1}{2} \left(\frac{\omega_{\text{p}}}{\omega} \right)^2 \left(1 + \frac{\delta n_e(r, z)}{n_e} - \frac{\langle a_0^2(r, z) \rangle}{2} \right) \right] \quad (1.4.26)$$

$$v_{\text{g}}(r, z) = c \left[1 - \frac{1}{2} \left(\frac{\omega_{\text{p}}}{\omega} \right)^2 \left(1 + \frac{\delta n_e(r, z)}{n_e} - \frac{\langle a_0^2(r, z) \rangle}{4} \right) \right] \quad (1.4.27)$$

Changes in v_g and v_ϕ in longitudinal direction will lead to self-bunching of the laser pulse and photon acceleration, respectively [WILKS et al. 1989]. Also, this dependence entails an energy redistribution within the electro-magnetic-field envelope by Raman scattering. A transverse v_g gradient will cause a deformation of the wakefield cross-section into a horseshoe-like shape and will thus enhance the electron beam focusing forces leading to a more stable confinement of the electron bunch [ESAREY et al. 1996]. The transverse v_ϕ -dependence drives self-focusing [BARNES et al. 1987; SUN et al. 1987; ABRAMYAN et al. 1992]. This effect arises from two mechanisms that have a ponderomotive origin (varying $\delta n_e(r)$) and a relativistic dependence (variations in $a_0(r)$ and therefore in electron inertia). Both of which will be investigated next.

Ponderomotive self-focusing

The longitudinal electron-momentum equation (1.4.5) is generalizable to also include transverse momentum components:

$$\frac{1}{c} \frac{d}{dt} (\gamma \vec{v}) = c \left(\nabla \phi_0 - \frac{1}{2\gamma} \nabla a_0^2 \right)$$

Here, the electron velocity \vec{v} can be regarded as slowly varying in comparison with the laser amplitude a_0 , therefore the left-hand side of this expression may be neglected. This is a reasonable assumption since the investigated variation in electron density is a consequence of the ponderomotive expulsion of electrons from areas of high intensity. Hence, the overall electron drift can be attributed to a laser-pulse-envelope effect. In this case, the equation simplifies to:

$$\nabla \phi_0 = \frac{1}{2\gamma} \nabla a_0^2 = \nabla \gamma \quad \text{with} \quad \gamma = \sqrt{1 + a_0^2} \quad \text{and} \quad \gamma \approx \gamma_\perp \gg \gamma_\parallel$$

The transverse plasma response and the change in electron density will then be described by (1.4.8) with ∇_\perp referring to the gradient perpendicular to the laser propagation direction:

$$n_0 = 1 + \left(\frac{c}{\omega_p} \right)^2 \nabla_\perp^2 \gamma$$

Averaged over an oscillation of $a_0^2(r)$ and considering the envelope defined in (1.4.24), this yields:

$$\begin{aligned} n_0(r) &= 1 + \left(\frac{c}{\omega_p} \right)^2 \frac{1}{2\sqrt{1 + \langle a_0^2(r) \rangle}} \left[\left(\nabla_\perp^2 \langle a_0^2(r) \rangle \right) - \frac{1}{2(1 + \langle a_0^2(r) \rangle)} \left(\nabla_\perp \langle a_0^2(r) \rangle \right)^2 \right] \\ &= 1 + \left(\frac{c}{\omega_p} \right)^2 \frac{\tilde{a}_0^2 e^{-\frac{r^2}{w^2}}}{2w^2 \sqrt{1 + \frac{1}{2} \tilde{a}_0^2 e^{-\frac{r^2}{w^2}}}} \left[\frac{2r^2}{w^2} \left(1 - \frac{1}{2 - \tilde{a}_0^2 e^{-\frac{r^2}{w^2}}} \right) - 1 \right] \end{aligned}$$

Hence, the density change on axis at $r = 0$ can be written as:

$$n_0(0) = 1 - \left(\frac{c}{\omega_p} \right)^2 \frac{\tilde{a}_0^2}{2w^2 \sqrt{1 + \frac{1}{2} \tilde{a}_0^2}} \quad (1.4.28)$$

Taking into account the expression for v_ϕ (1.4.26), the ponderomotive repulsion of electrons from areas of high intensity leads to a decrease in laser phase velocity on propagation axis and thus to a phase-front curvature resulting in focusing of the electro-magnetic wave. A phase-front normal offset from the central axis at distance w is tilted with respect to the propagation direction at center by an angle $\Xi \approx (v_{\phi,1} - v_{\phi,2})w^{-1}t$ for small Ξ . Here, the index 1 identifies the phase velocity at w , whereas 2 indicates v_ϕ on the central axis. Thus, the rate of change in w and its second time-derivative due to ponderomotive effects (subscript p) are given by:

$$\left. \frac{\partial w}{\partial t} \right|_p \approx -c\Xi = -ct \frac{v_{\phi,1} - v_{\phi,2}}{w} \quad \text{and} \quad \left. \frac{\partial^2 w}{\partial t^2} \right|_p = -c \frac{v_{\phi,1} - v_{\phi,2}}{w} \quad (1.4.29)$$

The calculated density variation together with (1.4.26) now causes the beam to collapse:

$$\left. \frac{\partial^2 w}{\partial t^2} \right|_p = \frac{1}{2} \left(\frac{\omega_p}{\omega} \right)^2 \frac{c^2}{w} (n_0 - 1) \quad (1.4.30)$$

That process is counteracted by self-diffraction of the Gaussian pulse envelope (subscript d). This effect is included in $w(z)$ of eq. (1.4.24) and can be rewritten using the diffraction time $\tau_R = z_R c^{-1}$. Then expressions for $w|_d$ and its second time derivative appear as follows:

$$w|_d = w_0 \sqrt{1 + \left(\frac{t}{\tau_R} \right)^2} \quad \text{and} \quad \left. \frac{\partial^2 w}{\partial t^2} \right|_d = \frac{c^2 \lambda^2}{w_0^3 \pi^2} \left[3 \left(\frac{w}{w_0} \right)^{-5} - 2 \left(\frac{w}{w_0} \right)^{-3} \right] \quad (1.4.31)$$

In order to obtain an estimate of n_0 for which ponderomotive self-focusing actually contracts the beam to a waist size smaller than w_0 , equations (1.4.30) and (1.4.31) are compared and a threshold at which these two processes balance each other is identified. Near the focus follows:

$$\left. \frac{\partial^2 w}{\partial t^2} \right|_{p+d} = \frac{c^2 \lambda^2}{w_0^3 \pi^2} \left[1 + \frac{1}{8} \frac{w_0^2}{c^2} (n_0 - 1) \omega_p^2 \left[1 - \left(\frac{\omega_p}{\omega} \right)^2 \right] \right] \quad (1.4.32)$$

Beam size reduction sets in when the term in the outer square brackets becomes negative for:

$$n_{0,\text{PSF}} < 1 - 8 \frac{c^2}{w_0^2} \frac{1}{\omega_p^2} \left[1 - \left(\frac{\omega_p}{\omega} \right)^2 \right]^{-1}$$

In case of typical experimental parameters ($\omega_p = 1.49 \cdot 10^{14} \text{ s}^{-1}$, $w_0 = 20 \mu\text{m}$, $\lambda = 800 \text{ nm}$ and $a_0 = 0.9$), this yields $n_{0,\text{PSF}} < 0.92$. From (1.4.28) the maximum density change on propagation axis is estimated to be $n_0 \approx 0.97$. Hence, the self-focusing effect caused by the ponderomotive expulsion of electrons alone is too weak to result in an enhanced laser intensity at focus, but nevertheless leads to an elongation of the distance over which the beam stays tightly confined.

Relativistic self-focusing

In the following, an evaluation of the self-focusing effect due to the relativistic increase of electron inertia (subscript r) generated by strong accelerating electric fields inside the laser

focus is presented [LITVAK 1970; MAX et al. 1974; SPRANGLE et al. 1987]. In this case, the phase-velocity difference ($v_{\phi,1} - v_{\phi,2}$) arising between two different positions along the laser phase-front in analogy to ansatz (1.4.29) is stemming from a contribution of the a_0 -dependent part of (1.4.26). This yields:

$$\left. \frac{\partial^2 w}{\partial t^2} \right|_r = -\frac{1}{8} \frac{c^2}{w} \frac{\omega_p^2}{\omega} a_0^2$$

Comparing to the defocusing originating from diffraction in analogy to (1.4.32) results in:

$$\left. \frac{\partial^2 w}{\partial t^2} \right|_{r+d} = \frac{c^2 \lambda^2}{w_0^3 \pi^2} \left[1 - \frac{1}{32} \frac{w_0^2}{c^2} a_0^2 \omega_p^2 \left[1 - \left(\frac{\omega_p}{\omega} \right)^2 \right] \right]$$

with the relativistic self-focusing threshold:

$$a_{0,\text{RSF}}^2 > 32 \frac{c^2}{w_0^2} \frac{1}{\omega_p^2} \left[1 - \left(\frac{\omega_p}{\omega} \right)^2 \right]^{-1} \quad (1.4.33)$$

For the above mentioned experimental parameters it is required that $a_0 > 0.57$, which is easily fulfilled. Thus relativistic self-focusing can be expected to play an important role in the interpretation of the results presented in chapters IV and V. Also, it is important to note that this threshold (1.4.33) depends on the product of the laser parameters $a_0^2 w_0^2$, which is proportional to the laser power P . Therefore this condition can be expressed as a power threshold defining the critical power P_c for which the condition $PP_c^{-1} > 1$ marks the onset of relativistic self-focusing with [SPRANGLE et al. 1987]:

$$P_c \approx 17 \left(\frac{\omega}{\omega_p} \right)^2 \text{ in GW} \quad (1.4.34)$$

Historically, the first experimental demonstration of a laser beam which self-focused and self-guided over several z_R has been conducted by BORGHESI et al. [1997].

As a side note, another mechanism affecting the total focusing behavior can be identified as ionization defocusing, which may occur inside a partially ionized plasma. An increased laser intensity on propagation axis will cause an increased ionization probability at the center of the pulse envelope and hence will raise the local electron density, enhancing diffraction. This may be unavoidable in plasmas consisting of atoms of high atomic number, but is of almost no concern in the case of the employed hydrogen plasma with an ionization threshold of $I_{\text{BSI}} \approx 1.4 \cdot 10^{14} \text{ Wcm}^{-2}$. Ionization induced diffraction for H_2 could only play a role several z_R before focus, but there the gas density is insignificantly low (confer chapter V).

I.IV.IV Laser guiding in preformed plasma-density structures

As has been mentioned before, changes in the transverse profile of the index of refraction may not only be exploited to increase the laser intensity beyond the electron-injection threshold, but may also be utilized to guide the laser beam over distances longer than several Rayleigh lengths

at relativistic intensities. In this way, the distance over which the laser pulse can drive and support the wakefield and effectively accelerate electrons can be extended allowing for higher electron energies (confer section I.IV.V). Besides self-guiding which is made possible through the aforementioned self-focusing effects, electro-magnetic waves can alternatively be guided by preformed density modulations inside the plasma medium (see chapter III). This externally imposed guiding structure is advantageous compared to relativistic self-guiding effects, since it is independent of the laser intensity and still works efficiently for resonant LWFA conditions in contrast to self-channeling [SPRANGLE et al. 1992].

A parabolic density variation perpendicular to the laser propagation direction of the form $\delta n_e(r) = \Delta n_e r^2 r_0^{-2}$ is suitable for confining a transverse Gaussian intensity envelope as defined in (1.4.24) over distances several times the length of z_R [SPRANGLE et al. 1992; DURFEE III and MILCHBERG 1993]. Δn_e is the electron density variation at radius r_0 . At sub-critical laser powers $P \ll P_c$ and sub-relativistic intensities $a_0 \ll 1$ the index of refraction is in good approximation given by (compare to 1.4.25):

$$\eta(r) = 1 - \frac{1}{2} \left(\frac{\omega_p}{\omega} \right)^2 \left[1 + \frac{\Delta n_e}{n_e} \left(\frac{r}{r_0} \right)^2 \right]$$

This expression can be evaluated with the help of the paraxial wave equation to describe the evolution of the Gaussian laser beam with spot radius $w(z)$ [ESAREY et al. 1994]:

$$\frac{d^2 R}{dz^2} = \frac{1}{z_R^2 R^3} \left(1 - \frac{\Delta n_e}{\Delta n_c} R^4 \right)$$

where $R = wr_0^{-1}$. Given that the density variation Δn_e equals the critical channel depth Δn_c , a Gaussian laser pulse with $w_0 = r_0$ will be guided. The critical channel depth is defined as [SPRANGLE and ESAREY 1992; SPRANGLE et al. 1992]:

$$\Delta n_c = \frac{1}{\pi r_e r_0^2} \approx 1.13 \cdot 10^8 \frac{1}{r_0^2} \text{ in cm}^{-3}$$

with the classical electron radius represented by $r_e = e^2(4\pi\epsilon_0 m_e c^2)$. If $\Delta n_e \neq \Delta n_c$, then the laser spot size will oscillate along z around its matched value, which can be obtained from $R^4 = \Delta n_c \Delta n_e^{-1}$ [ESAREY et al. 1996]. All this is valid for a sufficiently broad channel, such that the electro-magnetic wave is not influenced by the boundary conditions. These parabolic channels¹⁰ not only support Gaussian beams but a whole family of modes describable by Laguerre polynomials [UNGER 1977]. Although laser focii may usually be approximated very well by a Gaussian distribution, these higher order modes play an important role and may be excited inside a plasma waveguide when the dimensions of the guiding structure and the laser far-field are not well matched [DURFEE III et al. 1994]. In the extreme case of the channel size being smaller than the laser mode, no guiding occurs. If the guiding formation is only slightly

¹⁰ Alternatives to parabolic density gradients are under consideration as well, of which hollow channels seem to be the most promising [CHIOU et al. 1995].

bigger than the waist, laser-energy leakage will decrease the efficiency. In the experiments presented later, the channel-diameter to spot-size ratio is ~ 10 , resulting in negligible leakage confirmed by detected guiding efficiencies of more than 90 % (see chap. III).

I.IV.V Laser wakefield acceleration scaling laws and limits

As discussed before, plasma wakes sustain electric fields which allow for the acceleration of electrons to ultra-relativistic energies. In this context, some questions remain to be answered: What are the limitations of LWFA and how do they scale with laser and plasma parameters? Which electron energies can be expected? How does a laser-plasma-electron accelerator have to be designed in order to achieve the desired results? Answers to these issues may be found by investigating those effects which are responsible for the termination of the acceleration process, e.g. laser-energy depletion, electron dephasing, laser diffraction, and laser-plasma instabilities.

Laser energy depletion

A laser pulse continuously transfers energy to the plasma while driving a wake. The distance over which its total energy is depleted is called laser-depletion length L_{ed} [TING et al. 1990; BULANOV et al. 1992; TEYCHENNÉ et al. 1994]. This length can be found by demanding that the energy stored inside the wake along L_{ed} equals the energy contained within an electromagnetic field of resonant wakefield-excitation length L_{res} . Thus, $E_x^2 L_{\text{ed}} \simeq |\vec{E}_0|^2 L_{\text{res}}$ must be fulfilled. E_x denotes the longitudinal electric-field strength, $|\vec{E}_0|$ is the laser electric-field amplitude. According to ESAREY et al. [1996], this is true for:

$$L_{\text{ed}} \simeq \left(\frac{\omega}{\omega_p}\right)^2 \lambda_p \cdot \begin{cases} a_0^{-2} & \text{for } a_0 \lesssim 1 \\ a_0 (3\pi)^{-1} & \text{for } a_0 \gg 1 \end{cases} \quad (1.4.35)$$

For laser amplitudes $a_0 \lesssim 1$, the wakefield-energy-coupling efficiency grows with a_0^2 (cf. potential energy $\phi_{0,\text{max}}$ in eqs. 1.4.21), hence L_{ed} decreases. Exactly the opposite holds for $a_0 \gg 1$. The coupling efficiency decreases with $a_0 \rightarrow \infty$, since then $E_x \propto a_0$ (cf. electric field $e_{0,\text{max}}$ in eqs. 1.4.21) and $L_{\text{res}} \propto a_0$ [TING et al. 1990]. This yields an estimate of $L_{\text{ed}} = 3.1$ mm for typical conditions found in the experiments outlined in chapter V ($n_e = 7 \cdot 10^{18} \text{ cm}^{-3}$, $a_0 = 0.9$ and $\lambda = 800$ nm). However, this must only be regarded as a coarse approximation. It is important to bear in mind that (1.4.35) is strictly valid only for a resonant laser-pulse examined in a one-dimensional geometry. For longer pulses, L_{ed} lengthens by the distance the pulse propagates to self-modulate (cf. sec. I.IV.III). This process again is counteracted, because not the full initial laser energy will be captured in the self-shortened pulse. Also, L_{ed} may be enlarged for a set of given laser parameters by decreasing the plasma density, since $L_{\text{ed}} \propto n_e^{-3/2}$. Another possibility to overcome the energy depletion limitation is to employ a staged acceleration concept, in which several wakefields driven by several lasers accelerate the same electron bunch subsequently. Such a setup is technically quite demanding and has not been demonstrated, yet (cf. sec. VII.III).

Electron dephasing

An inherent limitation of LWFA is electron dephasing. The captured and accelerated electrons travel at a velocity approaching c . However, the laser and therefore the wakefields propagate at $v_g < c$ (see eq. 1.4.27). Hence, the electrons will slowly start to overtake the light wave, leave the accelerating electric field gradient and run into a decelerating field region. The maximum distance the electrons can travel inside the wake while being accelerated is called dephasing length L_d [LEEMANS et al. 1996; VOLFBEYN et al. 1999]. For a small $a_0 \lesssim 1$ this distance can be estimated by:

$$\Delta v \frac{L_d}{c} = \frac{\lambda_p}{2} \quad \Rightarrow \quad L_d = \frac{\lambda_p^3}{\lambda^2} \propto n_e^{-\frac{3}{2}}$$

Here, the velocity difference Δv is expressed through $c - v_g$. A more rigorous derivation, which is also valid at relativistic intensities, yields [ESAREY et al. 1996]:

$$L_d \simeq \left(\frac{\omega}{\omega_p} \right)^2 \lambda_p \cdot \begin{cases} 1 & \text{for } a_0 \lesssim 1 \\ 2a_0^2 \pi^{-1} & \text{for } a_0 \gg 1 \end{cases}$$

As can be seen, $L_d \propto n_e^{-3/2}$ implies again that a decrease in electron-plasma density will increase the distance over which electrons can be accelerated. Ultimately, this will also allow for higher electron energies (see next page). The behavior for $a_0 \gg 1$ can be understood, when considering the effective plasma-wavelength increase for such laser intensities, which based on larger electron inertias becomes a function of a_0 . For the experimental parameters given above, the dephasing length is calculated to be $L_d \approx 3.9$ mm, being quite similar to the energy-depletion length.

Laser diffraction

Diffraction of a laser beam constitutes another mechanism which sets an upper limit to the scalability of LWFA. In order to increase the electron energies to higher values, it is desirable to decrease the plasma density and therefore increase the acceleration distances. This implies that the wake-driving laser field has to maintain an intensity high enough to excite a significant wakefield over the full acceleration length. That is technically only feasible for distances on the millimeter to centimeter scale. Once the necessary acceleration length becomes longer than the achievable confocal laser parameter b , the laser pulse needs to be confined and guided by either self-guiding (section I.IV.III) or by preformed electron density gradients within the plasma medium (section I.IV.IV). In the experiments presented in chapter IV both effects are exploited. Without any guiding the beam would diffract after $b = 4.15$ mm in the used setup.

Laser-plasma instabilities

Laser-plasma instabilities can limit the performance of wakefield accelerators by degrading the acceleration conditions¹¹. Stimulated Raman scattering (SRS) for example may result in the

¹¹This statement is true for laser-pulse durations near wakefield resonance. In the case of long laser pulses with $c\tau_L \gg \lambda_p$ laser-plasma instabilities are actually imperative and desired (cf. HIDDING et al. [2006]). They

transport of energy out of the wake region [ANTONSEN and MORA 1992; KRUER 2003]. SRS describes a set of resonant three- and four-wave-mixing processes, during which a light field of frequency ω and wave vector \vec{k} interacts with or decays into an electron-plasma wave (ω_p, \vec{k}_p) and while doing so excites Stokes ($\omega - \omega_p, \vec{k} - \vec{k}_p$) and anti-Stokes components ($\omega + \omega_p, \vec{k} + \vec{k}_p$). Other instabilities grow due to locally differing electron densities and are all combined under the keyword self-modulation effects: The high plasma density in front of a wake-driving laser pulse, which results from the ponderomotive particle push, causes an increased diffraction of the leading edge of the laser and slowly erodes the pulse from the front. Accordingly, a laser pulse with a duration that is longer than the plasma wavelength λ_p will suffer from varying n_e along its longitudinal envelope causing the beam to locally diffract at the front of each wakefield bucket. This effect will also lead to periodic laser beam diameter modulations. In addition, a non-symmetric pulse profile forces local electron density changes in transverse direction and will cause the laser-beam-intensity centroid to oscillate. This mechanism is called laser hosing [SHVETS and WURTELE 1994; SPRANGLE et al. 1994].

Maximum electron-energy gain

Taking these LWFA limitations into account, the maximum energy gain W_e of an electron inside the wake can be evaluated. When assuming that injected electrons experience acceleration over the whole dephasing length, their final energy in the cold wave-breaking limit (1.4.22) will be:

$$W_c = eE_x L_d = m_e \omega_p v_p L_d \propto \frac{1}{n_e}$$

Accordingly, this is for the relativistic wave-breaking threshold [ESAREY and PILLOFF 1995]:

$$W_r = (4\gamma_p^3 - 3\gamma_p) m_e c^2$$

Even for a weakly relativistic laser pulse as used in the experimental part of this work ($a_0 \approx 0.9$), a maximum energy gain of $W_c \approx 990$ MeV over an acceleration distance of $L_d \approx 3.9$ mm seems possible. This of course is just a rough estimate, since the theoretical framework utilized here is essentially one dimensional and hence incomplete.

Limits of an analytical theory

In general, laboratory physics must be evaluated in all three spatial dimensions to include all important physical aspects in a proper manner. Hence, the 1D theory described in this chapter provides only a basic understanding of the main mechanisms involved in laser-wakefield acceleration. Moreover, even a more realistic description, i.e. a generalized non-linear three-dimensional LWFA fluid theory [ESAREY et al. 1997b], breaks down as soon as wave-breaking,

can temporally modulate the electro-magnetic wave to fulfill the plasma wave resonance condition in multiple wave buckets and excite an initial small-amplitude plasma oscillation by stimulated Raman scattering, which then can grow. Electron acceleration in this regime is referred to as self-modulated laser wakefield acceleration.

trapping, and subsequent particle acceleration become important, since those processes are of kinetic nature and cannot be completely described in a multi-dimensional analytical framework. Such a description requires numerical simulations. Particle-in-cell (PIC) codes have proven to be a powerful tool, which self-consistently describe LWFA in one, two or three dimensions (for more details on the working principle of PIC codes, see chapter VI). Among the first to employ this method in 2D were FORSLUND et al. [1985] and MORI et al. [1988] with the WAVE code. Later, more efficient simulations allowed for in-depth descriptions of particular mechanisms such as self-focusing and wave-breaking and their coaction [BULANOV et al. 1995]. The ever increasing computing power in the following years allowed for the simulation of laser-plasma systems in 3D during the mid-1990's. At that time, pioneering work was done by PUKHOV and MEYER-TER-VEHN [1996] and TZENG et al. [1996], which created the knowledge that laser-wakefield acceleration is not limited to sub-wave-breaking intensities. For the 3D case PUKHOV and MEYER-TER-VEHN [2002] discovered the existence of a new scheme of wakefield acceleration in the broken-wave regime, in which electrons are trapped by transverse injection into a solitary electron void traveling behind the driving laser pulse. This regime is commonly referred to as bubble acceleration. In order to provide deeper insight into this process and to identify those physical features, which are not captured in the analytic model discussed earlier, a tangible example of a particle-in-cell simulation will be reviewed in the following.

Figure 1.4.6 shows a typical, fully three-dimensional simulated time series of an electron-density distribution in a laser-driven-wakefield environment approaching the bubble regime, which was calculated using the PIC code OSIRIS [LEE et al. 2000]. Starting in (a), the laser pulse (on the right) has just crossed the vacuum-plasma boundary and is about to propagate further into the plasma slab. While doing so, it drives a strong plasma wake. This wakefield is distinctly displayed in subfigure (b). It is excited by means of the laser-ponderomotive force, which pushes electrons aside and creates an almost empty electron void trailing the electro-magnetic wave. Now, the displaced electrons are violently pulled back to the central axis by the resulting space-charge potentials, which create intense return currents along the outer ion-cavity surfaces. These electron streams clash right behind each wake trough and set up regions of immense negative charge density, which in time step (b) is not high enough yet to initialize electron trapping. Another feature observable here is a starting collapse of the tertiary wake bucket. In a pure bubble-acceleration scheme only the wakefield period at the rear side of the driving light pulse survives and can be harnessed for electron acceleration. The shape of such a solitary cavity is almost round when not loaded with electrons. It then resembles a bubble and hence is responsible for the name of the effect. Part (c) depicts the wakefield in a slightly advanced development stage. It may be seen that now also the second wakefield trough shows signs of decay owing to the fact that the laser pulse drives a stronger wake. This is possible due to self-focusing and self-compression of the beam, raising its intensity. A little later (d), the secondary trough has nearly vanished and first wave-breaking and electron injection into the primary wake can be witnessed. Contrary to the longitudinal wave-breaking theory in 1D (cf. section I.IV.II), the trapping process observed here is of transverse nature. It is fueled by

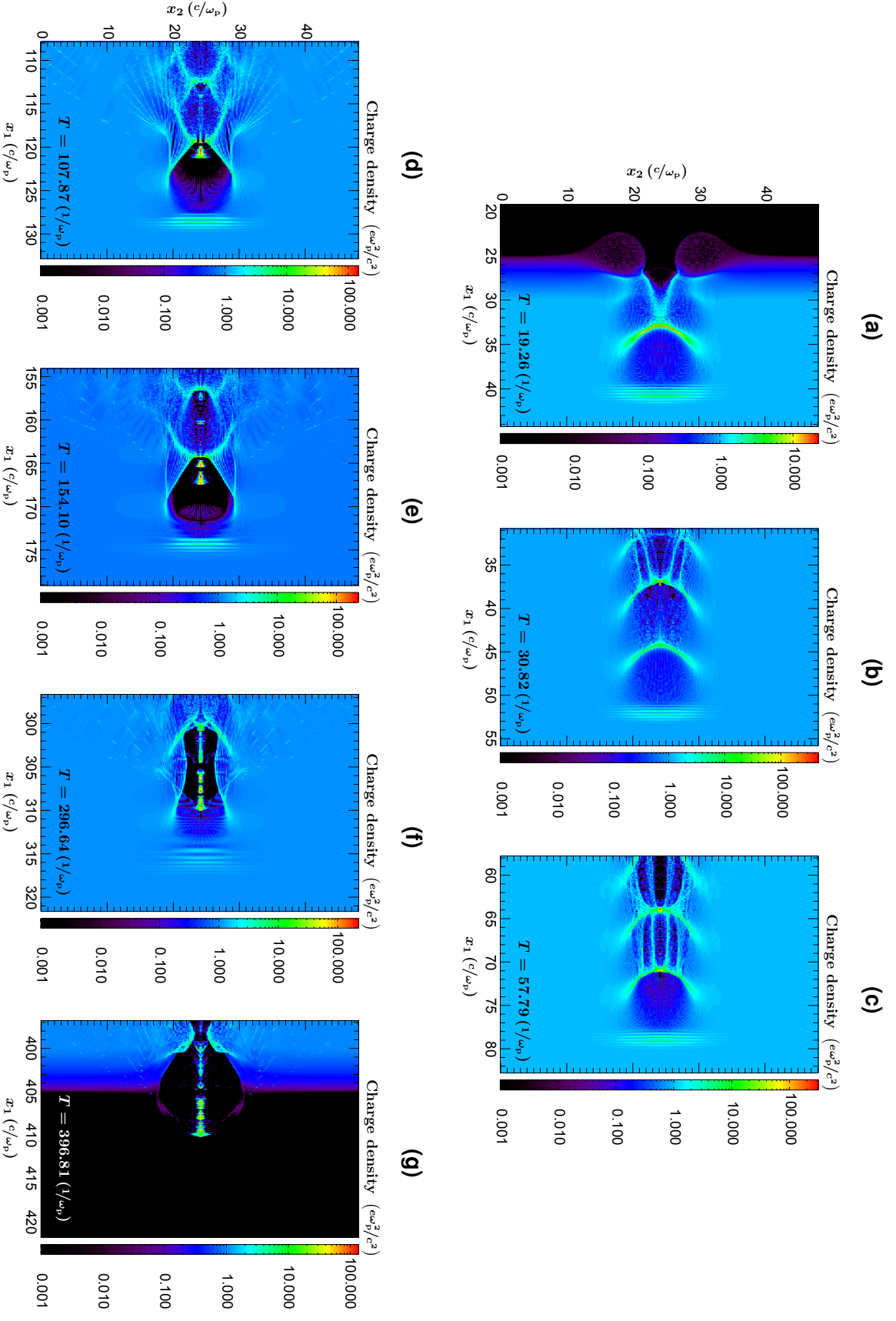


Figure 1.4.6 – LWFA time series of an electron-density distribution generated from a 3D PIC-calculation with parameters chosen as follows: $n_e = 1.7 \cdot 10^{19} \text{ cm}^{-3}$, $\tau_L = 17 \text{ fs}$, $a_0 = 3$, $\lambda = 800 \text{ nm}$, and $w_0 = 7.6 \mu\text{m}$.

high-transverse momentum electrons from the generated return currents [BULANOV et al. 1997] and has a notably reduced threshold, allowing for injection of electrons at moderate electric-field strength below $100 \text{ GV}\cdot\text{m}^{-1}$. This loading process continues until the space-charge field set up by the trapped electrons is high enough to significantly suppress the electric potential at the back of the bubble. That mechanism is called beam-loading. Subsequently, the injected particles are accelerated to speeds close to the speed of light caused by strong fields inside the ion cavity. Thereby, they become faster than the group velocity of the driver beam. However, this entails a weakening of the influence of the trapped electron space-charge field at the injection center, since the distance between the ultra-fast electron bunch and the bubble backside increases, which allows for the injection to restart (e). Moreover, some trapping inside the second decayed wake bucket occurs, but only leads to a few electrons with mediocre energies (cf. fig. 1.4.7 below). In addition, growing electron-stem fields induce an elongation of the formerly round bubble shape and over time cause significant deformations (f). Finally, the laser pulse reaches the plasma-vacuum interface, releasing the electron bunch into free space (g).

The evolution of the electron momentum in forward direction is of particular interest in this context. Figure 1.4.7 maps a time series of the longitudinal-momentum phase space along the laser-propagation axis x_1 . In (a), which corresponds to the charge-density profile given in figure 1.4.6a, the instantaneous longitudinal response of electrons to the laser field (high-frequency structure at the right) and to the excited Langmuir wave (low-frequency structure at the center) are illustrated. Here, the light wave causes electron-forward acceleration due to its magnetic-field component and due to longitudinal electric fields arising from the focused Gaussian-mode profile. This picture changes notably when electrons are trapped into a wake trough (compare to fig. 1.4.6d). Part (b) and the following time steps give an impression of the particle-energy evolution after injection. Wave-breaking at the rear sides of the primary and secondary buckets allow electrons to surf the longitudinal wakes for energy gains with $\gamma > 50$. In this specific example the electron-energy distribution is consistent with a plateau background in the energy-resolved number spectrum (fig. 1.4.8). After further acceleration (c), the bubble content (first bucket) reaches $\gamma \geq 200$ with a pronounced quasi-monoenergetic feature (cf. fig. 1.4.8), whereas the electrons in the collapsing secondary trough have not evolved significantly. The occurrence of the spike in the electron spectrum originates from the fact that the bulk of the trapped electrons are reaching the top of their $x_1 p_1$ -phase-space trajectory (compare to fig. 1.4.5), corresponding to their dephasing point. Thus, phase-space compression starts to set in, producing the spectral peak (fig. 1.4.8). The quality, e.g. energy spread of such a feature may be improved by controlling the time interval, during which electrons can spill into the cavity. This can be realized by either counterpropagating laser-pulse schemes [FAURE et al. 2006; RECHATIN 2008], or modulations in the plasma density [BRANTOV et al. 2008; GEDDES et al. 2008]. Moreover, the observed monoenergetic feature constitutes no steady state. Its deterioration sets in, when the electron bunch propagates just a little further (figs. 1.4.7d and 1.4.8).

In recent years, simulations of this type have allowed to analyze the complex behavior of the bubble scenario in a systematic way, which led to the refinement of scaling laws valid under

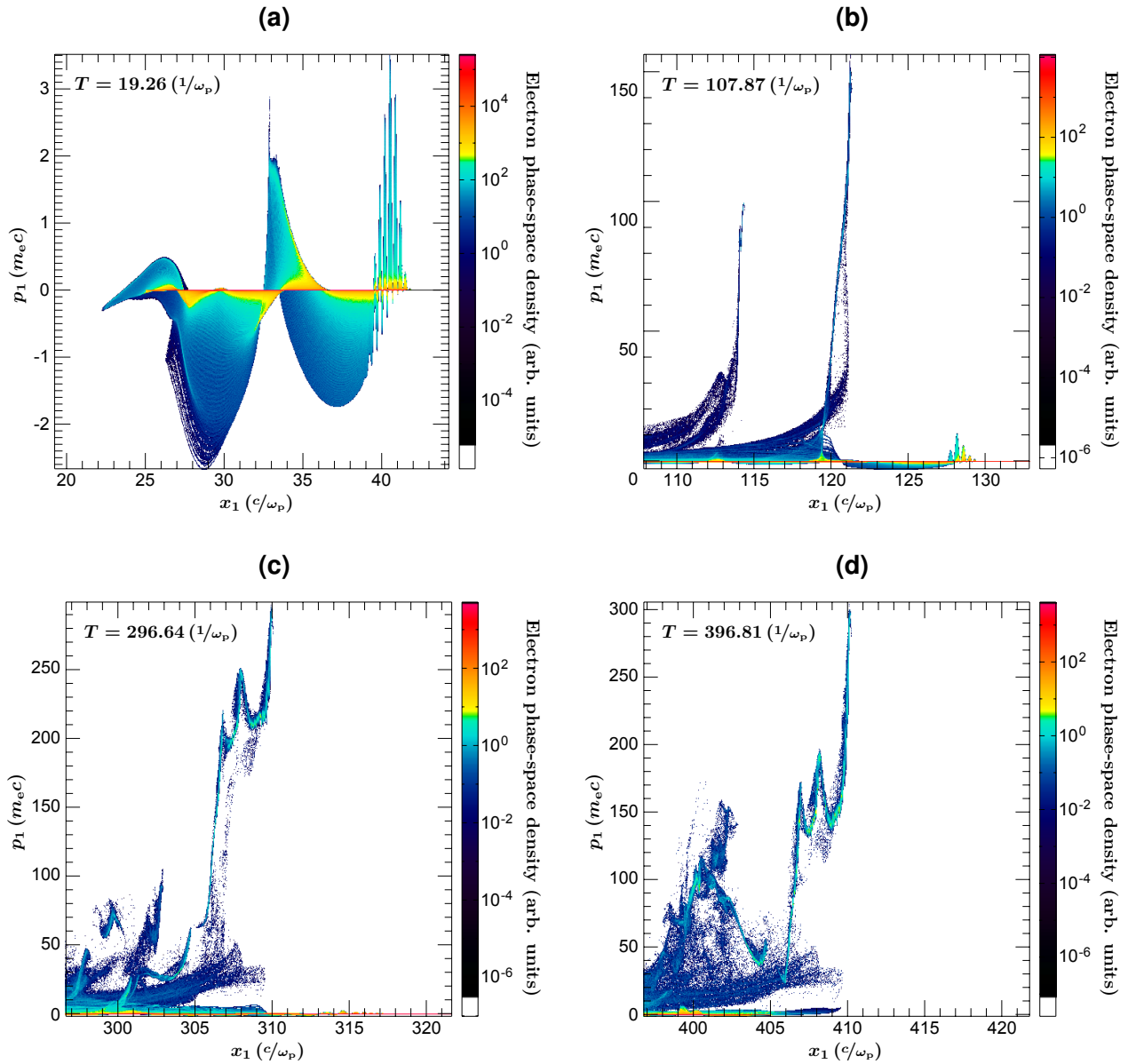


Figure 1.4.7 – Time series of longitudinal momentum space in laser propagation direction extracted from the same simulation as shown in figure 1.4.6.

relativistic ($a_0 \geq 1$) [LU et al. 2007] and ultra-relativistic ($a_0 \gg 1$) conditions [GORDIENKO and PUKHOV 2005]. Even today, this field is still thriving and subject to continuous development. Indeed, that evolution of particle-in-cell codes and algorithms is a prerequisite for making efficient use of novel computing platforms, such as those building on IBM’s cell-processor technology¹². This is important, since the treatment of laser-plasma interactions through PIC calculations is essentially limited by hardware constraints, e. g. the available processor power and memory size. Another limitation stems from an inherently finite computation accuracy. Small numerical errors may add up over time and cause numerical heating of the modeled system, which entails a violation of energy conservation. In a wakefield-simulation setting, this particular mechanism may manifest itself in an overestimated amount of trapped charge.

¹²For details see <http://www.research.ibm.com/cell/> or <http://www.lanl.gov/roadrunner/>.

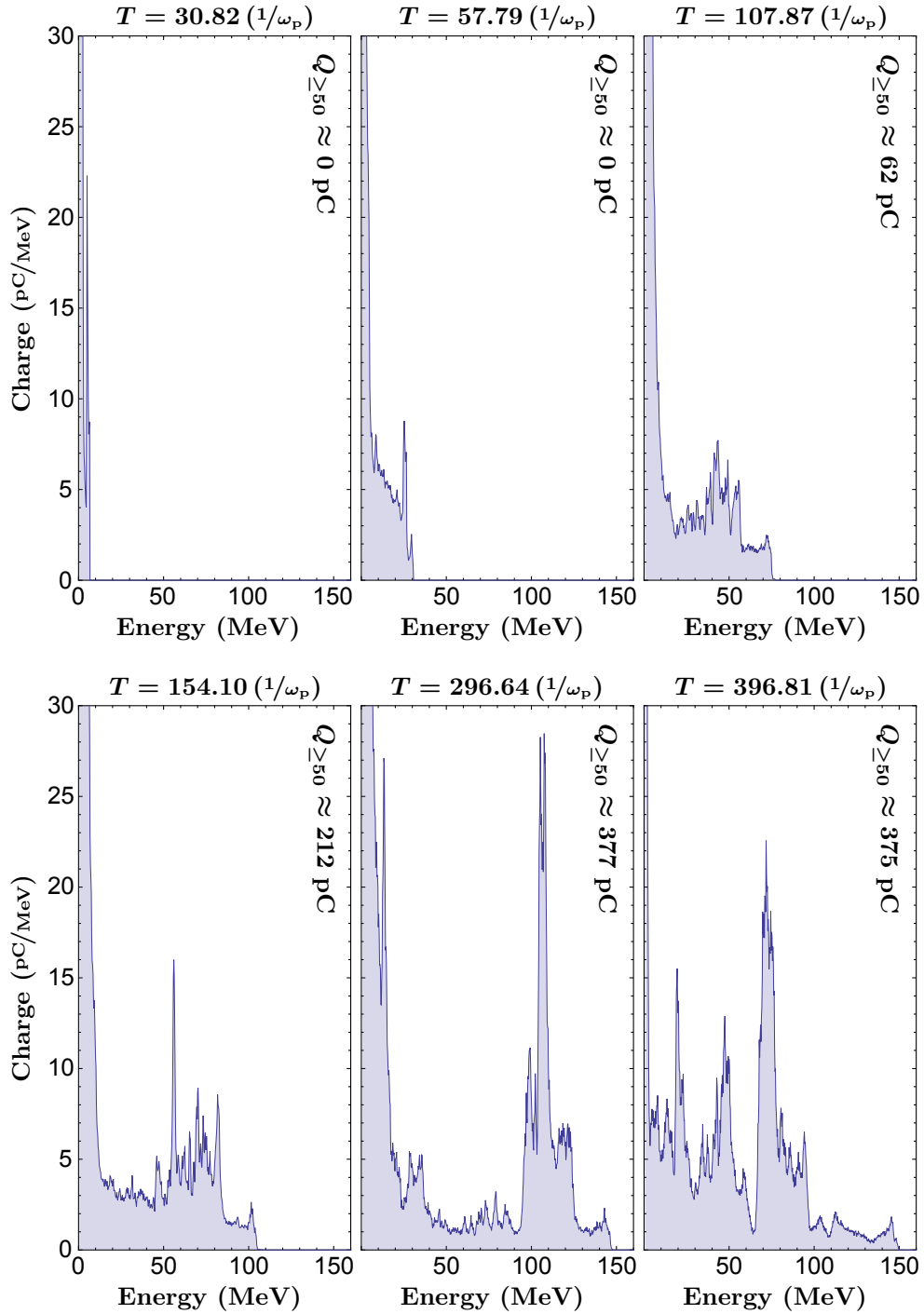


Figure 1.4.8 – LWFA time series of an electron-energy spectrum for the same set of simulation parameters as given in the caption to figure 1.4.6. Here, $Q_{\geq 50}$ denotes the amount of charge contained within each spectral distribution above an energy of 50 MeV.

I.V Experimental consequences and conclusions

The theoretical relations and models presented in this chapter help to establish several guidelines for the experimental conditions necessary to accelerate electrons by laser-driven plasma wakes. Therefore, they motivate the choice of experimental parameters in the following chapters. First, to reach highest possible electron energies, the electron plasma density needs to be decreased to a value which allows for equal dephasing and laser-guiding distances. Second, since wave-breaking will be responsible for electron injection into the wakefield, the achievable laser intensity at focus limits n_e to a lower threshold, which might exceed the value desirable for optimum electron dephasing. Third, in the case of no additional optical guiding of the intense laser beam, the confocal laser parameter b should be chosen to approximately equal or to slightly exceed L_d and L_{ed} . In the case of optical guiding, this constraint is relaxed, so that $L_d \approx L_{ed}$, whereas w_0 must be matched to the guiding mode of the employed waveguide. In the following chapters, these demands will be connected to quantitative measures resulting from the available laser-pulse parameters during the experiments.

Chapter II

The ATLAS high-field laser facility

Relativistic light intensities are a prerequisite for self-injected laser wakefield acceleration of electrons in an underdense plasma (confer chapter I). Nowadays, these very high energy flux densities can be readily achieved with femtosecond-duration, multi-terawatt laser bursts focused to spot sizes of micrometer scale, which are produced by a machine fitting on a table-top. The electron-acceleration results presented in this thesis (see chapters IV and V) are rendered possible by utilizing such a high-intensity laser, namely the upgraded ATLAS¹ high-field system at the Max-Planck-Institut für Quantenoptik. This device was set up partially in the framework of this dissertation. Therefore the layout, properties and specifications of ATLAS will be discussed in detail in section II.III. The preceding paragraphs give an overview about the bandwidth demands for short laser pulses (sec. II.I) and the consequences this entails for pulse amplification (sec. II.II).

II.I Bandwidth limit and pulse duration

Laser pulses with durations in the femtosecond-domain require large bandwidths in frequency space. This can be understood for instance when investigating a plane electro-magnetic wave of central frequency ω_0 with a Gaussian-shaped temporal envelope. In the following derivations, cubic and higher-order phase terms are neglected for the sake of simplicity. Under these conditions, such a light wave may mathematically be described by:

$$\begin{aligned} E(t) &= E_0 e^{-at^2} e^{i(\omega_0 t + \phi(t))} & \text{with} & & \phi(t) &= bt^2 + \mathcal{O}(t^3) \\ &= E_0 e^{-(a-ib)t^2} e^{i\omega_0 t} \end{aligned} \quad (2.1.1)$$

This corresponds to a temporal envelope profile in energy flux density of:

$$I(t) \propto |E(t)|^2 \propto e^{-2at^2}$$

where a represents a measure for the pulse duration and is related to the FWHM length in laser intensity $\Delta\tau = (2a^{-1} \ln 2)^{1/2}$. The parameter b defines the amount of quadratic phase.

¹ ATLAS is an acronym for **A**dvanced **T**itanium:sapphire **L**ASer.

The imaginary part of (2.1.1) describes the total phase ϕ_{tot} of the electric-field. Therefore an expression for the instantaneous frequency $\omega_i(t)$ can be given as:

$$\omega_i(t) = \frac{d\phi_{\text{tot}}}{dt} = \omega_0 + 2bt$$

Thus, the quadratic phase term in time corresponds to a linear time dependence of the instantaneous frequency of the pulse, called linear chirp. The frequency spectrum of the sample pulse $\tilde{E}(\omega)$ may be calculated by applying a Fourier transform to $E(t)$:

$$\begin{aligned} \tilde{E}(\omega) &= \frac{1}{\sqrt{2\pi}} \int_{-\infty}^{\infty} E_0 e^{-(a-ib)t^2 + i\omega_0 t} e^{-i\omega t} dt \\ &= \frac{E_0}{\sqrt{2(a-ib)}} e^{-\frac{(\omega-\omega_0)^2}{4(a-ib)}} \propto e^{-\frac{1}{4} \frac{a}{a^2+b^2} (\omega-\omega_0)^2 - i \frac{1}{4} \frac{b}{a^2+b^2} (\omega-\omega_0)^2} \end{aligned}$$

which yields a power spectrum of the form

$$\tilde{I}(\omega) \propto |\tilde{E}(\omega)|^2 \propto e^{-\frac{1}{2} \frac{a}{a^2+b^2} (\omega-\omega_0)^2} \propto e^{-4 \ln(2) \left(\frac{\omega-\omega_0}{\Delta\omega}\right)^2}$$

$\Delta\omega$ refers to the full width at half maximum spectral range span through which the corresponding frequency width $\Delta\nu$ can be expressed as:

$$\Delta\nu = \frac{\Delta\omega}{2\pi} = \frac{\sqrt{2 \ln 2}}{\pi} \sqrt{a \left[1 + \left(\frac{b}{a}\right)^2 \right]}$$

Hence, for a given pulse duration the presence of chirp leads to an increase in spectral bandwidth as compared to an unchirped pulse. Accordingly, chirp entails an elongation of the temporal profile for a fixed spectral bandwidth. On this account, it is possible to define a time-bandwidth-product (TBP) as a measure of phase distortions. For the investigated Gaussian pulse it reads:

$$\Delta\tau\Delta\nu = \frac{2 \ln 2}{\pi} \sqrt{1 + \left(\frac{b}{a}\right)^2} \approx 0.441 \sqrt{1 + \left(\frac{b}{a}\right)^2} \quad (2.1.2)$$

Therefore, the TBP of a Gaussian approaches its minimum $\Delta\tau\Delta\nu \rightarrow 0.441$ for $b \rightarrow 0$. Then the laser pulse is called transform limited, which physically means all spectral components have the same phase resulting in the shortest possible pulse duration for a given spectral shape. Time-bandwidth-products for a selection of commonly used temporal profiles can be found in table 2.1.1. From these it may be estimated that the synthesis of 40 fs FWHM duration laser pulses of Gaussian shape requires a minimum FWHM bandwidth in wavelength of ~ 23.5 nm, which is close to ATLAS parameters as will be discussed later. In general Heisenberg's uncertainty principle demands for arbitrarily formed envelopes that $\Delta\omega_{\text{RMS}}\Delta t_{\text{RMS}} \geq 1/2$ [SIEGMAN 1986], with both the duration and the bandwidth given in root mean square (RMS) values².

² The FWHM factor of ~ 0.441 in (2.1.2) changes to $1/2$ exactly when RMS conventions are applied instead.

Field envelope	Intensity profile in time t	Intensity profile in frequency ω	Minimum TBP (FWHM)	Duration $\Delta\tau$ (FWHM)
Gaussian	$\propto \exp\left[-2\left(\frac{t}{\tau_{\text{Ga}}}\right)^2\right]$	$\propto \exp\left[-\frac{1}{2}(\tau_{\text{Ga}}\omega)^2\right]$	0.441	$1.177 \tau_{\text{Ga}}$
Lorentzian	$\propto \left[1 + \left(\frac{t}{\tau_{\text{Lo}}}\right)^2\right]^{-2}$	$\propto \exp(-2\tau_{\text{Lo}} \omega)$	0.142	$1.287 \tau_{\text{Lo}}$
Hyperbolic secant	$\propto \text{sech}^2\left(\frac{t}{\tau_{\text{Se}}}\right)$	$\propto \text{sech}^2\left(\frac{\pi}{2}\tau_{\text{Se}}\omega\right)$	0.315	$1.763 \tau_{\text{Se}}$
Rectangular	$\propto \mathfrak{H}\left(\frac{\tau_{\text{Re}}}{2} - t \right)$	$\propto \text{sinc}^2(\tau_{\text{Re}}\omega)$	0.443	τ_{Re}

Table 2.1.1 – Full width at half maximum time-bandwidth-products and pulse durations for selected temporal laser-pulse envelopes. \mathfrak{H} denotes the Heavyside step function. Numbers are taken from KRAUSZ [2006].

II.II The concept of chirped-pulse amplification

Short and broadband laser pulses can readily be generated at nJ to μJ levels, e.g. in Titanium:sapphire oscillators (confer BRABEC and KRAUSZ [2000]). However, further direct amplification of these light bursts poses two significant problems. First, the intensity of an amplified short pulse can easily surpass the damage threshold of reflective and transmissive optics and thus can lead to destruction of the laser components. Second, the amplified laser pulse itself may degrade in quality. At high intensities the polarization response of any optically transparent medium shows a dependency on powers of the electric field larger unity and becomes essentially nonlinear. This also entails an intensity dependence of the index of refraction η , which can be written in lowest order approximation as:

$$\eta = \eta_0 + \eta_2 I$$

Here, η_0 is the refractive index in its commonly used form and η_2 is a factor that determines the linear intensity-related contribution (for a selection of values for η_0 and η_2 see table 2.2.1). This

Medium	η_0	η_2 (W^{-1}cm^2)	Data from
Sapphire	1.8	$2.9 \cdot 10^{-16}$	WEBER [1995]
Silicon	3.4	$2.7 \cdot 10^{-14}$	BLOEMBERGEN et al. [1969]
Fused silica	1.47	$3.2 \cdot 10^{-16}$	WEBER [1995]
SF-59	1.953	$3.3 \cdot 10^{-15}$	WEBER [1995]
BK-7	1.52	$3.4 \cdot 10^{-16}$	WEBER [1995]
Air	1.0003	$5.0 \cdot 10^{-19}$	PENNINGTON et al. [1989]
Vacuum	1.0	$1.0 \cdot 10^{-34}$	EULER and KOCKEL [1935]

Table 2.2.1 – The refractive index η_0 and the intensity-dependent factor η_2 of media often utilized in laser setups. A more extensive selection can be found in WEBER [1995] and BOYD [2003]. The quoted numbers are valid for laser wavelengths specified in the given reference.

intensity dependence may cause temporal phase distortions via self-phase modulation (SPM) and also may introduce spatial distortions of the laser pulse phase and intensity fronts, which can result in self-focusing (SF) or filamentation. The severity of these undesirable effects can be estimated with the help of the B -integral:

$$B = \frac{2\pi}{\lambda} \int_0^L \eta_2 I dx \quad (2.2.1)$$

The integration has to be executed along the laser beam path of total length L and take into account the nonlinear media-specific indices of refraction. Then B represents the amount of accumulated wave-front distortions owing to η_2 and is normalized to the laser wavelength λ . In order to ensure a good beam quality, the B -integral must be kept significantly below unity. Realistically, this limits the maximum intensity to which a laser-pulse can be directly amplified inside an active amplifier medium to $\sim 1 \text{ GW}\cdot\text{cm}^{-2}$ [MOUROU et al. 2006].

An increase in laser beam diameter and therefore a decrease in intensity during amplification is no feasible solution to this problem either. The reason is again twofold: First, this would require ever bigger optics throughout the whole laser chain, which would become very expensive and thus is economically unfavorable. But more importantly, the energy extraction efficiency of a laser beam inside an excited amplification material strongly depends on the seed laser input-energy fluence level F_{seed} [SIEGMAN 1986], which means F_{seed} must be maintained high while I should be low. Hence, the only possibility to boost light pulses in energy beyond the energy flux density threshold is to increase their pulse duration.

A milestone invention allowing for temporal stretching, subsequent amplification and reliable recompression of a broadband laser pulse at TW to PW peak powers is the chirped-pulse amplification (CPA) technique devised by STRICKLAND and MOUROU [1985] (see figure 2.2.1). In CPA in its most common form a short electro-magnetic pulse is sent through a grating-based stretcher which introduces positive group delay dispersion (GDD) [MARTÍNEZ 1987], thus chirps the pulse and elongates it by a factor usually on the order of 10^3 to 10^5 . Temporal stretching is accomplished by guiding different frequency components along different paths inside the stretcher resulting in runtime differences and GDD, which can be characterized by a stretcher-specific frequency-dependent phase shift:

$$\phi(\omega) = \phi_0 + \phi_1(\omega - \omega_0) + \phi_2(\omega - \omega_0)^2 + \phi_3(\omega - \omega_0)^3 + \dots \quad \text{with} \quad \phi_n = \left. \frac{1}{n!} \frac{d^n \phi}{d\omega^n} \right|_{\omega_0}$$

ϕ_0 corresponds to an overall frequency independent shift of the carrier-envelope phase, whereas ϕ_1 describes a time-delay of the whole laser-pulse. Neither of these processes contributes to an increase in pulse duration unlike phase orders of $n \geq 2$. The function $\phi(\omega)$ is usually quite complex and depends on the exact stretcher setup. For this reason it is important to utilize a matched stretcher-compressor pair such that the phase induced by the stretcher ϕ_{str} can be compensated for as closely as possible by the phase shift originating from the compressor

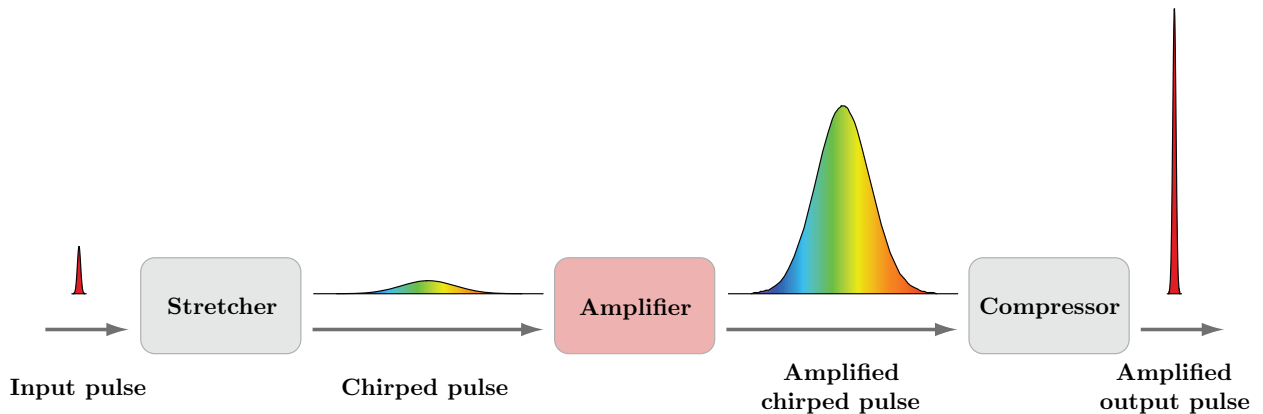


Figure 2.2.1 – In a chirped-pulse amplification (CPA) scheme, a short laser pulse is stretched in time to reduce its intensity during an ensuing amplification process. This elongation is introduced inside a stretcher, which strongly disperses the broad bandwidth pulse. The temporal frequency separation will be undone in a matching compressor setup after amplification. CPA allows for the generation of ultra-short (~ 20 fs) and ultra-powerful (~ 200 TW) laser bursts.

$\phi_{\text{Comp}} \approx -\phi_{\text{Str}}$. The matched configuration to the Martínez-stretcher (confer previous paragraph) is the Treacy-compressor [TREACY 1969]. Both are employed in the ATLAS laser system (confer figures 2.3.8a and 2.3.8b). If material dispersion in the laser chain could be neglected, then a perfect recompression of the stretched laser beam and compensation of all phase orders ϕ_n would be possible [PESSOT et al. 1987]. In reality the phase ϕ_{Mat} introduced by transmissive or reflective optics and even air is non-negligible and thus recompression by means of matched stretcher-compressor pairs remains imperfect, since now $\phi_{\text{Str}} + \phi_{\text{Comp}} + \phi_{\text{Mat}} \approx 0$ must be fulfilled. For the above mentioned Martínez-Treacy setup³ this is only exactly possible for ϕ_n with $n \leq 3$. However, the residual higher-order phase errors are typically small and pulse durations of $\Delta\tau \gtrsim 40$ fs FWHM are achievable without applying more sophisticated phase correction devices such as acousto-optic modulators [TOURNOIS 1997] or chirped multilayer dielectric mirrors [SZIPÓCS et al. 1994].

II.III ATLAS layout and laser pulse properties

ATLAS, the ultra-high-intensity laser system at the Max-Planck-Institut für Quantenoptik, provides light bursts of more than 20 TW peak power and generates focused intensities exceeding the relativistic threshold. These features prove to be essential for the success of the experiments detailed in this dissertation. ATLAS employs a CPA-scheme (confer section II.II) making it possible to harness the broad amplification bandwidth of titanium-doped sapphire crystals and consequently to synthesize laser pulses as short as ~ 40 fs FWHM containing ~ 1 J of energy. The basic layout of this machine is depicted in figure 2.3.1.

³ A number of matched stretcher-compressor arrangements with different dispersion properties have been demonstrated as well [LEMOFF and BARTY 1993; TOURNOIS 1993; WHITE et al. 1993; CHERIAUX et al. 1996].

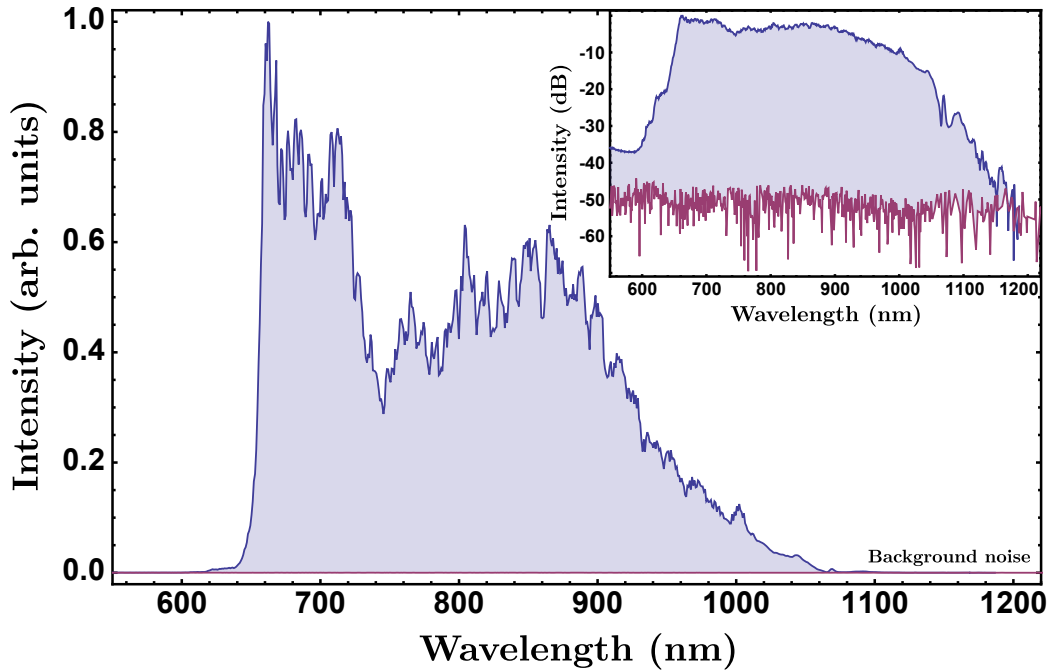


Figure 2.3.3 – Oscillator spectrum in linear representation and on logarithmic scale (inset). The red signal represents the level of background noise.

configuration, but can easily be reimplemented for future use.

After leaving the resonator, the generated pulse train propagates through a Faraday isolator, then is spatially filtered and afterwards guided to a first amplification stage. Like all following amplifier units, this multi-pass is based on titanium:sapphire as the active medium. Incoming laser pulses traverse this crystal on nine successive passes in a triangular shape (see figure 2.3.5). The amplification medium is pumped by a frequency doubled, Q-switched Continuum Minilite Nd:YAG laser with 25 mJ stored in each pulse of several nanoseconds duration arriving at 10 Hz repetition rate (table 2.3.1). The repetition rate mismatch between the seed and the pump system entails that only one in seven million oscillator pulses is amplified to the maximum extent (confer figure 2.3.4a) and as a consequence contains $\sim 2 \mu\text{J}$ of energy. These particular pulses will be extracted downstream in the laser chain and only they will receive a further energy boost in the following. This amplifier is referred to as a preamplifier, given that the amplification process occurs prior to a CPA-specific temporal elongation. Its purpose is to supply the next amplification stage, a regenerative amplifier (figure 2.3.6a), with an energetic seed, since regenerative amplifiers are prone to deterioration of the amplified spontaneous emission (ASE) contrast on a nanosecond scale when seeded at insufficient levels. The ASE contrast is defined as the ratio of the instantaneous intensity in an ASE pedestal to the laser peak intensity. This property proves to be of crucial importance for solid-density experiments, for which an inadequately high ASE intensity can cause ionization of the target, create a pre-plasma, and therefore significantly alter any interaction dynamics.

The effect of preamplification on the laser contrast at the ATLAS output has been investigated and is shown in figure 2.3.4 as a function of the preamplifier amplification factor f_A . Subfigure (a) visualizes the 70 MHz pulse train behind the amplifier and gives a definition of f_A . The

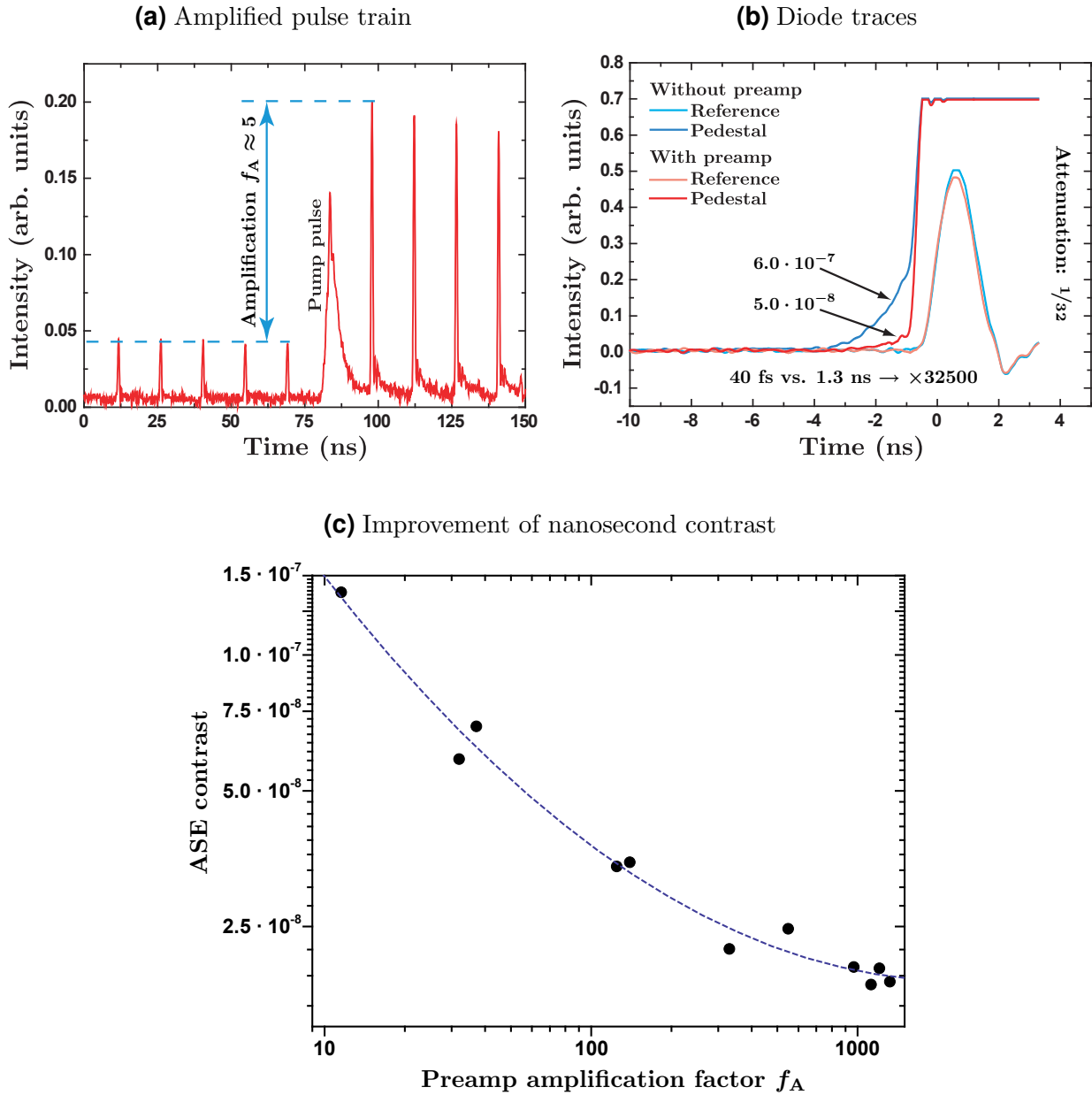


Figure 2.3.4 – (a) The amplification of a part of the oscillator pulse train prior to stretching allows for a high energy-fluence seeding of the regenerative amplifier, resulting in an improved laser contrast at the end of the laser chain. In this example a small amplification factor f_A of five is chosen for better clarity. However, larger f_A can improve the ASE contrast significantly as shown in (c). (b) This has been diagnosed comparing the traces of a saturated and an unsaturated PIN-diode at the ATLAS output.

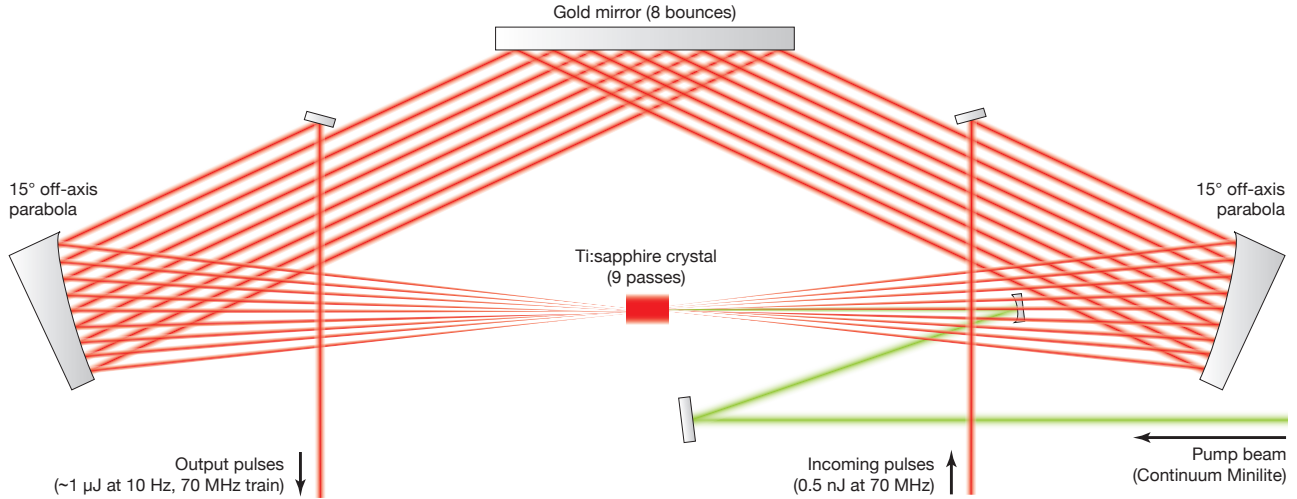


Figure 2.3.5 – Scheme of the preamplifier, which boosts pulse energy to the micro-joule level, thus providing a sufficient seed fluence for the regenerative amplifier to efficiently suppress amplified spontaneous emission.

quality of contrast was estimated by utilizing two PIN-diodes of equal properties, one observing a strongly attenuated laser signal that causes no saturation and hence yields a measure of the total contained energy. The other diode detects a stronger signal and heavily saturates when the main laser pulse arrives, but allows for the quantification of the amount of energy dumped onto its surface by prepulses and ASE background (b). Consequently, a comparison of the time scales during which these energies are impinging yields a ratio of intensities and thus gives an estimate of the nanosecond contrast. For maximum f_A this contrast approaches 10^{-8} , which agrees with an alternative measurement using a third-order autocorrelation technique (confer figure 2.3.10). An upper limit is imposed to the discussed preamplification scheme and the achievable amplification factor f_A by accumulated phase distortions of the amplified pulses. As discussed, the B -integral must be kept significantly below unity (see eq. 2.2.1). Therefore f_A is set to ~ 2000 in daily operation. However, this constraint does not limit the performance of ATLAS, since a significant further suppression of ASE is not expected from a further increase in preamplification strength owing to the convergent behavior displayed in figure 2.3.4c.

In a next step, the seed light is sent into a Martínez-stretcher configuration as described in section II.II (also confer figure 2.3.8a), in which the pulses become positively chirped and as a result are stretched in time to a duration of ~ 350 ps. The beam then passes through a second Faraday isolator, which protects the components upstream from damage by back reflections.

	Active medium	Rep. rate (Hz)	Duration (ns)	Pump energy or power	Wavelength (nm)	Pump for
Coherent Verdi V6	Nd:YVO ₄	cw	–	~ 3.5 W	532	Oscillator
Continuum Minilite II	Nd:YAG	10	3-5	25 mJ	532	Preamplifier
Continuum Surelite I	Nd:YAG	10	4-6	100 mJ	532	Regen. amp.
Continuum Powerlite	Nd:YAG	10	5-7	2×850 mJ	532	Multipass I
Continuum Macholite	Nd:YAG	10	5-7	2×1.7 J	532	Multipass II

Table 2.3.1 – Overview of pump-laser specifications for all ATLAS amplifier stages.

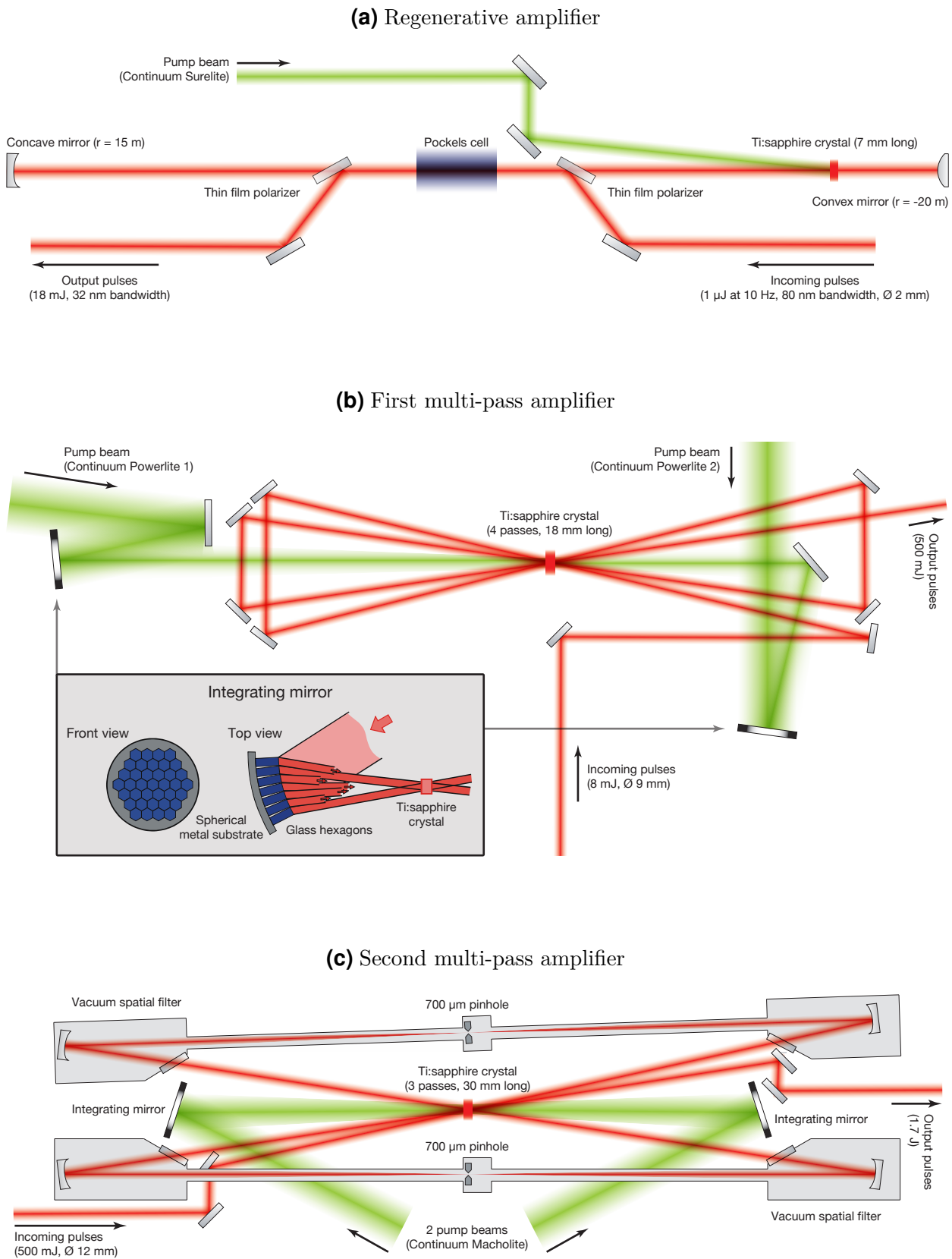


Figure 2.3.6 – Overview of the three final amplifier configurations.

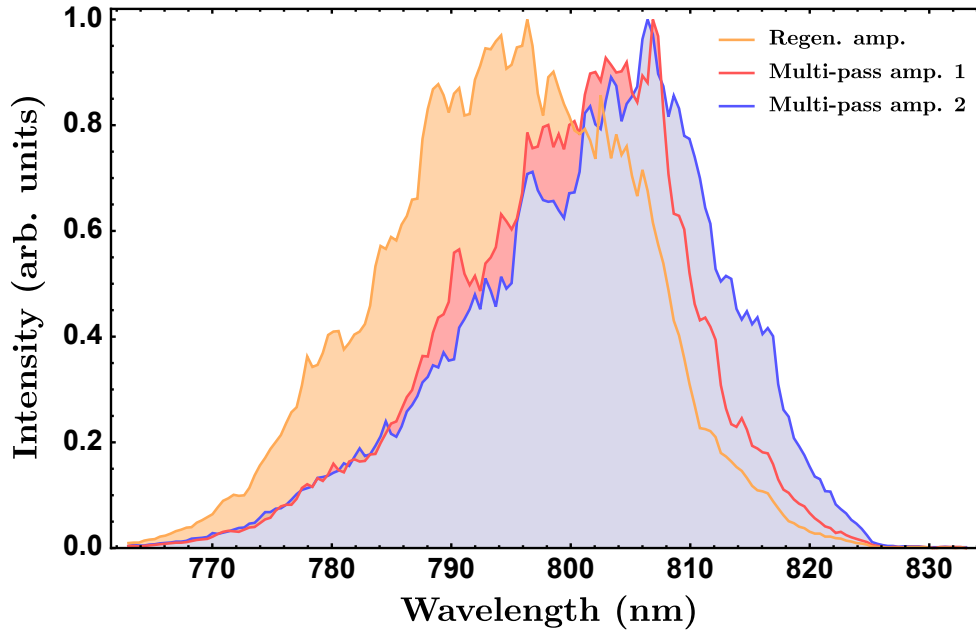


Figure 2.3.7 – Normalized laser spectra measured after the regenerative amplifier stage and after the first and second multi-pass amplifier.

Next, a Pockels cell reduces the beam repetition rate from the oscillator generated frequency at 70 MHz down to 10 Hz by filtering the pulses that have seen maximum gain in the preamplifier. Now, the stretched electro-magnetic waves can safely be amplified in the final three amplification stages, consisting of a regenerative amplifier (figure 2.3.6a), a four-pass bow-tie setup (figure 2.3.6b), and the final three-pass configuration (figure 2.3.6c). The corresponding pump laser specifications may be found in table 2.3.1. The regenerative amplifier is composed of a cavity encompassing a Ti:sapph crystal and a Pockels cell, which in combination with two thin film polarizers may couple light in and out of the resonator. The timing of this switch is adjusted in such a way that a laser pulse after being guided into the cavity executes 12 round-trips before being sent out again. During this time the pulse energy increases from a sub- μJ -level to about 18 mJ. Besides enforcing gain, the cavity also fulfills the function of a spatial filter. Only laser light that is matched to the eigenmode of the resonator will be amplified. Thus a spatially smooth beam escapes from this setup. Before being injected into the first booster amplifier, the pulses propagate through two Pockels cells, of which one has a fast rise-time of ~ 200 ps and which hence reduces prepulses and the ASE level by several orders of magnitude outside of its rise-time window. Both, the fast and the slow Pockels cell together are particularly useful to get rid of unwanted light leakage leaving the regenerative cavity on a nanosecond scale at a frequency defined by its round-trip time. Subsequently, the first of the following two multi-pass amplifiers increases the pulse energy to ~ 500 mJ, the second boosts it to ~ 1.7 J. This final amplifier can also be by-passed. Both units utilize integrating mirrors to average out spatial intensity distortions of the pump beams by decomposing their profiles into hexagonal sections and overlapping them inside the active medium. This greatly decouples the quality of the seed beam profile from the pump profiles. Moreover, the second booster amplifier is fully relay-imaged and helps to keep the seed profile clean by spatial filtering after every passage

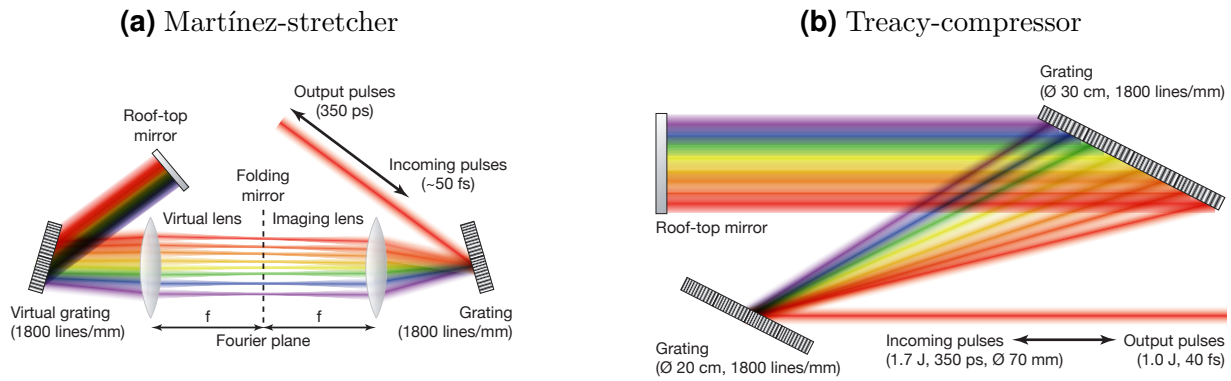


Figure 2.3.8 – The CPA-dispersion-management system implemented in ATLAS consists of a positive-chirp stretcher (a) (for the sake of symmetry and comprehensibility depicted with lenses in lieu of the actual reflective optics) and its matched negative-chirp counterpart (b).

through the $\text{Ti:Al}_2\text{O}_3$ -crystal. On its way along those three main amplifiers, the laser-beam diameter is enlarged from about one millimeter initially to approximately 12 mm in the final amplifier section in order to stay below the damage threshold of optics and coatings and to keep the B -integral at an acceptable level. The amplified light spectra after each stage are displayed in figure 2.3.7. Just a small fraction of the initial oscillator bandwidth (confer figure 2.3.3) is actually seeding the amplifier units. Owing to the bandwidth supported by the employed dielectric optics and the spectral transmission constraints of the stretcher, an approximately box-shaped spectrum of ~ 80 nm at full width around a central wavelength of 790 nm enters the cavity of the regenerative amplifier. Then, gain narrowing and spectral red-shift towards the maximum of the titanium:sapphire gain curve at 795 nm [MOULTON 1986] can be observed in the ensuing amplification process, which leads to a final bandwidth of 21.1 nm FWHM centered around 800 nm, corresponding to a Fourier-limited pulse length of 39.8 fs FWHM.

The fully amplified pulses of 350 ps duration are subsequently expanded to 70 mm in diameter and guided into a vacuum tank hosting the compressor setup (see figure 2.3.8b). Its two-grating configuration is matched to the aforementioned stretcher (figure 2.3.8a) and reverses the introduced positive chirp to a large extent. This has been confirmed by reconstruction of the spectral and temporal intensity and phase employing a simplified frequency-resolved optical gating (FROG) technique [KANE and TREBINO 1993], which is called GRENOUILLE⁴ [O'SHEA et al. 2001]. The results can be seen in figure 2.3.9. Here, a pulse duration of 43.8 fs FWHM and a FWHM bandwidth of 24.3 nm were retrieved with a FROG error of 0.007 and an RMS TBP of 0.76. The deviation from the theoretical TBP minimum of 0.5 can be explained by phase contributions from dispersion orders $n \geq 4$, which cannot be compensated for in the presented setup⁵. This investigation on a femtosecond scale is complemented by high

⁴The utilized device was a commercial Swamp Optics GRENOUILLE 8-20. For details on its principle of operation see <http://www.swampoptics.com/> on the world wide web.

⁵An acousto-optic modulator is implemented in the most recent ATLAS version. It is situated right at the stretcher exit and can introduce almost arbitrary spectral phase components. This allows for a correction of higher-order phase terms and is used to compress ATLAS pulses to sub-35 fs FWHM duration. However, this

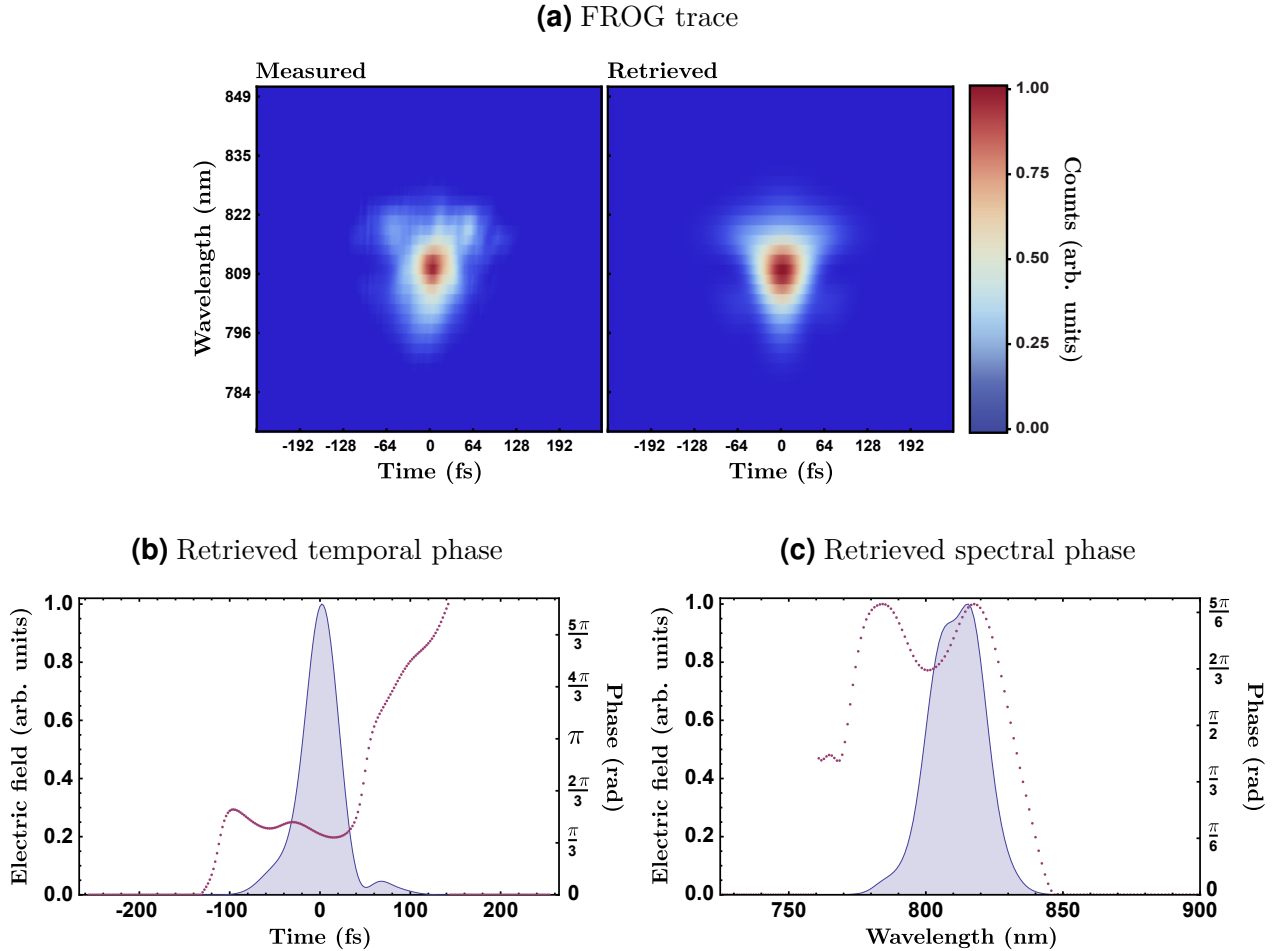


Figure 2.3.9 – (a) GRENOUILLE measurement of the (b) temporal and (c) spectral intensity and phase at the ATLAS output.

dynamic range third-order autocorrelation measurements [LUAN et al. 1993] to determine the pulse shape and contrast on a picosecond time scale (see figure 2.3.10). As may be seen, the ATLAS contrast reaches the 10^{-8} level at -4 ps, which is a remarkable result for such a system without using advanced pulse-cleaning techniques such as cross-phase modulation [JULLIEN et al. 2005], saturable absorbers [ITATANI et al. 1998; NANTEL et al. 1998], or plasma mirrors (e.g. THAURY et al. [2007]). The single prepulse visible in the examined time interval at -12 ps (at an intensity of 10^{-6} relative to the pulse peak intensity) likely comprises a ghost image of the stronger postpulse at $+12$ ps. However, owing to a rather poor sampling resolution of 100 fs, a definite conclusion cannot be drawn from their relative intensities.

In order to ensure a negligible amount of angular chirp, the output pulses have been characterized by inverted field autocorrelation [PRETZLER et al. 2000]. An angular chirp will result in a tilt of the intensity front and cause temporal and transverse spatial pulse broadening at focus and thus will reduce the overall intensity. Such a chirp can be introduced by non-parallel grating surfaces in the compressor alignment. In addition to a tilt of the intensity-pulse front, local distortions of the phase front may occur, e.g. from uneven optics surfaces, thermal lensing in media with a temperature gradient (amplifier crystals), or from B -integral issues. To correct

device has not been present during acquisition of the data presented in this work.

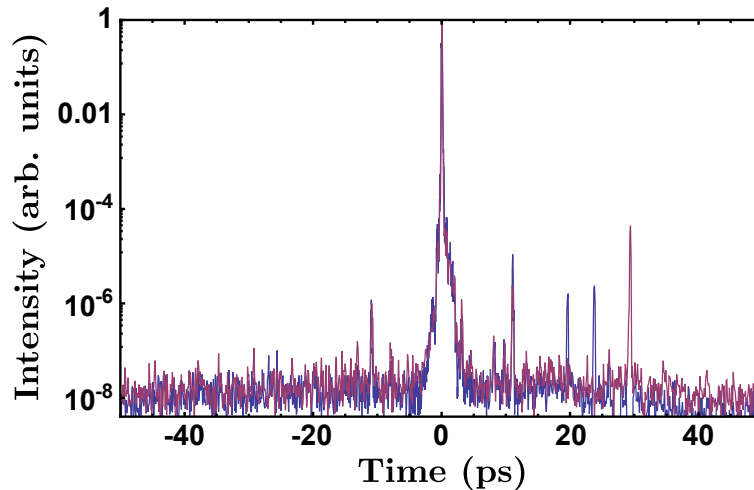


Figure 2.3.10 – Scanning third-order autocorrelation measurement of the picosecond contrast after compression for ATLAS utilizing one (red curve) or both (blue curve) multi-pass booster amplifiers.

for this effect, a deformable mirror is implemented in the optical path pre-compression. A closed-loop system processing signals from a Shack-Hartmann wavefront sensor [HARTMANN 1900; SHACK and PLATT 1971] controls 33 piezo-actuators behind the flexible surface of the mirror, which allows to generate a smooth phase front and maintain a good focusability of the beam (confer section III.II and figure 3.3.3).

After compression an ATLAS pulse contains about 1 J of energy corresponding to a compressor transmission efficiency of $> 60\%$ ⁶. The energy reproducibility has been analyzed by comparing shot-to-shot signal fluctuations from a PIN-diode and found to be as low as 2% RMS. Even for a beam diameter of 70 mm, this combination of short-pulse duration and amplitude requires the laser transport to the experimental chamber to occur under vacuum to prevent problems arising from a non-linear intensity dependence of the refractive index in air (see table 2.2.1).

II.IV Concluding remarks

The high-power (> 20 TW), short-pulse (~ 40 fs) ATLAS beam is well characterized in terms of temporal structure, reproducibility, phase- and intensity-front distortions. Its demonstrated specifications allow for the application of these pulses in experiments, which rely on relativistic intensities such as self-injected laser wakefield acceleration (see chapters IV and V), or which require light bursts with a well defined, high-quality temporal contrast as is needed for laser-plasma interaction studies at overcritical density, e.g. high-harmonic generation on surfaces [HÖRLEIN et al. 2008; NOMURA et al. 2008] or ion acceleration [HENIG et al. 2009].

⁶Transmission efficiencies as high as 72% have been measured after UV-cleaning the compressor gratings.

Chapter III

Propagation of relativistic laser pulses through a capillary discharge waveguide

The guiding of intense laser pulses over distances significantly longer than determined by their confocal parameter is a key requirement for a successful realization of laser wakefield acceleration with the goal to access peak electron energies W_e as high as possible. As discussed in section I.IV, the scaling of electron energy with plasma density ($W_e \propto n_e^{-1}$) in a weakly relativistic regime ($a_0 \approx 1$) dictates the use of an n_e as small as feasible. However, these dilute plasmas must feature an electron density still high enough to allow for self-injection. In such a scenario, the necessary electron acceleration distance to reach maximum momentum is expected to be far longer than the potential interaction distance over which unguided multi-terawatt laser pulses can maintain a sufficient energy flux density before they diffract.

To counteract diffraction, different techniques have been developed that allow for the confinement of relativistic beams over adequate distances. Self-focusing (see section I.IV.III) may be utilized, but is hard to control due to its nonlinear nature. Pre-shaped freely expanding plasma channels with shock-driven density discontinuities that grant waveguide properties have been proposed [SPRANGLE et al. 1992; DURFEE III and MILCHBERG 1993] and demonstrated to work well, but demand complex experimental setups with up to three powerful laser beams [GEDDES et al. 2004]. A similar idea incorporating a less complicated electrical igniter scheme was suggested, but has not been employed for electron acceleration, yet [LOPES et al. 2003]. Furthermore, narrow ($\leq 100 \mu\text{m}$ diameter) waveguide tubes have been shown to support direct guiding of intense beams but lack durability [DORCHIES et al. 1999]. Also, gas-filled capillaries can be deployed for guiding in various ways. When ignited with excessively high currents ($\gtrsim 5 \text{ kA}$), a Z-pinch effect causes a magneto-hydrodynamic channel implosion during which a transverse parabolic density-profile is generated, which facilitates laser channeling [HOSOKAI et al. 2000]. This process lasts for just a few tens of nanoseconds. Therefore this device is referred to as a fast capillary discharge waveguide. At lower currents wall-ablative polypropylene capillaries may generate a parabolic density profile [KAGANOVICH et al. 1999]. However, the lifetime of these structures is limited to a couple of hundred shots. The method of choice enabling guiding in the experiments presented here, is a slow capillary discharge waveguide [SPENCE and HOOKER 2000]. Its working principle will be introduced in the following. Sub-

sequently, its incorporation into the experimental setup for the realization of laser guiding and electron acceleration is illustrated. This setup is reviewed with an emphasis on the employed light diagnostics (section III.II; for electron-diagnostic specifications see section IV.I). Finally, the obtained guiding results will be analyzed (section III.III), preparing the execution and interpretation of the laser-wakefield-acceleration experiments presented in chapter IV.

III.I The slow capillary discharge waveguide

The employed slow capillary discharge waveguide consists of two rectangular sapphire slabs, each with a laser-machined half-cylindrical groove in its top or bottom surface, respectively (see figures 3.1.1a). These grooves are contacted together to form a 250 μm diameter channel of 15 mm length. In addition, one of the sapphire plates features a pair of 600 μm wide trenches leading to the central slot and acting as gas inlets. Hydrogen molecules (H_2) are streaming from the capillary Perspex housing gas reservoir (figure 3.1.1b) through those supply lines into the central capillary, where they set up a homogeneous gas distribution as detailed in section V.II at backing pressures ranging from about 50 to 600 mbar. This pressure can be controlled with the help of a hydrogen regulator and is diagnosed by a Leybold-Heraeus membrane gauge. The gas flow may be switched on and off using an electrically triggered solenoid valve. During the experiments described here and in the next chapter, this gas switch opens for more than 200 ms in order to ensure that a homogeneous steady-state gas distribution has developed before plasma is generated inside the interaction volume (confer section V.II).

The dissociation and ionization of hydrogen molecules is initiated by the breakdown of a 20 to 30 kV electric potential. This discharge occurs between two copper electrodes along the gas-filled channel. Figure 3.1.2 depicts a diagram of the electronic circuit responsible for ignition. Its mode of operation is as follows. A 2.7 nF capacitor¹ is charged to a maximum of 30 kV with the help of a Glassman DC power supply. Then, it contains up to 1.2 J of energy. The applied difference in electric potential and hence stored energy may be relayed to the capillary-waveguide electrodes by triggering a Perkin Elmer HY-3005 deuterium thyratron². This high-voltage switch has a particularly fast current rise-rate of $10^{11} \text{ A}\cdot\text{s}^{-1}$ and hence allows for immediate connection of the charged capacitor to the gas-filled channel. The impressed voltage easily exceeds the breakdown threshold for the gaseous medium and consequently, the discharge fires. After an initial spark, free electrons are accelerated quickly and drive an avalanche-ionization process, which creates a strong current of several hundred Ampères lasting for a few hundred nanoseconds (confer figure 3.3.1a). This current heats the plasma column rapidly. A major part of the energy initially stored in the capacitor is dedicated to drive that heating process, since just about 11 mJ are necessary to ionize the complete channel filling at $n_e = 7 \cdot 10^{18} \text{ cm}^{-3}$. The subsequent cooling of electrons and ionized hydrogen nuclei at the sapphire walls causes

¹In addition to the main capacitor, the coaxial cables, the capillary electrodes and other parts of the circuit do possess small amounts of capacitance. However, in a first order approximation this extra contribution can be neglected as it is estimated to increase the total capacitance by less than 300 pF.

²See <http://catalog.rell.com/rellecom/Images/Objects/9500/9438.PDF> for details.

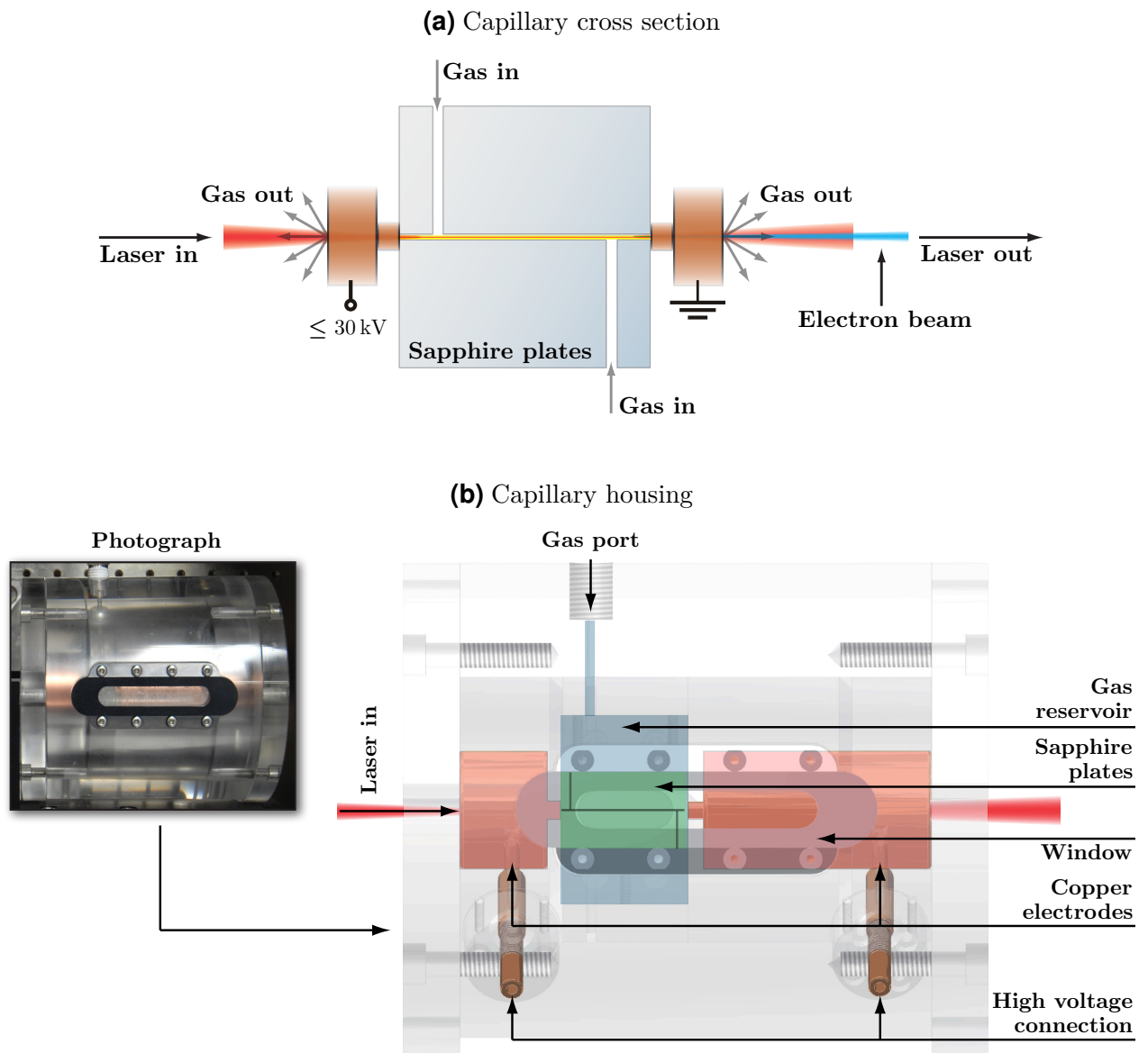


Figure 3.1.1 – (a) Cross section of a capillary discharge waveguide and (b) layout of the Perspex enclosure with high voltage connections and gas port.

a radial energy transport, which results in an increased electron density off-axis. After several tens of nanoseconds, this plasma distribution develops a parabolic transverse profile, which is ideal for guiding of Gaussian laser modes (confer section I.IV.IV).

The formation and temporal evolution of those plasma channels has been investigated in detail both theoretically [BOBROVA et al. 2001; BROKS et al. 2005, 2007] and experimentally [GON-SALVES et al. 2007; MARX 2008]. A characterization of the radial electron density profile as a function of time was performed for waveguides similar to those employed in this study using an interferometric technique (for details see MARX [2008])³. A measurement of the longitudinally averaged electron density is shown in figure 3.1.3. As may be seen, a parabolic plasma density profile forms after ~ 100 ns of current flow, resulting from the aforementioned interplay of ohmic heating and wall cooling. The guiding structure remains quasi-stationary for another ~ 150 ns before it decays. This matches well to results obtained from an investigation of laser-beam guiding in such a channel (cf. section III.III). Owing to those rather long characteristic times on a hundred nanosecond scale this kind of setup is called a slow capillary discharge waveguide.

III.II Experimental setup and laser diagnostics

The integration of the capillary waveguide into the general experimental configuration is illustrated in figure 3.2.1. This setup can be divided by function into four substructures: a laser beam preparation stage, the central laser-plasma interaction environment, and two separate diagnostics setups, one for the transmitted laser pulses, and another one for the generated electron beams. All of these are detailed in this section with the exception of the electron diagnostics. They will be discussed in the context of laser wakefield acceleration in preformed channels (section IV.I).

Preparation and characterization of high-intensity laser pulses

During the course of this study, the ATLAS facility (confer chapter II) delivered well characterized, ultra-short laser pulses with powers exceeding 20 TW into the experimental chamber via a vacuum transport system. Those light pulses were temporally analyzed close to the interaction volume by GRENOUILLE (see section II.III), which retrieved durations as short as 40 fs FWHM. For this measurement, a part of the beam was sent into the spectral-phase-and-intensity detector through a thin 3 mm quartz window and through 0.5 m of air. Calculations taking into account the well known dispersion properties of these materials suggest that their impact on pulse duration was small, causing an elongation of 3 fs FWHM at most. The average energy contained in each light pulse was determined with the help of a calibrated calorimeter (not shown in the setup scheme) to be 850 mJ right before entering the waveguide, correspond-

³The investigated capillaries featured a square-channel cross section in order to allow for straightforward interferometric measurements with phase-front aberrations as small as possible originating from a curvature of the inner sapphire walls. The differing wall shape, however, should only marginally influence the electron-density distribution and waveguide properties compared to capillaries with circular profiles [BROKS et al. 2007].

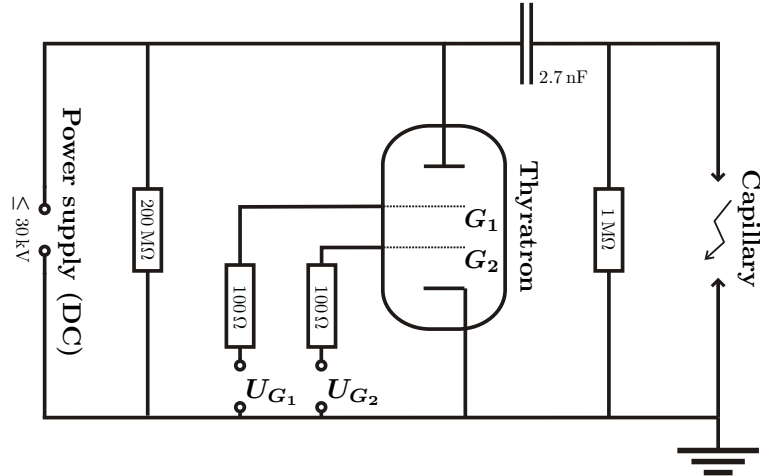


Figure 3.1.2 – Discharge circuit diagram. A DC power supply charges a 2.7 nF capacitor at 20 to 30 kV through a current limiting resistor (1 M Ω). This potential difference may then be relayed to the capillary electrodes by triggering a two-grating (G_1 and G_2) thyatron switch via the application of appropriate voltages U_{G_1} and U_{G_2} , causing a high-voltage breakdown in the gas-filled channel. For safety reasons, the capacitor will be slowly discharged through a 200 M Ω resistor when the power supply is turned off.

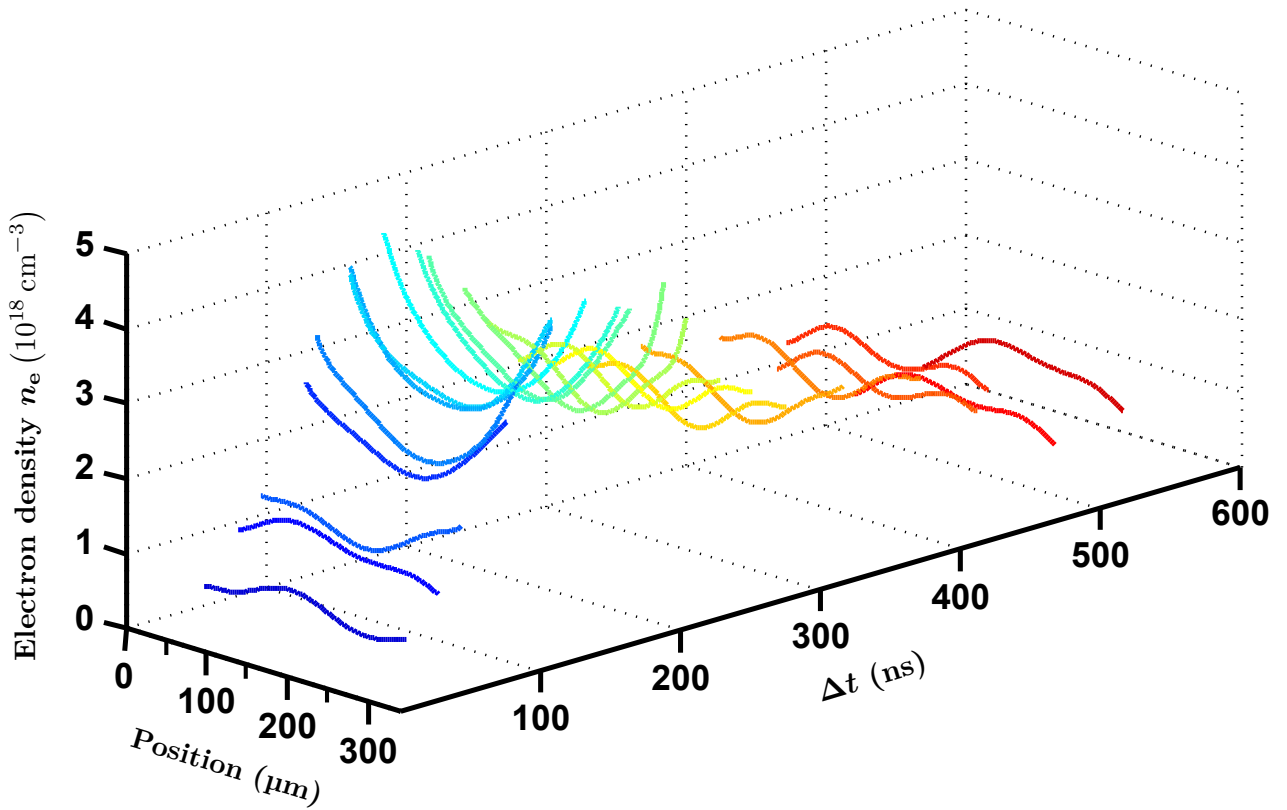


Figure 3.1.3 – Transverse time-dependent electron-density profile in a slow capillary discharge waveguide at 200 mbar backing pressure. A parabolic structure develops ~ 100 ns after ignition centered along the central channel axis and stays quasi-stationary for the next ~ 150 ns, allowing for guiding of Gaussian laser modes.

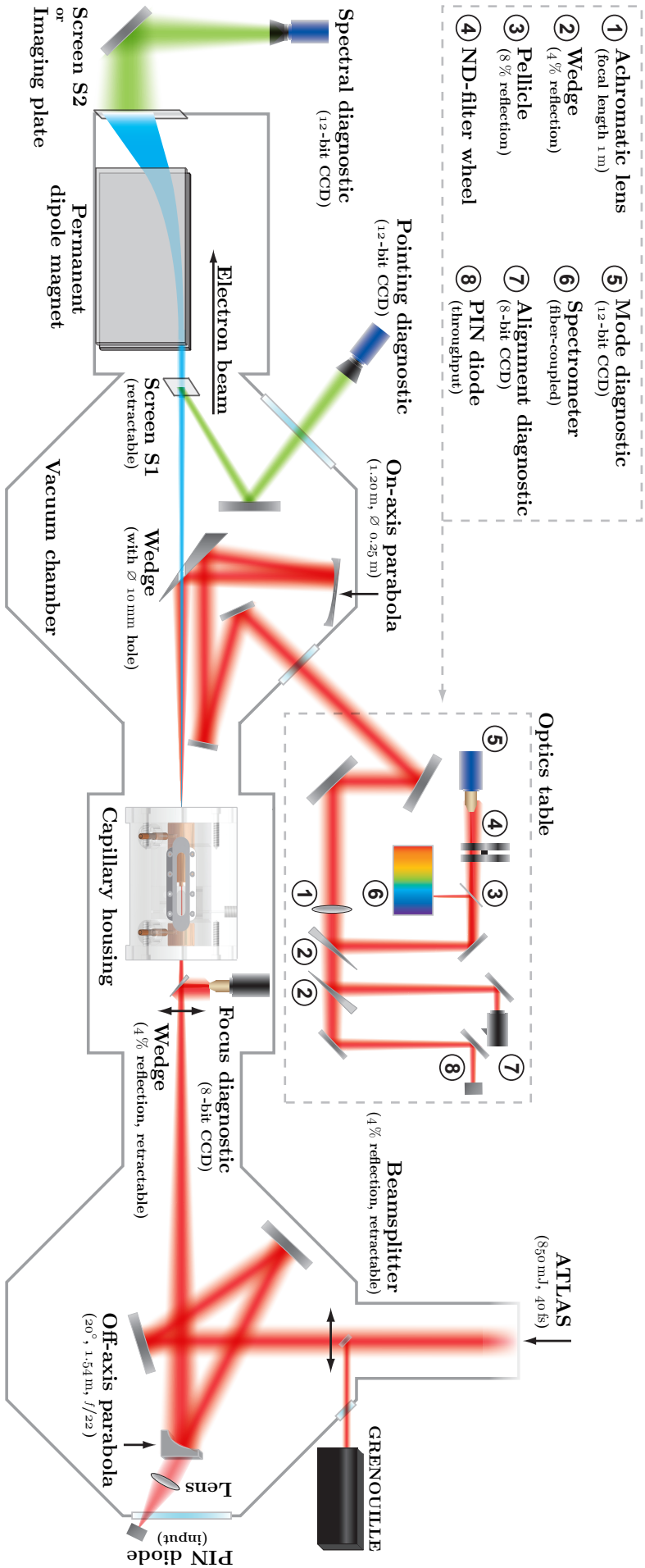


Figure 3.2.1 – Overview of the vacuum chamber setup and experimental diagnostics. These include detectors for the properties of accelerated electron bunches (energy spectrum, charge, divergence, beam pointing) as well as for characteristics of the incoming and guided laser pulses (energy, spatial quality, guiding efficiency, spectral phase and intensity).

ing to a beamline transport efficiency of $\sim 85\%$. Shot-to-shot fluctuations in pulse energy have been detected by imaging laser leakage through an off-axis parabolic mirror onto a Thorlabs PDA36A PIN-diode. This revealed typical RMS energy stabilities on a 2 to 3% level. The frontside of that dielectric off-axis parabola directed and focused the incoming light pulses in an $f/22$ geometry into the capillary entrance, situated at a distance of $f = 1.54$ m. Direction and position of the laser beam at focus were defined by centering the laser near-field on an alignment cross-hair at the parabola rear side, and by fixing the far-field to a predefined focal spot location. That position could be observed for an attenuated beam on a stationary 8-bit CCD camera with microscope objective, onto which the laser pulses were relayed by a quartz wedge attached to a motorized flip-mount with excellent reproducibility in space. Also, this camera provided a coarse estimate of the focal quality. For a high-resolution, high-dynamic range far-field characterization, the capillary discharge waveguide had to be removed and replaced by a 12-bit DataRay WinCamD beam-profile analyzer equipped with a $20\times$ magnification microscope objective. This yielded a FWHM beam diameter of $23\ \mu\text{m}$, a FWHM encircled energy fraction of 61%, and thus a Strehl ratio of 0.73 (see image at the left in figure 3.3.3). Shot-to-shot beam pointing variations were found to be small and were on the order of the focal spot radius. The spatial calibration of the profiler imaging system was carried out by introducing a cardboard grating with a lattice constant of $g = 100\ \text{m}^{-1}$ into the laser near-field. From the diffraction pattern appearing at focus, it was possible to deduce the magnification, since the distance z between two neighboring diffraction spots is given by $z \approx \lambda f g$ for small diffraction angles. In the end, after the previously described laser beam alignment was performed carefully, and the entrance of the empty sapphire capillary resided close to the position of the focal spot, and the channel tip and tilt was roughly aligned, light could scatter through the capillary tube and could be detected on the optical diagnostics table (the procedure for the capillary fine alignment is given in a later paragraph).

Investigation of transmitted light-pulse properties

Light passing through the sapphire channel was picked off by an uncoated BK7 wedge under 45° approximately 80 mm behind the capillary exit. This wedge featured a 5 mm radius hole at the beam center in order to allow for an eventually accelerated electron beam to traverse undisturbed. Next, the attenuated photon flux was diverted onto a spot close to the edge of a 250 mm diameter, 1.2 m focal length on-axis parabola for collimation. In this way, the propagation axes of the incoming and the outbound beam crossed under an angle of $\sim 5^\circ$ such that these beams could be separated easily. Further downstream the laser pulses bounced off the pick-off wedge for a second time, thus became less intense (by a factor of 10 for each s-polarized reflection) and were subsequently steered out of the vacuum chamber, through a thin window onto an optics table. There, the light beam was focused by a 1 m focal distance plano-convex achromat, split into several parts and then distributed to different diagnostics. An 8-bit camera monitored the beam near-field and was activated primarily during the coarse capillary waveguide prealignment process (see next paragraph). In addition, the sapphire channel exit was imaged

by the mentioned relay optics and a microscope objective ($20\times$) onto the CCD of a 12-bit PCO Pixelfly QE camera in order to characterize the quality of the guided laser modes. Furthermore, a fiber-coupled Ocean Optics HR2000 spectrograph recorded the corresponding laser spectra. While doing so, it was most important to ensure that no self-phase modulation of the beam had occurred during propagation through the lens and window in order to allow for a measurement of an unaltered signal. Retroactively, this justifies the need of a strong beam attenuation induced by the double-reflection from the pick-off wedge prior to any passage through material. In another diagnostics branch, a large-area (13 mm^2) PIN-diode identical to the one characterizing the capillary input signal (confer preceding paragraph) accommodated the whole laser spot and therefore allowed for identification of the capillary throughput efficiency. This was rendered possible by cross-calibrating those two diodes after removing the waveguide ($\equiv 100\%$ transmission) and taking reference measurements for various input energies. With these diagnostics on-hand, an optimization of the capillary alignment and discharge timing was performed before actual guiding experiments could take place under optimum conditions.

Fine alignment and triggering of the capillary discharge waveguide

The capillary-waveguide housing was mounted on three translation stages allowing for movement in all directions, and additionally rested on a rotation stage and a goniometer, which enabled a rotation of the assembly around the channel entrance point. Translation, tip and tilt were optimized by maximizing the laser throughput intensity⁴ and symmetry observed on the 8-bit camera for coarse alignment purposes and on the 12-bit camera for finer control. For this operation to be successful, it was helpful in a preliminary step to iteratively optimize the throughput by adjusting the rotation stage and goniometer, and to symmetrize the imaged pattern at the capillary exit via translation perpendicular to the laser propagation direction. The capillary entrance location along the beam propagation z-axis was adjusted in advance by overlapping the goniometer rotation point with the laser focus as accurately as possible. One method to achieve this demanded fixing a $\sim 100\ \mu\text{m}$ diameter pinhole on top of the rotation axis close to the pivot point, back lighting it, and imaging it, e.g. with the DataRay beam analyzer setup. After dismounting the pinhole, the translation stages were moved into a position from where the analyzer camera exactly imaged the laser focus. Then the capillary in its predefined location relative to the alignment stages was close to the optimum position for coupling the light into the waveguide structure. However, based on the obtained results a further fine-tuning in z-direction might have been necessary in some cases to achieve an enhanced guiding and also electron-acceleration performance. If needed, this was done while executing the adjustments detailed in the following and on the fly while performing the actual experiments.

Up to this point, the spatial capillary alignment often turned out to be insufficient to allow for effective laser transport through the channel. To reach a higher level of accuracy, the ad-

⁴While performing alignment procedures, it turned out to be of uttermost importance to reduce the utilized laser intensity at the sapphire-channel walls to a level well below $1 \cdot 10^{13}\text{ Wcm}^{-2}$. Higher energy flux densities caused ablation, which led to cracks in the sapphire frame and to clogging of the central pipe.

justment procedure was pursued again, but this time in parallel with the discharge creating a plasma density gradient suitable for light guiding. As a prerequisite, the sapphire plates were continuously flooded with hydrogen at 100 mbar filling pressure and the discharge circuit was triggered to cause a voltage breakdown inside the channel every two seconds. Since the laser was firing at 10 Hz repetition rate, every other second an image of a beam affected by the generated plasma column was read out by the cameras. These signals were noticeably different from the unguided transmission mode of operation. Then, the timing delay between the laser and the discharge trigger needed to be scanned in ~ 10 ns steps until a pinching of the pulses was observable with a confined beam radius equivalent to the matched spot size of the waveguide. These contracted spots had to reside in the center of the transmission signal obtained without the discharge being fired, otherwise translation and rotation had to be fine-adjusted as explained before. Once that symmetry condition was fulfilled, the spatial settings allowed for efficient light transport. The optimum timing was found by fine-scanning the delay between laser and discharge trigger as will be shown in the subsequent section.

The trigger system used in the experiments to be discussed worked as follows. A manually initiated trigger opened the solenoid valve, which then caused the sapphire structure to be filled with hydrogen gas for a defined time of ~ 250 ms. Moreover, a delayed trigger was automatically sent to the laser system after ~ 150 ms during the filling procedure. This timing difference of 100 ms between the laser firing and the valve closing was necessary, since ATLAS is synchronized to a 10 Hz clock, which resulted in a 100 ms full width (FW) uncertainty of the laser-pulse arrival time at the interaction volume. Then, the discharge unit was activated by a trigger signal dispatched from the ATLAS laser system, which arrived with an uncertainty of $\ll 1$ ns approximately 360 μ s before the incoming laser beam. An additive time delay could be introduced, which allowed to vary the onset of the high-voltage breakdown relative to this trigger pulse. The same signal also armed the diagnostics and the fully automatized data acquisition system. The absolute timing between the laser pulse arriving at the capillary entrance and the initiation of the discharge had been established before with an additional photo diode (not shown in figure 3.2.1) capturing the laser signal at focus and comparing the recorded trace to the timing of the discharge current curve. That curve was registered with a Rogowski coil embracing one feed cable connected to a high-voltage electrode. By this means, it was possible to determine the absolute arrival time difference to an accuracy of less than 1 ns after considering the group velocity of electric signals through the utilized coaxial cables. This measurement also unveiled an inherent shot-to-shot jitter of 4 ns FW exhibited by the discharge circuit with the laser pulses used as timing reference.

III.III Guiding of relativistic laser pulses

On the basis of experimental results obtained from the setup introduced in the preceding sections, the physical effects that may manifest during guiding of relativistic laser pulses in a parabolic plasma channel will be discussed below in a qualitative picture.

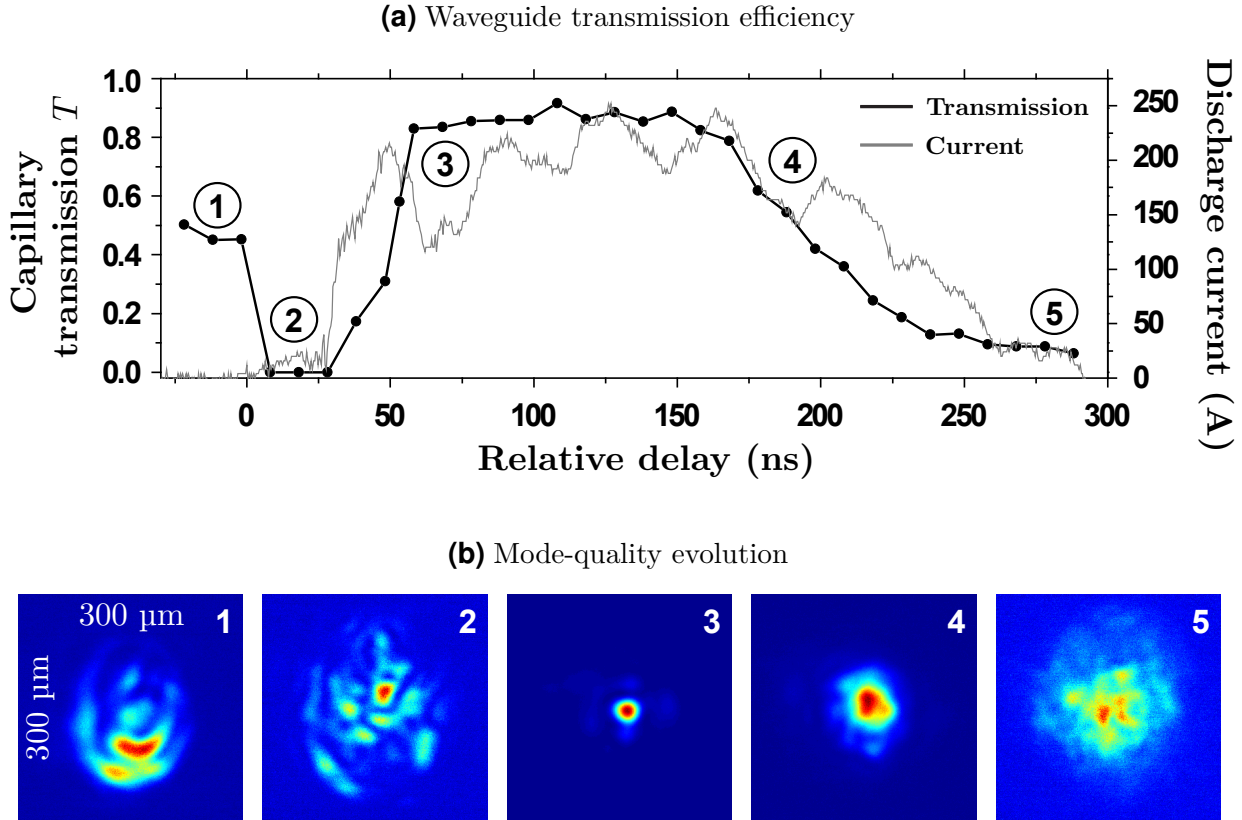


Figure 3.3.1 – (a) The waveguide transmission efficiency T and the discharge current as functions of the timing delay between the onset of the high-voltage breakdown and the arriving laser pulse. (b) Mode quality at the output of the channel in false-colors pertaining to regions 1 to 5. Each image is normalized to its maximum. The color-scale is equivalent to the one used in figure 3.3.3.

Figure 3.3.1a displays the transmitted energy fraction T deduced from the ratio of signal strengths of the input and throughput PIN-diodes as a function of the delay between the detected onset of the discharge current and the laser-arrival time at the capillary entrance with full-intensity laser shots ($a_0 \approx 0.9$). This curve possesses characteristic guiding features, from which five distinct regions may be identified, which are always present in the data regardless of the filling pressure (between 50 and 600 mbar). However, for differing pressure settings, the exact timescales covered by these regions and the obtained transmission values vary. The shape of this transmission chart is affected by a complex interplay of the evolution of the guiding channel, relativistic intensity propagation effects and energy transfer into an excited plasma wakefield. The data for the depicted guiding-efficiency curve was recorded at a pressure of 100 mbar, which corresponds to a mean electron plasma density of $n_e \approx 5 \cdot 10^{18} \text{ cm}^{-3}$ assuming complete ionization. Owing to that rather low density, very little energy is transferred from the laser pulse to the plasma and only a small wakefield is excited. This is suggested by the very efficient energy transport through the channel of more than 90% at peak (in region 3) and by the fact that no clear alteration of the laser spectrum could be observed, which would be expected due to photon acceleration and a longitudinally varying index of refraction in a wake

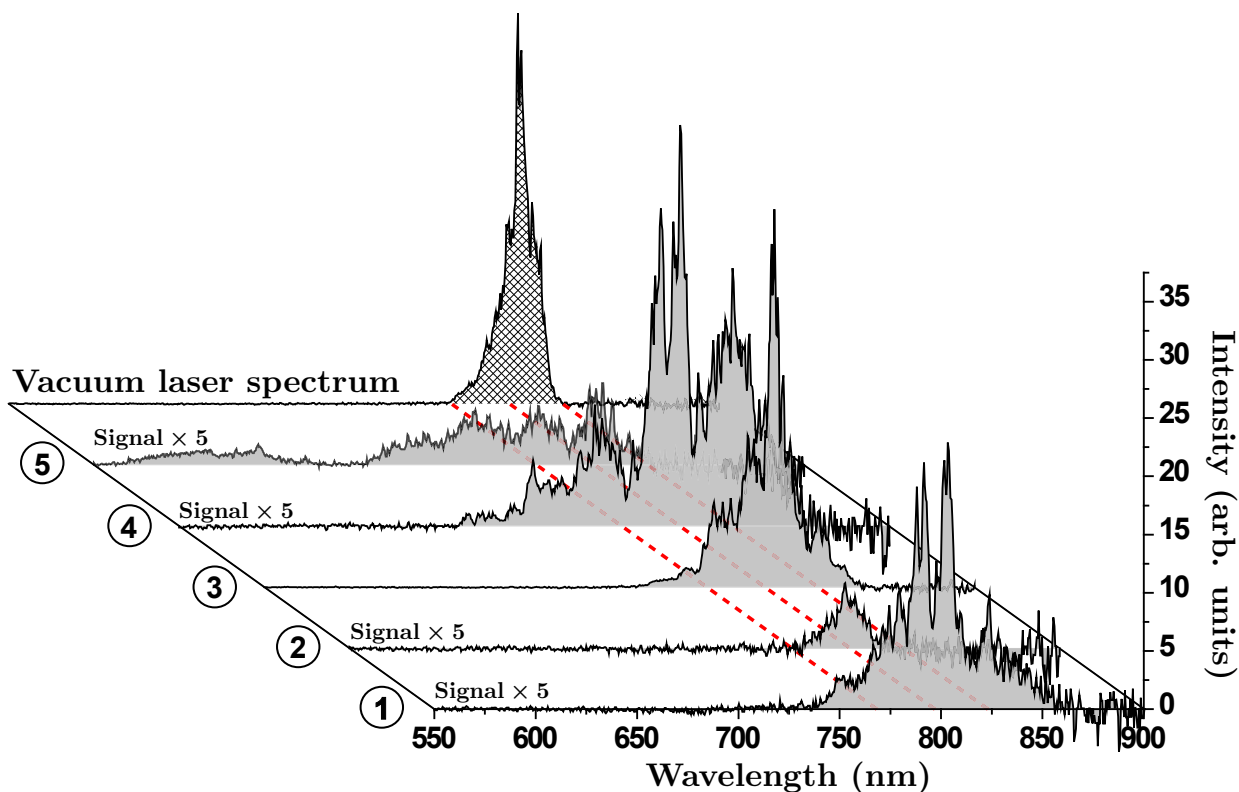


Figure 3.3.2 – Characteristic laser spectra under electron acceleration conditions for different laser-discharge time delays corresponding to the numbered regions defined in figure 3.3.1. The spectrum of the incident beam is shown for comparison, with the dashed red lines indicating its center and full width. Note that the curves for regions 1, 2, 4 and 5 are magnified by a factor of five.

structure. Hence figure 3.3.1a demonstrates a very clean guiding behavior with the corresponding guided laser profiles given in figure 3.3.1b. As a result of a small wakefield amplitude, no electron trapping and acceleration could be observed under these conditions.

Indeed, for settings which allow for laser electron acceleration in a wakefield, two curve attributes will change in a typical fashion. First T drops significantly due to the fact that laser energy is transferred to the wake and to a substantial number of relativistic electrons, and second the transmitted laser spectra will broaden in a characteristic way. Figure 3.3.2 presents light spectra belonging to laser beams transmitted through the waveguide in the different regions indicated in figure 3.3.1a, albeit obtained under an increased average plasma density of $n_e \approx 1 \cdot 10^{19} \text{ cm}^{-3}$ allowing for self-injected electron acceleration. The important features contained in plots 3.3.1 and 3.3.2 will be studied in the next paragraphs.

Moreover, an interpretation of the different guiding regions must include relativistic self-focusing effects as has been estimated in section I.IV.III. The critical power for self-focusing (1.4.34) with ATLAS is exceeded in uniform plasma densities above $1.9 \cdot 10^{18} \text{ cm}^{-3}$, which is always the case in the investigated parameter range. In addition, density channels of parabolic shape, which are present for certain discharge timings, have been identified to reduce this power threshold and enable self-focusing at even lower electron concentrations [BRANDI et al. 1993].

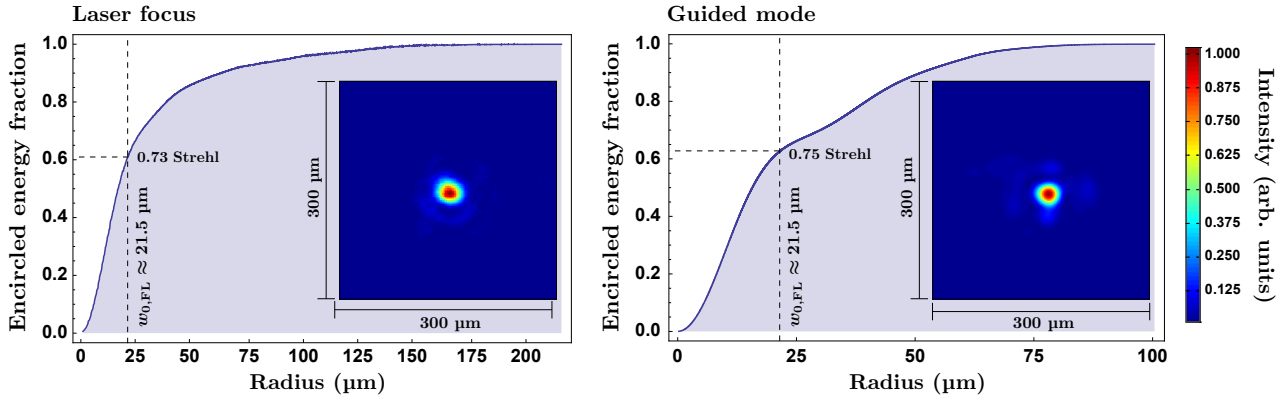


Figure 3.3.3 – Comparison of input mode and guided mode quality. The charts visualize the encircled energy fraction as a function of radius around the beam center. The energy ratio contained within the Fourier-limited radius of the input pulse is denoted by dashed lines in both diagrams. Comparing this value to the theoretical maximum yields the Strehl ratio, which is essentially conserved in this example.

Before the voltage breakdown is initialized, the laser pulse traverses a uniform gas volume, and dissociates and ionizes hydrogen molecules on its leading edge (region 1). Already at average plasma densities a little above $5 \cdot 10^{18} \text{ cm}^{-3}$ its intensity quickly becomes sufficient to drive a strong wakefield and enable electron trapping (confer chapter V). That is supported by the broadened throughput spectrum, which has been identified as an indicator of a laser driven wakefield interaction before [FAURE et al. 2005; ROWLANDS-REES et al. 2008]. In this regime, the light transmission does not exceed 50% since a transverse density gradient does not exist and hence guiding in preformed plasma structures cannot occur. Self-guiding is likely to confine the strong electro-magnetic waves over distances longer than their confocal range of $b \approx 3.6 \text{ mm}$ but not along the whole capillary length of 15 mm. Therefore the laser beam self-diffracts when still inside the channel. That can be inferred from the transmitted mode structure. In region 2, nanoseconds after the breakdown has been triggered, the capillary output signal becomes strongly distorted and the transmission drops to almost zero. Owing to considerable plasma-density non-uniformities originating from an inhomogeneous high-voltage sparking and thus an asymmetric energy deposition and plasma generation in the beginning, clean laser pulse propagation is not possible. This state lasts for $\sim 30 \text{ ns}$ and is referred to as *ionization phase* in the nonlocal thermal equilibrium model by BROKS et al. [2005]. That stage is followed by an expeditious rise in transmission efficiency T . During the *formation phase* (until $\sim 60 \text{ ns}$) plasma cooling on the walls becomes important and a guiding channel starts to form. Once the channel formation is complete, the *guiding phase* begins (region 3), during which the transmitted laser energy reaches a plateau of $T > 85\%$ over a period of $\sim 100 \text{ ns}$ (compare to the quasi-stationary plasma density cross-section in figure 3.1.3). The guided-mode profile is found to be of high-quality, similar to the input profile (confer figure 3.3.3) and relates to the matched spot size of the parabolic density gradient. Such a correlation explains the growth in transmitted spot diameter from region 3 to 4, which is linked to the evolution of the density gradient. An evolved plasma channel also entails a reduction of n_{axis} , the electron density on

laser propagation axis. The impact of this mechanism can be estimated with an empiric formula found by GONSALVES et al. [2007] yielding $n_{\text{axis}} \approx 2.3 \cdot 10^{18} \text{ cm}^{-3}$ at the transmission plateau. Despite of the fact that the parabolic-channel shape lowers the effective relativistic self-focusing threshold, this drop in on-axis density seems to prevail and in total reduces the influence of relativistic self-focusing effects, preventing the laser pulse from reaching intensities sufficient for wave-breaking. Indeed, no electron acceleration could be observed in region 3. Nevertheless, the spectral shape of the transmitted beam at $1 \cdot 10^{19} \text{ cm}^{-3}$ average density, corresponding to $n_{\text{axis}} \approx 4.6 \cdot 10^{18} \text{ cm}^{-3}$ shows some broadening, but not as striking as it appears at later times. This may be interpreted as a sign of only a weak wake excitation.

Subsequently, the temporal evolution of the guiding channel leads to a decrease in the transmitted laser energy for times later than 150 ns (region 4). Channeled electron acceleration has only been observed in this regime, and only for plasma densities above $n_{\text{axis}} = 3.2 \cdot 10^{18} \text{ cm}^{-3}$. This is accompanied by a significant spectral broadening and blue shift. Such a blue shift might originate from hydrogen recombination and reoccurring ionization in the leading edge of the light pulse [RAE and BURNETT 1992]. Since this spectral ionization-shift and electron acceleration occur coincidentally, ionization is suspected to play an important role for electron injection [ROWLANDS-REES et al. 2008]. Alternatively or additionally, the variation of the transverse density profile over time might allow for stronger spatial self-compression of the laser pulse and therefore may sanction wave-breaking and electron trapping. Also, a longitudinal density gradient could play a prominent role [BULANOV et al. 1998; SUK et al. 2001; HEMKER et al. 2002; GEDDES et al. 2008]. This question needs to be answered in a future study. At late times (region 5), when the discharge current decreases and ohmic heating decays, the aforementioned ionization processes extensively shift the transmitted light spectrum to shorter wavelengths and T declines strongly. Guiding cannot take place any longer.

In conclusion, the channeling of laser pulses with relativistic intensities ($a_0 \approx 0.9$) over distances eight times longer than their Rayleigh range has been demonstrated⁵. The confinement of these high energy flux density beams in a plasma will allow for the creation and support of a laser-driven wakefield over the full channel length, and thus should enable the acceleration of electrons to energies not accessible without such guiding structures. This will be investigated in the following chapter.

⁵Experiments utilizing a sapphire capillary of 33 mm length yielded similar transmission efficiencies of more than 90% and allowed for laser guiding over 17 times the Rayleigh range. However, no electron acceleration could be observed from these waveguides. Therefore, those results are not discussed in this thesis.

Chapter IV

Acceleration of electrons in a laser guiding plasma channel

The total energy of high-momentum quasi-monoenergetic electron beams generated by means of laser-wakefield processes has been shown to scale inversely proportional with the plasma electron density when the accelerating fields can be sustained over the full electron dephasing length (cf. sect. I.IV.V). Therefore, an efficient electron acceleration scheme requires the confinement of the wake driving light pulse over a similar distance. This distance is usually considerably longer than the laser beam confocal length, which in turn is given by the focusing geometry necessary to reach ultra-high intensities. A promising route to prevent such a relativistic electro-magnetic pulse from diffracting, is to apply external guiding structures, as introduced in chapter III. Here, the channeling of laser pulses with $a_0 \approx 0.9$ has been experimentally demonstrated over eight times their Rayleigh range with transmission efficiencies of $> 90\%$ by employing a slow capillary discharge waveguide. Such a device allows for the spatial extension of intense laser-plasma interaction in laser propagation direction and thus enables unprecedented electron energies from LWFA [LEEMANS et al. 2006; KARSCH et al. 2007]. The high-energy beams generated from the experimental setup introduced in chapter III will be presented and analyzed (sect. IV.II) following a discussion of the utilized electron diagnostics (sect. IV.I).

IV.I Electron diagnostics

A characterization of the accelerated electron bunches was conducted using two different techniques. The beam pointing and divergence was assessed with the help of a scintillating phosphor screen situated directly at the entrance of a permanent dipole magnet (S1 in figure 3.2.1). This screen could be retracted from the electron-beam path in order to allow for an undisturbed electron bunch propagation into the magnetic dipole field, which dispersed electrons of different energies and sent them onto a second charge-calibrated phosphorescence film (S2). In this way, the spectral charge distribution could be detected, as well as transverse beam pointing and divergence variations with energy that might have resulted from asymmetric wakefield excitations (confer chapter VI). Both of these diagnostics will be detailed next.

Beam pointing and divergence monitor (screen S1)

Scintillating screen S1 consists of a green-emitting converter film (type CAWO OG 16), which radiates at 545 nm when illuminated with X-rays or fast electrons. The number of released photons is expected to be proportional to the amount of deposited energy, which can safely be assumed to be almost constant for electrons with $\gamma \gtrsim 10$ and to grow linearly with the number of impinging equienergetic particles [GLINEC et al. 2006]. However, for such a detector saturation effects will emerge above a certain current-density threshold. Therefore, it would be of great interest and benefit in the future to check the assumptions stated above at a conventional particle source with tunable energy and current¹. The scintillator is composed of a rare earth phosphor powder ($\text{Gd}_2\text{O}_2\text{S:Tb}$) jacketed in a urethane binder. Hence, its resolution and sensitivity are determined by the size of the embedded phosphor pellets, with the lower spatial resolution limit being specified as $\sim 200 \mu\text{m}$ for this screen type. During the experiment, a 12-bit CCD camera (Point Grey Research Scorpion, 1600×1200 pixels) with objective lens read out the phosphorescence image through a 545 nm interference filter. This imaging system was capable of capturing $\sim 150 \mu\text{m}$ small structures, which were inherently spatially calibrated by a centimeter scale drawn on the phosphor-screen surface in both imaging dimensions. For practical reasons, it turned out to be important to screen the scintillator film from most of the light transmitted through the capillary discharge waveguide, owing to the large number of laser photons ($\sim 10^{19}$) compared to the band-pass filter extinction ratio of $< 10^{-4}$ and due to the fact that a non-negligible part of the laser spectrum shifted to 545 nm while interacting with the plasma. Therefore, a thin ($< 500 \mu\text{m}$) cardboard beam-stop was introduced into the laser-pulse path when then electron-beam pointing and divergence monitor was observed. This beam-stop was situated close to the phosphor screen to prevent significant scattering-induced smearing, which deteriorates the electron-pulse profile. In addition, stray light was carefully masked. The complete assembly consisting of S1 and the cardboard screen could be moved out of the electron-beam path in order to allow for an unobstructed propagation into the spectrometer and as a result enabled a clean spectral decomposition of the accelerated particle pulses.

Electron spectrometer and charge readout (screen S2)

For this purpose, the electron bunches were energetically dispersed in a magnetic dipole field of strength² $B_{\text{dm}} \approx 425 \text{ mT}$ and length $l_{\text{dm}} \approx 37 \text{ cm}$ (fig. 4.1.1). Consequently, electrons of differing energies hit a scintillating screen S2 (of same type as S1) at predetermined energy-

¹A recent calibration of the employed CAWO OG 16 film did not reveal any emission saturation at 40 MeV electron energy for incident charge fluxes of up to $65 \text{ pC}\cdot\text{mm}^{-2}$ impinging during a time window far shorter than the phosphorescence half-life ($\gtrsim 100 \mu\text{s}$). Owing to the fact that the following measurements do not cross this threshold, saturation is of no concern. These results emanate from experiments performed at the conventional electron source ELBE (Forschungszentrum Dresden-Rossendorf) after completion of the work at hand.

²A sophisticated recalibration of the electron spectrometer performed after completion of this thesis revealed a slightly higher average magnetic-field strength of 458 mT, which is an increase of +8% compared to the here given value of B_{dm} . Consequently, it implies that the electron energies stated throughout this work are systematically underestimated by approximately 8%. This is also supported by detection of the electron-energy dependent XUV-undulator-radiation spectrum as reported in FUCHS et al. [2009].

dependent distances $D(\gamma)$, such that an energy-resolved electron distribution could be measured by recording the scintillator emission, which was accomplished by utilizing a lead-shielded 12-bit CCD camera (PCO Pixelfly QE) equipped with an objective lens. Owing to geometrical restrictions, only energies exceeding ~ 100 MeV were captured. This assembly was shielded from laser photons by a 2 mm thin aluminum sheet fixed at the rear side of S2. Also, scattered laser and room light was screened by enclosing the complete observation setup. A millimeter scale attached alongside the phosphorescence screen provided an absolute spatial calibration. The well-defined³ position-energy dependence at the metal-film interface was reconstructed from the mapped field distribution of the permanent magnet utilizing three-dimensional single-particle-tracking simulations. This analysis is accompanied by an analytical description of that system, which has been developed in order to estimate the impact of electron beam divergence and pointing instabilities on the detected signal. It will be introduced in the following.

After traveling through the dipole magnet (see figure 4.1.1), the path deviation D of a single electron, which is detected on a screen tilted by an angle α around a pivot point at distance l_{inf} behind the spectrometer, can be written as (for a detailed derivation see appendix A):

$$D(\gamma) = \frac{1}{\cos \alpha} \left[l_z(\gamma) \frac{\partial H(\gamma)}{\partial l_{\text{sp}}} \Big|_{l_{\text{dm}}} + H(\gamma) \Big|_{l_{\text{dm}}} \right] \quad (4.1.1)$$

While the electron moves inside the magnetic field, l_{sp} denotes the distance from the particle position to the magnet-entrance plane, whereas l_z is the equivalent electron-to-exit-plane distance after having crossed the magnetic-field boundary at the spectrometer rear side:

$$l_z(\gamma) = \frac{l_{\text{inf}} - \tan(\alpha) H(\gamma) \Big|_{l_{\text{dm}}}}{1 + \tan(\alpha) \frac{\partial H(\gamma)}{\partial l_{\text{sp}}} \Big|_{l_{\text{dm}}}}$$

The electron path deviation H inside the magnet, measured normal to a reference trajectory of an infinitely energetic electron with negligible pointing variation δ , is given by:

$$H(\gamma) = \frac{\gamma m_e c}{e B_{\text{dm}}} \sqrt{1 - \gamma^{-2}} \left[\cos \left(\arcsin \left[\frac{e B_{\text{dm}}}{\gamma m_e c} \frac{l_{\text{sp}}}{\sqrt{1 - \gamma^{-2}}} - \sin \delta \right] - 2\delta \right) - \cos \delta \right] + l_{\text{fd}} \tan \delta$$

This equation contains the free-drift length l_{fd} defined as the distance from the source of a perfectly pointed ($\delta = 0$) reference electron to the spectrometer entrance. That parameter in combination with angle δ allows for the interpretation of pointing induced effects in the recorded electron spectra. Although the presented model assumes a homogeneous magnetic field filling the 1.5 cm wide gap between the spectrometer poles, it does generate a remarkably good match to the numerically tracked solution (confer figure 4.1.2).

Based on these results, it is now possible to quantitatively discuss the consequences of electron-beam divergence and pointing variations into the spectrometer aperture. Figure 4.1.3 shows the range of possible deviations $D(\gamma)$ for shot-to-shot pointing fluctuations of $\delta = \pm 8.3$ mrad (a)

³Strictly, this is only true, if electron-beam divergence and pointing errors are neglected.

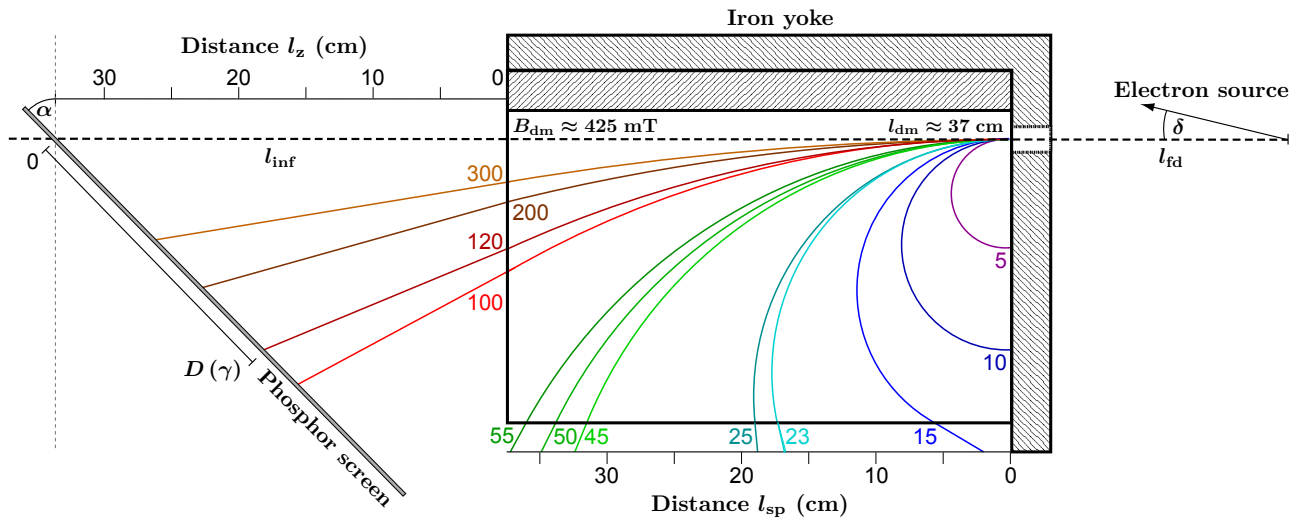


Figure 4.1.1 – Design of the permanent dipole magnet spectrometer and resulting electron paths. The colored numbers constitute the electron energy in MeV corresponding to an equivalently colored trajectory. All unspecified plotted variables are defined in section IV.I.

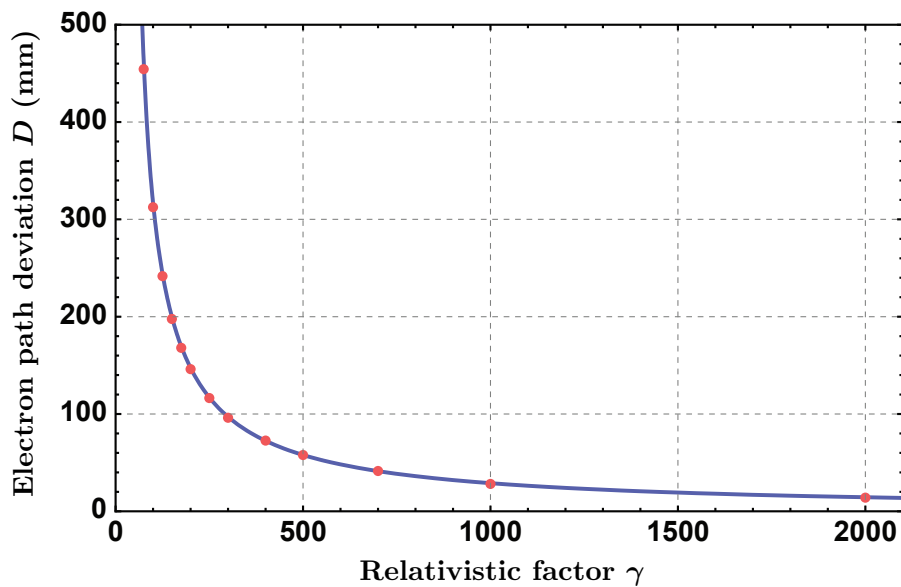


Figure 4.1.2 – The particle-tracking solution (red dots) of the measured spectrometer field agrees well with the results obtained from the derived model (4.1.1) with $B_{dm} = 0.40$ mT as a fit parameter (blue curve). Other quantities were taken as follows: $l_{inf} = 465$ mm, $\delta = 0$ and $\alpha = 0$.

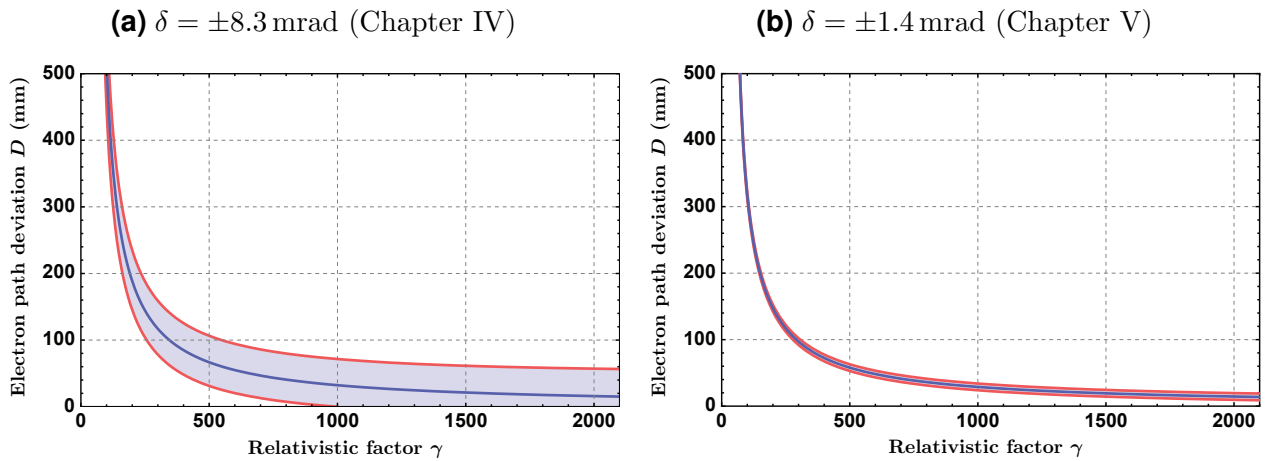


Figure 4.1.3 – The impact of pointing variations and divergence on measured electron spectra for the two spectrometer configurations as deployed in chapters IV and V with (a) $B_{\text{dm}} = 0.40$ mT, $l_{\text{fd}} = 1.1$ m, $l_{\text{inf}} = 397$ mm, $\alpha = 34.17^\circ$ and (b) $B_{\text{dm}} = 0.40$ mT, $l_{\text{fd}} = 1.1$ m, $l_{\text{inf}} = 465$ mm, $\alpha = 0^\circ$, respectively.

and $\delta = \pm 1.4$ mrad (b), which coincides with the measured RMS pointing fluctuations given in sections IV.II and V.III, respectively. From these plots, it is evident that beam divergence leads to a smearing of monoenergetic features and therefore results in artificial spectral broadening, while pointing fluctuations will cause a virtual spectral shift. Hence, it is principally desirable to have knowledge of divergence angle and pointing direction for each accelerated electron bunch in order to allow for a valid interpretation of its energy spectrum. However, in the current form of the experimental setup such data is impossible to obtain simultaneously. Low-angle scattering caused by phosphor monitor S1 and its cardboard light-shield inhibits the detection of a clean energy distribution and of position and divergence information at the same time, since the utilized screens are obstructing the electron beam path. Indeed, this issue is significant for unstable high-energy electron beams (confer figure 4.1.3a and section IV.II), whereas an electron beam of excellent stability enables meaningful statistics and thus consecutive collection of pointing and energy data. Thereby the implications of this problem are substantially reduced in the latter case (see figure 4.1.3b and chapter V). Nevertheless, methods do exist that would eliminate this issue completely, such as the detection of coherent or incoherent optical transition radiation [WARTSKI et al. 1973] from thin foils generated at the spectrometer entrance or localization by means of non-invasive beam position monitors [SHAFER 1990].

Besides shot-to-shot variations in electron beam properties, an additional source of error, which leads to uncertainties in the energy spectrum, represents the degree of accuracy to which the spectrometer transfer function and hence the magnetic field is known. The spatial field distribution also affects transverse focusing properties of the magnet, which must be taken into account for the analysis of divergence data measured on S2. These focusing forces have been investigated with the abovementioned particle-tracking simulations and are found to be of little importance in the described setup.

Furthermore, screen S2 was charge-calibrated by attaching a photostimulable phosphor detec-

tor, also called image plate, to its backside and irradiating the sandwiched package with a single broadband electron pulse. The signal emitted from S2 could then be compared to the calibrated metastable image-plate trace [TANAKA et al. 2005]. After six iterations, it was found that on average 95 electrons $\simeq 1.52 \cdot 10^{-17}$ C of charge resulted in a single count from the CCD chip. Using this calibration factor, the CCD images could be converted into absolute electron spectra. In a first step, background subtraction was performed and the images were integrated over a specified region of interest along lines of equal deviation $D(\gamma)$. Then, every data point was normalized to the width of its corresponding electron-energy interval. Finally, absolute energy coordinates were assigned, yielding electron spectra as can be seen, e.g. in fig. 4.2.2.

IV.II Generation of ultra-relativistic electron beams

ATLAS laser pulses (see chapter II) were focused into a capillary discharge waveguide to relativistic intensities as described in section III.II in order to accelerate electrons to ultra-relativistic momenta on a centimeter scale. The underlying physical process, namely laser wakefield acceleration, responsible for the generation of the required electric field strengths of more than 10 GVm^{-1} has been analyzed in detail in section I.IV. There, it was shown that wakefields in a plasma are driven efficiently only when the longitudinal dimension L of the driving laser pulse is close to a resonant length L_{res} that depends on plasma density n_e . ATLAS pulse durations of ~ 40 fs FWHM correspond to $L \approx 12 \mu\text{m}$, which would require $n_e \ll 10^{18} \text{ cm}^{-3}$. However, the used light pulses are not intense enough to cause electron injection at such low densities. Also, an intensity increase by means of stronger focusing cannot be easily achieved, since the focus size must stay matched to the waveguide mode. Therefore, the presented experiments were conducted at $n_e \gtrsim 3.2 \cdot 10^{18} \text{ cm}^{-3}$ on laser propagation axis, above which electron trapping and acceleration was observed. This fact does not contradict the laser-pulse-length-resonance requirement stated above. In the past, a number of studies have demonstrated LWFA in the blow-out or bubble regime [PUKHOV and MEYER-TER-VEHN 2002] with a larger LL_{res}^{-1} mismatch (e.g. HIDDING et al. [2006]). This is made possible by nonlinear effects arising from relativistic laser-plasma interaction, which are self-focusing (see section I.IV.III) and laser self-compression in a wakefield [FAURE et al. 2005]. These mechanisms have been confirmed by PIC simulations [BULANOV et al. 1995; TSUNG et al. 2004] and are expected to play an essential role in the presented investigation. Indeed, numerical simulations with the fully three-dimensional particle-in-cell code ILLUMINATION [GEISLER et al. 2006] suggest that self-focusing and self-compression are fundamental to bubble formation and particle trapping in the ATLAS parameter regime with the chosen electron densities. These simulations also identify transverse wave-breaking to be the dominant electron injection process [BULANOV et al. 1997].

Before discussing the properties of the accelerated beams, it has to be noted that the conducted LWFA experiments dictated to operate the ATLAS laser at its maximum specifications. A clear indication for this is shown in figure 4.2.1, in which the accelerated charge above 100 MeV energy is investigated as a function of the laser pulse duration. The pulse duration was altered by

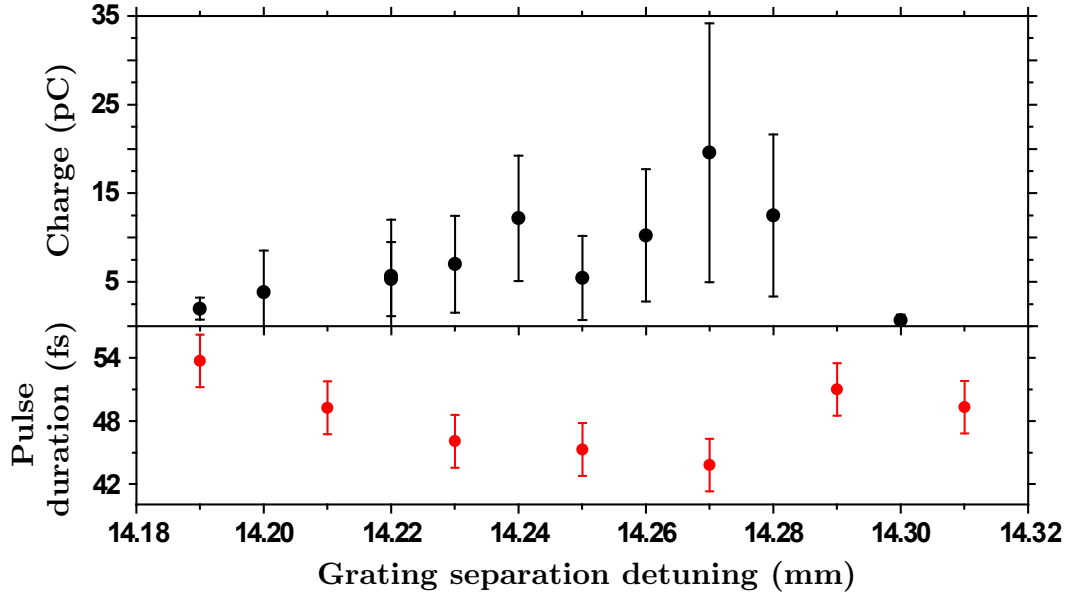


Figure 4.2.1 – The mean accelerated charge above 100 MeV energy and the laser pulse duration as a function of the grating separation detuning in the laser stretcher at an on-axis plasma density of $5 \cdot 10^{18} \text{ cm}^{-3}$.

detuning the grating separation in the ATLAS stretcher, resulting in a chirped and stretched laser pulse on target. An increase in FWHM pulse length, and hence a drop in intensity of 20 % diminishes the number of relativistic electrons by an order of magnitude. At even lower intensities, no electron acceleration could be detected at all with on-axis plasma densities of up to $1.4 \cdot 10^{19} \text{ cm}^{-3}$. This leads to the conclusion that these channeled experiments were performed at the threshold of accessing the LWFA acceleration regime, which might be part of the reason for the mediocre reproducibility found and detailed below.

The generated electron beams exhibit unique characteristics. Figure 4.2.2 presents five electron bunches with predominantly quasi-monoenergetic features ranging from 207 to 366 MeV with an energy spread of typically $\leq 20\%$. All shots were taken during the same data run at $n_{\text{axis}} \approx 5 \cdot 10^{18} \text{ cm}^{-3}$. False-color images of the phosphor screen S2 are depicted in the insets, which clearly show the tight spatial confinement transverse to the energy-dispersion direction. Sometimes, multiple peaks could be recorded (see figure 4.2.2e). Their appearance probability seems to be closely linked to plasma density, since an increase in n_e entails intensified temporal and transverse spatial break-up and filamentation of the driving laser beam, and therefore may lead to the creation of several loaded wakebuckets. Another peculiarity of this measurement is the large shot-to-shot variation in charge ranging from 6.3 to 31.5 pC for those five examples. These fluctuations are also salient on the energy scale, as may be seen in figures 4.2.3 and 4.2.4 with peak position variations of $\sim 30\%$ RMS. The first chart displays a series of CAWO screen images (S2) containing every produced electron bunch from the investigated data set (compare to figure 5.3.3). The latter illustration presents that data on equally scaled charge and energy axes allowing for an easier comparison. In this example, 36 out of a total of 52 laser pulses entering the plasma channel led to electron trapping and acceleration (69 %) with a mean accelerated charge of $20 \pm 15 \text{ pC}$. Data records obtained on other days feature trapping

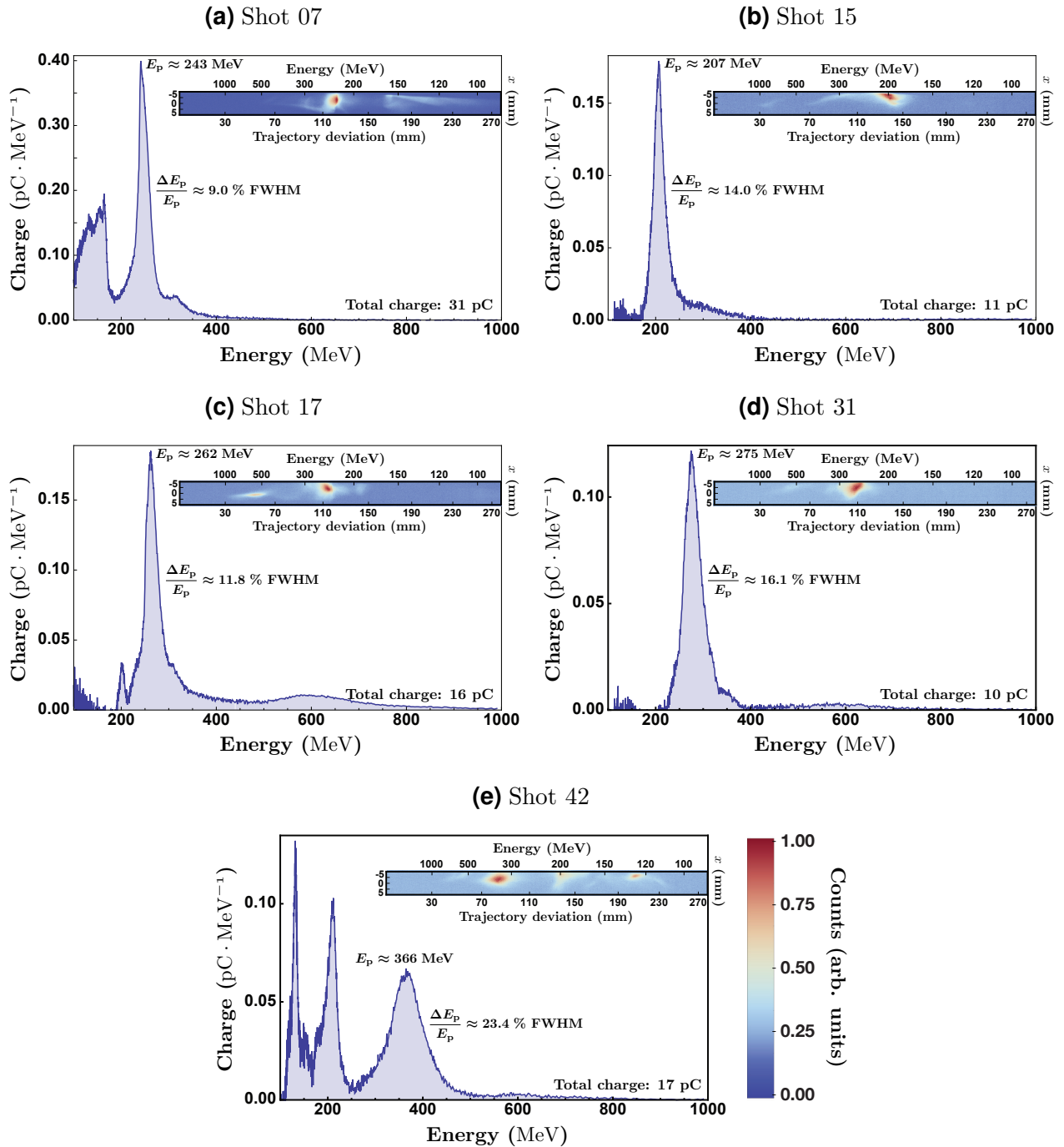


Figure 4.2.2 – Five quasi-monoenergetic electron beams accelerated at a density of $n_{\text{axis}} \approx 5 \cdot 10^{18} \text{ cm}^{-3}$ (a)-(e). The insets display false-color images of scintillating screen S2, from which the shown spectra were extracted.

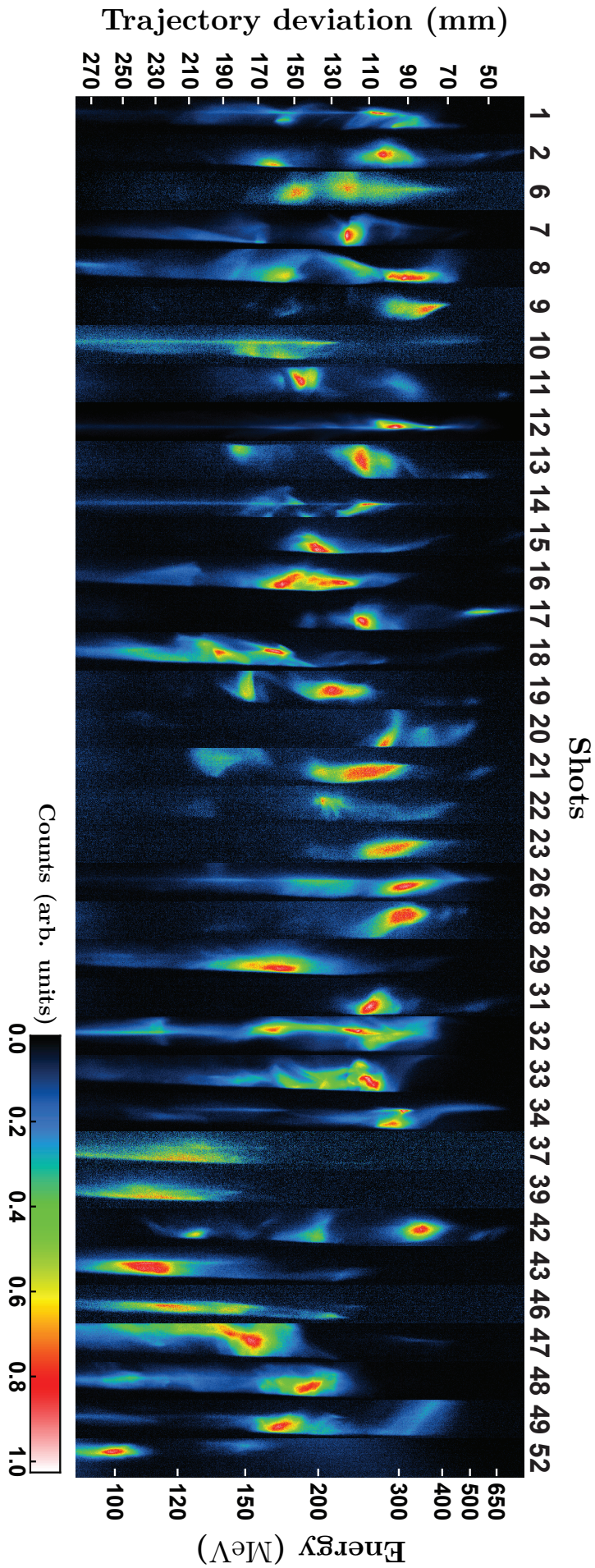


Figure 4.2.3 – False-color phosphor-screen images (S2) of the complete set of accelerated electron bunches from a run of 52 shots. The color scale matches the coloring used in figure 5.3.3 to allow for a comparison of the achieved parameter stability.

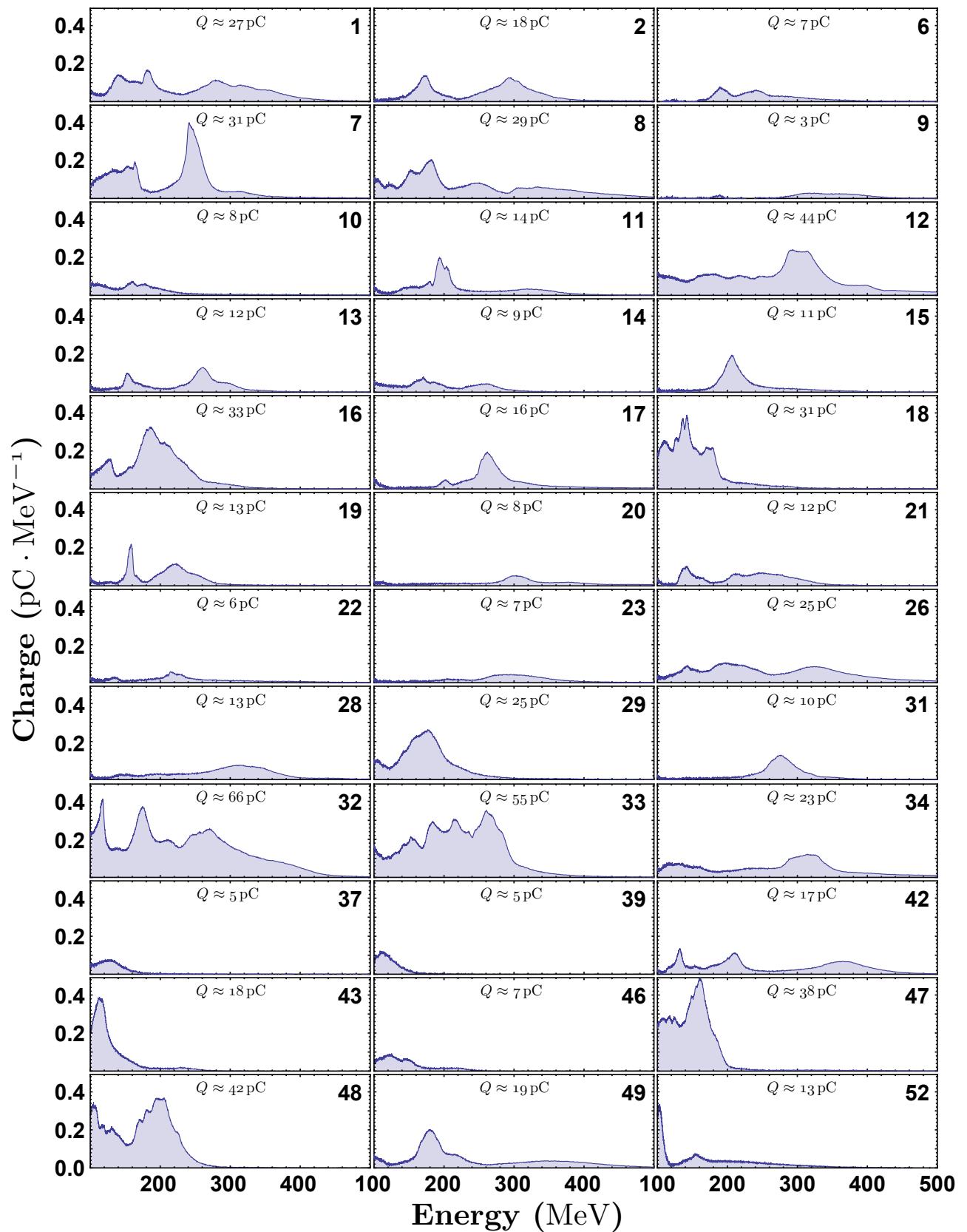


Figure 4.2.4 – Electron spectra originating from the data set shown in figure 4.2.3 on equally scaled charge and energy axes.

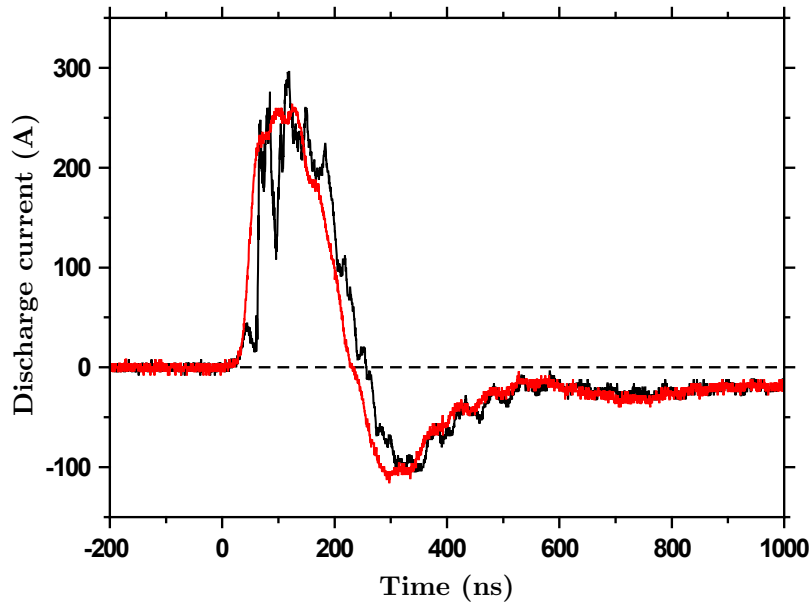


Figure 4.2.5 – Temporal evolution of the discharge current through the plasma column (black). Current spikes are smoothed by inducing preionization with a laser pulse arriving prior to breakdown ignition (red).

probabilities of up to 90 %, but suffer from similar reproducibility issues.

This instable behavior may appear due to two basic reasons: shot-to-shot variations in plasma parameters and fluctuations in laser-pulse characteristics. The nonlinear dependence of self-modulation effects on these attributes as well as a nonlinear wakefield excitation could presumably cause even small shot-to-shot irregularities in these parameters to have a considerable effect. However, from the reproducible experimental results of electron acceleration in a steady-state-flow gas cell (chapter V) it can be inferred that variations of the laser pulse intensity profile in the presented study will probably not have resulted in electron-beam fluctuations of such magnitude. Nevertheless, laser beam pointing variations might affect LWFA in plasma channels significantly more than it would alter wakefield acceleration in a gas cell, since the coupling of the electro-magnetic mode into the guiding density-gradient is sensitive to alignment on a few-micrometer scale length. The repeatability of the high-voltage breakdown for plasma generation and heating poses another relevant source of instability. The discharge control circuit exhibits an inherent time jitter of ~ 4 ns FW. This jitter covers almost the same scale as the time window in laser-to-discharge-onset delay, over which satisfactory electron acceleration can be observed (10 to 20 ns). Moreover, an unclean sparking from anode to cathode might lead to shot-to-shot changes in the plasma channel initialization and evolution, and hence could cause electron beam fluctuations. Figure 4.2.5 presents the discharge-current curve over time (black). Its development is characterized by strong and rapid fluctuations potentially linked to the mentioned sparking irregularities. These current spikes are smoothed out when a preionized plasma column is generated prior to the capacitor discharge (red curve). In the presented case, the wake-driving laser pulse was mistimed to arrive before the voltage breakdown fired. Therefore, the impact of this measure on acceleration stability could not be tested. Ideally, an additional synchronized laser beam would take over the preionization function, utilizing

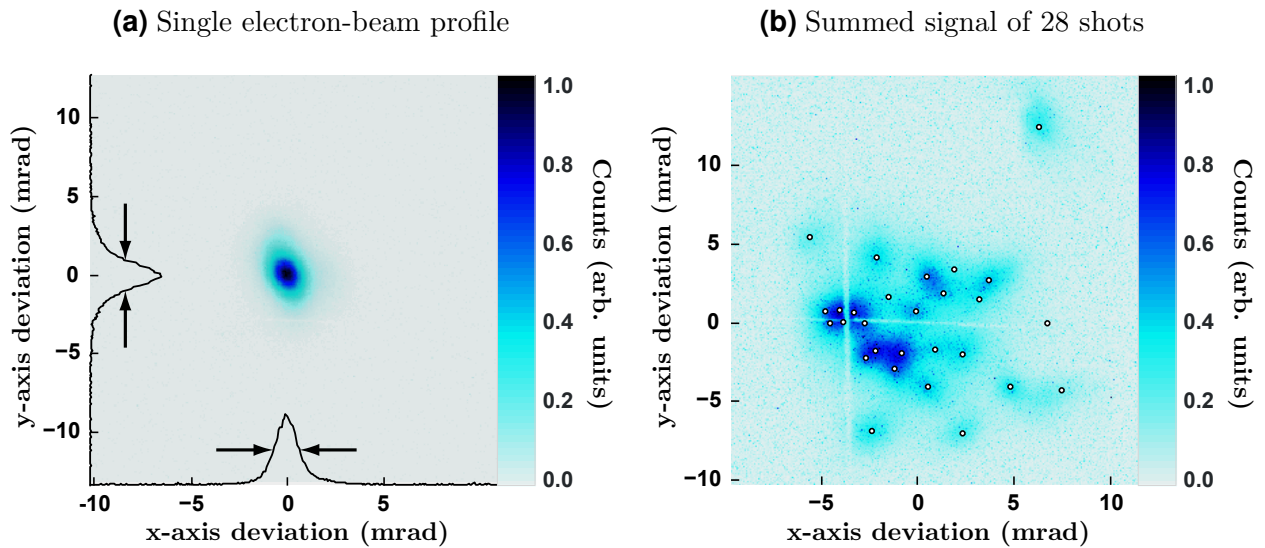


Figure 4.2.6 – (a) Characteristic trace of an electron bunch on phosphor screen S1 at $n_{\text{axis}} \approx 6.7 \cdot 10^{18} \text{ cm}^{-3}$. The lineouts through the peak indicate a divergence of 2.0 mrad. (b) The sum of 28 electron beam signals as shown in (a) as a measure for shot-to-shot pointing fluctuations. Small circles flag each electron-beam maximum. A cross in the background originates from pen markings on the screen.

short-wavelengths to take advantage of efficient multi-photon ionization of the gas medium (see section I.II.II). Whether this approach entails an electron beam stabilization has to be clarified in the future. Furthermore, LWFA in a plasma environment with reduced electron density could lead to more stable operation, which will be discussed in more detail in chapter V. It has to be remarked, that this would require an upgrade in ATLAS laser power or the application of alternative electron injection schemes (confer e.g. FAURE et al. [2006] or GEDDES et al. [2008]), since the current laser power would then be insufficient to drive wave-breaking in a comparable experimental geometry.

During the calibration of the magnetic spectrometer it was found that for multi-hundred MeV electrons, fluctuations in electron bunch pointing would substantially enlarge the error bars on the energy scale. The quality of beam pointing stability and divergence in this experiment has been examined by observation of the scintillation signal emitted off screen S1. An imprint of a single electron bunch at $n_{\text{axis}} \approx 6.7 \cdot 10^{18} \text{ cm}^{-3}$ can be seen in figure 4.2.6a. Its divergence is found to be 2.0 mrad FWHM in a beam shape appearing as a central peak surrounded by a low intensity halo. From the excellent confinement of high-energy features at screen S2 (confer figure 4.2.2), it may be reasoned that the intense central peak on S1 comprises exactly these ultra-relativistic electrons, whereas the halo most likely consists of low-energy particles, X-rays, transition radiation [GINZBURG 1996] and a few scattered fast electrons (confer appendix B). Averaged over the whole set of 28 shots, a mean divergence of 2.0 ± 1.0 mrad is detected. The sum of these 28 signals is displayed in figure 4.2.6b. An analysis of the peak position of each individual electron bunch reveals a shot-to-shot pointing variation of 8.3 mrad RMS, corresponding to the spectrometer calibration curve shown in figure 4.1.3a. Also, the pointing

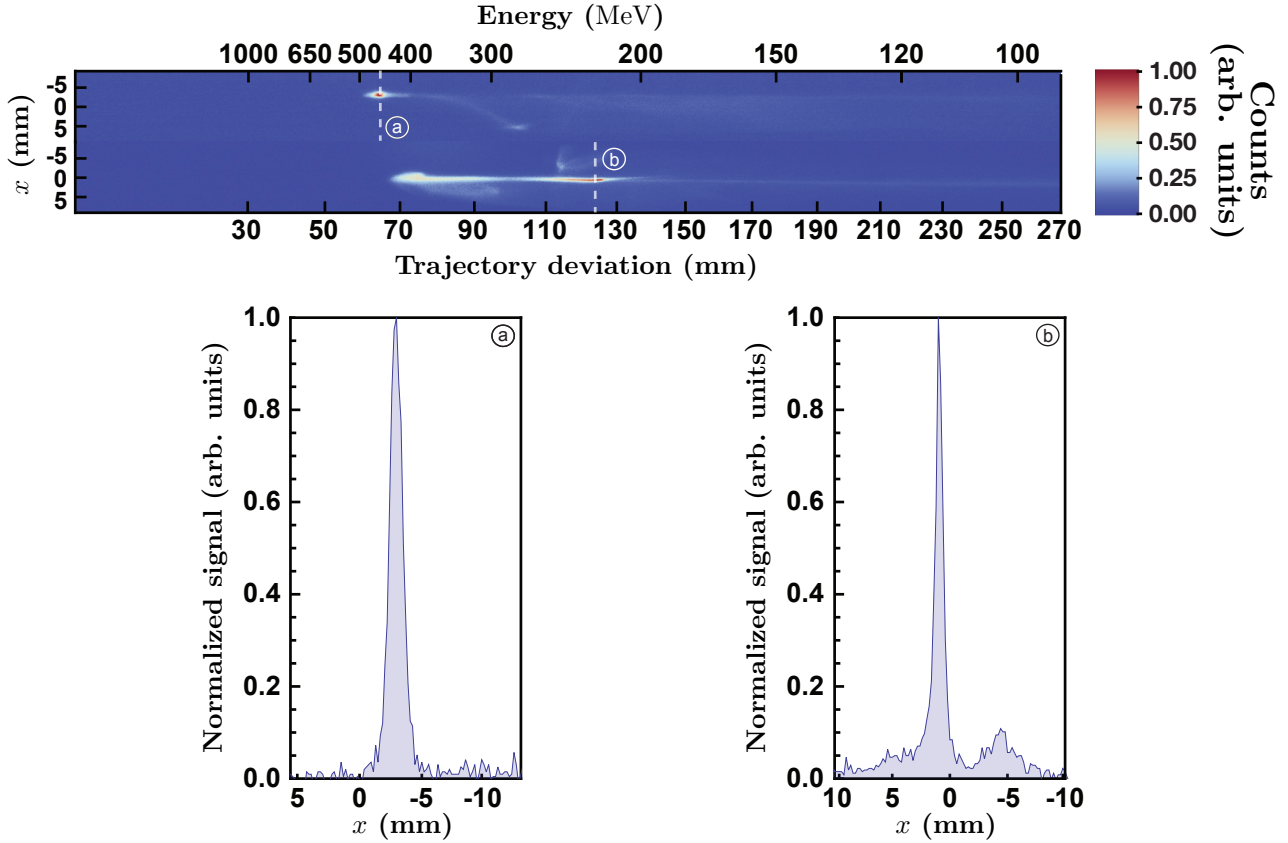


Figure 4.2.7 – False-color images of screen S2 show tightly confined electron beams in transverse direction. Profiles along lineouts (a) and (b) display FWHM divergences of only $\sim 500 \mu\text{rad}$ and $\sim 300 \mu\text{rad}$, respectively. Plasma densities were determined to be $n_{\text{axis}} \approx 8.4 \cdot 10^{18} \text{ cm}^{-3}$ (a) and $n_{\text{axis}} \approx 8.2 \cdot 10^{18} \text{ cm}^{-3}$ (b) during acquisition.

of each electron beam was directly compared with the pointing of the associated wake-driving laser shot, but no correlation could be found. This has been investigated by imaging the far-field of a weak transmission of the laser signal onto a 12-bit CCD camera after leaking through the last mirror substrate before the final focusing parabola.

Two examples of the most tightly confined electron beams encountered in an LWFA experiment to date are given in figure 4.2.7. They exhibit a FWHM divergence along the indicated lineouts at positions (a) and (b) of $\sim 500 \mu\text{rad}$ and $\sim 300 \mu\text{rad}$, respectively. Both of these shots contain just a few pC of charge, which suggests that negligible space-charge effects might have allowed for such collimation.

Finally, the recorded phosphorescence screen images of dispersed electron beams, accelerated to energies possibly exceeding 500 MeV can be seen in figure 4.2.8. Even features extending close to one gigaelectronvolt may be identified. However, during the calibration of the employed electron spectrometer it was found that electrons with as little as 300 MeV of energy can create a signal at path deviations D corresponding to 1 GeV when the here determined pointing fluctuations of 8.3 mrad RMS are considered. Hence the uncertainty in the measured spectra is high and consequently they must be taken with care. In addition, these extremely energetic features were recorded at an on-axis plasma density of $n_{\text{axis}} \approx 1.0 \cdot 10^{19} \text{ cm}^{-3}$, which

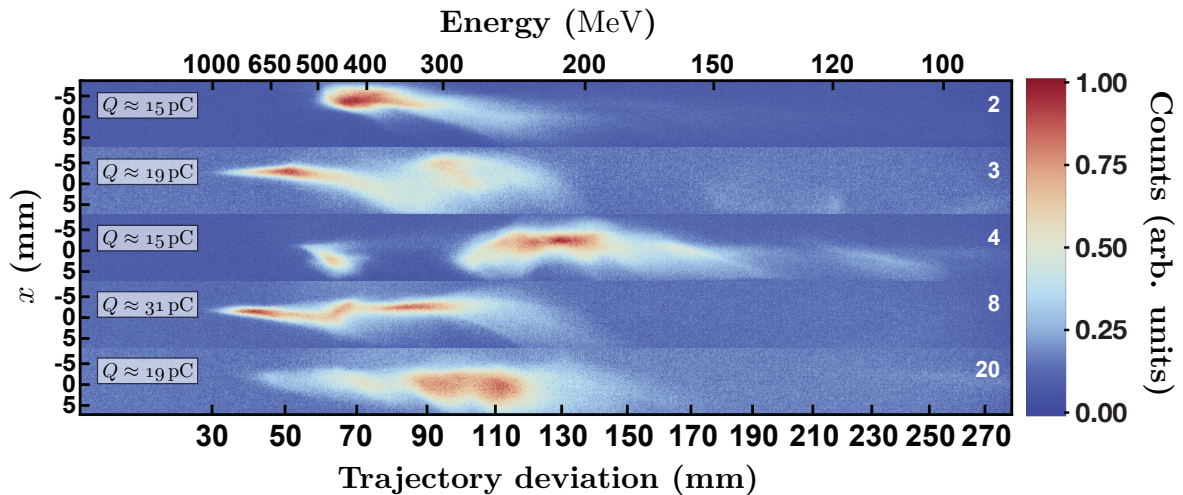


Figure 4.2.8 – Dispersed electron bunches exhibiting features at energies of seemingly more than 500 MeV at a plasma density of $n_e \approx 1.0 \cdot 10^{19} \text{ cm}^{-3}$ on screen S2. However, the significance of these results is questionable owing to an inappropriate spectrometer (confer section IV.I).

is a significantly higher electron density than was used for the acceleration of 200 to 400 MeV electron beams as depicted in figure 4.2.2 with $n_{\text{axis}} \approx 5.0 \cdot 10^{18} \text{ cm}^{-3}$. Theory would imply that given the laser-wakefield interaction extends over a range of at least 5.2 mm, which constitutes the dephasing length for the low-density regime and is reasonable considering the fact that a guiding channel is used, then the maximum achievable beam energy W_e should decrease with n_{axis} . This contradicts the presented experimental findings. Indeed, what has been diagnosed during experimentation are increased fluctuations in beam parameters, such as energy, charge and pointing stability with an increasing plasma density⁴. Thus the authenticity of the GeV-scale electron signals may be viewed as disputable.

IV.III Summary and conclusion

Laser wakefield acceleration of electrons has been demonstrated to allow for the generation of quasi-monoenergetic beams of several 100 MeV containing $\sim 10 \text{ pC}$ of charge by employing a capillary discharge waveguide to extend laser-plasma interaction distances. The achieved electron momenta exceed those that can be realized in a scenario without guiding for similar laser parameters (see next chapter). Additionally, electron beam divergences down to a few $100 \mu\text{rad}$ have been measured, which are the smallest reported on from a laser-electron-accelerator experiment to date [KARSCH et al. 2007]. However, the generated electron bunches suffer from considerable fluctuations in bunch energy, charge and pointing, which calls for a stabilization of these properties before those beams can be used for applications, such as the generation of XUV-undulator radiation [FUCHS et al. 2009] or, after significant improvements in the amount of accelerated charge and a reduction of the energy-spread, in the production of table-top free-electron-laser radiation [GRÜNER et al. 2007] (see also section VII.I).

⁴This is also true for the results obtained in a steady-state-flow gas-cell (confer chapter V).

Chapter V

Acceleration of stable electron beams from steady-state-flow gas cells

The fluctuations observed in all major attributes of laser-driven, quasi-monoenergetic electron beams from capillary discharge waveguides (see chap. IV) bring about severe complications for the further use of these electron bursts in actual applications. In this matter, it has been possible to identify the primary source of those shot-to-shot instabilities to originate from plasma irregularities created by variations in the electronic discharge breakdown itself. Therefore, the deployment of the afore utilized sapphire channels in a steady-state-flow gas-cell mode without the prior generation of a guiding plasma column allows for the creation of a highly reproducible gas-density profile and thus a particularly stable interaction environment, resulting in laser-accelerated low-divergence electron beams of unprecedented simultaneous shot-to-shot reproducibility in all key features [OSTERHOFF et al. 2008]. Laser-wakefield acceleration in gas cells of this type provides a simple and reliable source of relativistic electrons with well defined properties, which have been demonstrated to allow for applications such as the production of XUV-undulator radiation [FUCHS et al. 2009]. Moreover, this degree of stability enables experiments that require reproducibility and depend on meaningful statistics, e.g. the investigation of the influence of laser pulse-front tilt on LWFA [POPP et al. 2009] or electron source imaging with miniature quadrupole lenses for improved beam control [WEINGARTNER 2008].

V.I Context and motivation of the study

In section I.IV.I it was found that the ponderomotive force of a laser pulse traveling through underdense plasma can excite a plasma wave with longitudinal electric fields larger than $10 \text{ GV}\cdot\text{m}^{-1}$. These fields may be utilized to accelerate electrons to ultra-relativistic energies on a centimeter-scale. For this process to occur, the electrons need to acquire an initial momentum to be injected into the generated wakefield structure. As discussed in section I.IV.II, this can be facilitated by the laser pulse itself when its intensity reaches the injection threshold, which depends on the electron plasma density n_e . That mechanism is most efficient when the longitudinal laser size $L = c\tau_L$ with pulse duration τ_L is comparable to its transverse dimensions and

approximately equal to the resonant wakefield excitation length L_{res} . However, even a laser pulse that initially does not satisfy these conditions can potentially be matched to these constraints by self-compression [WILKS et al. 1989; FAURE et al. 2005] and relativistic self-focusing [BARNES et al. 1987; SUN et al. 1987], with the latter taking place above a critical laser power P_c (see equation 1.4.34). Owing to a non-linear dependence on the laser and plasma parameters, both of these pulse-shaping effects may cause significant fluctuations in the resulting electron-beam properties due to small shot-to-shot variations in laser and plasma conditions. Most LWFA experiments published to date have relied to some extent on such a non-linear laser-pulse evolution prior to the acceleration process and at the same time demonstrated only limited stability (exceptions are the studies by FAURE et al. [2006] and SCHMID et al. [2008]). Nevertheless, laser wakefield acceleration must not be regarded as an unstable process per se. Hence, for delivering high-quality and stable electron bunches that allow for applications, it is preferable to choose laser and plasma conditions that permit direct access to efficient wakefield excitation and electron injection without relying on the aforementioned non-linearities, or, if the latter is not feasible, to minimize fluctuations of the laser and plasma parameters and thus reduce the consequences of non-linear pulse-shaping mechanisms.

Lately, a number of studies have been dedicated to improve control over electron beam reproducibility. Stabilizing the bunch energy has been demonstrated in a complex two-beam setup [FAURE et al. 2006]. Other groups have analyzed the laser and plasma-parameter space in order to optimize acceleration conditions [HOSOKAI et al. 2003; LEEMANS et al. 2006; MANGLES et al. 2007; NAKAMURA et al. 2007]. In this chapter the generation of high-quality laser-accelerated electron beams of unprecedented simultaneous stability in energy, charge, divergence and pointing direction is reported. The presented experiment is based on the same simple setup as utilized in chapter IV with the crucial difference of using the gas-filled capillary target in a stable mode, which abstains from external preionization, and thereby minimizes shot-to-shot plasma fluctuations and consequently improves electron bunch shot-to-shot reproducibility. In contrast to previous work employing such a design [LEEMANS et al. 2006; KARSCH et al. 2007], the target gas is ionized by the wake-driving laser pulse and not by an electrical discharge circuit.

V.II Steady-state-flow gas-cell properties and experimental setup

The utilized gas-cell construction occurs in analog fashion to the capillary waveguide assembly described in section III.I. This kind of gas vessel is found to be long-lived in steady-state-flow mode, since erosion of the inner walls by the laser has no detectable influence on the generated electron beams¹. This is also supported by the fact that experiments with new and

¹ This statement is based on acceleration results obtained with a single gas cell that was in use over a period of nine months, which corresponds to several thousand laser shots. During this time the channel widened inhomogeneously to a diameter larger than 400 μm without affecting the properties of the accelerated electron beams in a significant way. No degradation in performance was observed until the inner capillary profile

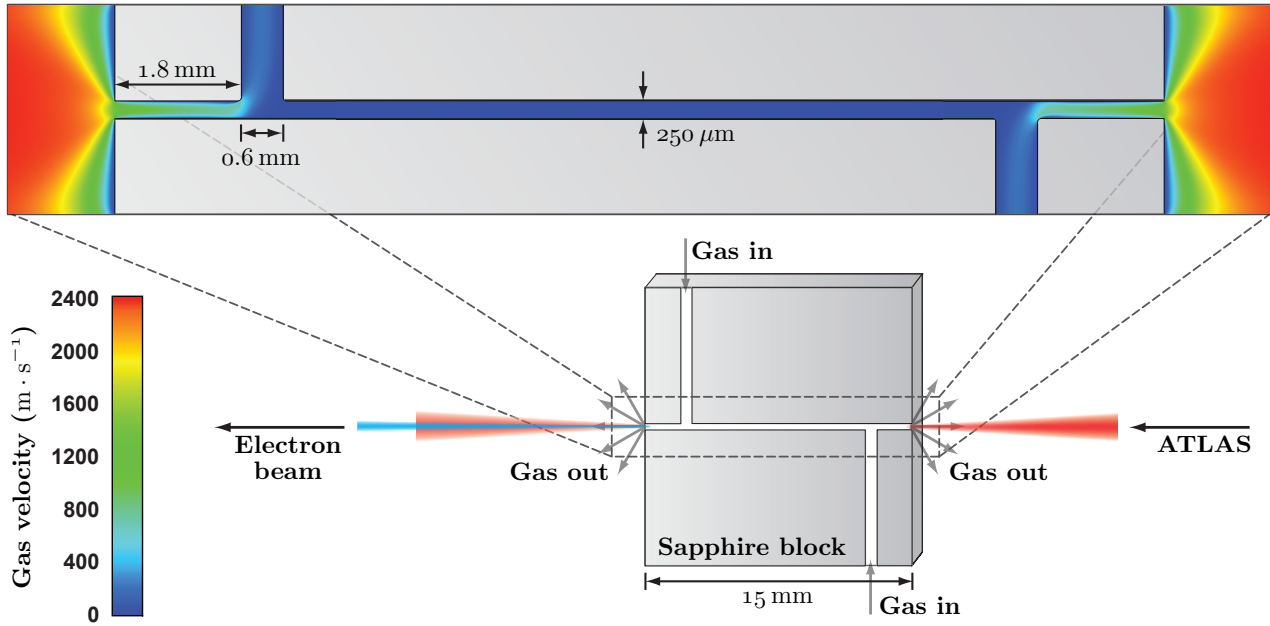


Figure 5.2.1 – Cross section of a steady-state-flow gas cell with two gas inlets. The magnified part shows color-coded gas-flow velocities in a steady-state regime from a FLUENT simulation at 130 mbar filling pressure.

homogeneously shaped cells of various diameters ranging from 200 to 300 μm yielded similar results, suggesting that unlike in the previous chapters and unlike in NAKAMURA et al. [2007] the waveguide properties of these structures do not play a prominent role here. Figure 5.2.1 shows the cell cross section.

During the experiment, the channel is filled with hydrogen passing through a valve and two gas slots at backing pressures of up to 490 mbar. Simulations were carried out [MARX 2008] to determine the resulting gas flow using the 2D coupled-implicit-solver version of the FLUENT code, which numerically solves the Navier-Stokes equations and in this particular case uses the κ - ϵ -model to account for turbulence [ZIEREP and BÜHLER 1991].

The gas cell investigated in this work reduces target density fluctuations threefold compared to conventional supersonic gas jets. First, negligible gas flow occurs within the central interaction volume. The magnified section in figure 5.2.1 displays the steady-state flow velocities along the whole channel for a typical backing pressure of 130 mbar. An almost perfectly homogeneous and stationary gas distribution develops between the inlets covering 80% of the channel length (see figure 5.2.2). In addition, the residual flow at the cell exits and supply slots is only marginally turbulent and the mass specific turbulent kinetic energy κ is low. Second, no supersonic shock fronts propagate through the medium, a phenomenon which may occur in high-Mach gas jets. Finally, the valve opening process has no influence on the actual density distribution inside the channel since the time it takes the valve to open (\sim a few ms) is two orders of magnitude smaller than the cell filling time in pulsed operation (\sim 200 ms) and is irrelevant in continuous-flow mode. A scan of the filling time revealed that a destabilization of the electron-acceleration

approached the diameter of the gas inlets (600 μm). At the end of the cell lifetime, chunks of sapphire broke off the walls and cluttered the central channel rendering it unusable.

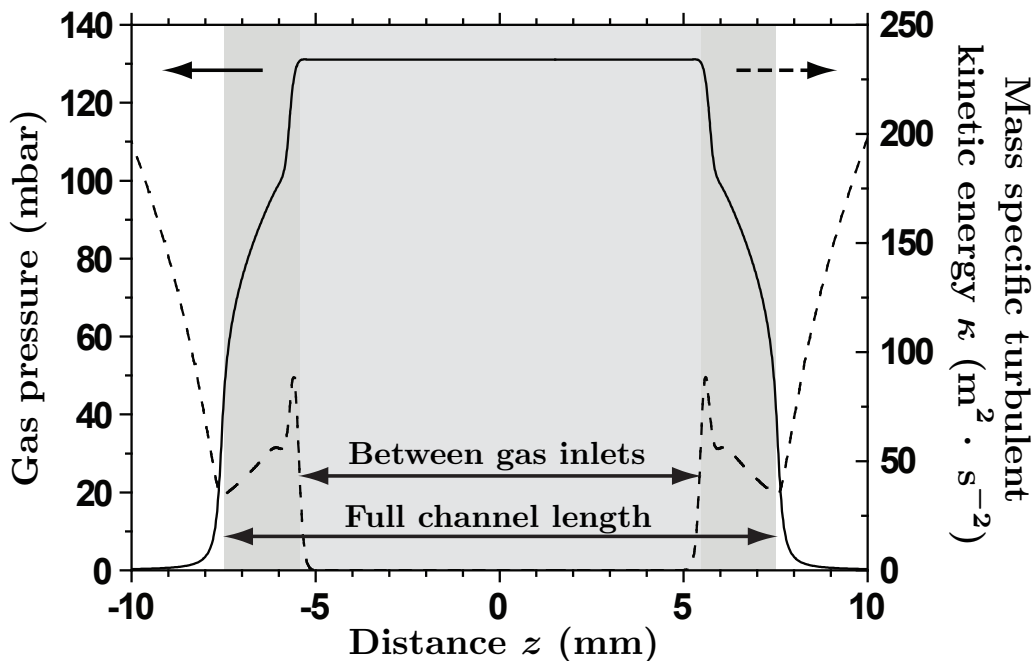


Figure 5.2.2 – Steady-state gas-pressure profile (solid line) and the mass specific turbulent kinetic energy κ (dashed line) along the central channel axis derived from the FLUENT simulation shown in figure 5.2.1.

conditions is only noticeable for valve opening times of less than ~ 50 ms. Therefore initial fluctuations equilibrate before the arrival of the laser pulse and a steady-state, laminar gas flow arises resulting in a reproducible, homogeneous gas distribution.

The driver laser in this experiment was the ATLAS Ti:sapphire-system (see chapter II). It delivered 20 TW, 850 mJ, 42 fs FWHM pulses on target at a central wavelength of $\lambda \approx 800$ nm. The configurations, devices and techniques used to determine the specifications of the incoming laser pulses, to characterize the light transmitted through the gas cell and to evaluate the attributes of the accelerated electron bunches have already been described in detail in sections III.II and IV.I. A scheme of the full setup is depicted in figure 3.2.1. Again, an $f/22$ focusing geometry was employed. This allowed to radially confine the laser pulse at focus into a spot with a diameter of 23 μm FWHM and a Strehl ratio of larger 0.7 resulting in an average vacuum FWHM focal intensity of $1.7 \cdot 10^{18} \text{ W} \cdot \text{cm}^{-2}$ and a normalized laser vector potential of $a_0 \approx 0.9$. The electron beams generated from this setup have been investigated in terms of charge, energy, pointing direction and divergence. The remarkable shot-to-shot stability of these parameters allowed for systematic studies with good statistics, which will be presented in the following.

V.III Experimental results and interpretation

Figure 5.3.1 displays the negative charge Q of accelerated particles with energies ≥ 100 MeV measured at screen S2 as a function of n_e . The electron density is deduced from the hydrogen fill pressure assuming complete ionization within the laser focus. Electrons are injected into the wake at densities above $\sim 4 \cdot 10^{18} \text{ cm}^{-3}$ facilitated by laser self-modulation effects (see remarks

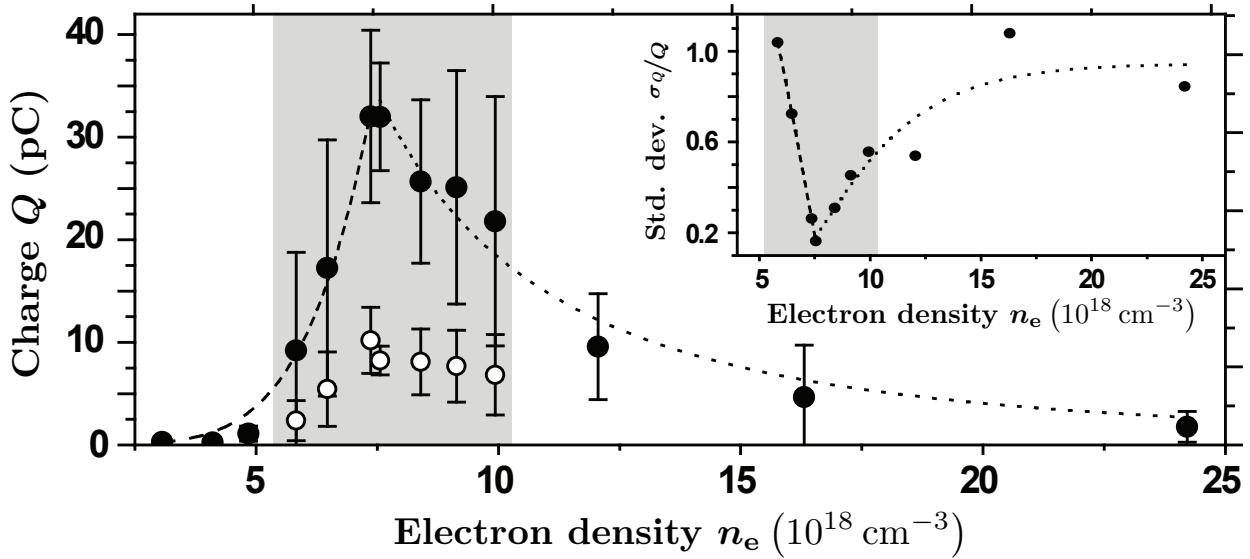


Figure 5.3.1 – The negative charge Q of electron bunches accelerated to energies > 100 MeV as a function of the plasma density n_e . Each data point is averaged over up to 50 shots. The inset displays the relative shot-to-shot standard deviation σ_Q of charge Q vs. n_e . In the shaded areas the electron beams are predominantly quasi-monoenergetic. Hollow circles represent the average FWHM charge contained within Gaussian peaks of $\Delta E_p \cdot E_p^{-1} = 10\%$ FWHM.

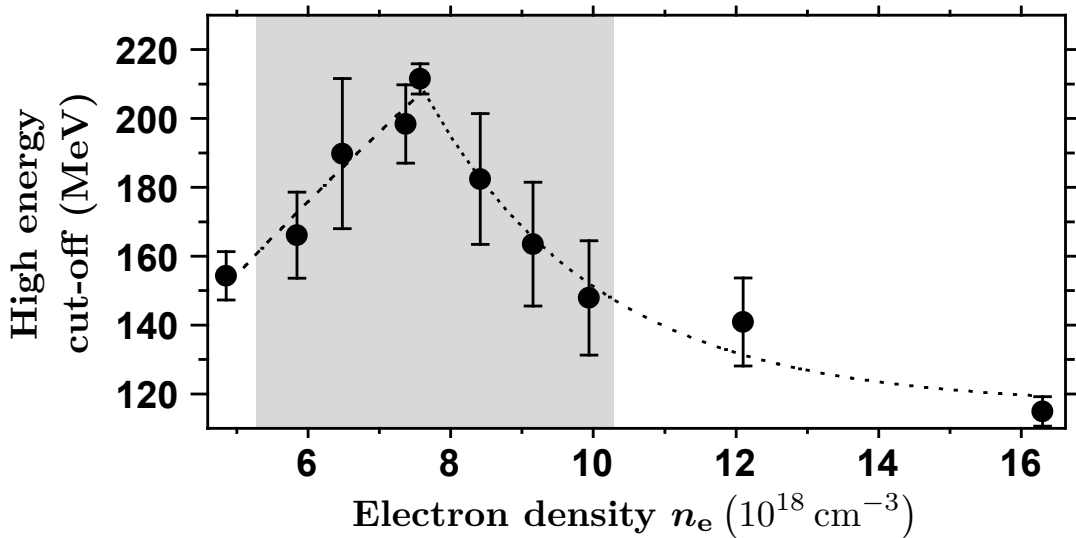


Figure 5.3.2 – The sharp high energy cut-off threshold as a function of the plasma density n_e . In the shaded area the electron spectrum contains predominantly quasi-monoenergetic features.

on PIC-simulations at the end of this section). At $n'_e \approx 7.3 \cdot 10^{18} \text{ cm}^{-3}$ a maximum amount of charge $Q' \approx 32 \text{ pC}$ is detected with shot-to-shot fluctuations as low as 16 % RMS. Figure 5.3.2 shows the corresponding high cut-off energies vs. n_e from the same data set. It may be recognized that in analogy to figure 5.3.1 this measurement features its energy maximum and its highest reproducibility also exactly at n'_e .

The data on either side of this maximum can be interpreted as follows: For densities $n_e < n'_e$ an increase towards n'_e in charge, energy and stability is observed. In this regime the distance d over which injected electrons are accelerated in the wakefield is governed by the focusing geometry of the laser modified by relativistic self-focusing and energy depletion effects, and not by the electron dephasing length $L_d > d$. The laser energy depletion length $L_{ed} \propto n_e^{-1}$ (according to LU et al. [2007]) decreases with density as fast as the critical self-focusing threshold $P_c \propto n_e^{-1}$. Therefore the distance over which the self-focusing effect can be maintained does not depend on density. At $n_e < n'_e$ this results in an almost constant acceleration distance d . Since the longitudinal electric field of the wake E_x is proportional to $\sqrt{n_e}$, the electron energy $W_e \propto E_x d$ increases accordingly, as does the number of electrons above 100 MeV owing to a more efficient wave-breaking with higher density, boosting the amount of accelerated charge. This was confirmed by fitting functions of the form $f(n_e) = \mathbf{a} \cdot n_e^{\mathbf{b}_\mathbf{r}}$ to the rising slopes of the data presented in figures 5.3.1 and 5.3.2 with the index $\mathbf{r} \in \{Q, E\}$ denoting the matched values for the respective scan. $\mathbf{b}_E \approx 0.64 \pm 0.12$ can be assigned to the electron-density vs. cut-off-energy plot, which supports the interpretation above and is close to the theoretical expectation of $\mathbf{b}_{E,\text{th}} = 1/2$. Furthermore, a least-square fit to the rising slope of the charge-against-density distribution yields $\mathbf{b}_Q \approx 5.56 \pm 0.46$ and thus shows a rapid increase of ultra-relativistic electrons with plasma density. This identifies the dominant effect responsible for the sudden change in charge as an enhanced injection probability with increasing n_e . A simple model² rules out this increase to originate from accelerating an increasing number of particles, which were less energetic at lower n_e , to detectable energies of $> 100 \text{ MeV}$.

With n_e approaching n'_e the dephasing length converges to d with $L_d \approx 4 \text{ mm}$, representing the longest distance over which electrons are accelerated and setting a lower limit on the length over which the laser pulse is self-guided and confined to high intensities. This constitutes the transition to a dephasing-limited regime for densities $n_e > n'_e$, in which the dephasing length L_d becomes smaller than the distance over that the wakefield can be driven and hence $W_e \propto E_x L_d \propto n_e^{-1}$. Thus the high energy cut-off (see figure 5.3.2) and the charge above

²In a simple picture, the spectral shape of the accelerated electron bunches may be regarded as a box of constant height with the number of electrons per energy interval given by N' (confer figure 5.3.3b). This box can be observed in energy space between a lower hard limit of $W_{e,l} \approx 100 \text{ MeV}$ and an upper boundary given by the high-energy cut-off $W_{e,u}$ depending on n_e . Hence, the total contained charge can be expressed as:

$$Q_{\text{box}} = (W_{e,u} - W_{e,l}) \cdot N'$$

According to TZOUFRAS et al. [2007] the number of electrons \tilde{N} , which can possibly be trapped into a wakefield trough before injection discontinues, scales as $\tilde{N} \propto n_e^{-1/2}$, which consequently leads to $N' \propto n_e^{-1/2}$. The scaling of $W_{e,u}$ depends on the regime under investigation. For $n_e < n'_e$, $W_{e,u} \propto n_e^{1/2}$ is true and thus Q_{box} should be about constant. For $n_e > n'_e$ this changes to $W_{e,u} \propto n_e^{-1}$ resulting in $Q_{\text{box}} \propto n_e^{-3/2}$.

100 MeV (see figure 5.3.1) both decrease with higher density.

Indeed, these statements are supported by the results obtained from functions $g(n_e) = \mathbf{c} \cdot n_e^{\mathfrak{d}_E}$ adapted to fit the down-slope of the investigated parameter scans. They show that the decreasing cut-off energy with electron density is reproduced almost exactly according to linear theory ($\mathfrak{d}_{E,\text{th}} = -1$) with $\mathfrak{d}_E \approx -0.95 \pm 0.18$. Also $\mathfrak{d}_Q \approx -2.17 \pm 0.31$ scales in a comparable fashion to the behavior predicted for the charge². This indicates that alongside dephasing, a reduction of the beam-loading threshold with increasing plasma density diminishes Q . The decreased stability for $n_e > n'_e$ can be ascribed to a growing deviation from the LWFA resonance condition with $L > L_{\text{res}}$ mentioned before, leading to filamentation and temporal laser break-up.

The onset of the filamentation processes can be observed in some of the energy-resolved electron beams obtained at n'_e (confer figure 5.3.3a). False-color images of screen S2 show the dispersed bunches accelerated by 40 consecutive laser shots. It may be seen that every shot led to electron acceleration. The electron spectra in this regime exhibit a plateau background of 22 ± 5 pC with a quasi-monoenergetic peak containing 10 ± 4 pC of charge at 198 ± 12 MeV appearing in 80 % of the cases (figure 5.3.3b). These features are stable in energy with a standard deviation of 6 % for the electron peak and 3 % for the high-energy cut-off at 217 ± 6 MeV. The energy spread of the peak $\Delta E_p \cdot E_p^{-1}$ amounts to 8.2 % FWHM with $\Delta E_p \approx 16.3$ MeV.

At a decreased density of $n_e \approx 6.8 \cdot 10^{18} \text{ cm}^{-3}$ the plateau vanishes and only the quasi-monoenergetic part remains (figure 5.3.3c). This comes at the expense of a reduced peak charge (7 ± 3 pC), reduced electron energy (122 ± 3 MeV) and a reduced injection probability (71 %), which indicates that the laser pulses are only just above the injection threshold. Nevertheless, the average FWHM energy spread $\Delta E_p \approx 16.2$ MeV remains almost unchanged. This implies that the energy spread might originate from the trapping and early acceleration processes. Remarkably, the peak energy stability improves to 2.5 % RMS, which is the best shot-to-shot reproducibility in an LWFA experiment achieved and published to date. The remaining variations in the acceleration process can be attributed to residual gas fluctuations, shot-to-shot jitter in laser energy (2.0 % RMS)³ and pulse duration, but also to electron pointing deviations into the dipole magnet introducing an uncertainty, which will be investigated in the following.

The accumulated signal of 74 electron bunches and the locations of their maxima on S1 are presented in figure 5.3.4a. Here, the beam pointing within the spectrometer deflection plane varies by 1.4 mrad RMS. For a fixed electron energy this fluctuation translates into apparent energy fluctuations on screen S2 with standard deviations of 1.7 % at 122 MeV ($n_e \approx 6.8 \cdot 10^{18} \text{ cm}^{-3}$) and 3.1 % at 198 MeV ($n'_e \approx 7.3 \cdot 10^{18} \text{ cm}^{-3}$). This can be estimated with the help of (4.1.1). Therefore, the real energy stability might have been significantly more favorable than stated above. However, owing to low-angle scattering introduced by screen S1, the pointing and energy spectrum of an electron beam could not be measured simultaneously. Analyzing every shot from figure 5.3.4a individually yields a distribution of the electron bunch divergences. Figure 5.3.4b shows such a single electron beam imprint (divergence of 1.6 mrad FWHM). The average value

³Although the electron-energy fluctuations should be related to the laser-energy jitter, a measurable shot-to-shot correlation between the two could not be found. This is supported by the corresponding sample correlation coefficient [BRONŠTEIN et al. 1999] determined to be $r \approx 0.11$ for the data set at $n_e \approx 7.3 \cdot 10^{18} \text{ cm}^{-3}$.

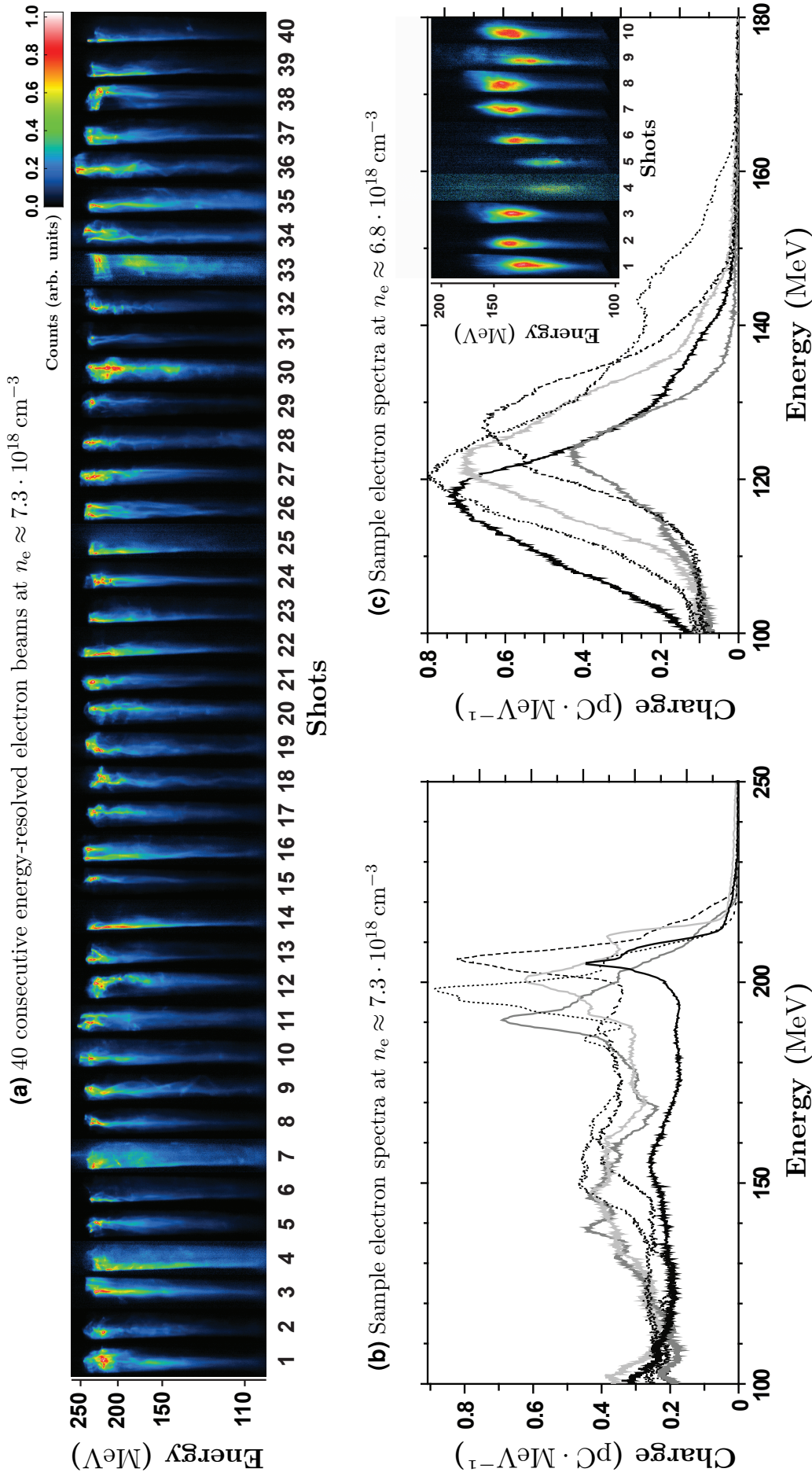


Figure 5.3.3 – (a) False-color images of 40 consecutive, spatially-dispersed electron beams on screen S2 ($n_e \approx 7.3 \cdot 10^{18} \text{ cm}^{-3}$). The color scale is normalized for each shot. Five sample electron spectra from the same data set are given in (b). (c) Five exemplary spectra for an electron density of $n_e \approx 6.8 \cdot 10^{18} \text{ cm}^{-3}$. Ten consecutive images of S2 under these conditions are presented in the inset.

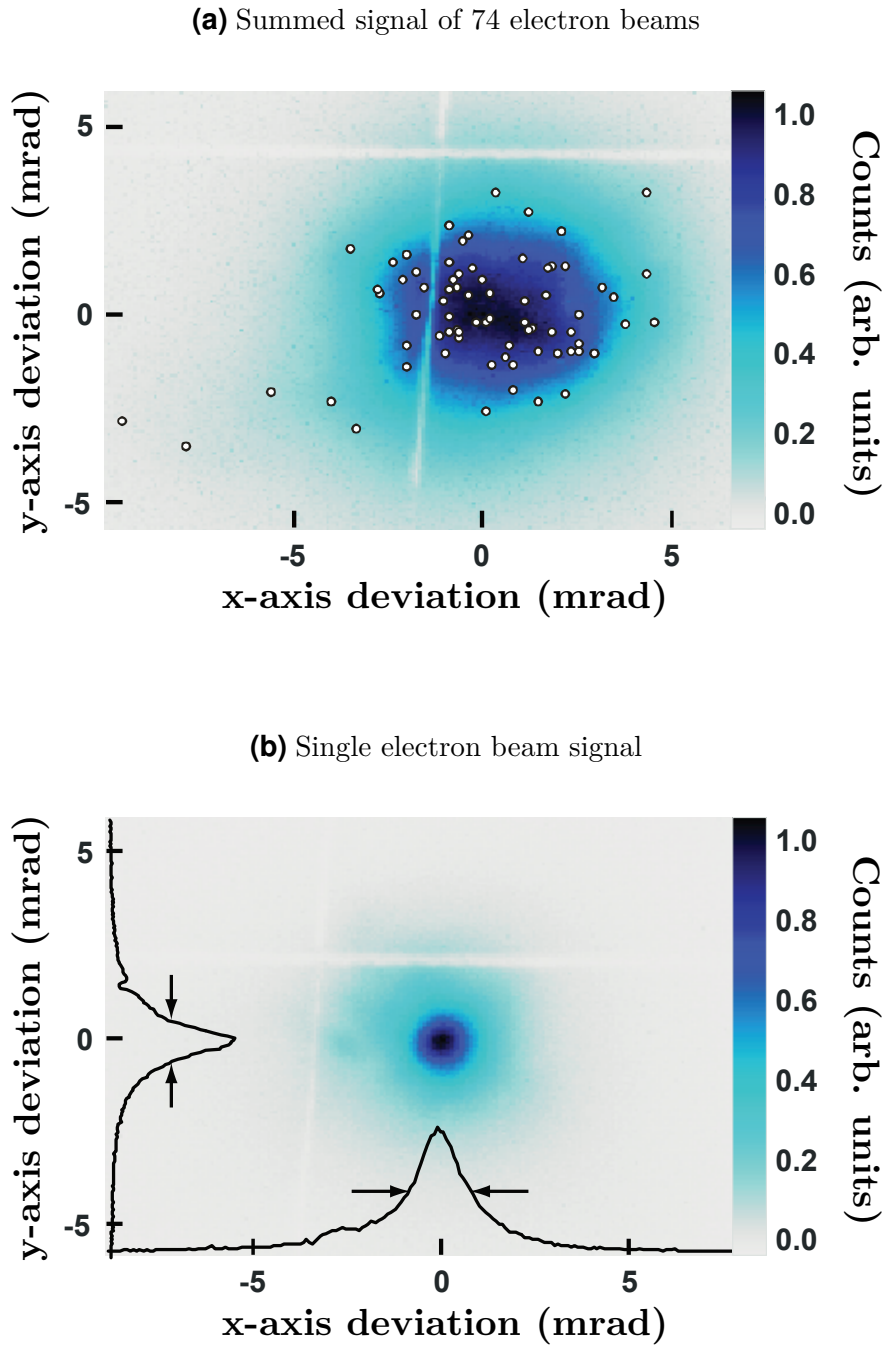


Figure 5.3.4 – Phosphorescence screen images at the dipole spectrometer entrance (S1). (a) Summed signal of 74 electron beams (in false-color) and the peak positions of the individual shots (dots) at $n_e \approx 7.8 \cdot 10^{18} \text{ cm}^{-3}$. RMS shot-to-shot pointing fluctuations under these conditions are 1.4 mrad (y-axis) and 2.2 mrad (x-axis). (b) False-color signal of a single electron beam with a FWHM divergence of 1.6 mrad. The crosses in the background originate from pen markings on the screen.

	CDW	SGC
Injection probability	$\sim 90\%$	$\rightarrow 100\%$
Electron energies (MeV)	~ 300	~ 200
Energy fluctuations (RMS)	30 %	2.5 %
Energy spread (RMS)	$> 5\%$	$> 2\%$
Charge in peak (pC)	~ 10	~ 10
Charge fluctuations (RMS)	75 %	16 %
Divergence (mrad RMS)	0.9	0.9
Pointing stability (mrad RMS)	8.3	1.4

Table 5.3.1 – A comparison of the properties of laser wakefield accelerated electrons for either a capillary discharge waveguide (CDW; confer chapter IV) or a steady-state-flow gas cell (SGC) being used as a target.

of all 74 shots is 2.1 ± 0.5 mrad FWHM. Assuming a transverse Gaussian beam profile⁴ this corresponds to 0.9 mrad RMS. This divergence is smaller by almost a factor of two compared to other studies (e.g. LEEMANS et al. [2006]), and originates predominantly from collective electron dynamics, trapping and intra-bunch Coulomb repulsion, whereas the contribution of scattering off background particles is negligible. This will be shown in appendix B.

3D-simulations of the laser-plasma interaction have been performed with the particle-in-cell code ILLUMINATION [GEISLER et al. 2006] to determine the role of pulse-shaping effects under the prevailing experimental conditions. The results suggest that electron trapping in the laser wake occurs only after the laser pulse has undergone significant self-focusing and -compression. This is supported by the fact that relativistic electrons were solely detected in the experiment for laser powers well above P_c , which is exceeded for $n_e > 2 \cdot 10^{18} \text{ cm}^{-3}$ with ATLAS parameters. Therefore, the dramatic improvement in stability over the work presented in chapter IV and in KARSCH et al. [2007] (for a quantitative comparison confer table 5.3.1) can be attributed to the modified gas target only. As was demonstrated in chapter III, the pre-shaping of the transverse and longitudinal electron-density profiles by means of an electrical breakdown and subsequent plasma cooling [SPENCE and HOOKER 2000] allowed for guiding of the laser light over several Rayleigh lengths. This facilitated longer acceleration distances and higher electron energies, but introduced significant shot-to-shot density-profile variations. The elimination of these fluctuations led to reproducible plasma conditions and electron beams in this study.

V.IV Summary and conclusion

In conclusion, electron bunches from LWFA were generated showing excellent stability by utilizing a hydrogen cell as the laser-plasma interaction volume. The virtue of this experiment lies

⁴The actual spatial distribution of the electron bunches cannot directly be obtained from the measured beam signal on S1 since betatron radiation and scattered low-energy electrons generate a halo around the central peak and therefore mask the profile in the wings.

in the improvement and simultaneous shot-to-shot stability of electron beam key parameters (divergence, pointing direction, charge and energy). Such beam stability is of crucial importance to the success of laser-driven electron sources for applications such as the generation of undulator radiation [FUCHS et al. 2009; SCHLENVOIGT et al. 2008] or free-electron lasers [GRÜNER et al. 2007]. Further, this concept has the benefit of simplicity compared to other setups (e.g. FAURE et al. [2006]) and unlike gas jets or capillary discharge waveguides can easily be scaled to very high repetition rates exceeding 1 kHz by employing continuous gas-flow.

Chapter VI

Electron-betatron-motion excitation by angularly chirped laser pulses

Since the early days of laser-wakefield acceleration, scientists have fostered the idea of utilizing the betatron motion of electrons inside a wakefield trough as an intense source for coherent photons with energies reaching into the X-ray band [WHITTUM et al. 1990]. However, this endeavor has proven to be a difficult task, given that until recently no handle existed for the systematic manipulation and coordination of electron-betatron orbits. In this chapter the influence of an angularly chirped and pulse-front tilted laser beam on LWFA will be investigated through numerical simulations, which suggest that such kind of electro-magnetic waves might provide the sought-after control over betatron trajectories. Therefore, a quick explanation of particle-in-cell codes will be given first (section VI.I), which is followed by an introduction into the physics of betatron motion and radiation (section VI.II), before the consequences of angular chirp in a laser field on wakefield generation will be discussed (section VI.III). This chapter is completed by the computational analysis of electron trapping and acceleration in such a scenario, which is also supported by preliminary experimental evidence (section VI.IV).

VI.I Basics of particle-in-cell calculations

Laser-driven wakefield generation, wave-breaking and electron acceleration in a tenuous plasma can generally not be treated by analytic theory owing to a highly nonlinear electron motion at relativistic intensities and the complicated interplay between high intensity laser pulses and large amplitude plasma wakes (as discussed in chapter I). Therefore, only numerical simulations provide means for virtually full-featured and instructive theoretical investigations.

In the case of kinetic particle calculations for laser wakefield acceleration, particle-in-cell (PIC) codes¹ have proven to be powerful tools, which helped to advance the field tremendously (see e.g. PUKHOV and MEYER-TER-VEHN [2002]). PIC codes describe the laser-plasma-interaction environment in close approximation to the actual system. In a real plasma, many individual particles interact with each other by self-consistently generated electro-magnetic fields. In PIC

¹For further details see HOCKNEY and EASTWOOD [1981]; DAWSON [1983]; BIRDSALL and LANGDON [1991]; VILLASENOR and BUNEMAN [1992].

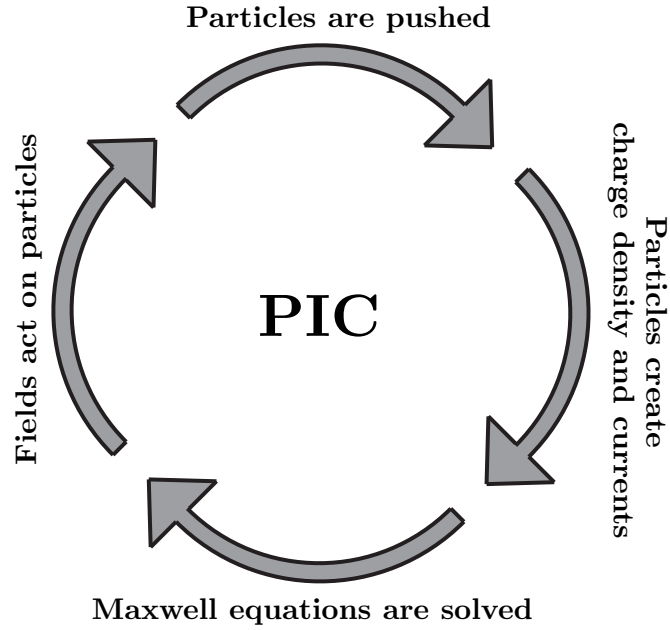


Figure 6.1.1 – A simple particle-in-cell algorithm calculation cycle.

simulations, these fields are discretized on a multi-dimensional spatial grid, whereas particles move continuously. Furthermore, the number of particles is significantly reduced compared to an actual plasma by merging 10^3 to 10^5 physical particles of the same species into one macroparticle, which features the same charge-to-mass ratio. Those macroparticles may be viewed as finite-sized clouds of an ensemble of real particles at similar speed. Such a macroparticle approach is mandatory to reduce the requirements for computational power, since simulation time scales approximately proportional with the number of simulated particles N_p . This simplified PIC picture is intuitive, leads to an applicable description of LWFA physics, and by today's standards represents the most complete manner of accessing wakefield acceleration in theory.

The working principle of PIC codes may briefly be summarized in the following way (also see figure 6.1.1). Starting from initial (macro)particle distributions and currents, and from discrete, initial conditions representing the state of the electro-magnetic fields on the grid, Maxwell's equations are solved. Thus, the field grid is modified and subsequently acts on the particles. Consequently each particle is moved inside the simulation volume according to the calculated solution of its equation of motion driven by the electro-magnetic grid potentials. The generated particle streams represent currents and set up new charge-density distributions. This again requires the solution of Maxwell's equations and initiates the next calculation cycle.

In that process, the duration of the discrete time-step $\delta\tau_C$, for which the particle motion and field propagation is calculated, can usually not be chosen arbitrarily. It must obey the Courant-Friedrichs-Lewy condition [COURANT et al. 1928], which couples spatial and temporal resolution and takes care of physically correct dispersion effects in laser propagation direction. This coupling of the discretization of space and time has an important consequence. Information only needs to be exchanged between neighboring grid cells, which makes PIC simulations perfectly suitable for large-scale parallelization without causing substantial data flow [DECYK

1995]. For more in-depth information about particle-in-cell formalisms, techniques and background knowledge refer to e.g. PUKHOV [2003].

Nowadays, PIC calculations are extensively used in laser-plasma physics. Examples of sophisticated codes are VLPL [PUKHOV 1999], VORPAL [NIETER and CARY 2004], ILLUMINATION [GEISLER et al. 2006] and OSIRIS [LEE et al. 2000]. The latter tool is utilized in section VI.IV to trace back energy-dependent pointing variations in a laser-wakefield accelerated electron beam to originate from betatron oscillations induced by angularly chirped laser pulses.

VI.II Formation of electron-betatron oscillations

Electron-betatron oscillations may emerge due to the radial restoring forces acting inside the electron void behind a wake-driving laser pulse (confer Panofsky-Wenzel theorem in section I.IV.I). In such a scenario, transversely injected relativistic electrons feature transverse momenta when initially trapped into the wave bucket, and subsequently oscillate around the on-axis potential minimum of that channel for as long as the wake structure stays intact [WHITTUM et al. 1990]. Their oscillation frequency $\omega_\beta = ck_\beta$ for small radial-excursion amplitudes $r_\beta \ll k_\beta^{-1}$ is given by [ESAREY et al. 2002]:

$$\omega_\beta = \frac{\omega_p}{\sqrt{2\gamma}}$$

As a result, these continuously oscillating electrons emit synchrotron radiation of wavelength:

$$\lambda_x \simeq \frac{\lambda_\beta}{2\gamma^2 N_\beta} \left(1 + \frac{K_\beta^2}{2} \right) \quad (6.2.1)$$

Here, N_β denotes the harmonic number. As may be seen, this expression describes a wavelength scaling equivalent to that of undulator radiation (cf. sec. VII.I), and consequently there exists a plasma-wiggler strength parameter $K_\beta = \gamma k_\beta r_\beta$, which in analogy to the undulator parameter K determines the appearance of betatron radiation for harmonics larger than unity for $K_\beta \rightarrow 1$ [ESAREY et al. 2002; KISELEV et al. 2004]. Such an emission has been experimentally confirmed for photon energies in the keV-range [ROUSSE et al. 2004]. Moreover this radiation source has been proposed for the construction of an ion-channel X-ray laser (ICL) [WHITTUM et al. 1990] with an operation principle similar to that of a SASE-FEL [KONDRATENKO and SALDIN 1979; BONIFACIO et al. 1984]. Unfortunately, the concept of a SASE-ICL is hard to realize, since unlike in a SASE-FEL, for which K does not depend on electron beam parameters, K_β is a function of both γ and r_β . Owing to the predominantly transverse injection mechanism occurring after bubble formation, and thus strongly varying transverse momenta for the injected electrons and therefore differing r_β , each electron will experience a different K_β , which places serious constraints on the realizability of the ICL concept. However, a narrow energy-spread electron bunch, which is trapped at an off-axis position inside the wakefield bucket, may allow to overcome this issue [ESAREY et al. 2002]. PIC simulations showing the feasibility of an off-axis injection by means of controlling the laser pulse angular chirp are reported in sec. VI.IV.

VI.III Asymmetric wakefield excitation by angularly chirped laser pulses

An angular chirp $C_a = d\varphi/d\lambda$, i.e. a variation in the propagation direction of all spectral laser components (cf. fig. 6.3.1a), may easily emerge in short-pulse CPA-systems from a non-parallel alignment of grating surfaces in stretcher or compressor units [PRETZLER et al. 2000]. Different wavelengths λ traveling along different paths under angles $\Delta\varphi(\lambda)$ with respect to the direction of the central laser frequency λ_c set up slightly tilted, wavelength-dependent virtual phase fronts. It is of importance to note that in contrast to these virtual phase fronts, the actual laser phase fronts remain unchanged in comparison with a similar but unchirped electro-magnetic wave. Therefore, the introduction of angular chirp does not change the effective beam propagation direction. However, it causes a spectral phase shift in its transverse dimension x :

$$\Delta\phi(\lambda, x) \approx \frac{2\pi}{\lambda} \Delta\varphi(\lambda) (x - x_0)$$

This leads to an x -dependent linear phase chirp of:

$$\left. \frac{d\phi(\lambda, x)}{d\lambda} \right|_{\lambda=\lambda_c} = \frac{2\pi}{\lambda_c} C_a (x - x_0)$$

Such phase chirp corresponds to a perpendicular group delay with $\omega_c = 2\pi c/\lambda_c$:

$$\Delta t_g(x) = \left. \frac{d\phi(\omega, x)}{d\omega} \right|_{\omega=\omega_c} = \frac{2\pi}{\omega_c} C_a (x - x_0)$$

Hence, the laser intensity front is tilted with respect to its phase fronts by (see figure 6.3.1b):

$$\alpha_I \approx \lambda_c C_a$$

A laser-pulse-front tilt (PFT) of a similar type can also arise from a combination of spatial and temporal chirp without demanding an angular-chirp component [AKTURK et al. 2004]. Therefore, the following discussion will focus on temporally compressed light pulses, for which PFT may exclusively develop from a spectrally varying propagation direction. Locally, this tilt of the intensity front barely affects pulse duration, which is the reason why small tilts are rather hard to detect in the laser near-field². However, they can have significant impact on the laser intensity at focus. Indeed, when an angularly chirped beam is focused down and approaches the far-field, the situation decisively changes (cf. fig. 6.3.2). For such a scenario, α_I grows along the axis of beam propagation until the laser pulse enters its Rayleigh range. There, its spectral components become spatially separated by $\Delta x(\lambda) = f C_a (\lambda - \lambda_c)$, i.e. spatially chirped, which drives two distinct mechanisms that again reduce α_I and at the same time lower the maximum

²Among the most sensitive techniques for angular chirp diagnosis are spectrally-resolved inverted field auto-correlation [VARJÚ et al. 2002] and GRENOUILLE [AKTURK et al. 2003].

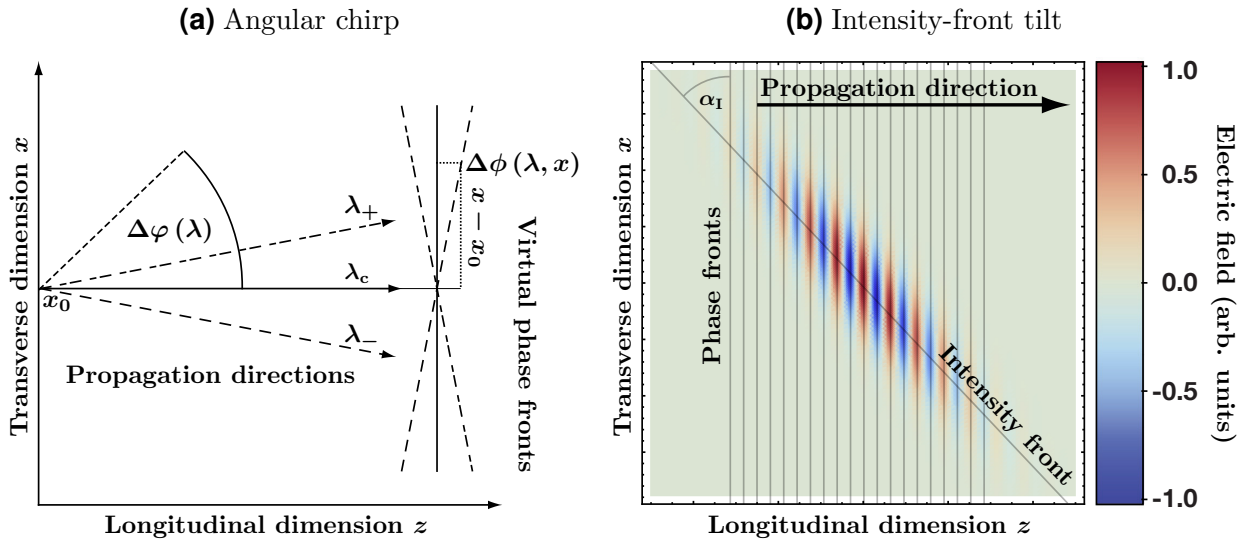


Figure 6.3.1 – Different spectral laser components traveling under different angles $\Delta\varphi(\lambda)$ with respect to the propagation direction of the central laser wavelength λ_c are associated with virtual phase fronts, which set up position-dependent spectral phase shifts $\Delta\phi(x)$ (a). These shifts create a perpendicular group delay and cause a tilt of the laser intensity front relative to the laser phase fronts (b).

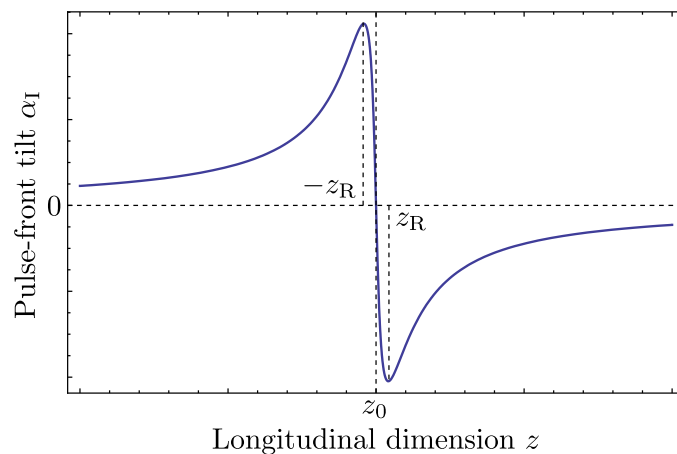


Figure 6.3.2 – Intensity-front tilts of angularly chirped laser pulses display a rapid evolutionary behavior near focus. When approaching the Rayleigh range z_R , the absolute value of α_I is maximized, just before collapsing to zero at the focal position z_0 . After passage through focus, the tilt flips and its direction becomes inverted.

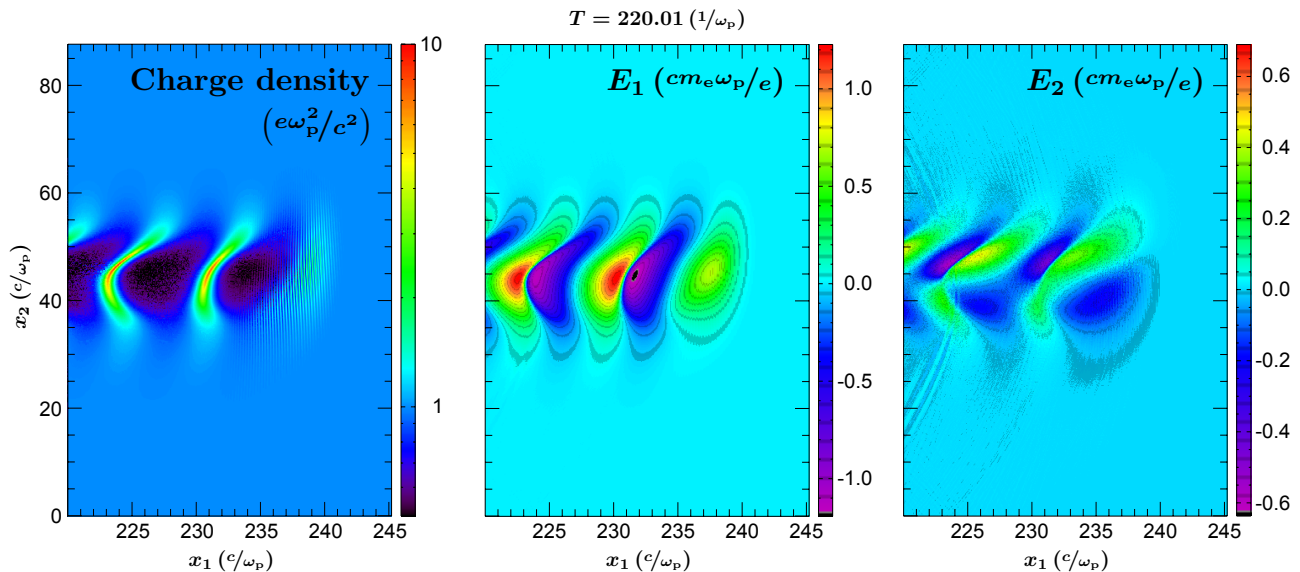


Figure 6.3.3 – Asymmetric wakefield excited by an angularly chirped laser pulse. The charge density, and longitudinal (E_1) and transverse (E_2) electric-field components are shown just before wave-breaking.

achievable intensity as compared to a similar but unchirped pulse. Here, f denotes the focal length of the employed focusing setup. First, this spectral separation process produces an elliptically shaped spot profile near focus with an elongated axis within the plane of PFT. Second, local spectral decomposition leads to bandwidth narrowing and hence an extended pulse duration, which in addition also varies along x . These two effects cause the intensity-front tilt to rapidly decrease, to disappear right at focus and to flip after crossing the focal plane. Moreover, each of these processes entails a decrease in total intensity, which is given by approximately the same factor of \mathfrak{J} in the special case of Gaussian pulse envelopes in space and time with a FWHM wavelength bandwidth of $\Delta\lambda$ and a small angular chirp³ (for a derivation see PRETZLER et al. [2000]):

$$\mathfrak{J} = \sqrt{1 + \left(\frac{f C_a \Delta\lambda}{w_0 \sqrt{2 \ln 2}} \right)^2}$$

Thus, the total intensity drop at focus due to an angular chirp in the near-field scales as $\sim \mathfrak{J}^2$. For the experimental results presented in the next section \mathfrak{J}^2 can be expected to not exceed 1.1 with $f = 1.54$ m, $\Delta\lambda \approx 25$ nm, $w_0 = 23$ μm and $C_a < 0.1$ $\mu\text{rad}\cdot\text{nm}^{-1}$.

The application of such intensity-front-tilted light pulses in laser wakefield acceleration brings about some interesting consequences. This has been investigated by numerical simulations using the particle-in-cell code OSIRIS in a phase-space configuration of two spatial and three momentum dimensions. Figure 6.3.3 displays a simulated wakefield just before wave-breaking with the generated charge-density distribution, and longitudinal (E_1) and transverse (E_2) electric-field components induced by a $\tau_L = 40$ fs FWHM, $a_0 = 2$ laser pulse focused over $f = 1.54$ m to a waist size of $w_0 = 22$ μm into a plasma of $n_e = 7 \cdot 10^{18}$ cm^{-3} average density. When initialized at focus with the focal plane situated just before the vacuum-plasma boundary, the

³More precisely, the condition $|2\pi f C_a| \ll |\Delta x \Delta \lambda^{-1}|$ must be fulfilled [GU et al. 2004; POPP et al. 2009].

light wave does not excite a strong wake from the very beginning owing to a mismatch of pulse duration and plasma wavelength. For this reason, laser-pulse self-compression and focusing are necessary to help forming a high-amplitude wake, which is almost ready to break after the electro-magnetic wave has traveled along a distance of roughly 500 μm . Over this propagation length the strongly angularly chirped ($C_a \approx 0.2 \mu\text{rad}\cdot\text{nm}^{-1}$) and hence at focus spectrally decomposed beam develops an intensity-front tilt. As may be seen, this tilt drives an asymmetric wakefield, leading to strong distortions of the electron density before and behind every wake period and to asymmetric electric fields inside the electron voids. Such a scenario differs from LWFA with angularly unchirped laser beams in two ways. First, the asymmetry in electron density and thus the refractive-index gradient at the position of the laser beam forces the complete system of laser pulse trailed by the wake to deviate from its original propagation direction. This provides a handle for a systematic manipulation of the pointing of an accelerated electron beam and is discussed in detail in POPP et al. [2009]. The second effect alters the way electrons are trapped and accelerated within the wake and is investigated next.

VI.IV The phenomenology of induced collective electron-betatron orbits

In order to discuss the implications of electron injection with angularly chirped laser pulses in a proper manner it is not sufficient to employ the two-dimensional simulation geometry in space, which was used in section VI.III, since electron trapping in 2D varies notably from wave-breaking processes observed in a full-featured three-dimensional numerical calculation (whereas pulse-front tilt is a purely two-dimensional effect). Therefore, 3D simulations have been conducted allowing to include all important physical aspects. However, such computations demand a lot of power, which is the reason why a new set of simulation parameters needed to be chosen in order to allow for these calculations to finish within a day on 128 processors of an IBM Power6 super-computer⁴. In this context, the ratio of laser pulse duration to plasma wavelength has been reduced. This enables the use of smaller simulation box sizes and hence eases hardware requirements. In summary, the altered parameters are $a_0 = 3$, $n_e = 1.7 \cdot 10^{19} \text{ cm}^{-3}$, and $\tau_L = 17 \text{ fs}$. Although these quantities are different from the specifications of the experiments presented later in this section, they will nevertheless allow for a valid qualitative interpretation of a modified electron trapping behavior in an asymmetric wake structure.

Figure 6.4.1a visualizes a time series of these simulation results showing the wake generated by an angularly chirped light pulse of $C_a = 0.017 \mu\text{rad}\cdot\text{nm}^{-1}$ beginning with the time of incipient electron trapping (leftmost window $T = 88.61 \text{ w}_p^{-1}$) and ending shortly before release of these electrons into vacuum (rightmost window $T = 238.85 \text{ w}_p^{-1}$). Owing to an asymmetric electric-field distribution (see section VI.III) the electron injection center is shifted off the central wakefield axis. Hence, all injected electrons are forced onto an oscillating trajectory

⁴For details see <http://www.rzg.mpg.de/computing/hardware/Power6/about-the-system>.

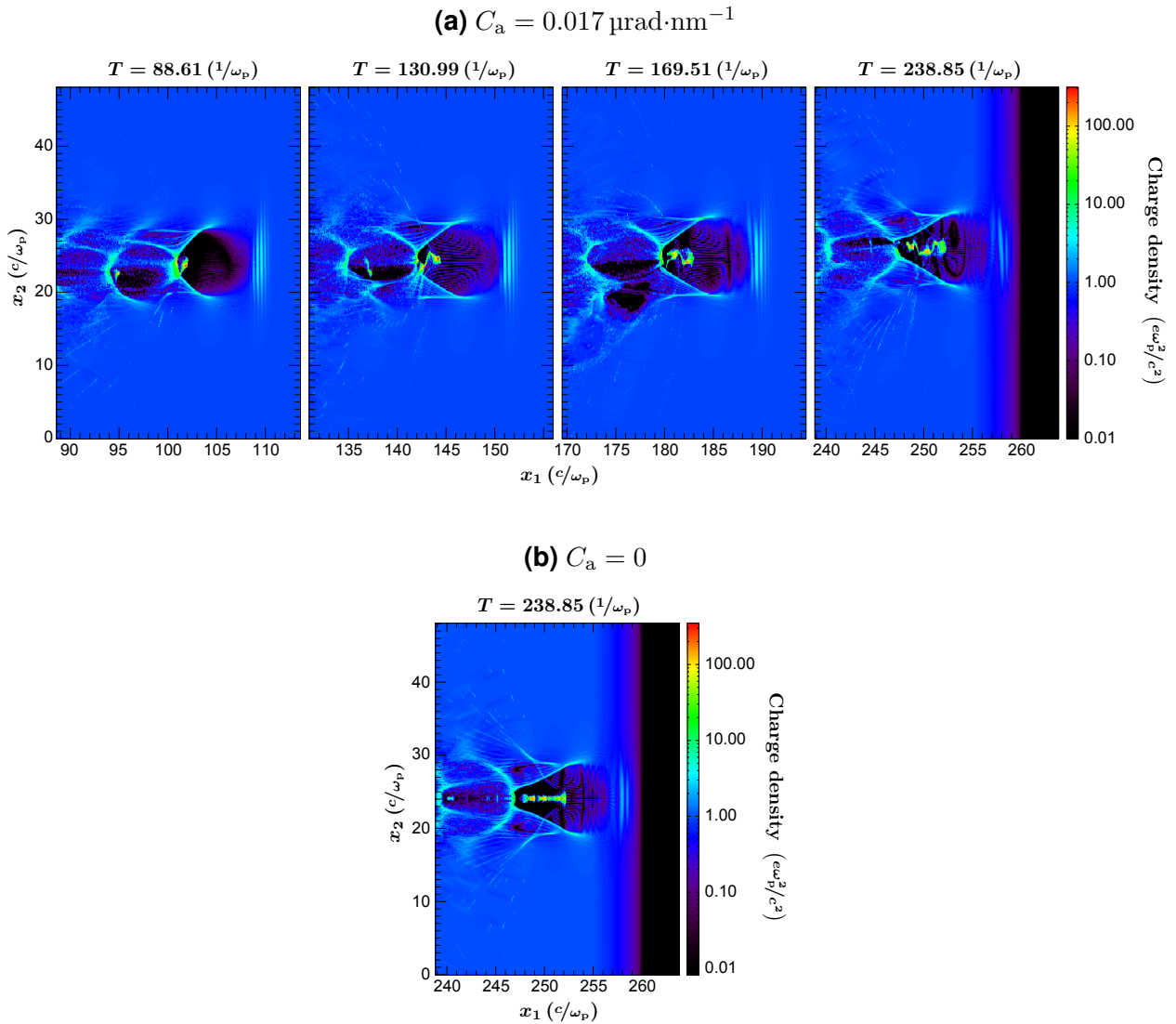


Figure 6.4.1 – Three-dimensional particle-in-cell simulation of an angularly chirped laser pulse, which drives a wakefield through a plasma. Along its way, electrons are trapped off-axis and subsequently accelerated until the vacuum boundary is reached (a). The time series depicts the electron-bunch dynamics inside the wake bucket and shows collective electron-betatron oscillations. Subfigure (b) displays the final time step of a simulation result for the same parameter set as used in (a), but without angular chirp. No collective oscillations can be observed.

with amplitude r_β and wavelength λ_β around the transverse potential minimum of the wake bucket. These oscillations have not been observed without an angular-chirp component (figure 6.4.1b). Moreover, a longitudinally bunched electron-stem structure is created. This behavior may also be seen for bubble stems in the case of $C_a = 0$ (cf. section I.IV.V), but in this case originates from a combination of longitudinal and transverse bunch motion. Trapped electrons induce localized beam loading at the rear side of the void and thus cause a local suppression of the electric field, which counteracts wave-breaking at the very position of the injection center. When these inhibiting electrons transversely oscillate away from the injection point while being longitudinally accelerated, the electric field can regenerate and again permit trapping. This should alter the electron-stem bunching frequency as compared to a symmetrically driven wake. The amplitude and wavelength of the described collective oscillations can be extracted from the simulations to be $r_\beta \approx 1.3 \mu\text{m}$ and $\lambda_\beta \approx 100 \mu\text{m}$, respectively. In conjunction with the observed electron energies corresponding to a relativistic γ in the range between 150 and 250 (cf. fig. 6.4.2), the first harmonic wavelength spectrum of the emitted betatron radiation is estimated with (6.2.1) to be situated around 170 nm. Owing to the strong link between the electron energy and $K_\beta^2 \propto \gamma^2$ the total bandwidth of the generated betatron spectrum is only weakly influenced by γ itself, which cancels in the dominating K_β^2 -term, but is rather governed by variations in r_β and by $K_\beta > 10$, which causes broadband spectral emission [WILLE 1996]. Admittedly, these are purely theoretical considerations, since no betatron-radiation spectrum can be extracted from the performed numerical calculations. This would require simulations with a tenfold higher resolution in x_1 -direction, and since time and space are coupled via the Courant condition (see section VI.I), that would also demand a time-step decrease of similar magnitude, hence increasing computation time by a factor of ~ 100 .

Furthermore, the wiggling motion seen in the charge-density plots (figure 6.4.1a) gives rise to asymmetric and rippled structures in $p_1 p_2$ -electron-phase space (figure 6.4.3a), which do not appear when a laser with an untilted intensity front is applied (figure 6.4.3b). Also evident is a global shift of the transverse electron momentum away from $p_2 = 0$ corresponding to a net deviation of the electron bunch from the initial axis of laser propagation [POPP et al. 2009].

In order to qualitatively verify these theoretical findings, laser-wakefield acceleration experiments have been performed in the same setup as detailed in chapter V with nearly identical laser and plasma parameters ($a_0 \approx 0.9$, $\tau_L \approx 42 \text{ fs}$ FWHM, $\lambda_c \approx 800 \text{ nm}$, and $n_e \approx 8.7 \cdot 10^{18} \text{ cm}^{-3}$). Additionally, an angular chirp was introduced into the beam by detuning the parallel alignment of the compressor gratings while maintaining the laser pulse duration. This chirp was characterized by means of inverted field autocorrelation (IFA) for the images of phosphorescence screen S2 shown as parts (a) and (b) of figure 6.4.4 ($C_a \leq 0.007 \mu\text{rad}\cdot\text{nm}^{-1}$ in both cases), and for (c) by spectrally resolved IFA with $C_a \approx 0.027 \mu\text{rad}\cdot\text{nm}^{-1}$ (for details on the different IFA versions see VARJÚ et al. [2002]). Figure 6.4.4 can be regarded as a $p_1 p_2$ -plot, since the measured electron energy $W_e \propto \gamma$ is essentially proportional to longitudinal momentum for ultra-relativistic speeds owing to $p_1 \gg p_2$ and $p_1 \propto \gamma \beta_x$ with $\beta_x \approx 1$. In transverse direction the detected electron-path deviation x depends mainly on the transverse electron velocity and

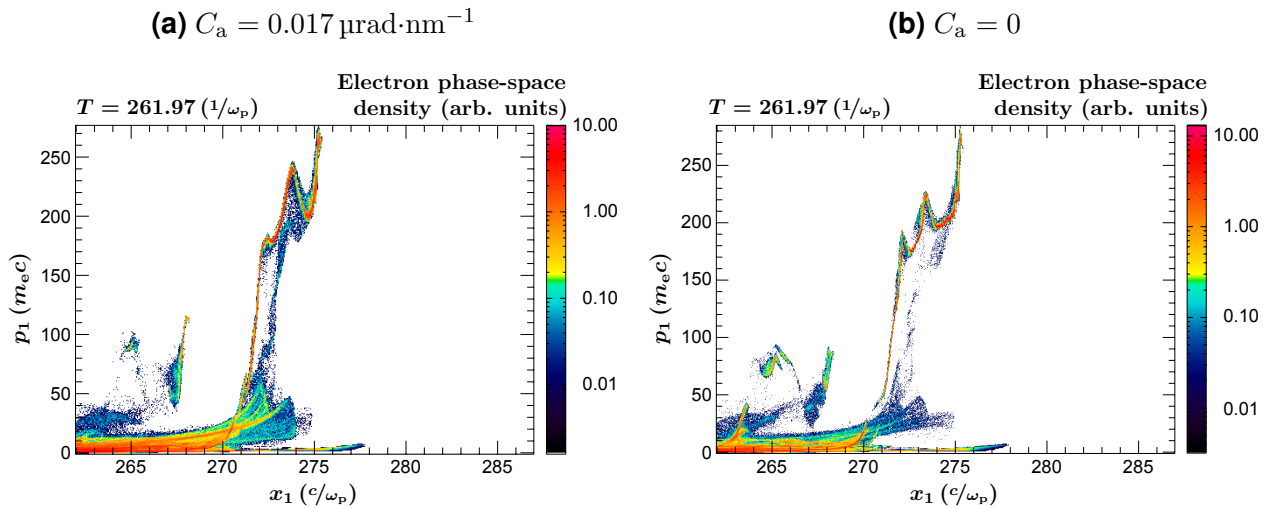


Figure 6.4.2 – Phase space ($x_1 p_1$) after the bubble electrons have crossed the plasma-vacuum boundary. A tilted (a) or untilted (b) laser intensity front provides LWFA conditions that result in comparable longitudinal momentum distributions. (b) features marginally higher particle energies due to a slightly higher intensity at focus (cf. sec. VI.III).

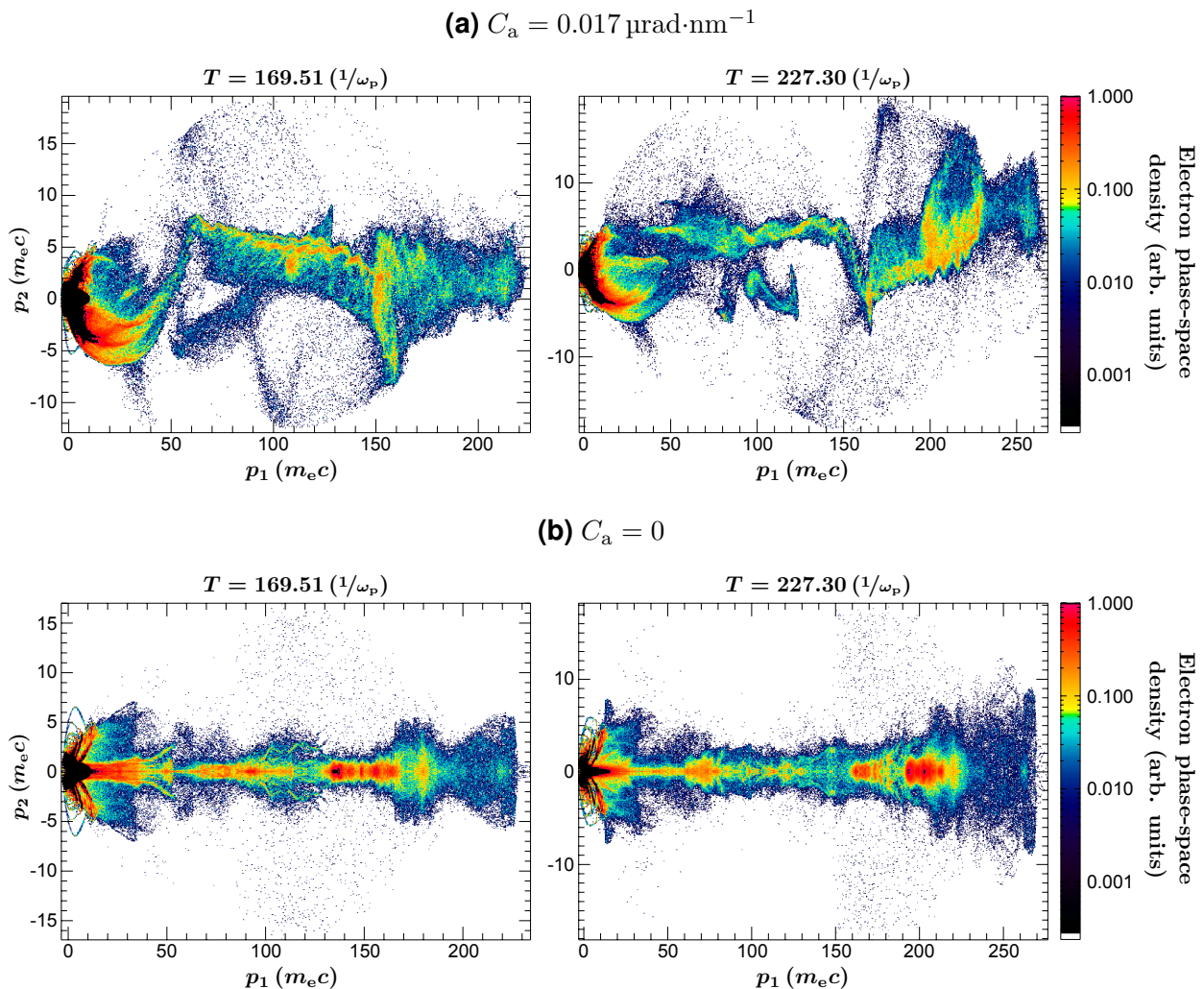


Figure 6.4.3 – Electron-phase-space diagrams ($p_1 p_2$) for two different time steps in the case of a laser pulse with (a) and without (b) angular chirp.

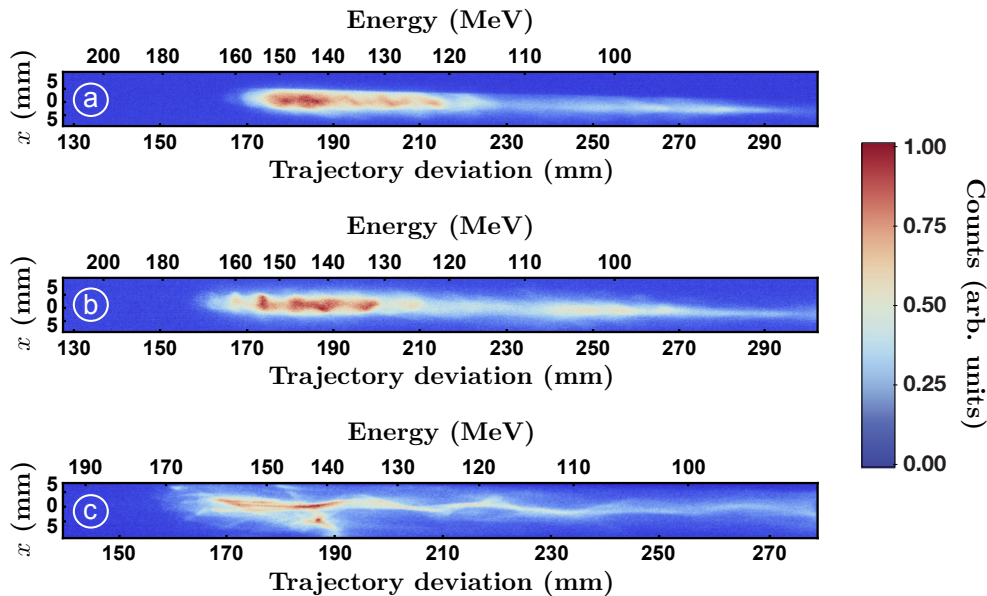


Figure 6.4.4 – Experimental evidence of induced electron-betatron oscillations detected on phosphor screen S2. Here, laser pulses with angular chirps of $C_a \leq 0.007 \mu\text{rad}\cdot\text{nm}^{-1}$ (a and b) and $C_a \approx 0.027 \mu\text{rad}\cdot\text{nm}^{-1}$ (c) have been used to drive asymmetric LWFA processes.

hence is in good approximation a direct function of p_2 . As may be seen, qualitative agreement is found between the rippled structures appearing in the simulated and the measured equivalent of p_1p_2 -phase space for $C_a \neq 0$. If these detected corrugated formations indeed originate from collective betatron oscillations of an LWFA electron stem⁵, then it should be possible to record a scan of characteristic angular-chirp dependent betatron-photon spectra in a future study. In addition to that and in agreement with the above presented simulations, a global electron bunch deviation from the initial laser propagation axis could be experimentally observed. It is analyzed in POPP et al. [2009].

VI.V Concluding remarks

The possibility of an off-axis electron injection into a laser wakefield by means of controlling the laser-beam angular chirp has been demonstrated in full-featured three-dimensional particle-in-cell simulations. Moreover, experimental evidence suggests the feasibility of this approach in experiments, although a proof in the form of an angular-chirp susceptible betatron-radiation spectrum remains to be found. Thinking further ahead, this mechanism might open the door for the construction of an ion-channel laser [WHITTUM et al. 1990]. If off-axis injection could be combined with a control over the time window during which electron-trapping occurs, which has been demonstrated by FAURE et al. [2006] and RECHATIN [2008], in such a way that a very localized and monoenergetic bunch is accelerated along a well-determined oscillating trajectory in resonance with its own emitted betatron radiation, then micro-bunching and possibly lasing might be observable [ESAREY et al. 2002].

⁵GLINEC et al. [2008] suggest another, but certainly less likely explanation.

Chapter VII

Concluding thoughts on future applications and developments

Electron pulses from state-of-the-art laser-wakefield accelerators have demonstrated quasi-monoenergetic energy distributions reaching up to a GeV with energy spreads of considerably less than 10% FWHM [LEEMANS et al. 2006; KARSCH et al. 2007; HAFZ et al. 2008]. These beams typically contain on the order of 10^8 to 10^9 electrons concentrated into a momentum phase-space of low transverse-emittance (~ 1 mm·mrad) [FRITZLER et al. 2004]. The electron-pulse length has been inferred from theory and particle-in-cell simulations to be a fraction of the corresponding plasma wavelength, therefore electron bursts are assumed to last for an ultra-short time (~ 10 fs) [PUKHOV and MEYER-TER-VEHN 2002], and hence create currents of > 10 kA. Over the last years, stability issues arising from the nonlinear nature of self-injected LWFA and laser-plasma fluctuations have become more and more manageable through modified injection schemes [FAURE et al. 2005; GEDDES et al. 2008] and, as a result of the work at hand, reproducible targets [OSTERHOFF et al. 2008]. Also, tailoring these relativistic electron aggregations in peak energy [FAURE et al. 2005], energy spread [RECHATIN 2008] and pointing direction [POPP et al. 2009] is rendered possible nowadays within certain limits. Such progression in technology and understanding, in addition to the improvement of laser-driven electron beams in quality and availability as disclosed in this dissertation, will eventually lead to their regular deployment in applications, if that enormous evolutionary pace can be sustained. Some prospective and eagerly anticipated developments will be outlined in the following sections on the basis of four different examples, which by no means constitute an extensive list of open scientific questions and challenges that need to be tackled in the field of LWFA.

VII.1 Laser-driven undulator-radiation sources and table-top free-electron lasers

Two of the signature applications envisioned for such beams is driving undulator-radiation sources and free-electron lasers. Typical linear undulators consist of magnetic-dipole structures in n_U periodic arrangements of length λ_U (confer e.g. WILLE [1996], ONUKI and ELLEAUME

[2003], or ATTWOOD [2007]). Electrons propagating within the central undulator plane perpendicular to the undulator magnetic field will start to perform individual wiggling motions of resonant spatial periodicity λ_U , which correspond to figure-eight motions in a co-moving frame of reference. Owing to these figure-eight trajectories and the relativistic electron momenta, the perpendicularly accelerated charges send out photons in a forward cone of angle $\Theta_U \propto \gamma^{-1}$ at a wavelength λ_R and its harmonics. This is described by the undulator-resonance condition:

$$\lambda_R = \frac{\lambda_U}{2N_U\gamma^2} \left(1 + \frac{K^2}{2} + \gamma^2\Theta_U^2 \right)$$

In this expression, N_U denotes the harmonic number. $K = e\lambda_U\tilde{B}(2\pi m_e c)^{-1}$ represents the so called wiggler or undulator parameter, where \tilde{B} is the maximum magnetic field strength within the plane of electron propagation. For $K = 1$, these electrons travel exactly within the opening angle of their respective radiation fields, which thus can act back on each emitting electron with high efficiency. However, since an ensemble of electrons will initially be randomly distributed in the undulator field, the electrons do not share the same phase. Hence, the described radiation process is incoherent and the number of radiated photons N_{ph} grows proportional to the number of wiggling electrons N_e .

In contrast, in a free-electron laser configuration $N_{\text{ph}} \propto N_e^2$ holds true. Here, the radiation mechanism becomes coherent, since all electrons radiate with similar phase. This can be pictured intuitively, when considering the aforementioned coupling of the radiation field to the electrons, which will cause a spatial oscillation of electron energies (photon emission results in energy loss, absorption in energy gain). The changed energy distribution corresponds to a spatially oscillating velocity distribution, which after some specific propagation distance will evolve into a spatial electron density variation of characteristic length λ_U . That process is called microbunching. Now, these microbunches emit photons in phase, leading to coherent superposition of radiation and thus in return to amplified bunching and hence amplified radiation. If the described mechanism starts from background noise, it is called self-amplification of spontaneous emission (SASE). What makes LWFA-driven FELs particularly interesting is their potentially reduced size by a factor on the order of 10 compared to conventionally driven sources (usually tens of meters long), owing to a favorable scaling of the distance over which the emitted photon flux saturates with electron-beam current.

Indeed, such an all-optically driven free-electron laser has not been build, yet. This is due to the fact that the onset of FEL operation depends critically on the quality of the utilized electron bunches, namely on beam current, on tight spatial confinement and on transverse and longitudinal emittances. The latter is particularly problematic and dictates a local beam-energy spread of less than the Pierce parameter ρ [BONIFACIO et al. 1984], which for LWFA-FELs is typically on the order of 0.1% (also confer section VII.II). Once such strict electron-pulse specifications can be met, a laser-driven FEL promises to constitute a unique photon source, which may yield ~ 60 GW of peak power at a wavelength of 0.25 nm in a 4 fs duration flash (confer GRÜNER et al. [2007]). Nevertheless, laser-accelerated electron beams have been successfully

used to generate undulator radiation in the visible to near-infrared range [SCHLENVOIGT et al. 2008] and, just recently, at wavelengths below 10 nm [FUCHS et al. 2009], the latter employing the stable electron source described in chapter V of this dissertation.

VII.II Controlled injection for low energy spread electron-beam generation

As discussed in section VII.I, an electron-pulse energy spread of considerably less than 1% is key to allow for LWFA-driven FEL operation. Hence, a reduction of the longitudinal emittance of laser-accelerated electron bunches is a high priority goal on various research agendas. Currently, three main strategies exist that may lead to a solution of this issue. DE LOOS et al. [2006] are pursuing the idea of feeding pre-accelerated narrow energy spread 6 MeV-electrons created by a conventional radio-frequency photoinjector into a laser-plasma wakefield. A main problem of this approach arises from the rather long initial electron-pulse duration of ~ 100 fs, which is limited by RF-technology and Coulomb repulsion. That kind of spatially dispersed charge distribution captured into a wakefield structure will experience varying accelerating field strengths at different positions along the bunch. Therefore it will be difficult to maintain excellent longitudinal emittance. Such an external-injection technique may prove successful only in an experimental configuration, in which the original electron-bunch length is considerably shorter than the plasma-oscillation wavelength. In addition, the synchronization of the wake-driving light burst to the RF-cavity timing has proven problematic on a femtosecond-time scale. Hence, only laser-triggered injection methods might yield applicable answers. In general, minimizing the time-window during which electron trapping occurs, entails a reduction in energy spread, since for short trapping periods every injected particle may be accelerated over a similar distance with a similar electric field profile. Moreover, if the maximum acceleration distance, which ends at the electron-dephasing point in momentum-phase space, is slightly exceeded, then an accompanying minimization of the bunch-energy spread can be achieved by longitudinal momentum compression (confer figure 1.4.5). As a matter of course, such a scheme requires exact control over the trapping process, which may be acquired by employing a two-laser beam setup [FAURE et al. 2005]. Varying the intensity and focal position of the injection pulse allows for altering the trapping-time window and the acceleration length, respectively. Preliminary experiments have demonstrated the feasibility of this method yielding RMS spreads of 1% around ~ 200 MeV of electron energy [RECHATIN 2008]. A different way to manage electron injection with high accuracy represents controlled Langmuir wave-breaking at steep plasma-density gradients [BULANOV et al. 1998; SUK et al. 2001; HEMKER et al. 2002]. Recently, GEDDES et al. [2008] have adopted this technique and created stable, low longitudinal momentum spread (~ 170 keV/ c) electron bunches, albeit at sub-MeV/ c average momenta. Further acceleration of these beams in a second energy-spread maintaining LWFA-stage of lower density may allow for driving a free-electron laser in an all-optical scheme in the future.

VII.III Staged accelerator concepts

The scalability of laser-driven wakefields to support electron-beam energies beyond the 10 GeV frontier [KATSOULEAS 2006] potentially permits their application in an advanced particle-collider concept. Indeed, the construction of such a machine is an ambitious task, which requires an implementation of acceleration units working in series and thus motivates the research towards the realization of staging. Modern petawatt-class laser facilities are expected to enable LWFA in a single stage to access electron energies of several GeV [LU et al. 2007]. However, a single laser system allowing for peak energies that may compete with today's modern particle colliders would have to feature light-peak powers several orders of magnitude higher than currently available. Therefore, tens of optically synchronized petawatt-laser beams could drive tens of successive wakefield-acceleration units, each one operating with longitudinal electric fields in excess of 10 GVm^{-1} . Such an assembly would enable the creation of TeV-class electron pulses in a machine of some hundred meters length, which compared with conventional collider technology constitutes a reduction in accelerator size and costs by a factor of ~ 100 .

Nevertheless, peak-particle energy does not represent the only challenge for an application of laser-accelerated electrons in high-energy physics. A principal attribute governing collider-design considerations is the event rate for the physical process of interest. This event rate is proportional to the beam luminosity L , given by (see e.g. MUSIOL et al. [1988]):

$$L = \frac{f_{\text{rep}} N_{\text{part}}^2}{4\pi\sigma_x\sigma_y}$$

Here, f_{rep} is the bunch repetition rate and N_{part} the number of particles contained in each bunch, σ_x and σ_y describe the spot size at the collision point in transverse dimensions. It is no exaggeration to state that the requirements for a next-generation particle collider allowing for measurable access to novel particle physics are immense regardless of the acceleration technique used, e.g. electron collisions at 250 GeV demand that $L \approx 10^{34} \text{ cm}^{-2}\text{s}^{-1}$, which calls for particle beams focusable to nanometer-size spots [KATSOULEAS 2006]. Hence, laser-driven colliders at the forefront of particle physics will remain a visionary concept for the next decades.

VII.IV Temporal electron-bunch characterization

A unique feature of laser-accelerated electron pulses is their ultra-short nature. While particle-in-cell codes and theoretical considerations have predicted bunch durations of just a few femtoseconds [PUKHOV and MEYER-TER-VEHN 2002; GEISLER et al. 2006], an experimental proof is still missing. Indeed, this property is of vital interest for the feasibility of the all-optically-driven FEL concept (sec. VII.I) and accounts for the potential of applying this source of coherent radiation e.g. for time-resolved single molecular imaging [NEUTZE et al. 2000].

According to simulations, the few-cycle laser sources planned or operated at MPQ such as the upcoming Petawatt Field Synthesizer (PFS) [KARSCH et al. 2008] or the LWS-10 system

[TAVELLA et al. 2006] are able to create these very short electron bursts when focused into high plasma-density environments of $n_e > 10^{19} \text{ cm}^{-3}$. The detection of their duration however is difficult. Electro-optic sampling, a default technique often used at conventional particle accelerators, is limited to pulse durations well above 50 fs FWHM and therefore unsuitable [VAN TILBORG et al. 2006]. An applicable alternative is the spectroscopy of the coherent cut-off region of infrared to terahertz transition radiation, which is emitted when electrons pass a refractive index boundary [JACKSON 1975]. The radiated photon spectrum from such a process is directly related to electron-bunch shape and duration [VAN TILBORG et al. 2004; DELSIM-HASHEMI 2008]. However, this correlation is not unique, with the consequence that a retrieval of pulse duration must assume a model for the electro-magnetic phase of different radiation components, since the measured spectrum does not contain phase information, and hence cannot deliver a fail-safe bunch-length proof. Several other ideas exist, which promise to provide unambiguous results but are more complicated to realize, such as the exploitation of the laser-assisted Auger-decay effect [SCHINS et al. 1994], attosecond streaking [RECKENTHAELER et al. 2008], inverse free-electron laser electron-bunch slicing [SEARS et al. 2005, 2008] or the optical replica synthesizer [ANGELOVA et al. 2008]. Nevertheless, the true duration of laser-wakefield accelerated electron pulses lacks confirmation and thus remains their last major undetermined property.

Appendix A

An analytical dipole-spectrometer model

The path deviation experienced by a single electron when propagating through a magnetic field of strength \vec{B}_{dm} and longitudinal dimension l_{dm} in a configuration as depicted in figure 4.1.1, is governed by the Lorentz force \vec{F}_L . The corresponding equation of motion can be written as:

$$\gamma m_e \frac{d^2 \vec{r}}{dt^2} = -e \left(\frac{d\vec{r}}{dt} \times \vec{B}_{\text{dm}} \right) \quad (\text{A.1})$$

Here, γ is the relativistic factor associated with the electron and \vec{r} describes its position vector. Without loss of generality, the magnetic field is chosen to point into x-direction, whereas the electron travels within the y - z -plane. Then (A.1) transforms into:

$$\gamma m_e \frac{d^2}{dt^2} \begin{pmatrix} y \\ z \end{pmatrix} = e B_{\text{dm}} \frac{d}{dt} \begin{pmatrix} -z \\ y \end{pmatrix} \quad (\text{A.2})$$

Since $\frac{d}{dt} \vec{r} \perp \vec{F}_L$, the time derivative of (A.2) is given by:

$$\gamma m_e \frac{d^3}{dt^3} \begin{pmatrix} y \\ z \end{pmatrix} = e B_{\text{dm}} \frac{d^2}{dt^2} \begin{pmatrix} -z \\ y \end{pmatrix} \quad (\text{A.3})$$

Combining (A.2) with (A.3) allows for the decoupling of coordinates y and z :

$$\frac{d^3}{dt^3} \begin{pmatrix} y \\ z \end{pmatrix} = -\omega_{\text{ce}}^2 \frac{d}{dt} \begin{pmatrix} y \\ z \end{pmatrix}$$

with $\omega_{\text{ce}} = e B_{\text{dm}} (\gamma m_e)^{-1}$ being the relativistic electron cyclotron frequency. A solution to this set of differential equations has the form:

$$\begin{aligned} y &= \frac{C_1}{\omega_{\text{ce}}} \sin(\omega_{\text{ce}} t) - \frac{C_2}{\omega_{\text{ce}}} \cos(\omega_{\text{ce}} t) + C_3 \\ z &= \frac{D_1}{\omega_{\text{ce}}} \sin(\omega_{\text{ce}} t) - \frac{D_2}{\omega_{\text{ce}}} \cos(\omega_{\text{ce}} t) + D_3 \end{aligned} \quad (\text{A.4})$$

C_χ and D_χ with $\chi \in \{1, 2, 3\}$ are integration constants to be determined. Inserting (A.4) into (A.2) yields the relations $C_1 = D_2$ and $C_2 = -D_1$. The remaining coefficients depend on the electron's position and velocity, when entering the magnetic field, and are derived as follows. In order to treat electron-pointing variations appropriately, additional parameters are introduced: l_{fd} defines the shortest free-drift distance from a point-like electron source to the magnet and δ accounts for angular fluctuations in electron emission. Then, the initial conditions are:

$$\begin{aligned} y(0) &= l_{fd} \tan \delta & z(0) &= 0 \\ \frac{dy}{dt}(0) &= c \sqrt{1 - \frac{1}{\gamma^2}} \sin \delta & \frac{dz}{dt}(0) &= c \sqrt{1 - \frac{1}{\gamma^2}} \cos \delta \end{aligned}$$

From these connections, C_χ and D_χ may be expressed as:

$$\begin{aligned} C_1 &= c \sqrt{1 - \frac{1}{\gamma^2}} \sin \delta & C_2 &= -c \sqrt{1 - \frac{1}{\gamma^2}} \cos \delta & C_3 &= l_{fd} \tan \delta - \frac{c}{\omega_{ce}} \sqrt{1 - \frac{1}{\gamma^2}} \cos \delta \\ D_1 &= c \sqrt{1 - \frac{1}{\gamma^2}} \cos \delta & D_2 &= c \sqrt{1 - \frac{1}{\gamma^2}} \sin \delta & D_3 &= \frac{c}{\omega_{ce}} \sqrt{1 - \frac{1}{\gamma^2}} \sin \delta \end{aligned}$$

As a result, $y(t)$ and $z(t)$ are obtained as:

$$\begin{aligned} y(t) &= \frac{c}{\omega_{ce}} \sqrt{1 - \frac{1}{\gamma^2}} [\cos(\omega_{ce}t - \delta) - \cos \delta] + l_{fd} \tan \delta \\ z(t) &= \frac{c}{\omega_{ce}} \sqrt{1 - \frac{1}{\gamma^2}} [\sin(\omega_{ce}t + \delta) + \sin \delta] \end{aligned}$$

In a next step, the electron path deviation H inside the magnet, measured normal to a reference trajectory of an infinitely energetic electron with $\delta = 0$ must be determined as a function of γ . Therefore, the time t_{sp} is found, which an electron takes to travel a distance of length l_{sp} in z :

$$z(t_{sp}) = l_{sp}$$

$$\Rightarrow t_{sp} = \frac{1}{\omega_{ce}} \left[\arcsin \left(\frac{\omega_{ce}}{c} \frac{l_{sp}}{\sqrt{1 - \frac{1}{\gamma^2}}} - \sin \delta \right) - \delta \right]$$

$$\Rightarrow H(\gamma) = y(t_{sp}) = \frac{c}{\omega_{ce}} \sqrt{1 - \frac{1}{\gamma^2}} \left[\cos \left(\arcsin \left[\frac{\omega_{ce}}{c} \frac{l_{sp}}{\sqrt{1 - \frac{1}{\gamma^2}}} - \sin \delta \right] - 2\delta \right) - \cos \delta \right] + l_{fd} \tan \delta$$

This completes the description of the electron trajectory inside the spectrometer magnet. In the end, an expression is sought to be composed, which describes the deviation D as measured on a screen tilted by an angle α around a pivot point located at distance l_{inf} behind the spectrometer exit plane. First, the equivalent of path deviation $H(\gamma)$ behind the magnet is written as:

$$D'(\gamma) = \left. \frac{\partial H(\gamma)}{\partial l_{sp}} \right|_{l_{dm}} l_z(\gamma) + H(\gamma)|_{l_{dm}}$$

In this equation l_z denotes the distance from the electron position to the spectrometer exit plane. D' must intersect with the detection screen given through:

$$D'' = \frac{1}{\tan \alpha} [l_{\text{inf}} - l_z(\gamma)]$$

By demanding $D' = D''$, the cut set yields:

$$l_z(\gamma) = \frac{l_{\text{inf}} - \tan(\alpha) H(\gamma)|_{l_{\text{dm}}}}{1 + \tan(\alpha) \left. \frac{\partial H(\gamma)}{\partial l_{\text{sp}}} \right|_{l_{\text{dm}}}}$$

Finally this results in the desired function:

$$D(\gamma) = \frac{D'(\gamma)}{\cos \alpha} = \frac{1}{\cos \alpha} \left[l_z(\gamma) \left. \frac{\partial H(\gamma)}{\partial l_{\text{sp}}} \right|_{l_{\text{dm}}} + H(\gamma)|_{l_{\text{dm}}} \right]$$

Appendix B

Electron-beam scattering off plasma particles and gas molecules

The scattering probabilities for electrons contained in an ultra-relativistic bunch with plasma particles and gas molecules while traveling through a capillary and an evacuated target chamber is of interest for evaluating the significance of their contribution towards the measured electron beam divergences. An analysis of this issue can be simplified by separating the problem into two scenarios. The first case: an electron scattering event occurs inside plasma during the acceleration phase or after the laser pulse has deteriorated and is not sufficiently intense anymore to drive a wakefield, but still retains enough energy flux density to ionize the gas completely. The second case: an electron scattering event occurs inside the vacuum chamber with a residual background gas atom. These possibilities will be investigated in the following.

In general, the probability \mathfrak{W} of detecting a scattered particle within an infinitesimal range of deflection angles $d\Theta$ can be written as:

$$\mathfrak{W}(d\Theta) = \frac{dN(d\Theta)}{N}$$

Here dN describes the differential number of scattered particles as a function of $d\Theta$ from a set of N initially incident particles. In the following derivation, it must be ensured that the probability for scattering to happen is small such that a single particle does not experience multiple-scattering events. Then, it is valid to define:

$$\begin{aligned} dN &= Na_s d\sigma \\ &= Na_s \frac{d\sigma}{d\Omega} \frac{d\Omega}{d\Theta} d\Theta \end{aligned}$$

The differential cross-section $d\sigma(d\Omega)^{-1}$ depends on the type of scattering event. It describes the probability to detect a scattered particle per solid angle Ω . This angle is related to the deflection angle Θ by $\Omega = 2\pi(1 - \cos\Theta)$. Moreover, the scatter-center area density a_s may be expressed as the product of scatter-center volume density n_s and propagation distance l_s

through the medium. Therefore, \mathfrak{W} can be rewritten:

$$\mathfrak{W} = n_s l_s \frac{d\sigma}{d\Omega} \frac{d\Omega}{d\Theta} d\Theta$$

Hence, the integrated probability $\mathfrak{W}_{\text{out}}$ of finding a scattered particle outside a cone of opening angle Θ_{min} is:

$$\mathfrak{W}_{\text{out}}(\Theta_{\text{min}}) = \int_{\Theta_{\text{min}}}^{2\pi} n_s l_s \frac{d\sigma}{d\Omega} \frac{d\Omega}{d\Theta} d\Theta \quad (\text{B.1})$$

The type of scattering reaction defines the differential cross-section to use. While propagating through plasma inside the gas cell, the relativistic electrons potentially scatter off free electrons (Møller-scattering) or ionized hydrogen cores (Mott-scattering). For Mott-scattering the differential cross-section is given by (e.g. MUSIOL et al. [1988]):

$$\left. \frac{d\sigma}{d\Omega} \right|_{\text{Mott}} = \left. \frac{d\sigma}{d\Omega} \right|_{\text{Rutherford}} \left(1 - \beta^2 \sin^2 \frac{\Theta}{2} \right) = \frac{(Ze^2)^2}{(4\pi\epsilon_0)^2 4E_{\text{tot}}^2 \sin^4 \frac{\Theta}{2}} \cdot \left(1 - \beta^2 \sin^2 \frac{\Theta}{2} \right) \quad (\text{B.2})$$

Mott-scattering comprises the effects of Rutherford-scattering (see e.g. MESCHEDE [2006]) and delivers similar results for small deflection angles Θ . In addition the differential Mott cross-section contains a factor that describes magnetic spin interaction, which becomes important for relativistic electrons ($\beta \rightarrow 1$) and large scattering angles.

The differential cross-section for Møller-scattering can be expressed as [MUSIOL et al. 1988]:

$$\left. \frac{d\sigma}{d\Omega} \right|_{\text{Møller}} = \left(\frac{r_e}{2} \right)^2 \left(\frac{m_e c}{|\vec{p}_{\text{cms}}|} \right)^2 \frac{(3 + \cos^2 \Theta)^2}{\sin^4 \Theta} \quad (\text{B.3})$$

with the classical electron radius:

$$r_e = \frac{1}{4\pi\epsilon_0} \frac{e^2}{m_e c^2} \approx 2.818 \cdot 10^{-15} \text{ m}$$

Here, the electron momentum \vec{p}_{cms} is defined in a center of mass coordinate system and in good approximation can be written as $|\vec{p}_{\text{cms}}| \approx \gamma\beta m_e c$, since the momenta of the interacting species (ultra-relativistic electrons and plasma electrons) differ by orders of magnitude.

Under typical conditions, e.g. for a steady-state-flow gas cell experiment (confer chapter V) with $Z = 1$, $\beta \approx 1$ and $\gamma = 400$, equations (B.2) and (B.3) yield differential cross-sections that may be used to integrate expression (B.1). From the analysis of figure 5.3.2 it is known that the electron acceleration process inside the gas cell happens over a distance of $d \approx 4$ mm in an initially electron-free cavity or bubble. During this phase only electron-ion scattering needs to be taken into account. In addition, there remains a residual propagation distance of a maximum of ~ 10 mm through quasi-neutral hydrogen plasma at a density of $n_s = n_e = n_{\text{H}^+} \approx 5 \cdot 10^{18} \text{ cm}^{-3}$. Along this path, the hydrogen atoms within the capillary can be expected to be fully ionized, since the utilized laser pulse is intense enough that even when filling the complete channel diameter of $\sim 250 \mu\text{m}$, its electric fields are still more than two orders of magnitude above the

BSI-ionization threshold for hydrogen (confer to table 1.2.1).

The lower resolution limit of the CAWO OG 16 phosphorescence screen¹ at position S1 fixes Θ_{\min} to 100 μrad . As a result the probability to detect an electron outside a cone with a scattering angle of Θ_{\min} is $\mathfrak{W}_{\text{out,Mott}}(100 \mu\text{rad}) \approx 4.3 \cdot 10^{-3}$ for Mott-scattering (with $l_s = 14 \text{ mm}$). The same parameter set determines the chance to observe significant contributions from Møller-scattering to be $\mathfrak{W}_{\text{out,Møller}}(100 \mu\text{rad}) \approx 3.1 \cdot 10^{-3}$ (with $l_s = 10 \text{ mm}$). Hence, the total intra-gas-cell scattering probability amounts to $\sim 7.4 \cdot 10^{-3}$, meaning that only about 0.7% of the accelerated particles undergo a noticeable trajectory deviation due to the discussed effects.

Additionally, there exists a finite probability for each particle out of the ensemble of relativistic electrons to scatter off a residual hydrogen molecule along its path through the vacuum chamber. This has been investigated using the GEANT 4 toolkit², which can simulate the passage of relativistic particles through matter. All electrons were initialized to propagate as a perfectly monoenergetic ($\gamma = 400$) and pencil-like beam over a distance of $l_s = 2 \text{ m}$ through a gaseous hydrogen medium of 10^{-2} mbar pressure. This leads to an upper estimate of the scattering probability, since the real pressure distribution inside the vacuum chamber drops monotonically along l_s from 10^{-2} mbar measured close to the gas cell to $\sim 10^{-4} \text{ mbar}$ behind the electron spectrometer. The obtained simulation results suggest that just one in about 10^6 particles produces a detectable scattering event.

In general, it may be stated that the divergences, which are presented in this work, do not originate from particle scattering events, but rather must be attributed to the transverse electron trapping mechanism, to collective electron dynamics inside the wakefield and to a lesser degree to intra-bunch Coulomb repulsion. The latter is known from extensive space-charge studies with the particle tracking tool GPT [BECKER 2007].

¹See http://www.cawo.com/pages/framesets/fs_po_so.htm on the world wide web.

²See <http://geant4.web.cern.ch/geant4/> on the world wide web.

Appendix C

List of fundamental constants

The natural constants used throughout this work are listed in the following according to their order of appearance in the document. All values below are given in SI-units, which is also true for every other variable and quantity specified in this thesis, unless stated otherwise.

c	$2.998 \cdot 10^8 \text{ m/s}$	Speed of light in vacuum
ϵ_0	$8.854 \cdot 10^{-12} \text{ As/(Vm)}$	Electric permittivity of free space
μ_0	$1.257 \cdot 10^{-7} \text{ Vs/(Am)}$	Magnetic permeability of free space
\hbar	$1.055 \cdot 10^{-34} \text{ Js}$	Reduced Planck constant
e	$1.602 \cdot 10^{-19} \text{ As}$	Absolute charge of an electron
m_e	$9.109 \cdot 10^{-31} \text{ kg}$	Electron rest mass
α	$7.297 \cdot 10^{-3}$	Fine-structure constant
k_B	$1.381 \cdot 10^{-23} \text{ J/K}$	Boltzmann constant

References

- ABRAMYAN, L. A., A. G. LITVAK, V. A. MIRONOV, A. M. SERGEEV, and F. J. CROWNE. Self-focusing and relativistic waveguiding of an ultrashort laser pulse in a plasma. *Soviet Physics, Journal of Experimental and Theoretical Physics* **75** (6), 978–982 [1992]
- ACHENBACH, J. The god particle. *National Geographic* **3** [2008]
- ADAMS, D. *The hitchhiker's guide to the galaxy*. Pan Books, London [1979]
- AGOSTINI, P., G. BARJOT, J. BONNAL, G. MAINFRAY, C. MANUS, and J. MORELLEC. Multiphoton ionization of hydrogen and rare gases. *IEEE Journal of Quantum Electronics* **4** (10), 667–669 [1968]
- AKHIEZER, A. I. and R. V. POLOVIN. Theory of wave motion of an electron plasma. *Soviet Physics, Journal of Experimental and Theoretical Physics* **3** (5), 696–705 [1956]
- AKTURK, S., M. KIMMEL, P. O'SHEA, and R. TREBINO. Measuring pulse-front tilt in ultrashort pulses using GRENOUILLE. *Optics Express* **11** (5), 491–501 [2003]
- AKTURK, S., X. GU, E. ZEEK, and R. TREBINO. Pulse-front tilt caused by spatial and temporal chirp. *Optics Express* **12** (19), 4399–4410 [2004]
- AMMOISOV, M. V., N. B. DELONE, and V. P. KRAINOV. Tunnel ionization of complex atoms and of atomic ions in an alternating electromagnetic field. *Soviet Physics, Journal of Experimental and Theoretical Physics* **64** (6), 1191–1194 [1986]
- ANGELOVA, G., V. ZIEMANN, A. MESECK, P. SALÉN, P. VAN DER MEULEN, M. HAMBERG, M. LARSSON, J. BÖDEWADT, S. KHAN, A. WINTER, H. SCHLARB, F. LÖHL, E. SALDIN, E. SCHNEIDMILLER, and M. YURKOV. Results from the optical replica experiment in FLASH. *Proceedings of the European Particle Accelerator Conference* pages 1332–1334 [2008]
- ANTONSEN, T. M. and P. MORA. Self-focusing and Raman scattering of laser pulses in tenuous plasmas. *Physical Review Letters* **69** (15), 2204–2207 [1992]
- ATTWOOD, D. *Soft X-rays and extreme ultraviolet radiation: principles and applications*. Cambridge University Press, London [2007]

- AUGST, S., D. STRICKLAND, D. D. MEYERHOFER, S. L. CHIN, and J. H. EBERLY. Tunneling ionization of noble gases in a high-intensity laser field. *Physical Review Letters* **63** (20), 2212–2215 [1989]
- AUGUSTE, T., P. MONOT, L. A. LOMPRES, G. MAINFRAY, and C. MANUS. Multiply charged ions produced in noble gases by a 1 ps laser pulse at $\lambda = 1053$ nm. *Journal of Physics B* **25** (20), 4181–4194 [1992]
- BARDSLEY, J. N., B. M. PENETRANTE, and M. H. MITTLEMAN. Relativistic dynamics of electrons in intense laser fields. *Physical Review A* **40** (7), 3823–3835 [1989]
- BARNES, D. C., T. KURKI-SUONIO, and T. TAJIMA. Laser self-trapping for the plasma fiber accelerator. *IEEE Transactions on Plasma Science* **15** (2), 154–160 [1987]
- BAUER, D., P. MULSER, and W.-H. STEEB. Relativistic ponderomotive force, uphill acceleration, and transition to chaos. *Physical Review Letters* **75** (25), 4622–4625 [1995]
- BECKER, S. Private communication [2007]
- BEREZHIANI, V. I. and I. G. MURUSIDZE. Relativistic wake-field generation by an intense laser pulse in a plasma. *Physics Letters A* **148** (6–7), 338–340 [1990]
- BIRDSALL, C. K. and A. B. LANGDON. *Plasma physics via computer simulation*. Adam Hilger, New York [1991]
- BLOEMBERGEN, N., W.K. BURNS, and M. MATSUOKA. Reflected third harmonic generated by picosecond laser pulses. *Optics Communications* **1** (4), 195–198 [1969]
- BOBROVA, N. A., A. A. ESAULOV, J.-I. SAKAI, P. V. SASOROV, D. J. SPENCE, A. BUTLER, S. M. HOOKER, and S. V. BULANOV. Simulations of a hydrogen-filled capillary discharge waveguide. *Physical Review E* **65** (1), 016407 [2001]
- BOHM, D. and E. P. GROSS. Theory of plasma oscillations. A. Origin of medium-like behavior. *Physical Review* **75** (12), 1851–1864 [1949]
- BONIFACIO, R., C. PELLEGRINI, and L. M. NARDUCCI. Collective instabilities and high-gain regime in a free electron laser. *Optics Communications* **50** (6), 373–378 [1984]
- BONSE, U. and M. HART. An X-ray interferometer. *Applied Physics Letters* **6** (8), 155–156 [1965]
- BORGHESI, M., A. J. MACKINNON, L. BARRINGER, R. GAILLARD, L. A. GIZZI, C. MEYER, O. WILLI, A. PUKHOV, and J. MEYER-TER-VEHN. Relativistic channeling of a picosecond laser pulse in a near-critical preformed plasma. *Physical Review Letters* **78** (5), 879–882 [1997]
- BOYD, R. W. *Nonlinear optics*. Academic Press, San Diego, 2nd edition [2003]

- BRABEC, T. and F. KRAUSZ. Intense few-cycle laser fields: frontiers of nonlinear optics. *Reviews of Modern Physics* **72** (2), 545–591 [2000]
- BRANDI, H. S., C. MANUS, G. MAINFRAY, and T. LEHNER. Relativistic self-focusing of ultraintense laser pulses in inhomogeneous underdense plasmas. *Physical Review E* **47** (5), 3780–3783 [1993]
- BRANTOV, A. V., T. ZH. ESIRKEPOV, M. KANDO, H. KOTAKI, V. YU. BYCHENKOV, and S. V. BULANOV. Controlled electron injection into the wake wave using plasma density inhomogeneity. *Physics of Plasmas* **15** (7), 073111 [2008]
- BRILLOUIN, L. La mécanique ondulatoire de Schrödinger: une méthode générale de résolution par approximations successives. *Comptes rendus de l'Académie des sciences* **183**, 24–26 [1926]
- BROKS, B. H. P., K. GARLOFF, and J. J. A. M. VAN DER MULLEN. Nonlocal-thermal-equilibrium model of a pulsed capillary discharge waveguide. *Physical Review E* **71** (1), 016401 [2005]
- BROKS, B. H. P., W. VAN DIJK, J. J. A. M. VAN DER MULLEN, A. J. GONSALVES, T. P. ROWLANDS-REES, and S. M. HOOKER. Modeling of a square pulsed capillary discharge waveguide for interferometry measurements. *Physics of Plasmas* **14** (2), 023501 [2007]
- BRONŠTEIN, I. N., K. A. SEMENDJAJEW, G. MUSIOL, and H. MÜHLIG. *Taschenbuch der Mathematik*. Verlag Harri Deutsch, Frankfurt am Main, 4th edition [1999]
- BULANOV, S., N. NAUMOVA, F. PEGORARO, and J. SAKAI. Particle injection into the wave acceleration phase due to nonlinear wake wave breaking. *Physical Review E* **58** (5), R5257–R5260 [1998]
- BULANOV, S. V., V. I. KIRSANOV, and A. S. SAKHAROV. Excitation of ultra-relativistic Langmuir waves by electromagnetic pulses. *Physica Scripta* **T30**, 208–209 [1990]
- BULANOV, S. V., V. I. KIRSANOV, and A. S. SAKHAROV. Limiting electric field of the wakefield plasma wave. *Soviet Physics, Journal of Experimental and Theoretical Physics Letters* **53** (11), 565–569 [1991]
- BULANOV, S. V., I. N. INOVENKOV, V. I. KIRSANOV, N. M. NAUMOVA, and A. S. SAKHAROV. Nonlinear depletion of ultrashort and relativistically strong laser pulses in an underdense plasma. *Physics of Fluids B: Plasma Physics* **4** (7), 1935–1942 [1992]
- BULANOV, S. V., F. PEGORARO, and A. M. PUKHOV. Two-dimensional regimes of self-focusing, wake field generation, and induced focusing of a short intense laser pulse in an underdense plasma. *Physical Review Letters* **74** (5), 710–713 [1995]

- BULANOV, S. V., F. PEGORARO, A. M. PUKHOV, and A. S. SAKHAROV. Transverse-wake wave breaking. *Physical Review Letters* **78** (22), 4205–4208 [1997]
- CAVALIERI, A. L., N. MÜLLER, T. UPHUES, V. S. YAKOVLEV, A. BALTŮSKA, B. HORVATH, B. SCHMIDT, L. BLÜMEL, R. HOLZWARTH, S. HENDEL, M. DRESCHER, U. KLEINEBERG, P. M. ECHENIQUE, R. KIENBERGER, F. KRAUSZ, and U. HEINZMANN. Attosecond spectroscopy in condensed matter. *Nature* **449**, 1029–1032 [2007]
- CHAPMAN, H. N., A. BARTY, M. J. BOGAN, S. BOUTET, M. FRANK, S. P. HAU-RIEGE, S. MARCHESINI, B. W. WOODS, S. BAJT, W. H. BENNER, R. A. LONDON, E. PLÖNJES, M. KUHLMANN, R. TREUSCH, S. DÜSTERER, T. TSCHENTSCHER, J. R. SCHNEIDER, E. SPILLER, T. MÖLLER, C. BOSTEDT, M. HOENER, D. A. SHAPIRO, K. O. HODGSON, D. VAN DER SPOEL, F. BURMEISTER, M. BERGH, C. CALEMAN, G. HULDT, M. M. SEIBERT, F. R. N. C. MAIA, R. W. LEE, A. SZÖKE, N. TIMNEANU, and J. HAJDU. Femtosecond diffractive imaging with a soft-x-ray free-electron laser. *Nature Physics* **2**, 839–843 [2006]
- CHEN, F. F. *Introduction to plasma physics and controlled fusion*. Plenum Press, New York, 2nd edition [1984]
- CHEN, P., J. M. DAWSON, R. W. HUFF, and T. KATSOULEAS. Acceleration of electrons by the interaction of a bunched electron beam with a plasma. *Physical Review Letters* **54** (7), 693–696 [1985]
- CHERIAUX, G., P. ROUSSEAU, F. SALIN, J. P. CHAMBARET, B. WALKER, and L. F. DIMAURO. Aberration-free stretcher design for ultrashort-pulse amplification. *Optics Letters* **21** (6), 414–416 [1996]
- CHERNIKOV, A. A., G. SCHMIDT, and A. I. NEISHTADT. Unlimited particle acceleration by waves in a magnetic field. *Physical Review Letters* **68** (10), 1507–1510 [1992]
- CHIOU, T. C., T. KATSOULEAS, C. DECKER, W. B. MORI, J. S. WURTELE, G. SHVETS, and J. J. SU. Laser wake-field acceleration and optical guiding in a hollow plasma channel. *Physics of Plasmas* **2** (1), 310–318 [1995]
- CLAYTON, C. E., K. A. MARSH, A. DYSON, M. EVERETT, A. LAL, W. P. LEEMANS, R. WILLIAMS, and C. JOSHI. Ultrahigh-gradient acceleration of injected electrons by laser-excited relativistic electron plasma waves. *Physical Review Letters* **70** (1), 37–40 [1993]
- COFFEY, T. P. Breaking of large amplitude plasma oscillations. *Physics of Fluids* **14** (7), 1402–1406 [1971]
- COURANT, R., K. FRIEDRICHS, and H. LEWY. Über die partiellen Differenzgleichungen der mathematischen Physik. *Mathematische Annalen* **100** (1), 32–74 [1928]

- DAIDO, H. Review of soft x-ray laser researches and developments. *Reports on Progress in Physics* **65** (10), 1513–1576 [2002]
- DALLA, S. and M. LONTANO. On the maximum longitudinal electric field of a large amplitude electron plasma wave excited by a short electromagnetic radiation pulse. *Physics Letters A* **173** (6), 456–461 [1993]
- DAWSON, J. and C. OBERMAN. High-frequency conductivity and the emission and absorption coefficients of a fully ionized plasma. *Physics of Fluids* **5** (5), 517–524 [1962]
- DAWSON, J. M. Particle simulation of plasmas. *Reviews of Modern Physics* **55** (2), 403–447 [1983]
- DE LOOS, M. J., S. B. VAN DER GEER, Y. M. SAVELIEV, V. M. PAVLOV, A. J. W. REITSMA, S. M. WIGGINS, J. RODIER, T. GARVEY, and D. A. JAROSZYNSKI. Radial bunch compression: path-length compensation in an rf photoinjector with a curved cathode. *Physical Review Special Topics – Accelerators and Beams* **9** (8), 084201 [2006]
- DECKER, C. D. and W. B. MORI. Group velocity of large amplitude electromagnetic waves in a plasma. *Physical Review Letters* **72** (4), 490–493 [1994]
- DECOSTER, A. Nonlinear travelling waves in a homogeneous cold collisionless plasma. *Physics Reports* **47** (5), 285–422 [1978]
- DECYK, V. K. Skeleton PIC codes for parallel computers. *Computer Physics Communications* **87** (1–2), 87–94 [1995]
- DELONE, N. B. and V. P. KRAINOV. *Multiphoton processes in atoms*. Springer Verlag, Heidelberg, 2nd edition [1994]
- DELSIM-HASHEMI, H. *Infrared single shot diagnostics for the longitudinal profile of the electron bunches at FLASH*. Dissertation, Universität Hamburg [2008]
- DIRAC, P. A. M. The quantum theory of the emission and absorption of radiation. *Proceedings of the Royal Society of London. Series A, Containing Papers of a Mathematical and Physical Character* **114** (767), 243–265 [1927]
- DITMIRE, T., J. ZWEIBACK, V. P. YANOVSKY, T. E. COWAN, G. HAYS, and K. B. WHARTON. Nuclear fusion from explosions of femtosecond laser-heated deuterium clusters. *Nature* **398**, 489–492 [1999]
- DORCHIES, F., J. R. MARQUÈS, B. CROS, G. MATTHIEUSSENT, T. VÉLIKOROUSOV, C. COURTOIS, P. AUDEBERT, J. P. GEINDRE, S. REBIBO, G. HAMONIAUX, and F. AMIRANOFF. Monomode guiding of 10^{16} W·cm² laser pulses over 100 Rayleigh lengths in hollow capillary dielectric tubes. *Physical Review Letters* **82** (23), 4655–4658 [1999]

- DRESCHER, M., M. HENTSCHEL, R. KIENBERGER, G. TEMPEA, C. SPIELMANN, G. A. REIDER, P. B. CORKUM, and F. KRAUSZ. X-ray pulses approaching the attosecond frontier. *Science* **291** (5510), 1923–1927 [2001]
- DROMEY, B., M. ZEPF, A. GOPAL, K. LANCASTER, M. S. WEI, K. KRUSHELNICK, M. TATARAKIS, N. VAKAKIS, S. MOUSTAIZIS, R. KODAMA, M. TAMPO, C. STOECKL, R. CLARKE, H. HABARA, D. NEELY, S. KARSCH, and P. NORREYS. High harmonic generation in the relativistic limit. *Nature Physics* **2**, 456–459 [2006]
- DURFEE III, C. G. and H. M. MILCHBERG. Light pipe for high intensity laser pulses. *Physical Review Letters* **71** (15), 2409–2412 [1993]
- DURFEE III, C. G., J. LYNCH, and H. M. MILCHBERG. Mode properties of a plasma waveguide for intense laser pulses. *Optics Letters* **19** (23), 1937–1939 [1994]
- EICKHOFF, H., R. BÄR, A. DOLINSKII, TH. HABERER, B. SCHLITT, P. SPILLER, U. WEINRICH, and THE GSI THERAPY PROJECT GROUP. HICAT – the German hospital-based light ion cancer therapy project. *Proceedings of the Particle Accelerator Conference* pages 694–698 [2003]
- EINSTEIN, A. Ist die Trägheit eines Körpers von seinem Energieinhalt abhängig? *Annalen der Physik* **323** (13), 639–641 [1905a]
- EINSTEIN, A. Über einen die Erzeugung und Verwandlung des Lichtes betreffenden heuristischen Gesichtspunkt. *Annalen der Physik* **322** (6), 132–148 [1905b]
- EINSTEIN, A. Über die Entwicklung unserer Anschauungen über das Wesen und die Konstitution der Strahlung. *Physikalische Zeitschrift* **10** (22), 817–825 [1909]
- EINSTEIN, A. Über den Einfluß der Schwerkraft auf die Ausbreitung des Lichtes. *Annalen der Physik* **340** (10), 898–908 [1911]
- EINSTEIN, A. Die Feldgleichungen der Gravitation. *Sitzungsberichte der Königlich Preussischen Akademie der Wissenschaften* pages 844–847 [1915]
- ESAREY, E., J. KRALL, and P. SPRANGLE. Envelope analysis of intense laser pulse self-modulation in plasmas. *Physical Review Letters* **72** (18), 2887–2890 [1994]
- ESAREY, ERIC, PHILLIP SPRANGLE, and JONATHAN KRALL. Laser acceleration of electrons in vacuum. *Physical Review E* **52** (5), 5443–5453 [1995]
- ESAREY, E. and M. PILLOFF. Trapping and acceleration in nonlinear plasma waves. *Physics of Plasmas* **2** (5), 1432–1436 [1995]
- ESAREY, E., P. SPRANGLE, J. KRALL, and A. TING. Overview of plasma-based accelerator concepts. *IEEE Transactions on Plasma Science* **24** (2), 252–288 [1996]

- ESAREY, E., R. F. HUBBARD, W. P. LEEMANS, A. TING, and P. SPRANGLE. Electron injection into plasma wakefields by colliding laser pulses. *Physical Review Letters* **79** (14), 2682–2685 [1997a]
- ESAREY, E., P. SPRANGLE, J. KRALL, and A. TING. Self-focusing and guiding of short laser pulses in ionizing gases and plasmas. *IEEE Journal of Quantum Electronics* **33** (11), 1879–1914 [1997b]
- ESAREY, E., C. B. SCHROEDER, W. P. LEEMANS, and B. HAFIZI. Laser-induced electron trapping in plasma-based accelerators. *Physics of Plasmas* **6** (5), 2262–2268 [1999]
- ESAREY, E., B. A. SHADWICK, P. CATRAVAS, and W. P. LEEMANS. Synchrotron radiation from electron beams in plasma-focusing channels. *Physical Review E* **65** (5), 056505 [2002]
- ESIRKEPOV, T., S. V. BULANOV, M. YAMAGIWA, and T. TAJIMA. Electron, positron, and photon wakefield acceleration: trapping, wake overtaking, and ponderomotive acceleration. *Physical Review Letters* **96** (1), 014803 [2006]
- EULER, H. and B. KOCKEL. Über die Streuung von Licht an Licht nach der Diracschen Theorie. *Naturwissenschaften* **23** (15), 246–247 [1935]
- FAURE, J., Y. GLINEC, A. PUKHOV, S. KISELEV, S. GORDIENKO, E. LEFEBVRE, J. P. ROUSSEAU, F. BURG, and V. MALKA. A laser-plasma accelerator producing monoenergetic electron beams. *Nature* **431** (7008), 541–544 [2004]
- FAURE, J., Y. GLINEC, J. J. SANTOS, F. EWALD, J.-P. ROUSSEAU, S. KISELEV, A. PUKHOV, T. HOSOKAI, and V. MALKA. Observation of laser-pulse shortening in nonlinear plasma waves. *Physical Review Letters* **95** (20), 205003 [2005]
- FAURE, J., C. RECHATIN, A. NORLIN, A. LIFSCHITZ, Y. GLINEC, and V. MALKA. Controlled injection and acceleration of electrons in plasma wakefields by colliding laser pulses. *Nature* **444** (7120), 737–739 [2006]
- FERMI, E. *Nuclear physics*. University of Chicago Press [1950]
- FITZPATRICK, R. *Introduction to plasma physics: a graduate level course*. Lecture notes, The University of Texas at Austin [2006]
- FORSLUND, D. W., J. M. KINDEL, W. B. MORI, C. JOSHI, and J. M. DAWSON. Two-dimensional simulations of single-frequency and beat-wave laser-plasma heating. *Physical Review Letters* **54** (6), 558–561 [1985]
- FRITZLER, S., E. LEFEBVRE, V. MALKA, F. BURG, A. E. DANGOR, K. KRUSHELNICK, S. P. D. MANGLES, Z. NAJMUDIN, J.-P. ROUSSEAU, and B. WALTON. Emittance measurements of a laser-wakefield-accelerated electron beam. *Physical Review Letters* **92** (16), 165006 [2004]

- FUBIANI, G., E. ESAREY, C. B. SCHROEDER, and W. P. LEEMANS. Beat wave injection of electrons into plasma waves using two interfering laser pulses. *Physical Review E* **70** (1), 016402 [2004]
- FUCHS, M., R. WEINGARTNER, A. POPP, ZS. MAJOR, S. BECKER, J. OSTERHOFF, R. HÖRLEIN, G. D. TSAKIRIS, U. SCHRAMM, T. P. ROWLANDS-REES, S. M. HOOKER, D. HABS, F. KRAUSZ, S. KARSCH, and F. GRÜNER. Table-top laser-driven ultrafast undulator radiation in the soft X-ray range. In preparation for *Nature* [2009]
- FUJI, T., J. RAUSCHENBERGER, A. APOLONSKI, V. S. YAKOVLEV, G. TEMPEA, T. UDEM, C. GOHLE, T. W. HÄNSCH, W. LEHNERT, M. SCHERER, and F. KRAUSZ. Monolithic carrier-envelope phase-stabilization scheme. *Optics Letters* **30** (3), 332–334 [2005]
- GEDDES, C. G. R., C. TÓTH, J. VAN TILBORG, E. ESAREY, C. B. SCHROEDER, D. BRUH-WILER, C. NIETER, J. CARY, and W. P. LEEMANS. High-quality electron beams from a laser wakefield accelerator using plasma-channel guiding. *Nature* **431** (7008), 538–541 [2004]
- GEDDES, C. G. R., K. NAKAMURA, G. R. PLATEAU, C. TÓTH, E. CORMIER-MICHEL, E. ESAREY, C. B. SCHROEDER, J. R. CARY, and W. P. LEEMANS. Plasma-density-gradient injection of low absolute-momentum-spread electron bunches. *Physical Review Letters* **100** (21), 215004 [2008]
- GEISSLER, M., J. SCHREIBER, and J. MEYER-TER VEHN. Bubble acceleration of electrons with few-cycle laser pulses. *New Journal of Physics* **8**, 186 [2006]
- GIBBON, P. *Short pulse laser interactions with matter*. Imperial College Press, London [2005]
- GINZBURG, V. L. Radiation by uniformly moving sources (Vavilov-Cherenkov effect, transition radiation, and other phenomena). *Physics-Uspekhi* **39** (10), 973–982 [1996]
- GLINEC, Y., J. FAURE, A. GUENIE-TAFO, V. MALKA, H. MONARD, J. P. LARBRE, V. DE WAELE, J. L. MARIGNIER, and M. MOSTAFAVI. Absolute calibration for a broad range single shot electron spectrometer. *Review of Scientific Instruments* **77** (10), 103301 [2006]
- GLINEC, Y., J. FAURE, A. LIFSCHITZ, J. M. VIEIRA, R. A. FONSECA, L. O. SILVA, and V. MALKA. Direct observation of betatron oscillations in a laser-plasma electron accelerator. *Europhysics Letters* **81** (6), 64001 [2008]
- GOLDSTON, R. J. and P. H. RUTHERFORD. *Plasmaphysik - Eine Einführung*. Vieweg Verlag, Wiesbaden [1998]
- GONSALVES, A. J., T. P. ROWLANDS-REES, B. H. P. BROKS, J. J. A. M. VAN DER MULLEN, and S. M. HOOKER. Transverse interferometry of a hydrogen-filled capillary discharge waveguide. *Physical Review Letters* **98** (2), 025002 [2007]

- GORBUNOV, L. M. and V. I. KIRSANOV. Excitation of plasma waves by an electromagnetic wave packet. *Soviet Physics, Journal of Experimental and Theoretical Physics* **66**, 290–294 [1987]
- GORDIENKO, S. and A. PUKHOV. Scalings for ultrarelativistic laser plasmas and quasimonoenergetic electrons. *Physics of Plasmas* **12** (4), 043109 [2005]
- GORDON, D., K. C. TZENG, C. E. CLAYTON, A. E. DANGOR, V. MALKA, K. A. MARSH, A. MODENA, W. B. MORI, P. MUGGLI, Z. NAJMUDIN, D. NEELY, C. DANSON, and C. JOSHI. Observation of electron energies beyond the linear dephasing limit from a laser-excited relativistic plasma wave. *Physical Review Letters* **80** (10), 2133–2136 [1998]
- GRÜNER, F., S. BECKER, U. SCHRAMM, T. EICHNER, M. FUCHS, R. WEINGARTNER, D. HABS, J. MEYER-TER VEHN, M. GEISSLER, M. FERRARIO, L. SERAFINI, B. VAN DER GEER, H. BACKE, W. LAUTH, and S. REICHE. Design considerations for table-top, laser-based VUV and x-ray free electron lasers. *Applied Physics B: Lasers and Optics* **86** (3), 431–435 [2007]
- GU, X., S. AKTURK, and R. TREBINO. Spatial chirp in ultrafast optics. *Optics Communications* **242** (4–6), 599–604 [2004]
- HAFZ, N., M. S. HUR, G. H. KIM, C. KIM, I. S. KO, and H. SUK. Quasimonoenergetic electron beam generation by using a pinholelike collimator in a self-modulated laser wakefield acceleration. *Physical Review E* **73** (1), 016405 [2006]
- HAFZ, N. A. M., T. M. JEONG, I. W. CHOI, S. K. LEE, K. H. PAE, V. V. KULAGIN, J. H. SUNG, T. J. YU, K.-H. HONG, T. HOSOKAI, J. R. CARY, D.-K. KO, and J. LEE. Stable generation of GeV-class electron beams from self-guided laser-plasma channels. *Nature Photonics* **2**, 571–577 [2008]
- HARTMANN, J. Bemerkungen über den Bau und die Justierung von Spektrographen. *Zeitschrift für Instrumentenkunde* **20**, 47–58 [1900]
- HEMKER, R. G., N. M. HAFZ, and M. UESAKA. Computer simulations of a single-laser double-gas-jet wakefield accelerator concept. *Physical Review Special Topics – Accelerators and Beams* **5** (4), 041301 [2002]
- HENDERSON, R. The potential and limitations of neutrons, electrons and x-rays for atomic resolution microscopy of unstained biological molecules. *Quarterly Reviews of Biophysics* **28** (2), 171–193 [1995]
- HENIG, A., D. KIEFER, M. GEISSLER, S. G. RYKOVANOV, R. RAMIS, R. HÖRLEIN, J. OSTERHOFF, ZS. MAJOR, S. KARSCH, F. KRAUSZ, D. HABS, and J. SCHREIBER. Laser-driven shock acceleration of ion beams from spherical mass-limited targets. *Physical Review Letters*, accepted for publication [2009]

- HENTSCHEL, M., R. KIENBERGER, CH. SPIELMANN, G. A. REIDER, N. MILOSEVIC, T. BRABEC, P. CORKUM, U. HEINZMANN, M. DRESCHER, and F. KRAUSZ. Attosecond metrology. *Nature* **414**, 509–513 [2001]
- HERRMANN, J. Theory of Kerr-lens mode locking: role of self-focusing and radially varying gain. *Journal of the Optical Society of America B: Optical Physics* **11** (3), 498–512 [1994]
- HIDDING, B., K.-U. AMTHOR, B. LIESFELD, H. SCHWOERER, S. KARSCH, M. GEISSLER, L. VEISZ, K. SCHMID, J. G. GALLACHER, S. P. JAMISON, D. JAROSZYNSKI, G. PRETZLER, and R. SAUERBREY. Generation of quasimonoenergetic electron bunches with 80-fs laser pulses. *Physical Review Letters* **96** (10), 105004 [2006]
- HOCKNEY, R. W. and J. W. EASTWOOD. *Computer simulation using particles*. McGraw-Hill Education, London [1981]
- HÖRLEIN, R., Y. NOMURA, J. OSTERHOFF, ZS. MAJOR, S. KARSCH, F. KRAUSZ, and G. D. TSAKIRIS. High harmonics from solid surfaces as a source of ultra-bright XUV radiation for experiments. *Plasma Physics and Controlled Fusion* **50** (12), 124002 [2008]
- HOSOKAI, T., M. KANDO, H. DEWA, H. KOTAKI, S. KONDO, N. HASEGAWA, K. NAKAJIMA, and K. HORIOKA. Optical guidance of terawatt laser pulses by the implosion phase of a fast Z-pinch discharge in a gas-filled capillary. *Optics Letters* **25** (1), 10–12 [2000]
- HOSOKAI, T., K. KINOSHITA, A. ZHIDKOV, K. NAKAMURA, T. WATANABE, T. UEDA, H. KOTAKI, M. KANDO, K. NAKAJIMA, and M. UESAKA. Effect of a laser prepulse on a narrow-cone ejection of MeV electrons from a gas jet irradiated by an ultrashort laser pulse. *Physical Review E* **67** (3), 036407 [2003]
- HOSOKAI, T., K. KINOSHITA, T. OHKUBO, A. MAEKAWA, M. UESAKA, A. ZHIDKOV, A. YAMAZAKI, H. KOTAKI, M. KANDO, K. NAKAJIMA, S. V. BULANOV, P. TOMASSINI, A. GIULIETTI, and D. GIULIETTI. Observation of strong correlation between quasimonoenergetic electron beam generation by laser wakefield and laser guiding inside a preplasma cavity. *Physical Review E* **73** (3), 036407 [2006]
- HSIEH, C.-T., C.-M. HUANG, C.-L. CHANG, Y.-C. HO, Y.-S. CHEN, J.-Y. LIN, J. WANG, and S.-Y. CHEN. Tomography of injection and acceleration of monoenergetic electrons in a laser-wakefield accelerator. *Physical Review Letters* **96** (9), 095001 [2006]
- HUMPHRIES, S. *Principles of charged particle acceleration*. John Wiley & Sons, New York [1999]
- ITATANI, J., J. FAURE, M. NANTEL, G. MOUROU, and S. WATANABE. Suppression of the amplified spontaneous emission in chirped-pulse-amplification lasers by clean high-energy seed-pulse injection. *Optics Communications* **148** (1–3), 70–74 [1998]

- JACKSON, J. D. *Classical electrodynamics*. John Wiley & Sons, New York, 2nd edition [1975]
- JAROSZYNSKI, D. A., R. BINGHAM, E. BRUNETTI, B. ERSFELD, B. VAN DER GEER, J. GALLACHER, R. ISSAC, P. JAMISON, D. JONES, M. DE LOOS, A. LYACHEV, V. PAVLOV, A. REITSMA, Y. SAVELIEV, G. VIEUX, and S. M. WIGGINS. Radiation sources based on laser-plasma interactions. *Philosophical Transactions of the Royal Society A* **364**, 689–710 [2006]
- JULLIEN, A., O. ALBERT, F. BURGY, G. HAMONIAUX, J.-P. ROUSSEAU, J.-P. CHAMBARET, F. AUGÉ-ROCHEREAU, G. CHÉRIAUX, J. ETCHEPARE, N. MINKOVSKI, and S. M. SALTIEL. 10^{-10} temporal contrast for femtosecond ultraintense lasers by cross-polarized wave generation. *Optics Letters* **30** (8), 920–922 [2005]
- KAGANOVICH, D., A. TING, C. I. MOORE, A. ZIGLER, H. R. BURRIS, Y. EHRLICH, R. HUBBARD, and P. SPRANGLE. High efficiency guiding of terawatt subpicosecond laser pulses in a capillary discharge plasma channel. *Physical Review E* **59** (5), R4769–R4772 [1999]
- KANE, D. J. and R. TREBINO. Single-shot measurement of the intensity and phase of an arbitrary ultrashort pulse by using frequency-resolved optical gating. *Optics Letters* **18** (10), 823–825 [1993]
- KANE, J., D. ARNETT, B. A. REMINGTON, S. G. GLENDINNING, J. CASTOR, R. WALLACE, A. RUBENCHIK, and B. A. FRYXELL. Supernova-relevant hydrodynamic instability experiments on the NOVA laser. *Astrophysical Journal* **478** (1), L75–L78 [1997]
- KARSCH, S., J. OSTERHOFF, A. POPP, T. P. ROWLANDS-REES, ZS. MAJOR, M. FUCHS, B. MARX, R. HÖRLEIN, K. SCHMID, L. VEISZ, S. BECKER, U. SCHRAMM, B. HIDDING, G. PRETZLER, D. HABS, F. GRÜNER, F. KRAUSZ, and S. M. HOOKER. GeV-scale electron acceleration in a gas-filled capillary discharge waveguide. *New Journal of Physics* **9**, 415 [2007]
- KARSCH, S., ZS. MAJOR, J. FÜLÖP, I. AHMAD, T.-J. WANG, A. HENIG, S. KRUBER, R. WEINGARTNER, M. SIEBOLD, J. HEIN, C. WANDT, S. KLINGEBIEL, J. OSTERHOFF, R. HÖRLEIN, and F. KRAUSZ. The petawatt field synthesizer: a new approach to ultrahigh field generation. In *Advanced Solid-State Photonics* [2008]
- KATSOULEAS, T. and J. M. DAWSON. Unlimited electron acceleration in laser-driven plasma waves. *Physical Review Letters* **51** (5), 392–395 [1983]
- KATSOULEAS, T. and W. B. MORI. Wave-breaking amplitude of relativistic oscillations in a thermal plasma. *Physical Review Letters* **61** (1), 90–93 [1988]
- KATSOULEAS, T. Plasma accelerators race to 10 GeV and beyond. *Physics of Plasmas* **13** (5), 055503 [2006]

- KAW, P. and J. DAWSON. Relativistic nonlinear propagation of laser beams in cold overdense plasmas. *Physics of Fluids* **13** (2), 472–481 [1970]
- KELDYSH, L. V. Ionization in the field of a strong electromagnetic wave. *Soviet Physics, Journal of Experimental and Theoretical Physics* **20**, 1307–1314 [1965]
- KINGHAM, R. J. and A. R. BELL. Enhanced wakefields for the 1d laser wakefield accelerator. *Physical Review Letters* **79** (24), 4810–4813 [1997]
- KISELEV, S., A. PUKHOV, and I. KOSTYUKOV. X-ray generation in strongly nonlinear plasma waves. *Physical Review Letters* **93** (13), 135004 [2004]
- KONDRATENKO, A. M. and E. L. SALDIN. Generation of coherent radiation by a relativistic-electron beam in an undulator. *Doklady Physics* **24**, 986 [1979]
- KRAMERS, H. A. Wellenmechanik und halbzahlige Quantisierung. *Zeitschrift für Physik* **39** (11), 828–840 [1926]
- KRAUSZ, F. *Photonics I and II*. Lecture notes, Ludwig-Maximilians-Universität München [2006]
- KRUER, W. L. *The physics of laser plasma interactions*. Westview Press, Boulder [2003]
- LAMBROPOULOS, P. Mechanisms for multiple ionization of atoms by strong pulsed lasers. *Physical Review Letters* **55** (20), 2141–2144 [1985]
- LAWSON, J. D. Lasers and accelerators. *IEEE Transactions on Nuclear Science* **26** (9), 4217–4219 [1979]
- LEE, S., T. KATSOULEAS, R. HEMKER, and W. B. MORI. Simulations of a meter-long plasma wakefield accelerator. *Physical Review E* **61** (6), 7014–7021 [2000]
- LEEMANS, W. P., C. W. SIDERS, E. ESAREY, N. E. ANDREEV, G. SHVETS, and W. B. MORI. Plasma guiding and wakefield generation for second-generation experiments. *IEEE Transactions on Plasma Science* **24** (2), 331–342 [1996]
- LEEMANS, W. P., P. CATRAVAS, E. ESAREY, C. G. R. GEDDES, C. TÓTH, R. TRINES, C. B. SCHROEDER, B. A. SHADWICK, J. VAN TILBORG, and J. FAURE. Electron-yield enhancement in a laser-wakefield accelerator driven by asymmetric laser pulses. *Physical Review Letters* **89** (17), 174802 [2002]
- LEEMANS, W. P., B. NAGLER, A. J. GONSALVES, C. TÓTH, K. NAKAMURA, C. G. R. GEDDES, E. ESAREY, C. B. SCHROEDER, and S. M. HOOKER. GeV electron beams from a centimetre-scale accelerator. *Nature Physics* **2** (10), 696–699 [2006]
- LEMOFF, B. E. and C. P. J. BARTY. Quintic-phase-limited, spatially uniform expansion and recompression of ultrashort optical pulses. *Optics Letters* **18** (19), 1651–1653 [1993]

- LITVAK, A. G. Finite-amplitude wave beams in a magnetoactive plasma. *Soviet Physics, Journal of Experimental and Theoretical Physics* **30**, 344–347 [1970]
- LOPES, N. C., G. FIGUEIRA, L. O. SILVA, J. M. DIAS, R. FONSECA, L. CARDOSO, C. RUSSO, C. CARIAS, G. MENDES, J. VIEIRA, and J. T. MENDONÇA. Plasma channels produced by a laser-triggered high-voltage discharge. *Physical Review E* **68** (3), 035402 [2003]
- LU, W., M. TZOUFRAS, C. JOSHI, F. S. TSUNG, W. B. MORI, J. VIEIRA, R. A. FONSECA, and L. O. SILVA. Generating multi-GeV electron bunches using single stage laser wakefield acceleration in a 3D nonlinear regime. *Physical Review Special Topics – Accelerators and Beams* **10** (6), 061301 [2007]
- LUAN, S., M. H. R. HUTCHINSON, R. A. SMITH, and F. ZHOU. High dynamic range third-order correlation measurement of picosecond laser pulse shapes. *Measurement Science and Technology* **4** (12), 1426–1429 [1993]
- MAINFRAY, G. and G. MANUS. Multiphoton ionization of atoms. *Reports on Progress in Physics* **54** (10), 1333–1372 [1991]
- MAKSIMCHUK, A., S. GU, K. FLIPPO, D. UMSTADTER, and V. YU. BYCHENKOV. Forward ion acceleration in thin films driven by a high-intensity laser. *Physical Review Letters* **84** (18), 4108–4111 [2000]
- MALKA, V., S. FRITZLER, E. LEFEBVRE, M.-M. ALEONARD, F. BURGY, J.-P. CHAMBARET, J.-F. CHEMIN, K. KRUSHELNICK, G. MALKA, S. P. D. MANGLES, Z. NAJMUDIN, M. PITTMAN, J.-P. ROUSSEAU, J.-N. SCHEURER, B. WALTON, and A. E. DANGOR. Electron acceleration by a wake field forced by an intense ultrashort laser pulse. *Science* **298** (5598), 1596–1600 [2002]
- MANGLES, S. P. D., C. D. MURPHY, Z. NAJMUDIN, A. G. R. THOMAS, J. L. COLLIER, A. E. DANGOR, E. J. DIVALL, P. S. FOSTER, J. G. GALLACHER, C. J. HOOKER, D. A. JAROSZYNSKI, A. J. LANGLEY, W. B. MORI, P. A. NORREYS, F. S. TSUNG, R. VISKUP, B. R. WALTON, and K. KRUSHELNICK. Monoenergetic beams of relativistic electrons from intense laser-plasma interactions. *Nature* **431** (7008), 535–538 [2004]
- MANGLES, S. P. D., A. G. R. THOMAS, O. LUNDH, F. LINDAU, M. C. KALUZA, A. PERS-SON, C.-G. WAHLSTRÖM, K. KRUSHELNICK, and Z. NAJMUDIN. On the stability of laser wakefield electron accelerators in the monoenergetic regime. *Physics of Plasmas* **14** (5), 056702 [2007]
- MARTÍNEZ, O. E. Design of high-power ultrashort pulse amplifiers by expansion and recompression. *IEEE Journal of Quantum Electronics* **23** (8), 1385–1387 [1987]

- MARX, B. *Interferometrie eines Plasmadichtegradienten in einer Gasentladungskapillare*. Diploma thesis, Ludwig-Maximilians-Universität München [2008]
- MAX, C. E., J. ARONS, and A. B. LANGDON. Self-modulation and self-focusing of electromagnetic waves in plasmas. *Physical Review Letters* **33** (4), 209–212 [1974]
- MAXWELL, J. C. On physical lines of force. *The London, Edinburgh and Dublin Philosophical Magazine and Journal of Science* **21** (139), 161 et seq. [1861]
- MCKINSTRIE, C. J. and D. F. DUBOIS. A covariant formalism for wave propagation applied to stimulated Raman scattering. *Physics of Fluids* **31** (2), 278–287 [1988]
- MESCHEDE, D. *Gerthsen Physik*. Springer Verlag, Heidelberg, 23rd edition [2006]
- MEYERHOFER, D. D. High-intensity-laser-electron scattering. *IEEE Journal of Quantum Electronics* **33** (11), 1935–1941 [1997]
- MILOSEVIC, N., V. P. KRAINOV, and T. BRABEC. Relativistic theory of tunnel ionization. *Journal of Physics B* **35** (16), 3515–3529 [2002]
- MIURA, E., K. KOYAMA, S. KATO, N. SAITO, M. ADACHI, Y. KAWADA, T. NAKAMURA, and M. TANIMOTO. Demonstration of quasi-monoenergetic electron-beam generation in laser-driven plasma acceleration. *Applied Physics Letters* **86** (25), 251501 [2005]
- MODENA, A., Z. NAJMUDIN, A. E. DANGOR, C. E. CLAYTON, K. A. MARSH, C. JOSHI, V. MALKA, C. B. DARROW, C. DANSON, D. NEELY, and F. N. WALSH. Electron acceleration from the breaking of relativistic plasma waves. *Nature* **377**, 606–608 [1995]
- MOMOSE, A., T. TAKEDA, Y. ITAI, and K. HIRANO. Phase-contrast X-ray computed tomography for observing biological soft tissues. *Nature Medicine* **2**, 473–475 [1996]
- MOORE, C. I., J. P. KNAUER, and D. D. MEYERHOFER. Observation of the transition from thomson to compton scattering in multiphoton interactions with low-energy electrons. *Physical Review Letters* **74** (13), 2439–2442 [1995]
- MOORE, C. I., A. TING, S. J. MCNAUGHT, J. QIU, H. R. BURRIS, and P. SPRANGLE. A laser-accelerator injector based on laser ionization and ponderomotive acceleration of electrons. *Physical Review Letters* **82** (8), 1688–1691 [1999]
- MORI, W. B., C. JOSHI, J. M. DAWSON, D. W. FORSLUND, and J. M. KINDEL. Evolution of self-focusing of intense electromagnetic waves in plasma. *Physical Review Letters* **60** (13), 1298–1301 [1988]
- MORI, W. B. The physics of the nonlinear optics of plasmas at relativistic intensities for short-pulse lasers. *IEEE Journal of Quantum Electronics* **33** (11), 1942–1953 [1997]

- MOULTON, P. F. Spectroscopic and laser characteristics of Ti:Al₂O₃. *Journal of the Optical Society of America B: Optical Physics* **3** (1), 125–133 [1986]
- MOUROU, G. A., T. TAJIMA, and S. V. BULANOV. Optics in the relativistic regime. *Reviews of Modern Physics* **78** (2), 309–371 [2006]
- MUSIOL, G., J. RANFT, R. REIF, and D. SEELIGER. *Kern- und Elementarteilchenphysik*. VCH Verlagsgesellschaft, Weinheim [1988]
- NAKAMURA, K., B. NAGLER, Cs. TÓTH, C. G. R. GEDDES, C. B. SCHROEDER, E. ESAREY, W. P. LEEMANS, A. J. GONSALVES, and S. M. HOOKER. GeV electron beams from a centimeter-scale channel guided laser wakefield accelerator. *Physics of Plasmas* **14** (5), 056708 [2007]
- NANTEL, M., J. ITATANI, A.-C. TIEN, J. FAURE, D. KAPLAN, M. BOUVIER, T. BUMA, P. VAN ROMPAY, J. NEES, P. P. PRONKO, D. UMSTADTER, and G. A. MOUROU. Temporal contrast in Ti:sapphire lasers: characterization and control. *IEEE Journal of Selected Topics in Quantum Electronics* **4** (2), 449–458 [1998]
- NEUTZE, R., R. WOUTS, D. VAN DER SPOEL, E. WECKERT, and J. HAJDU. Potential for biomolecular imaging with femtosecond x-ray pulses. *Nature* **406**, 752–757 [2000]
- NIETER, C. and J. R. CARY. VORPAL: a versatile plasma simulation code. *Journal of Computational Physics* **196** (2), 448–473 [2004]
- NOBLE, R. J. Plasma-wave generation in the beat-wave accelerator. *Physical Review A* **32** (1), 460–471 [1985]
- NOMURA, Y., R. HÖRLEIN, P. TZALLAS, B. DROMEY, S. RYKOVANOV, Zs. MAJOR, J. OSTERHOFF, S. KARSCH, L. VEISZ, M. ZEPF, D. CHARALAMBIDIS, F. KRAUSZ, and G. D. TSAKIRIS. Attosecond phase locking of harmonics emitted from laser-produced plasmas. *Nature Physics*, advance online publication [2008]
- NUCKOLLS, J., L. WOOD, A. THIESSEN, and G. ZIMMERMAN. Laser compression of matter to super-high densities: thermonuclear (CTR) applications. *Nature* **239**, 139–142 [1972]
- ONUKI, H. and P. ELLEAUME. *Undulators, wigglers and their applications*. CRC Press, Boca Raton [2003]
- O'SHEA, P., M. KIMMEL, X. GU, and R. TREBINO. Highly simplified device for ultrashort-pulse measurement. *Optics Letters* **26** (12), 932–934 [2001]
- OSTERHOFF, J., A. POPP, Zs. MAJOR, B. MARX, T. P. ROWLANDS-REES, M. FUCHS, M. GEISSLER, R. HÖRLEIN, B. HIDDING, S. BECKER, E. A. PERALTA, U. SCHRAMM, F. GRÜNER, D. HABS, F. KRAUSZ, S. M. HOOKER, and S. KARSCH. Generation of stable,

- low-divergence electron beams by laser wakefield acceleration in a steady-state-flow gas cell. *Physical Review Letters* **101** (8), 085002 [2008]
- OSTERHOFF, J., A. POPP, ZS. MAJOR, B. MARX, T. P. ROWLANDS-REES, M. FUCHS, R. HÖRLEIN, F. GRÜNER, D. HABS, F. KRAUSZ, S. M. HOOKER, and S. KARSCH. Stable laser-driven electron beams from a steady-state-flow gas cell. In *Advanced Accelerator Concepts* (edited by C. SCHROEDER, E. ESAREY, and W. P. LEEMANS). *AIP Conference Proceedings*, accepted for publication [2009]
- PANOFSKY, W. K. H. and W. A. WENZEL. Some considerations concerning the transverse deflection of charged particles in radio-frequency fields. *Review of Scientific Instruments* **27** (11), 967–967 [1956]
- PAUL, P. M., E. S. TOMA, P. BREGER, G. MULLOT, F. AUJE, PH. BALCOU, H. G. MULLER, and P. AGOSTINI. Observation of a train of attosecond pulses from high harmonic generation. *Science* **292** (5522), 1689–1692 [2001]
- PENNINGTON, D. M., M. A. HENESIAN, and R. W. HELLWARTH. Nonlinear index of air at 1.053 μm . *Physical Review A* **39** (6), 3003–3009 [1989]
- PERELOMOV, A. M., V. S. POPOV, and M. V. TERENT'EV. Ionization of atoms in an alternating electric field. *Soviet Physics, Journal of Experimental and Theoretical Physics* **23**, 924–934 [1966]
- PESSOT, M., P. MAINE, and G. MOUROU. 1000 times expansion/compression of optical pulses for chirped pulse amplification. *Optics Communications* **62** (6), 419–421 [1987]
- PICHÉ, M. and F. SALIN. Self-mode locking of solid-state lasers without apertures. *Optics Letters* **18** (13), 1041–1043 [1993]
- PLANCK, M. Ueber das Gesetz der Energieverteilung im Normalspectrum. *Annalen der Physik* **309** (3), 553–563 [1901]
- POPP, A., J. OSTERHOFF, ZS. MAJOR, R. HÖRLEIN, M. FUCHS, R. WEINGARTNER, J. VIEIRA, M. MARTI, R. A. FONSECA, L. O. SILVA, S. M. HOOKER, F. KRAUSZ, and S. KARSCH. Steering laser-wakefield-accelerated electrons by controlling the laser pulse-front tilt. In preparation for *Physical Review Letters* [2009]
- POYNTING, J. H. *Collected scientific papers*. Cambridge University Press, London [1920]
- PRETZLER, G., A. KASPER, and K. J. WITTE. Angular chirp and tilted light pulses in CPA lasers. *Applied Physics B: Lasers and Optics* **70** (1), 1–9 [2000]
- PUKHOV, A. and J. MEYER-TER-VEHN. Relativistic magnetic self-channeling of light in near-critical plasma: three-dimensional particle-in-cell simulation. *Physical Review Letters* **76** (21), 3975–3978 [1996]

- PUKHOV, A. and J. MEYER-TER-VEHN. Relativistic laser-plasma interaction by multi-dimensional particle-in-cell simulations. *Physics of Plasmas* **5** (5), 1880–1886 [1998]
- PUKHOV, A., Z.-M. SHENG, and J. MEYER-TER-VEHN. Particle acceleration in relativistic laser channels. *Physics of Plasmas* **6** (7), 2847–2854 [1999]
- PUKHOV, A. Three-dimensional electromagnetic relativistic particle-in-cell code VLPL (Virtual Laser Plasma Lab). *Journal of Plasma Physics* **61** (3), 425–433 [1999]
- PUKHOV, A. and J. MEYER-TER-VEHN. Laser wake field acceleration: the highly non-linear broken-wave regime. *Applied Physics B: Lasers and Optics* **74** (4–5), 355–361 [2002]
- PUKHOV, A. Strong field interaction of laser radiation. *Reports on Progress in Physics* **66** (1), 47–101 [2003]
- QUESNEL, B. and P. MORA. Theory and simulation of the interaction of ultraintense laser pulses with electrons in vacuum. *Physical Review E* **58** (3), 3719–3732 [1998]
- RAE, S. C. and K. BURNETT. Detailed simulations of plasma-induced spectral blueshifting. *Physical Review A* **46** (2), 1084–1090 [1992]
- RANDALL, S. Extra dimensions and warped geometries. *Science* **296** (5572), 1422–1427 [2002]
- RECHATIN, C. Private communication [2008]
- RECKENTHAELER, P., M. CENTURION, V. S. YAKOVLEV, M. LEZIUS, F. KRAUSZ, and E. E. FILL. Proposed method for measuring the duration of electron pulses by attosecond streaking. *Physical Review A* **77** (4), 042902 [2008]
- ROUSSE, A., K. T. PHUOC, R. SHAH, A. PUKHOV, E. LEFEBVRE, V. MALKA, S. KISELEV, F. BURG, J.-P. ROUSSEAU, D. UMSTADTER, and D. HULIN. Production of a keV x-ray beam from synchrotron radiation in relativistic laser-plasma interaction. *Physical Review Letters* **93** (13), 135005 [2004]
- ROWLANDS-REES, T. P., C. KAMPERIDIS, S. KNEIP, A. J. GONSALVES, S. P. D. MANGLES, J. G. GALLACHER, E. BRUNETTI, T. IBBOTSON, C. D. MURPHY, P. S. FOSTER, M. J. V. STREETER, F. BUDDE, P. A. NORREYS, D. A. JAROSZYNSKI, K. KRUSHELNICK, Z. NAJMUDIN, and S. M. HOOKER. Laser-driven acceleration of electrons in a partially ionized plasma channel. *Physical Review Letters* **100** (10), 105005 [2008]
- SCHINS, J. M., P. BREGER, P. AGOSTINI, R. C. CONSTANTINESCU, H. G. MULLER, G. GRILLON, A. ANTONETTI, and A. MYSYROWICZ. Observation of laser-assisted Auger decay in argon. *Physical Review Letters* **73** (16), 2180–2183 [1994]
- SCHLENVOIGT, H.-P., K. HAUPT, A. DEBUS, F. BUDDE, O. JÄCKEL, S. PFOTENHAUER, H. SCHWOERER, E. ROHWER, J. G. GALLACHER, E. BRUNETTI, R. P. SHANKS, S. M.

- WIGGINS, and D. A. JAROSZYNSKI. A compact synchrotron radiation source driven by a laser-plasma wakefield accelerator. *Nature Physics* **4** (2), 130–133 [2008]
- SCHMID, K., L. VEISZ, F. TAVELLA, S. BENAVIDES, R. TAUTZ, D. HERRMANN, A. BUCK, B. HIDDING, A. MARCINKEVICIUS, U. SCHRAMM, M. GEISSLER, J. MEYER-TER VEHN, D. HABS, and F. KRAUSZ. Few-cycle-laser-driven electron acceleration. Submitted to *Physical Review Letters* [2008]
- SCHROEDER, C. B., P. B. LEE, J. S. WURTELE, E. ESAREY, and W. P. LEEMANS. Generation of ultrashort electron bunches by colliding laser pulses. *Physical Review E* **59** (5), 6037–6047 [1999]
- SEARS, C. M. S., E. R. COLBY, B. M. COWAN, R. H. SIEMANN, J. E. SPENCER, R. L. BYER, and T. PLETTNER. High-harmonic inverse-free-electron-laser interaction at 800 nm. *Physical Review Letters* **95** (19), 194801 [2005]
- SEARS, C. M. S., E. COLBY, R. ISCHEBECK, C. MCGUINNESS, J. NELSON, R. NOBLE, R. H. SIEMANN, J. SPENCER, D. WALZ, T. PLETTNER, and R. L. BYER. Production and characterization of attosecond electron bunch trains. *Physical Review Special Topics – Accelerators and Beams* **11** (6), 061301 [2008]
- SHACK, R. V. and B. C. PLATT. Production and use of a lenticular Hartmann screen. *Journal of the Optical Society of America* **61**, 656 [1971]
- SHAFER, R. Beam position monitoring. *AIP Conference Proceedings* **212**, 26–58 [1990]
- SHVETS, G. and J. S. WURTELE. Instabilities of short-pulse laser propagation through plasma channels. *Physical Review Letters* **73** (26), 3540–3543 [1994]
- SIEGMAN, A. E. *Lasers*. University Science Books, Sausalito [1986]
- SNAVELY, R. A., M. H. KEY, S. P. HATCHETT, T. E. COWAN, M. ROTH, T. W. PHILLIPS, M. A. STOYER, E. A. HENRY, T. C. SANGSTER, M. S. SINGH, S. C. WILKS, A. MACK-INNON, A. OFFENBERGER, D. M. PENNINGTON, K. YASUIKE, A. B. LANGDON, B. F. LASINSKI, J. JOHNSON, M. D. PERRY, and E. M. CAMPBELL. Intense high-energy proton beams from petawatt-laser irradiation of solids. *Physical Review Letters* **85** (14), 2945–2948 [2000]
- SOLEM, J. C. Imaging biological specimens with high-intensity soft x-rays. *Journal of the Optical Society of America B: Optical Physics* **3** (11), 1551–1565 [1986]
- SPENCE, D. E., P. N. KEAN, and W. SIBBETT. 60-fsec pulse generation from a self-mode-locked Ti:sapphire laser. *Optics Letters* **16** (1), 42–44 [1991]
- SPENCE, D. J. and S. M. HOOKER. Investigation of a hydrogen plasma waveguide. *Physical Review E* **63** (1), 015401 [2000]

- SPRANGLE, P., C.-M. TANG, and E. ESAREY. Relativistic self-focusing of short-pulse radiation beams in plasmas. *IEEE Transactions on Plasma Science* **15** (2), 145–153 [1987]
- SPRANGLE, P., E. ESAREY, A. TING, and G. JOYCE. Laser wakefield acceleration and relativistic optical guiding. *Applied Physics Letters* **53** (22), 2146–2148 [1988]
- SPRANGLE, P., E. ESAREY, and A. TING. Nonlinear theory of intense laser-plasma interactions. *Physical Review Letters* **64** (17), 2011–2014 [1990]
- SPRANGLE, P. and E. ESAREY. Interaction of ultrahigh laser fields with beams and plasmas. *Physics of Fluids B: Plasma Physics* **4** (7), 2241–2248 [1992]
- SPRANGLE, P., E. ESAREY, J. KRALL, and G. JOYCE. Propagation and guiding of intense laser pulses in plasmas. *Physical Review Letters* **69** (15), 2200–2203 [1992]
- SPRANGLE, P., J. KRALL, and E. ESAREY. Hose-modulation instability of laser pulses in plasmas. *Physical Review Letters* **73** (26), 3544–3547 [1994]
- STARTSEV, E. A. and C. J. MCKINSTRIE. Multiple scale derivation of the relativistic ponderomotive force. *Physical Review E* **55** (6), 7527–7535 [1997]
- STRICKLAND, D. and G. MOUROU. Compression of amplified chirped optical pulses. *Optics Communications* **56** (3), 219–221 [1985]
- STUPAKOV, G. V. and M. S. ZOLOTOROV. Ponderomotive laser acceleration and focusing in vacuum for generation of attosecond electron bunches. *Physical Review Letters* **86** (23), 5274–5277 [2001]
- SUK, H., N. BAROV, J. B. ROSENZWEIG, and E. ESAREY. Plasma electron trapping and acceleration in a plasma wake field using a density transition. *Physical Review Letters* **86** (6), 1011–1014 [2001]
- SUN, G.-Z., E. OTT, Y. C. LEE, and P. GUZDAR. Self-focusing of short intense pulses in plasmas. *Physics of Fluids* **30** (2), 526–532 [1987]
- SZIPÓCS, R., K. FERENCZ, C. SPIELMANN, and F. KRAUSZ. Chirped multilayer coatings for broadband dispersion control in femtosecond lasers. *Optics Letters* **19** (3), 201–203 [1994]
- TABAK, M., J. HAMMER, M. E. GLINSKY, W. L. KRUEER, S. C. WILKS, J. WOODWORTH, E. M. CAMPBELL, M. D. PERRY, and R. J. MASON. Ignition and high gain with ultra-powerful lasers. *Physics of Plasmas* **1** (5), 1626–1634 [1994]
- TAJIMA, T. and J. M. DAWSON. Laser electron accelerator. *Physical Review Letters* **43** (4), 267–270 [1979]

- TANAKA, K. A., T. YABUCHI, T. SATO, R. KODAMA, Y. KITAGAWA, T. TAKAHASHI, T. IKEDA, Y. HONDA, and S. OKUDA. Calibration of imaging plate for high energy electron spectrometer. *Review of Scientific Instruments* **76** (1), 013507 [2005]
- TAVELLA, F., A. MARCINKEVICIUS, and F. KRAUSZ. 90 mJ parametric chirped pulse amplification of 10 fs pulses. *Optics Express* **14** (26), 12822–12827 [2006]
- TAYLOR, A., M. DUNNE, S. BENNINGTON, S. ANSELL, I. GARDNER, P. NORREYS, T. BROOME, D. FINDLAY, and R. NELMES. A route to the brightest possible neutron source? *Science* **315** (5815), 1092–1095 [2007]
- TEYCHENNÉ, D., G. BONNAUD, and J.-L. BOBIN. Electrostatic and kinetic energies in the wake wave of a short laser pulse. *Physics of Plasmas* **1** (6), 1771–1773 [1994]
- THAURY, C., F. QUÉRÉ, J.-P. GEINDRE, A. LEVY, T. CECCOTTI, M. BOUGEARD, P. MONOT, F. RÉAU, P. D’OLIVEIRA, P. AUDEBERT, R. MARJORIBANKS, and P. MARTIN. Plasma mirrors for ultrahigh-intensity optics. *Nature Physics* **3**, 424–429 [2007]
- TING, A., E. ESAREY, and P. SPRANGLE. Nonlinear wake-field generation and relativistic focusing of intense laser pulses in plasmas. *Physics of Fluids B: Plasma Physics* **2** (6), 1390–1394 [1990]
- TING, A., K. KRUSHELNICK, C. I. MOORE, H. R. BURRIS, E. ESAREY, J. KRALL, and P. SPRANGLE. Temporal evolution of self-modulated laser wakefields measured by coherent thomson scattering. *Physical Review Letters* **77** (27), 5377–5380 [1996]
- TOURNOIS, P. New diffraction grating pair with very linear dispersion for laser pulse compression. *Electronics Letters* **29** (16), 1414–1415 [1993]
- TOURNOIS, P. Acousto-optic programmable dispersive filter for adaptive compensation of group delay time dispersion in laser systems. *Optics Communications* **140** (4–6), 245–249 [1997]
- TREACY, E. B. Optical pulse compression with diffraction gratings. *IEEE Journal of Quantum Electronics* **5** (9), 454–458 [1969]
- TSUNG, F. S., R. NARANG, W. B. MORI, C. JOSHI, R. A. FONSECA, and L. O. SILVA. Near-GeV-energy laser-wakefield acceleration of self-injected electrons in a centimeter-scale plasma channel. *Physical Review Letters* **93** (18), 185002 [2004]
- TSYTOVICH, V. N., U. DE ANGELIS, and R. BINGHAM. Beat-wave-wake acceleration by short high intensity laser pulses. *Comments on Plasma Physics and Controlled Fusion* **12**, 249–256 [1989]

- TZENG, K.-C., W. B. MORI, and C. D. DECKER. Anomalous absorption and scattering of short-pulse high-intensity lasers in underdense plasmas. *Physical Review Letters* **76** (18), 3332–3335 [1996]
- TZOFRAS, M., W. LU, F. S. TSUNG, C. HUANG, W. B. MORI, J. VIEIRA, R. A. FONSECA, and L. O. SILVA. The physical picture of beam loading in the blowout regime. *Proceedings of the Particle Accelerator Conference* pages 3061–3063 [2007]
- UIBERACKER, M., TH. UPHUES, M. SCHULTZE, A. J. VERHOEF, V. YAKOVLEV, M. F. KLING, J. RAUSCHENBERGER, N. M. KABACHNIK, H. SCHRÖDER, M. LEZIUS, K. L. KOMPA, H.-G. MULLER, M. J. J. VRAKING, S. HENDEL, U. KLEINEBERG, U. HEINZMANN, M. DRESCHER, and F. KRAUSZ. Attosecond real-time observation of electron tunnelling in atoms. *Nature* **446**, 627–632 [2007]
- UMSTADTER, D., J. K. KIM, and E. DODD. Laser injection of ultrashort electron pulses into wakefield plasma waves. *Physical Review Letters* **76** (12), 2073–2076 [1996a]
- UMSTADTER, D., S.-Y. CHEN, A. MAKSIMCHUK, G. MOUROU, and R. WAGNER. Nonlinear optics in relativistic plasmas and laser wake field acceleration of electrons. *Science* **273** (5274), 472–475 [1996b]
- UNGER, H. G. *Planar optical waveguides and fibers*. Clarendon Press, Oxford [1977]
- VAN TILBORG, J., C. B. SCHROEDER, E. ESAREY, and W. P. LEEMANS. Pulse shape and spectrum of coherent diffraction-limited transition radiation from electron beams. *Laser and Particle Beams* **22**, 415–422 [2004]
- VAN TILBORG, J., C. B. SCHROEDER, C. V. FILIP, Cs. TÓTH, C. G. R. GEDDES, G. FUBIANI, R. HUBER, R. A. KAINDL, E. ESAREY, and W. P. LEEMANS. Temporal characterization of femtosecond laser-plasma-accelerated electron bunches using terahertz radiation. *Physical Review Letters* **96** (1), 014801 [2006]
- VARJÚ, K., A. P. KOVÁCS, G. KURDI, and K. OSVAY. High-precision measurement of angular dispersion in a CPA laser. *Applied Physics B: Lasers and Optics* **74** (S1), S259–S263 [2002]
- VILLASENOR, J. and O. BUNEMAN. Rigorous charge conservation for local electromagnetic field solvers. *Computer Physics Communications* **69** (2–3), 306–316 [1992]
- VOLFBEYN, P., E. ESAREY, and W. P. LEEMANS. Guiding of laser pulses in plasma channels created by the ignitor-heater technique. *Physics of Plasmas* **6** (5), 2269–2277 [1999]
- VORONOV, G. S. and N. B. DELONE. Ionization of xenon atom by electric field of ruby laser emission. *Soviet Physics, Journal of Experimental and Theoretical Physics Letters* **1**, 66–68 [1965]

- WANG, P. X., Y. K. HO, X. Q. YUAN, Q. KONG, N. CAO, A. M. SESSLER, E. ESAREY, and Y. NISHIDA. Vacuum electron acceleration by an intense laser. *Applied Physics Letters* **78** (15), 2253–2255 [2001]
- WARTSKI, L., J. MARCOU, and S. ROLAND. Detection of optical transition radiation and its application to beam diagnostics. *IEEE Transactions on Nuclear Science* **20** (3), 544–548 [1973]
- WEBER, M. J. *CRC handbook of laser science and technology: optical materials*. CRC Press, Boca Raton [1995]
- WEINBERG, S. A model of leptons. *Physical Review Letters* **19** (21), 1264–1266 [1967]
- WEINGARTNER, R. Private communication [2008]
- WENTZEL, G. Eine Verallgemeinerung der Quantenbedingungen für die Zwecke der Wellenmechanik. *Zeitschrift für Physik* **38** (7), 518–529 [1926]
- WHITE, W. E., F. G. PATTERSON, R. L. COMBS, D. F. PRICE, and R. L. SHEPHERD. Compensation of higher-order frequency-dependent phase terms in chirped-pulse amplification systems. *Optics Letters* **18** (16), 1343–1345 [1993]
- WHITTUM, D. H., A. M. SESSLER, and J. M. DAWSON. Ion-channel laser. *Physical Review Letters* **64** (21), 2511–2514 [1990]
- WILKS, S. C., J. M. DAWSON, W. B. MORI, T. KATSOULEAS, and M. E. JONES. Photon accelerator. *Physical Review Letters* **62** (22), 2600–2603 [1989]
- WILLE, K. *Physik der Teilchenbeschleuniger und Synchrotronstrahlungsquellen*. B. G. Teubner, Stuttgart, 2nd edition [1996]
- WOODWARD, P. M. A method of calculating the field over a plane. *Journal of the Institution of Electrical Engineers* **93**, 1554–1558 [1947]
- YANOVSKY, V., V. CHVYKOV, G. KALINCHENKO, P. ROUSSEAU, T. PLANCHON, T. MATSUOKA, A. MAKSIMCHUK, J. NEES, G. CHERIAUX, G. MOUROU, and K. KRUSHELNICK. Ultra-high intensity, 300-TW laser at 0.1 Hz repetition rate. *Optics Express* **16** (3), 2109–2114 [2008]
- ZIEREP, J. and K. BÜHLER. *Strömungsmechanik*. Springer Verlag, Heidelberg [1991]
- ZINTH, W. and H.-J. KÖRNER. *Physik III: Optik, Quantenphänomene und Aufbau der Atome*. R. Oldenbourg Verlag, München, 3rd edition [1998]

Acknowledgements

Science is an unfair business. Under typical circumstances, numerous people are involved in the creation of a scientific project, its setup, execution, and evaluation. However, just a few of them are usually given the credit they deserve. This especially applies for all the work that culminates in the compilation of a dissertation, which in the end bears only a single author's name. Therefore I would like to acknowledge everybody, who notably contributed to the document at hand. Specifically, but not exclusively, these people are:

- **Prof. Dr. Ferenc Krausz**, my doctoral advisor, has always been a source of inspiration and support. He is a very ambitious and respectable person and a great group leader. I would like to thank him for having given me the opportunity to work in such an outstanding environment.
- **Prof. Dr. Stefan Karsch** directly supervised my work. He is a constant driving force and probably knows more about high-intensity laser design and laser-plasma physics than anybody else I know, even though he would deny that, if you asked him. I admire a lot his talent to intuitively grasp even most complicated physical processes with ease. Besides, he masters a subtle way of conveying the importance of political correctness, precise schedules and the art of accounting to the interested observer.
- **Prof. Dr. Klaus Witte** kindly volunteered as a reviewer for this thesis.
- **Dr. Zsuzsanna Major** is the heart and soul of our electron-acceleration group. She is unbelievably helpful, easy to get along with and usually has a good advice at the right moment. Her near-native mastery of the English language (including an unmistakable accent) turns out to be invaluable when all sorts of documents need to be written and corrected. Nagyon jó veled dolgozni – töktök!
- **Antonia Popp** spent countless hours working on the electron-acceleration setup and on the automated data acquisition system. She is a great lab mate and without her the discussed experiments would never have taken place.
- **Benjamin Marx** put a lot of effort into characterizing the gas-density profiles and gas-flow properties of our capillary waveguides.
- **Rainer Hörlein** and **Elisabeth Magerl**, my longtime office mates, had to endure my increased presence during the last six months while I was feverishly preparing this

manuscript. Particularly, Elisabeth had to suffer from my obsession to always work in front of an open window – with little dependence on the weather outside.

- **Sergey Rykovanov** is a fantastic comrade and taught me how to play basketball the Russian way, which arguably constitutes the only technique to defend the Ukrainian elbow attack... One might ask, how the heck that concerns the completion of this work. Well, the answer is easy: without basketball and the occasional late night out, I probably would have finished a couple of weeks earlier (but definitely a little grumpier).
- **Matthias Fuchs, Raphael Weinberger, and Prof. Dr. Florian Grüner** are members of the magnificent LMU-undulator crew. They are not only a pleasure to work with in the lab (for different reasons, not just noises), they also managed to compile a very successful experiment. In addition, I have to thank Raphael for a full-blown set of new nicknames and Matthias for illegal accommodation.
- **Dr. Simon Hooker** transferred his knowledge and blueprints of capillary discharge waveguides directly from the University of Oxford to Garching, and hence helped to initiate the experiments presented here. His graduate student **Tom Rowlands-Rees** introduced us into the magic of capillary alignment with a remarkable attention to detail. By the way, he not only is a very clever guy, but also the true inventor of both, lists and diagrams.
- I want to thank **Prof. Dr. Luís Silva** and his group members **Prof. Dr. Ricardo Fonseca, Michael Marti** and **Jorge Vieira** for the warm welcome and an enjoyable stay in Lisbon, where they furnished me with the skills to handle and understand their PIC code OSIRIS. Since then they have straightforwardly been supporting us in the best possible manner.
- **Frau Schütz** and **Frau Wild** are administratively world-leading and organizationally excellent. Almost everything they do miraculously works out. I wish they had time to help in the lab...
- **Herr Haas, Herr Fischer, and Herr Böswald** were extremely cooperative with fixing, designing, building, indexing, and preserving all sorts of hardware, gadgets and indispensable experimental components.
- Of course, there would have been no experimental setup without the work of the two machine-shop teams at MPQ and LMU. Many cheers to them!
- **Inga** has always been there for me, even though most of Germany lay between us.
- My parents, **Maria** and **Franz-Josef** had the patience and prudence to actively support me throughout my educational career, no matter which path I took. For this I am sincerely grateful. I am also thankful that they did not name me Ingo.

Curriculum vitae

Contact information

Name Jens Osterhoff
Address Theresienstraße 122
80333 München
Germany
Phone +49 (151) 22622254 mobile
+49 (89) 23548696 home
E-mail jens.osterhoff@mac.com



Personal data

Date and place of birth September 9, 1979 in Damme, Germany
Citizenship German **Gender** male

Academic experience and education

Max-Planck-Institut für Quantenoptik in Garching, Germany **since February 2005**
and **Ludwig-Maximilians-Universität München**, Germany

Doctoral candidate in physics, February 2009

- Dissertation title: “Stable, ultra-relativistic electron beams by laser-wakefield acceleration”
- Supervisor: Prof. Dr. Ferenc Krausz

Graduate research assistant within the excellence cluster framework of the Munich-Center for Advanced Photonics (MAP)

The University of Texas at Austin, U.S.A. **August 2003 - December 2004**

Master of Arts in physics, awarded in December 2004

- Thesis title: “Ultrahigh intensity laser-launched radiative blast waves related to supernova remnant formation”
- Supervisor: Prof. Dr. Todd Ditmire

Graduate research assistant at the Texas Center for High Intensity Laser Science (TCHILS)

Julius-Maximilians-Universität Würzburg, Germany **October 2000 - July 2003**

Vordiplom in physics, awarded in October 2002

- Minor subject as graduate student: bioinformatics
- Minor subject as undergraduate student: chemistry

Teaching assistant for undergraduate-level physics lab courses (October 2002 - July 2003)

Allgemeines Gymnasium Lohne, Germany **August 1992 - June 1999**

Abitur, awarded in June 1999

- Advanced coursework in mathematics and physics

Academic scholarships

C. Paul Boner Graduate Fellowship in Physics **September 2003 - May 2004**

Deutscher Akademischer Austausch Dienst **September 2003 - May 2004**

e-fellows.net GmbH & Co. KG **September 2001 - March 2008**

Professional memberships

Optical Society of America (OSA) **since February 2006**

Deutsche Physikalische Gesellschaft (DPG) **since February 2005**

Additional professional experience

St.-Franziskus-Hospital in Lohne, Germany **August 1999 - July 2000**
Administration secretary (civilian service)

Administrative responsibilities at the patient admission and emergency room

Oldenburgische Volkszeitung Druckerei und Verlag KG in Vechta, Germany, and
Delmenhorster Kreisblatt Verlag RIECK GmbH & Co. KG in Delmenhorst, Germany
Freelance journalist **September 1997 - October 2000**

Coverage of local and regional sport events for the sports departments of the newspapers *Oldenburgische Volkszeitung*, *Oldenburgische Volkszeitung am Sonntag*, and *Delmenhorster Kreisblatt*

Scientific publications and honors

Awards

- [1] Recipient of the *2008 Advanced Accelerator Concepts Workshop Poster Prize* for “outstanding scientific research and presentation” in the field of laser-plasma accelerators.

Publications

The following entries are arranged in reversed chronological order of appearance.

- [12] J. OSTERHOFF, A. POPP, ZS. MAJOR, B. MARX, T. P. ROWLANDS-REES, M. FUCHS, R. HÖRLEIN, F. GRÜNER, D. HABS, F. KRAUSZ, S. M. HOOKER, and S. KARSCH. Stable laser-driven electron beams from a steady-state-flow gas cell. *Advanced Accelerator Concepts* (edited by C. SCHROEDER, E. ESAREY, and W. P. LEE-MANS). *AIP Conference Proceedings*, accepted for publication [2009]
- [11] A. HENIG, D. KIEFER, M. GEISSLER, S. G. RYKOVANOV, R. RAMIS, R. HÖRLEIN, J. OSTERHOFF, ZS. MAJOR, S. KARSCH, F. KRAUSZ, D. HABS, and J. SCHREIBER. Laser-driven shock acceleration of ion beams from spherical mass-limited targets. *Physical Review Letters*, accepted for publication [2009]
- [10] J. OSTERHOFF, D. R. SYMES, A. D. EDENS, A. S. MOORE, E. HELLEWELL, and T. DITMIRE. Radiative shell thinning in intense laser-driven blast waves. *New Journal of Physics*, accepted for publication [2009]
- [9] Y. NOMURA, R. HÖRLEIN, P. TZALLAS, B. DROMEY, S. RYKOVANOV, ZS. MAJOR, J. OSTERHOFF, S. KARSCH, L. VEISZ, M. ZEPF, D. CHARALAMBIDIS, F. KRAUSZ, and G. D. TSAKIRIS. Attosecond phase locking of harmonics emitted from laser-produced plasmas. *Nature Physics*, advance online publication [2008]
- [8] R. HÖRLEIN, Y. NOMURA, J. OSTERHOFF, ZS. MAJOR, S. KARSCH, F. KRAUSZ, and G. D. TSAKIRIS. High harmonics from solid surfaces as a source of ultra-bright XUV radiation for experiments. *Plasma Physics and Controlled Fusion* **50** (12), 124002 [2008]
- [7] J. OSTERHOFF, A. POPP, ZS. MAJOR, B. MARX, T. P. ROWLANDS-REES, M. FUCHS, M. GEISSLER, R. HÖRLEIN, B. HIDDING, S. BECKER, E. A. PERALTA,

- U. SCHRAMM, F. GRÜNER, D. HABS, F. KRAUSZ, S. M. HOOKER, and S. KARSCH. Generation of stable, low-divergence electron beams by laser wakefield acceleration in a steady-state-flow gas cell. *Physical Review Letters* **101** (8), 085002 [2008]
- [6] J. A. FÜLÖP, ZS. MAJOR, A. HENIG, S. KRUBER, R. WEINGARTNER, T. CLAUSNITZER, E.-B. KLEY, J. OSTERHOFF, R. HÖRLEIN, F. KRAUSZ, and S. KARSCH. Short-pulse optical parametric chirped-pulse amplification for the generation of high-power few-cycle pulses. *New Journal of Physics* **9** (12), 438 [2007]
- [5] S. KARSCH, J. OSTERHOFF, A. POPP, T. P. ROWLANDS-REES, ZS. MAJOR, M. FUCHS, B. MARX, R. HÖRLEIN, K. SCHMID, L. VEISZ, S. BECKER, U. SCHRAMM, B. HIDDING, G. PRETZLER, D. HABS, F. GRÜNER, F. KRAUSZ, and S. M. HOOKER. GeV-scale electron acceleration in a gas-filled capillary discharge waveguide. *New Journal of Physics* **9** (11), 415 [2007] (IOP select)
- [4] D. R. SYMES, J. OSTERHOFF, R. FÄUSTLIN, M. MAURER, A. C. BERNSTEIN, A. S. MOORE, E. T. GUMBRELL, A. D. EDENS, R. A. SMITH, and T. DITMIRE. Production of periodically modulated laser driven blast waves in a clustering gas. *High Energy Density Physics* **3** (3–4), 353–357 [2007]
- [3] T. DITMIRE, M. HOHENBERGER, D. R. SYMES, K. W. MADISON, F. BUERSENGS, R. HARTKE, J. OSTERHOFF, A. HENIG, and A. D. EDENS. Intense femtosecond laser driven explosions of heteronuclear clusters. *Femtochemistry VII* (edited by W. CASTLEMAN JR.). ISBN 0-444-52821-0. Elsevier Science [2006]
- [2] T. DITMIRE, M. HOHENBERGER, D. R. SYMES, K. W. MADISON, F. BUERSENGS, R. HARTKE, J. OSTERHOFF, A. HENIG, and A. D. EDENS. Explosions of methane and deuterated methane clusters irradiated by intense femtosecond laser pulses. *Superstrong Fields in Plasmas* (edited by D. BATANI and M. LONTANO). ISBN 0-7354-0319-8. *AIP Conference Proceedings* **827** (1), 109–118 [2006]
- [1] F. BUERSENGS, K. W. MADISON, D. R. SYMES, R. HARTKE, J. OSTERHOFF, W. GRIGSBY, G. DYER, and T. DITMIRE. Angular distribution of neutrons from deuterated cluster explosions driven by femtosecond laser pulses. *Physical Review E* **74** (1), 016403 [2006]

Submitted manuscripts

- [1] ZS. MAJOR, S. TRUSHIN, I. AHMAD, M. SIEBOLD, C. WANDT, S. KLINGEBIEL, T.-J. WANG, J. A. FÜLÖP, A. HENIG, S. KRUBER, R. WEINGARTNER, A. POPP, J. OSTERHOFF, R. HÖRLEIN, J. HEIN, V. PERVAK, A. APOLONSKI, F. KRAUSZ, and S. KARSCH. Basic concepts and current status of the Petawatt Field Synthesizer – a new approach to ultrahigh field generation. Submitted to *The Review of Laser Engineering* [2009]

Manuscripts in preparation

- [3] M. FUCHS, R. WEINGARTNER, A. POPP, ZS. MAJOR, S. BECKER, J. OSTERHOFF, R. HÖRLEIN, G. D. TSAKIRIS, U. SCHRAMM, T. P. ROWLANDS-REES, S. M. HOOKER, D. HABS, F. KRAUSZ, S. KARSCH, and F. GRÜNER. Table-top laser-driven ultrafast undulator radiation in the soft X-ray range.

- [2] A. POPP, J. OSTERHOFF, ZS. MAJOR, R. HÖRLEIN, M. FUCHS, R. WEINGARTNER, J. VIEIRA, M. MARTI, R. A. FONSECA, L. O. SILVA, S. M. HOOKER, F. KRAUSZ, and S. KARSCH. Steering laser-wakefield-accelerated electrons by controlling the laser pulse-front tilt.

- [1] M. BEHMKE, R. HÖRLEIN, Y. NOMURA, J. KEYLING, J. OSTERHOFF, ZS. MAJOR, S. KARSCH, F. KRAUSZ, D. HEMMERS, G. D. TSAKIRIS, and G. PRETZLER. Temporal characteristics of coherent wakefield laser harmonics generated at solid surfaces.

